SYNTHESIS OF SOLID ACID CATALYSTS FROM KAOLIN FOR EFFICIENT PRODUCTION OF BIODIESEL FROM SHEA BUTTER

PETER ADENIYI ALABA

FACULTY OF ENGINEERING
UNIVERSITY OF MALAYA
KUALA LUMPUR

2015

SYNTHESIS OF SOLID ACID CATALYSTS FROM KAOLIN FOR EFFICIENT PRODUCTION OF BIODIESEL FROM SHEA BUTTER

PETER ADENIYI ALABA

DISSERTATION SUBMITTED IN FULFILMENT OF THE REQUIREMENTS FOR THE DEGREE OF MASTER OF ENGINEERING SCIENCE

FACULTY OF ENGINEERING
UNIVERSITY OF MALAYA
KUALA LUMPUR

2015

ABSTRACT

This study reports synthesis of solidacid catalyst from cheaper raw materials for efficient biodiesel production. The dissertation consists of six main research section including: (1) Synthesis and characterization of ordered solidacid catalyst from kaolin; (2) Synthesis and characterization of hierarchical nanoporous HY zeolite from acid activated kaolin; (3) Synthesis of nanoporous HY zeolites from activated kaolin, a central composite design (CCD) optimization study; (4) Synthesis and application of hierarchical mesoporous HZSM-5 for biodiesel production; (5) Synthesis and characterization of sulfated HY zeolite (SHY) for biodiesel production; (6) Comparative pyrolysis kinetics study of biodiesel produced from Mesoporous ZSM-5 zeolites and Microporous ZSM-5. Towards synthesis of solidacid kaolinite, all the kaolinites peaks in the starting material disappeared after the thermal and acid activation. However, most of the crystalline peaks reappeared with greater intensities at the (0211) band after NaOH impregnation. Further, the crystallinity index calculated by weighted intensity ratio index (WIRI) at (0211) band showed superior crystallinity for the synthesized material than the starting kaolin. This work demonstrates that impregnation of NaOH on amorphous aluminosilicate is a novel route for synthesizing of crystalline solidacid.

The results hierarchical mesoporous HYzeolites synthesis indicated that aging time and crystallization time determine the hierarchical factor of the synthesized HY zeolite. Incorporation of appropriate amount of NaCl is also towards enhancing the textural properties. Further, this process was optimized by varying the aging and crystallization time as well as amount of NaOH solvent using CCD. All the process variables were found to be statistically significant for high crystallinity and SSA while only NaOH solvent is statistically significant for optimal hierarchy factor.

In the quest for facile synthesis, more active solid acid, the produced zeolite in the last section was with sulfated groups. The effect of sulfate ions was observed on the textural and acidity properties as well as its catalytic activity. SHY gave biodiesel yield of 90.76% at 200 °C for 6 h while hierarchical HY gave yield of 72.42% at the same condition. This indicates that both pore structure and acid strength decide the activity of solid acids catalysts in biodiesel production.

Hierarchical mesoporous ZSM-5 (HMZeol) was also tested for biodiesel production. The catalysts synthesis was by desilication of conventional ZSM-5 with aqueous solution of NaOH (0.3 and 0.4 M). The sample treated with 0.4 M NaOH (0.4HMZeol) maximum biodiesel yield (82.12%) at 5:1 (methanol/oil) molar ratio, 1 wt % catalyst, and 3 h reaction time at 200 ^{o}C. However, further increase in the parameters decreases the yield. Contrarily, 0.3HMZeol shows increase in yield with increase in operating parameters.

The pyrolysis kinetics of some biodiesel produced in section 5 and that of the shea butter were carried by thermal decomposition using TGA equipment. The average activation energy was computed based on best-fitted models. The reference ZSM-5 biodiesel exhibits lower EA (63.59 KJ/mol) compared to 0.3HMZeol and 0.4HMZeol biodiesel (66.69 and 72.98 KJ/mol respectively). This is attributed to higher acidity of the microporous zeolites used for ZBio. However, the reference ZSM-5 exhibited lower conversion due to steric hindrance.

ABSTRAK

Kajian ini melaporkan sintesis pemangkin solidacid daripada bahan-bahan mentah yang lebih murah untuk pengeluaran biodiesel cekap. Disertasi ini terdiri daripada enam bahagian penyelidikan utama termasuk: (1) Sintesis dan pencirian mengarahkan pemangkin solidacid dari kaolin; (2) Sintesis dan pencirian nanoporous hierarki HY zeolite daripada asid kaolin diaktifkan; (3) Sintesis nanoporous zeolit HY dari kaolin diaktifkan, pusat reka bentuk komposit (CCD) kajian pengoptimuman; (4) Sintesis dan penggunaan hierarki mesoporous HZSM-5 untuk pengeluaran biodiesel; (5) Sintesis dan pencirian sulfated HY zeolite (SHY) untuk pengeluaran biodiesel; (6) Perbandingan kajian kinetik pirolisis biodiesel dihasilkan daripada mesoporous ZSM-5 zeolit dan Microporous ZSM-5. Ke Arah sintesis kaolinit solidacid, semua puncak kaolinites dalam bahan mula hilang selepas pengaktifan haba dan asid. Walau bagaimanapun, kebanyakan puncak kristal muncul semula dengan keamatan yang lebih besar pada (0211) band selepas NaOH penghamilan. Di samping itu, indeks penghabluran yang dikira dengan nisbah indeks intensiti wajaran (Wiri) di talian (0211) band menunjukkan penghabluran yang unggul menjadikan bahan disintesis daripada kaolin permulaan. Kerja ini menunjukkan bahawa hal memberi NaOH pada aluminosilikat amorfus adalah laluan baru untuk mensintesis daripada solidacid kristal.

Keputusan hierarki HYzeolites mesoporous sintesis menunjukkan bahawa penuaan dan masa penghabluran menentukan faktor hierarki HY zeolite yang disintesis. Pemerbadanan jumlah yang sesuai NaCl juga ke arah meningkatkan sifat-sifat tekstur. Di samping itu, proses ini telah dioptimumkan dengan mengubah penuaan dan masa penghabluran serta jumlah NaOH pelarut menggunakan CCD. Semua pembolehubah proses didapati statistik yang signifikan untuk penghabluran yang tinggi dan SSA

manakala hanya NaOH pelarut adalah statistik yang signifikan bagi faktor hierarki optimum.

Dalam usaha untuk sintesis facile, asid pepejal lebih aktif, zeolite yang dihasilkan dalam bahagian yang lepas adalah dengan kumpulan sulfated. Kesan functionalization diperhatikan pada tekstur dan keasidan sifat-sifat serta aktiviti sebagai pemangkin. SHY memberikan hasil biodiesel daripada 90,76% pada suhu 200 ° C selama 6 jam manakala hierarki HY memberikan hasil sebanyak 72,42% pada keadaan yang sama. Ini menunjukkan bahawa kedua-dua struktur liang dan kekuatan asid menentukan aktiviti asid pepejal pemangkin dalam pengeluaran biodiesel.

Hierarki mesoporous ZSM-5 (HMZeol) juga diuji untuk pengeluaran biodiesel. Sintesis pemangkin adalah dengan desilication daripada ZSM-5 konvensional dengan larutan NaOH (0.3 dan 0.4 M). Sampel dirawat dengan 0.4 M NaOH (0.4HMZeol) hasil biodiesel maksimum (82,12%) pada 5: 1 (metanol / minyak) nisbah molar, 1% berat pemangkin, dan 3 h masa tindak balas pada 200 ^{o}C. Walau bagaimanapun, peningkatan selanjutnya dalam parameter berkurangan hasil. Sebaliknya, 0.3HMZeol menunjukkan peningkatan dalam hasil dengan peningkatan dalam parameter operasi.

Kinetik pirolisis beberapa biodiesel dihasilkan dalam seksyen 5 dan mentega shea yang telah dijalankan oleh penguraian terma menggunakan peralatan TGA. Kami mengira tenaga pengaktifan purata berdasarkan model terbaik dipasang. Rujukan ZSM-5 biodiesel mempamerkan EA yang lebih rendah (63.59 KJ / mol) berbanding 0.3HMZeol dan 0.4HMZeol (masing-masing 66,69 dan 72,98 KJ / mol) biodiesel. Ini adalah disebabkan oleh keasidan tinggi daripada zeolit microporous digunakan untuk ZBio. Walau bagaimanapun, rujukan ZSM-5 yang dipamerkan penukaran yang lebih rendah disebabkan oleh halangan sterik.

ACKNOWLEDGEMENTS

Firstly, I would like to express my sincere appreciation to my supervisor Prof. Dr. Wan Mohd. Ashri Wan Daud for availing me opportunity to work with him for the period of my candidature. Sir, I am grateful for your kindness, patience, encouragement and guidance during my candidature at University of Malaya. This work would not have come to fruition without your wise counsel. Further, the effort of friends like Olumide Bolarinwa Ayodele and Yahaya Muhammad Sani are much appreciated.

I would also like to appreciate the research grant from Fundamental Research Grant Scheme (FRGS) Grant (Project No: FP031-2013A) under University of Malaya. Without the help of FRGS grant, this work would have been a daydream.

Moreover, words are not enough to appreciate my lovely wife, Chidinma Alaba and my children Esther and Jasper for being there for me throughout this period. You have supported me all through. This work is yours as much as it is mine because of your unconditional love and sacrifice. You have waited so long for this to happen and I am glad your efforts are crowned with a desired success.

Above all glory be to the Lord of exceeding grace for his strange works and strange acts in my life. Father, I thank you for your unspeakable gifts.

TABLE OF CONTENTS

LIST OF FIGURES

LIST OF TABLES

CHAPTER 1: INTRODUCTION

1.1 Background

Greenhouse gasses emissions via fossil fuel utilization from several sectors such as transportation, heat, and power generation constitute environmental hazards (Graça *et al*., 2010). Further, the fuels are nonrenewable, often scarce with unpredictable prices. Moreover, the global crude oil reserve is said to be near depletion because of wide utilization of these conventional fuels (Demirbas, 2009). These makes it imperative to seek alternative and better sources of fuel to ensure a sustainable energy security.

Biomass with oil qualities, such as algae, edible and non-edible vegetable oils possess high propensity for biofuel and other chemicals production that can replace fossil fuel-derived products (Botas *et al*., 2012; Demirbas, 2009). These biofuels are obtainable via transesterification, thermal cracking (pyrolysis), co-blending with VGO and microemulsion of biomass (Gómez *et al*., 2013). Moreover, biofuels are readily available locally, environmental friendly, accessible, reliable and sustainable fuel derived from renewable sources which support both ecosystem and human heath as well as long-term goals on tolerable emission (Demirbas, 2007). Fast pyrolysis is one of the commonly used methods for biofuel production because it is economically viable and thermally efficient (Apaydin-Varol *et al*., 2014). The product of this synthesis could be gaseous, liquid or solid biofuels. The liquid biofuel could be bio-crude, synthetic oils and biodiesels (Balat, 2009).

Generally, the major drawback of biofuels is the oxygen contents attributed to the presence of carboxylic groups (Phung *et al*., 2012). In order to proffer solution to biofuels oxygen content, several studies have been done proving that hydrodeoxygenation (HDO) process is a useful method of producing excellent diesel fuel. However, HDO is not economically feasible because it requires high-pressure and large amounts of hydrogen

derived from fossil fuels. These requirements cause negative effects on the carbon footprint of the bioprocess (Bozell & Petersen, 2010). An alternative route for deoxygenating biofuels is thermocatalytic deoxygenation, which proceeds at a lower temperature and atmospheric pressure without hydrogen. Similarly, catalytic cracking differs from HDO as it does not require the use of hydrogen at high-pressure. However, short catalyst-lifetime because of deactivation and low H/C ratio hinders the industrial applicability of the process. This limitation leads to a production of low-grade fuels with lower heating value than fossil fuels (Mortensen, Grunwaldt *et al*., 2011). Presently, the most popular strategy for biofuel production is transesterification (Farag *et al*., 2012).

Generally, transesterification proceeds with the aid of homogeneous basic catalysts. These include KOH, NaOH and other hydroxides (Carrero *et al.*, 2011b). The preference of homogeneous basic catalysts to their acidic counterpart is basically due to their better activity (Farag *et al*., 2012). However, transesterification with homogeneous basic catalysts have various drawbacks. These include catalyst separation to purify the biodiesel, soap formation and separation of glycerol requires large amount of water which production of wastewater (Intarapong *et al*., 2012; Reinoso *et al*., 2014; Xie *et al*., 2006). Moreover, homogeneous acid catalysts corrode the reactor and are very difficult to separate from the product. Therefore, it is pertinent to seek an alternative for the homogeneous catalyst to avoid catalyst separation corrosion and pollution issues.

Heterogeneous catalysts are suitable eco-friendly alternatives because of their ease of separation from the reaction medium, corrosion reduction and reusability (de Almeida *et al*., 2008). Their development could aid process design for the continuous production of biodiesel to minimize purification costs. However, they gives rather lower biodiesel yield due to drawbacks such as leaching and diffusion limitations (Carrero *et al.*, 2011a; Helwani *et al*., 2009; Reinoso *et al*., 2014; Zabeti *et al*., 2009). The FFA and phospholipid

content of the feedstock also affect the performance of heterogeneous because they tend to poison the catalyst (Besson & Gallezot, 2003).

For better performance in biodiesel production process, an efficient heterogeneous catalyst needs mesopores to minimize steric hindrance, higher acid strength, and density as well as thermal and hydrothermal stability to minimize poisoning and leaching. Super acids are promising catalysts for biodiesel production because they simultaneously convert both the triglycerides and FFA, which circumvent the threat posed by FFA. Chemists synthesized them in both solid and forms liquid and their amazing acid strength makes it easier to carry out problematic reactions under satisfactory experimental conditions. For instance, Misono and Okuhara (1993) reported that activation of alkanes proceeds at low temperatures over superacid catalyst. Conventional superacids such as liquid HF and AlCl [sub 3] have been cited hazardous to the environment, but solid superacids are more attractive for industrial utilization. Solid superacid catalysts are indeed more environmentally benign in many industrial processes (Misono & Okuhara, 1993).

Recently, several authors had tested heteropoly acids, inorganic metal oxide as well as sulfonic and sulfuric acid based resins as solid superacid catalysts for transesterification of triglycerides and esterification of FFA (de Almeida *et al*., 2008; Furuta *et al*., 2004a, 2006; Jitputti *et al*., 2006). Sulfated inorganic metal oxides exhibit stronger super acidity compared to 100% sulfuric acid (H0 ≤-12) (Yang *et al*., 2003). This is because metal oxides are chemically stable, environmentally benign and possess remarkable acid-base and redox properties (Kour & Paul, 2015). One of the most popular sulfated metal oxide catalysts is sulfated-zirconia (SZ). SZ has been proved an efficient superacid for both esterification and transesterification. Kiss *et al*. (2006) did a comparative study on various solid acids including ion exchange resins, zeolites and inorganic metal oxides for lauric

acid esterification using different alcohol. They reported that SZ exhibits the best performance because zeolites are limited being microporous while low thermal stability is the bane of ion exchange resins. SZ is a promising catalyst for several industrial processes of commercial importance due to its super acid strength (Reddy & Patil, 2009; Saravanan *et al*., 2012b; Yadav & Nair, 1999). Saravanan *et al*. (2012a, 2012b) also reported the outstanding performance of SZ in esterification of caprylic acid and myristic acid at mild temperature and low catalyst loading.

Other sulfated metal oxides with remarkable performance include Titania, silica and combination of both. Recently, several authors have investigated the use of sulfated silicas as catalysts for esterification and transesterification (de Almeida *et al*., 2008; Testa *et al*., 2010, 2013). The report of Ropero-Vega *et al*. (2010) shows that sulfate ion addition to Titania by incipient impregnation of ammonium sulfate inculcated super acidity to the Titania. This engenders remarkable activity when used to esterify fatty acids.

Ordered mesoporous silicas and aluminosilicates such as MCM-41, HMS, SBA-15 and USY zeolite are viable support due to their high specific surface area (SSA) and hierarchical mesoporosity (Testa *et al*., 2010, 2014; Usai *et al*., 2013; Venezia *et al*., 2011). The major problems attributed to such materials are hydrophobicity and lower catalytic activity as compared to microporous zeolites (Ryoo *et al*., 1999). However, functional groups that are more reactive are added to improve the surface hydrophobicity as well as reactivity. Testa *et al*. (2013) comparatively studied glycerol acetylation over different solid acid catalysts. They reported that mesoporous sulfated silica showed superior performance with respect to reactivity.

Alternatively, cheap material like modified kaolin has proved a viable solid acid catalyst for several reactions: esterification (da Silva Jr *et al*., 2013; de Oliveira *et al*., 2012; do Nascimento *et al*., 2011), cracking (Panda & Singh, 2011), debuthylation (Mahmoud & Saleh, 1999) and aromatization (Wang *et al*., 2007). Modified kaolin, seemingly develops important acidity, thereby becoming a promising solid acid catalyst that is capable of biofuel upgrading. In this study, modified commercial zeolite, modified kaolin as well as zeolites produced from modified kaolin were investigated. The catalysts characterizations were by FTIR, BET, XRF and XRD. The aim of this study is to develop a novel integrated approach to synthesis solid acid catalyst for biodiesel production via transesterification. The catalyst is intended to be hydrothermally stable and capable of suppressing active sites deactivation. The proposed starting material for the synthesis is kaolin. Moreover, modification conventional zeolites will be investigated.

1.2 Problem Statement

Bio-oil such as vegetable oils have certain limitations, which disqualified them from being used as an alternative energy source. These include low heating value, incomplete volatility, acidity, and incompatibility with standard petroleum fuels, which significantly restrict its application. However, this is not but without a solution. The general solution is transformation to biodiesel. To do this efficiently, rational design of viable solidacid catalyst is essential.

1.3 Objectives of study

The objectives of this research work include the following;

I. To synthesize of solid acid catalysts from kaolin and post synthesis from the ZSM-5 zeolite.
II. To characterize the prepared catalysts using XRD, FTIR, NH_3-TPD, etc.

III. To test catalytic activities of the synthesized catalysts on biodiesel production form shea butter.

IV. To determine the decomposition kinetics of the produced biodiesel.

1.4 Scope

This study focused on the use of kaolin as the basic raw material for rational design of a novel solid acid catalyst for efficient biodiesel production from shea butter. The activity of the novel catalyst was compared with that of modified conventional ZSM-5. Further, the textural properties and the acidity of the catalysts samples were analyzed. The produced biodiesel was also characterized to check its quality. These is itemized as follows:

I. Catalyst design

II. Methanolisis of shea butter

III. Characterization of the catalysts & biodiesel

IV. Comparison with modified commercial catalysts.

1.5 Dissertation Structure

This dissertation consists of five main chapters;

Chapter 1: This chapter provides an overview of the literature and discusses previous findings concerning recent development in solidacid catalyst development for biodiesel production. It also defines the objectives and problem statement of this study.

Chapter 2: This Chapter entails results of a literature survey on the development of solidacid catalysts for biodiesel production. It includes an overview of solid acid catalysts development, the starting materials such as ZSM-5 zeolite and kaolin and their properties. Further, modification strategies such as thermal, chemical activation as well as functionalization with sulfate groups for synthesis of solidacid catalysts from the starting

materials are discussed. A part of this work has been accepted in press, RSC advances, 2015, DOI: 10.1039/C5RA18884A.

Chapter 3: Synthesis and characterization of highly ordered solidacid catalyst from kaolin. This chapter describes the synthesis highly ordered solidacid kaolinite catalysts, Synthesis and characterization of hierarchical nanoporous HY zeolite from acid activated kaolin and its optimization study using central composite design, in fulfilment of objective 1 & 2. The work demonstrates that impregnation of NaOH on amorphous aluminosilicate is a novel route for synthesizing of crystalline solidracid catalysts. A part of this work was presented at the 2014 Regional conference on chemical Engineering, Yogyakarta, Indonesia, December 23, 2014 (ISBN: 978-602-71398-0-0). Another part was published in Chinese Journal of catalysis (2015) 36: 1846–1851. DOI: 10.1016/S1872-2067(15)60962-7. http://www.sciencedirect.com/science/journal/18722067, while the remaing part is under review.

Chapter 4: Synthesis and application of hierarchical mesoporous HZSM-5 for biodiesel production from shea butter. This chapter describes post-synthesis of hierarchical mesoporous ZSM-5 zeolites from conventional ZSM-5 in fulfilment of objective 1 to 3. This work has been published in Journal of the Taiwan Institute of Chemical Engineers (2015) 000:1-8. http://dx.doi.org/10.1016/j.jtice.2015.09.006

Chapter 5: Synthesis and characterization of sulfated hierarchical nanoporous HY zeolite for efficient transesterification of shea butter. This chapter describes the functionalization of the hierarchical nanoporous HY zeolite synthesized in chapter 4 with sulfate group, to enhance the acidity towards efficient biodiesel production. This fulfilled objective 1 to 3. The work shows that both pore structure and acid strength decide the

activity of solid acids catalysts in biodiesel production. This work is under review in the journal titled “Catalysis Surveys from Asia”.

Chapter 6: A Comparative Study on Thermal Decomposition Behavior of Biodiesel Samples Produced from Shea Butter over Micro and Mesoporous ZSM-5 zeolites using Different Kinetic Models. This chapter comparatively investigated the kinetic triplets of some of the biodiesel samples produced in chapter 6 in fulfilment of objective 4. The work helps to predict the stability of the products. This work is under review in the journal titled “Journal of thermal analysis and calorimetry”.

Chapter 7: This is the conclusion and recommendation section, which summarizes important results associated with the research objectives.

CHAPTER 2: LITERATURE REVIEW

2.1 Introduction

Generally, one can use homogeneous basic or acid or their heterogeneous counterpart as catalysts for biodiesel production. However, homogeneous basic are said to be about 4000 times faster than heterogeneous catalysts (Farag *et al*., 2012). This is because they dissolve in the reaction medium to facilitate interaction with the reactants. However, they are not reusable. Likewise, the process is plagued by soap formation, corrosion of reaction medium and production of a large amount of wastewater during glycerol separation.

Solid acid catalysts are in principle much more suitable heterogeneous catalyst for biodiesel production (Rinaldi *et al*., 2009). This is because of their ease of separation from the product thereby making it reusable. Furthermore, they do not corrode the reaction medium nor pose any environmental challenge when disposed (Yang *et al*., 2003).

2.2 Enhanced Zeolites

Zeolites as crystalline molecular sieve had been used widely in modern industrial processes such as adsorption and catalysis, especially in petrochemical and biodiesel industry simply because zeolites materials possess high thermal and chemical stability, high surface area and adjustable pore size (Hölderich *et al*., 1997; Verhoef *et al*., 2001). However, in most cases, the major limitation of zeolites is their micropore size between ~0.5 and 1.5 nm (Xu *et al*., 2009). This pore size limitation prevents large molecules from reacting effectively over these microporous materials (Rinaldi *et al*., 2009).

In order to find solution to the diffusion problem of reactants in zeolites matrix, synthesis of aluminosilicate materials with flexible mesopore size, such as SBA-15 (Zhao *et al*., 1998) and MCM-41 (Kresge *et al*., 1992) have been successful since around 1990s.

Mesoporous zeolites allow diffusion of bulk molecules because of their large pore size thereby overcoming the drawback of microporous zeolites. Nevertheless, they exhibited lower hydrothermal stability and acid sites than conventional zeolites, which restricts their usage in several of industrial applications and reactions. Later on, scientists made immense effort at improving the framework crystallinity of these mesoporous materials for industrial applications, but all the efforts at improving the hydrothermal strength and the acid sites of the structural framework proved abortive (Liu, 2012).

Later on, efforts were made to incorporate the outstanding qualities of microporous and mesoporous zeolites to synthesize mesoporous zeolite materials with improved crystalline structure. These includes, carbon materials (Kim *et al*., 2003; Tao *et al*., 2003), zeolite products hydrolysis or zeolite seeds assemblage to an ordered mesoporous phase (Liu *et al*., 2000, 2001; Ooi *et al*., 2004; Wang *et al*., 2006; Zhang *et al*., 2001), simultaneous treatment of the mixture of microporous and mesoporous (Prokešová *et al*., 2003a, 2003b), acid and alkaline leaching (Corma *et al*., 1999; Groen *et al*., 2004; Groen *et al*., 2005; Groen *et al*., 2006; Groen *et al*., 2007), partial recrystallization of pre-assembled mesoporous walls of the materials into zeolite matrix (Campos *et al*., 2006), zeolites primal building units coating on the wall of the pores of pre-synthesized mesoporous aluminosilicate (Trong *et al*., 2001, 2003). However, some of the synthesized materials were far from the expected, morphology-wise (Na *et al*., 2010).

Generally, most recently used strategies can be grouped into three. The first is zeolite synthesis with larger micropores (Blasco *et al*., 2002; Avelino *et al*., 2001; Davis, 1989; Davis *et al*., 2002; Freyhardt *et al*., 1996; Jiang *et al*., 2010; Sastre *et al*., 2004; Strohmaier *et al*., 2003; Sun *et al*., 2009). The second is zeolite synthesis in the form of nanoparticles for rapid diffusion (Tosheva *et al*., 2005). The third is zeolite synthesis with mesopores generation during the zeolite crystallization using a structural directing agent (SDA) or

acid/alkaline leaching or hydrothermal treatment (Jacobsen *et al.*, 2000a; Schüth, 2003; Wang *et al*., 2010).

Larger pores mean micropore aperture with over 12-membered ring (12MR) (Davis, 2002). They are synthesized hydrothermally using bulky organic amine as a porogen (pore generator) (Davis, 2002). The synthesis conditions were quickly optimized using high throughput method (Liu *et al*., 2012). Modification with germanium improved the produced mesoporous aluminosilicate appreciably (Blasco *et al*., 2002; Corma *et al*., 2001; Liu *et al*., 2012; Sastre *et al*., 2004). Germanium modified zeolite with over 30MR pore apertures were produced using high throughput synthesis method through rational design of bulky surfactants (Liu *et al*., 2012). However, the synthesized material is called germanosilicate, which is less stable than zeolite chemically (Liu *et al*., 2012). In the synthesis of nano-size crystalline zeolites, rapt attention is needed in order to control the synthesis conditions to end crystallization before bulky crystals start to develop. The synthesis is often carried out using the OH units of surfactant at low temperature, under Na^+ deficient and diluted conditions (Liu *et al*., 2012; Tosheva *et al*., 2005). Intra-crystalline mesopores could be generated from post-synthesis treatment of pre-synthesized zeolite. These synthesis strategies are well suited for large-scale synthesis. However, the formation of uniform mesopores is very difficult. Moreover, the pre-synthesized samples should be mixed with caution to avoid loss of crystallinity or complete dissolution (Liu *et al.*, 2012). The direct development of intra-crystalline mesopores could be by addition of hard mesoporous template (Schüth, 2003). There are various kinds of nano-templates such as carbon nanoparticles and nano-tubes. However, this process is unfavorable thermodynamically with respect to entropy. Thus, crystallization of zeolite should be made to occur inside the template pores or in a confined space between template particles in a dry gel synthesis manner (Jacobsen *et al*.,

2000a). For soft templates, the meso-porogens or templates must have a sufficiently high affinity for zeolite matrix.

Hydrothermal treatment has been faced with the challenges of crystallization time, surface area, purity, and yield (Wang *et al*., 2010). Mostly, the challenges can be surmounted by introduction of zeolite seed (such as silicalite-1 or ZSM-5) in small amount in a template-free synthesis to further improve the framework structure of the hydrothermally synthesized material, the material was further treated by alkali leaching as reported by Liu *et al*. (2012). The zeolite possesses highly ordered mesopores in addition to the microporous structure after removal of the template through calcinations. These types of zeolites are called hierarchical mesoporous zeolites. This material is capable of exhibiting dual merit of two micro and mesopore structure. The micropore takes care of shape or size selectivity while the mesopore takes care of facile diffusion pathway inside the pore wall.

2.2.1 Hierarchical mesoporous zeolites

Hierarchical mesoporous zeolites are composite materials with more than one level of porosity. Their mesoporosity did not severely penalize their microporosity (Holm *et al*., 2011; Ishihara *et al*., 2012; Na *et al*., 2011b; Wang *et al*., 2010). This mesoporous materials are popular in several industrial applications such as catalytic cracking (Kim *et al*., 2010), Friedel-Crafts alkylations (Fan *et al*., 2008; Sun & Prins, 2008), phenol tert-butylation (Xu *et al*., 2008), esterification (Li *et al*., 2013), transesterification (Farag *et al*., 2012) and oxidation of benzene to phenol (Koekkoek *et al*., 2011). Design of hierarchical mesoporous zeolite is a proven approach through enhanced manipulation of microporous crystals in catalyst development towards efficient mass transport as well as shape selectivity (Hartmann, 2004; Perez-Ramirez *et al*., 2008). Kim *et al*. 2005 synthesized hierarchical mesoporous zeolite from by post synthesis of MFI zeolite using

organosilane surfactants as the mesopore template. They reported that the synthesized materials showed remarkably long catalyst lifetime (more than three times the reference MFI zeolite) in methanol to hydrocarbon reaction. The longevity of the catalyst was attributed to facile diffusion of coke precursors through the mesopore of the catalyst and short diffusion distance. This minimized fouling by coke formation while the catalyst exhibited high stability.

2.2.2 Estimation of diffusion limitation

In heterogeneous catalysis using zeolite, diffusion limitation has to be considered, most especially to substantiate the enhancement via zeolites mesoporosity. We need to take proper account of internal mass transfer (transfer of the reacting species within the porous catalyst) Figure 2.1. When the reactants reach the surface of the catalyst particles, it continues to travel by diffusion. The effective diffusivity inside catalyst particle is lower than the free diffusion due to the porosity (i.e. only a fraction of the volume is available for diffusion) and the tortuosity of the particle. Knudsen diffusion occurs in very narrow pores (Louis, 2010; Chen *et al*., 1994; Hamilton *et al*., 1974; Hawthorn, 1974). The estimation of mass transfer limitation is given by Thiele module as follows:

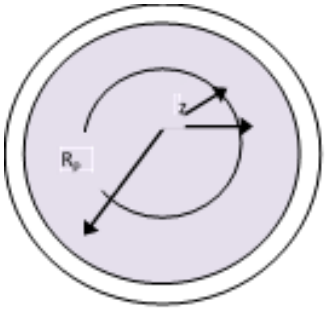

Figure 2.1: Internal mass transfer.

Effective diffusivity for free diffusion:

$$D_{eff,I} = \frac{\varepsilon p Di}{\delta} \quad (2.1)$$

Effective diffusivity for Knudsen diffusion:

$$Dk = 97 rpore \sqrt{T/Mi} \quad (2.2)$$

Thiele module is given by:

$$\phi = \mathrm{L}\frac{\mathrm{r(Rp)}}{\sqrt{2\mathrm{kVDeff}}} \quad (2.3)$$

where:

D_{eff} = effective diffusivity

r(Rp) = reaction rate at the surface

L = diffusion length

kV = maximum mass transfer rate

Since the concentration is lower inside the particle than at the surface, the reaction rate will also be typically lower. The decrease in observed reaction rate can be accounted for by the effectiveness factor as follows:

$$\boldsymbol{\eta} = \frac{\gamma A, obs}{\gamma A, surf} \quad (2.4)$$

Where $\gamma A,obs$ is the rate of reaction observed and $\gamma A,surf$ is the reaction rate at surface conditions (i.e. reaction rate without mass transfer limitation).

If ϕ is small (<<1), there will be no problem with mass transfer limitation (η=1). If ϕ >1, there will be effects to mass transfer limitation (η <1). Louis *et al*. (2010) developed mesoporous zeolite coated on glass monolith. They estimated the Thiele module, ϕ =

0.01, whereas $\phi = 4.0$ was computed for conventional ZSM-5 (Figure 2.2). This evinces that the synthesized materials operate expeditiously and do not have diffusion constraints. Whereas, diffusion limitation seriously disturbs the performance of the conventional ZSM-5 zeolite, since the whole part of the catalyst is not utilized for the reaction.

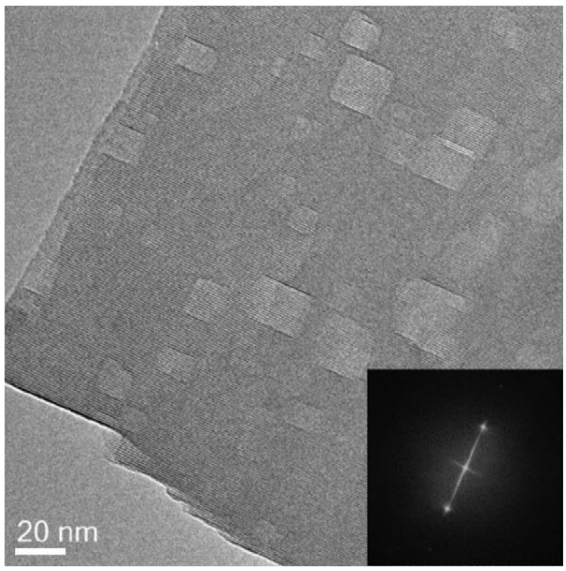

Figure 2.2: MFI zeolite crystal TEM image. Inset: image of the FFT (Louis, 2010).

2.2.3 Synthesis Strategies

2.2.3.1 Desilication and re-assembly strategy

Because this strategy is very straight forward, it has recently gained significant attention. This method has been applied to various zeolites such as FER, MFI, BEA and MOR (Groen *et al*., 2004; Groen, *et al*., 2005; Groen *et al*., 2004; Groen *et al*., 2006; Yoo *et al*., 2012). In an aqueous alkali solution, less reactive aluminol sites help to maintain the zeolite structure, while, silica were extracted, leading to more porous structures.

Desilication offers more adjustable pores and conserves the Brønsted acid sites, while dealumination which is a well-known post-synthesis strategy for increasing the pore size zeolite framework (Groen *et al*., 2005; Müller *et al*., 2000). Generally, well-tailored

mesoporosity is obtained by changing the Si/AL ratio of the main zeolites, reaction time, the reaction temperature, and concentration of the alkali via desilication. However, this method greatly reduce the crystallinity of the materials by ~30% as estimated by XRD and nitrogen sorption measurement and the external surface area enhancement is ascribed to pores larger than 10 nm (Groen *et al*., 2004, 2005, 2006; Yoo *et al*., 2012).

However, according to Yoo *et al*. (2012) the challenge of reduced crystallinity could be solved by strategic re-assembly method adopted from pseudomorphic transformation concept. The extracted species of silicates, aluminol, and ZSM-5 zeolite crystals fragments can be reunited with the main zeolite structure by hydrothermal treatment with the aid of surfactant (Figure 2.3). Physicochemical characteristics of the mesoporous zeolites synthesized by desilication or combined desilication and re-assembly strategies could be characterized by scanning and transmission electron microscopy (TEM and SEM), solid state 27Al and 29Si magic-angle-spinning (MAS) NMR, nitrogen sorption measurements, elemental analysis by inductively coupled plasma spectroscopy (ICP), temperature programmed ammonia desorption (TPD) and X-ray diffraction (XRD). The synthesized product of alkaline treatment exhibits a dual-mesopore size distribution of ~3 nm and ~10-30 nm, external surface area increase of ~ 83% of the original zeolite matrix based on the calculated micropore pore volumes from nitrogen sorption measurements, and ~ 77% computed from XRD measurements. The XRD and TEM of the products indicate that the desilication and re-assembly processes took place simultaneously to synthesize a dua-pore material. Re-assembling the extracted Si atom and other fragments by micellization of a surfactant leads to formation of smaller pore size of ~ 3nm, whereas desilication leads to formation of larger pore size of ~10-30 nm in the zeolite matrix.

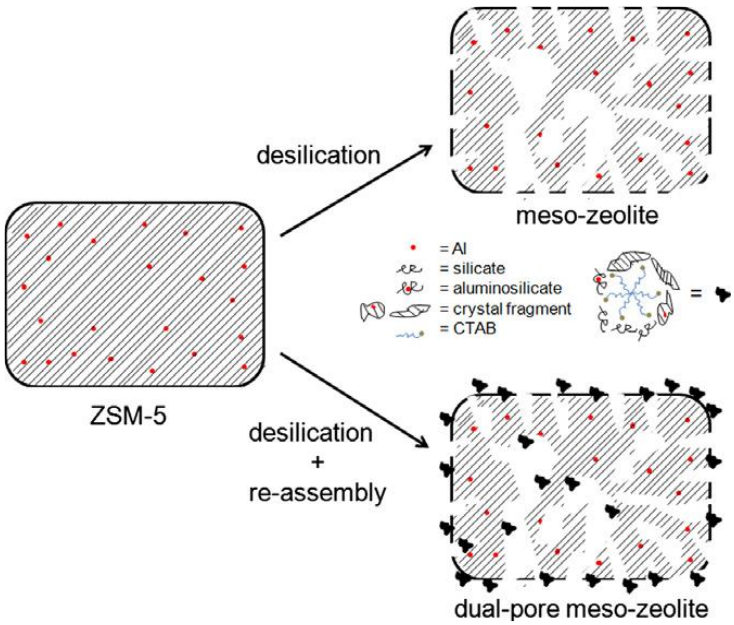

Figure 2.3: A schematic diagram illustrating mesoporous zeolite formation through desilication (upper right) and desilication and re-assembling process (bottom right) (Yoo *et al*. 2012).

2.2.3.2 Dual template mechanism

The dual template mechanism is the synthesis method that employs two different templates to generate micro and mesopore in the zeolite materials. One of the templates is to generate mesopore and the other to generate micropore simultaneously. Figure 2.4 below shows a typical dual mechanism, where both CTMA+ (cetiltrimethylammonium) and TPA+ (tetrapropylammonium) ion act as templates for the mesoporous MCM-41 and microporous ZSM-5 framework, respectively. The hybrid MCM-41/ZSM-5 formation is as a result of the charge compensation caused by the TPA+ ions on the MCM-41 matrix.

In a study of Coriolano *et al*. (2013), synthesis using dual template was done by firstly, preparing a reactive hydrogel of ZSM5, aged for 40 h at ~25 °C, and crystallized at 90 °C for the zeolite seed generation. The mesopore was formed by adding of cetiltrimethylammonium bromide (CTMABr) and water solution to the seeds, leading to a formation of new micelles (Figure 2.5). The mixture was heated in an autoclave at 125

°C, between 6 - 12 days. The highest order of hybrid ZSM-5/MCM-41 was obtained on day 7 of the synthesis. The hybrid materials obtained at day 8 and 9 of the synthesis are poorly ordered mesoporous zeolite crystal, while, for day 12, predominantly ZSM-5 zeolite was formed. The synthesis of ZSM-5 zeolite combined with the bulk of MCM-41 must be limited to seven days, thereby preventing the second step of crystallization. By increasing the synthesis time, some crystal of ZSM-5 could be synthesized and further impregnated into MCM-41 already synthesized. Therefore, the blend of ZSM-5 and MCM-41 zeolite in the hybrid system could be synthesized by fixing microporous ZSM-5 zeolite particles on the cylindrical wall of the MCM-41 mesopore (Figure 2.4).

In the hybrid ZSM-5/MCM-41 material obtained on the day 7, the XRD pattern shows a negligible micropores volume, showing that access of N_2 to the micropores was prevented. This can be ascribed to the ZSM-5 framework structure formation in the mesoporous MCM-41 framework core. Herein, amorphous silica has been deposited on the obtained ZSM-5 crystals, which blocked nitrogen molecules from accessing their micropores. The amorphous silica produced during the mesoporous ZSM-5 zeolite formation was also discovered by Funz *et al*. (2006).

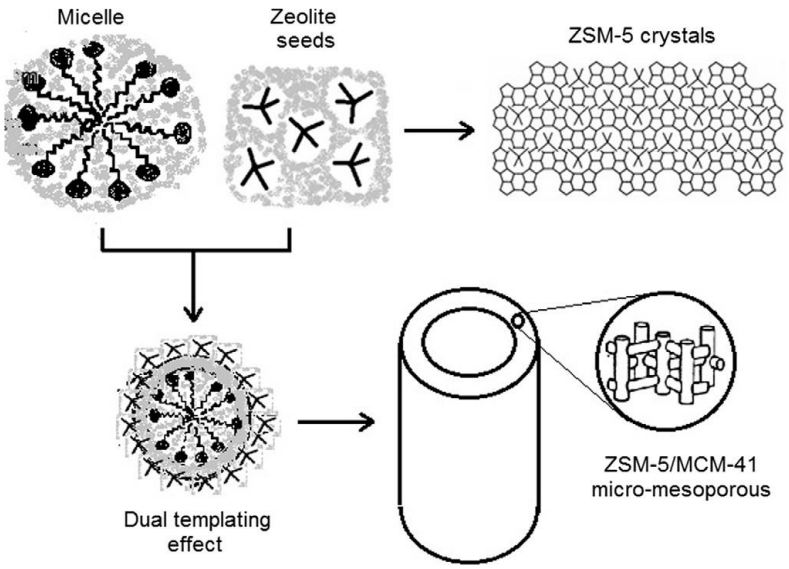

Figure 2.4: Proposed dual templating mechanism for hybrid micro-mesoporous ZSM-5/MCM-41 material synthesis (Coriolano et al., 2013).

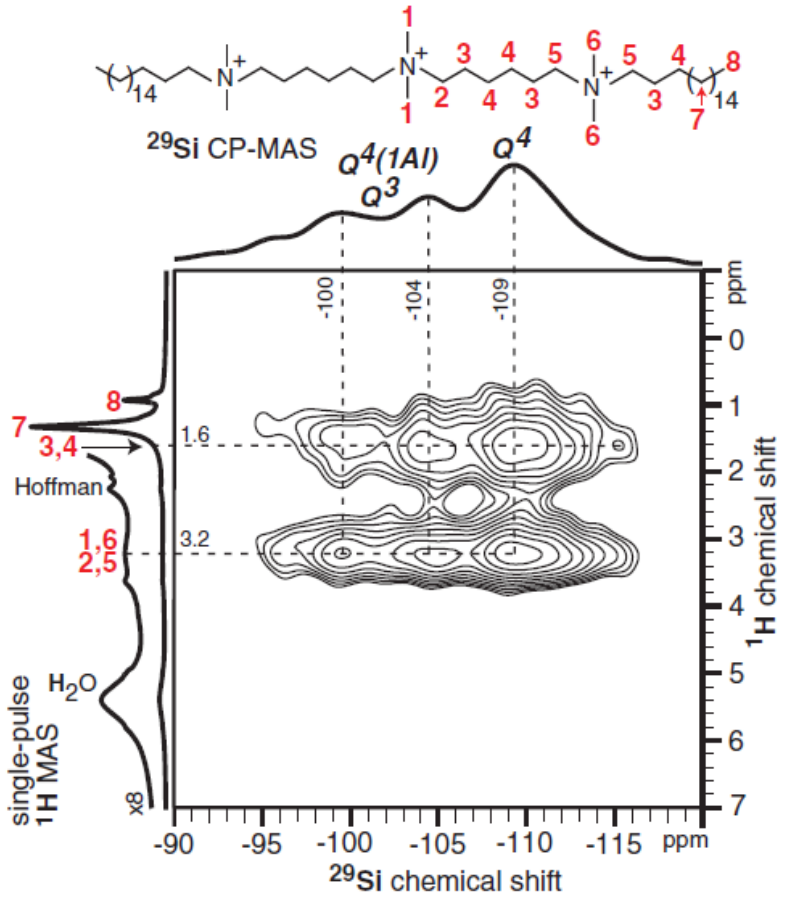

Figure 2.5: Solid state 2D 29Si(1H) HETCOR NMR spectrum of the hexagonal MMS (Si/Al = 15). 1D 29Si CP MAS and the single-pulse 1H MAS spectra are shown along the horizontal and the vertical axes, respectively (Na et al., 2011).

2.2.3.3 Direct synthesis by dual-functional surfactant approach

Dual-functional surfactants are single surfactants that can simultaneously generate micro and mesopores. An example of dual functional surfactant is a Gemini surfactant, which functionally played a dual role as both microporous zeolite SDA and mesopore template simultaneously (Liu *et al*., 2012).

Gemini surfactants, also known as dimeric surfactants are characterized with two hydrophobic head units and two hydrophilic units in the molecules, in contrast to conventional surfactants that possess a single hydrophobic head unit and a single hydrophilic unit. Gemini surfactants can be about ten to a thousand times more active on the surface than commercial surfactants with similar but single hydrophilic and

hydrophobic units in the molecules. Their design is to support both the formation of nanocrystalline and liquid crystal-like meso-structural order of the zeolite structure. In the studies of Choi *et al*. (2009); Jung *et al*. (2012); Na *et al*., (2011b); Na *et al*. (2011) the dual role of the Gemini dual-porogenic are illustrated by nuclear magnetic resonance spectroscopy and 2D heteronuclear correlation (Vega, 1988), which simplifies the molecular proximity of the surfactant to specific structural moieties. The 2D 29Si(1H) HETCORNMR spectrum (Figure 2.5) exposes the important role of the AlIV units in directing the zeolite structures crystallization. A separately acquired 1D 29Si cross polarization (CP) magic-angle-spinning (MAS) spectrum (horizontal axis) exhibit broad signal attributed to Qn 29Si aluminosilicate structure (Barrett *et al*., 1951; Janicke *et al*., 1998; Jin *et al*., 2012; Saito *et al*., 1995) with increasing condensation rate. A single-pulse 1H MAS spectrum (vertical axis) exposed partial resolution of 1H signal from the porogen molecules with its proton chemical shift assignments shown in 2d 13C(1H) HETCOR NMR spectrum.

In dua-porogenic driven synthesis scheme, the porogen aggregates generated the mesopores, while, microporous zeolite crystal structure are formed by multiple AlIV units. The wall size and structural topology are controllable with the aid of surfactants with different gemini-like head units. The pore size are designed in accordance with the addition of hydrophobic growth increase agents or by the tail end of the surfactant (Na *et al*., 2011b). The porous structure and strong zeolite framework acid sites lead to substantial enhancement of the catalytic performance of several organic reactions that involves large molecules as compared to conventional zeolite or amorphous MMSs. MMSs crystals are also useful for selective adsorbent in protein synthesis base on molecular size. Enzymes species with a large size can be immobilized by means of van der Waals forces, covalent bonding, or electrostatically interacts with the zeolite matrix.

Moreover, MMSs synthesis can be extended to the remaining inorganic component, like aluminophosphates (Choi *et al*., 2006; Kruk *et al*., 2001; Lee *et al*., 2005; Na *et al*., 2011b).

2.2.3.4 Hydrothermal synthesis

This is a conveniently mesoscale template free route for hierarchical structured ZSM-5 zeolite synthesis. It could be done by steaming with or without zeolite or silicalite1 seed. Seed assisted strategy of hydrothermal synthesis helps to care of some challenges related with crystallization time, purity and yield to obtain highly crystalline zeolite products enriched with large surface area as well as large pores (Wang *et al*., 2010). The presence of special intersecting channel system in the framework of ZSM-5 zeolite with a straight 10-member ring (10MR) channel parallel to the b-axis and a zig-zag 10MR channel, which protrude towards the a-axis (Anthony, 1996; Krishna *et al*., 2001; Wang *et al*., 2010; Yu *et al*., 2006) makes ordered ZSM-5 with c-axis-oriented nanorods is of vital importance. This is due to their enriched and exposed pore opening as well as shortened channels. Highly ordered ZSM-5 zeolites with enhanced surface area as well as enriched mesopores are produced via this strategy. The improvement on the catalytic properties of the product is ascribed to its ease of access to the active sites caused by a reduced microporous channel and opening of intra-crystal mesopore which remarkably widened zeolite field of application (Wang *et al*., 2010).

The pre-added seeds in the synthesis solution play a vital role inducing the formation of highly ordered ZSM-5 zeolite structure. The added seeds function as the initial crystal core to initiate secondary nucleation and growth of the nano-sized ZSM-5 zeolite crystal along their preferred plane via 1,6-hexylenediamine (Bell *et al*., 2008; Cundy *et al*., 2005; Davis *et al*., 2006; Sandeep *et al*., 2007; Na *et al*., 2011a; Wang *et al*., 2010). This leads to a formation of a new type of highly ordered porous zeolite through partial intergrowth

of ZSM-5 nano-rod in a similar direction. Such oriented aggregation has been reported as mechanism for crystal growth, producing monocrystalline frameworks (Niederberger *et al*., 2006; Wang *et al*., 2010; Yuwono *et al*., 2010; Zhang *et al*., 2005). Wang *et al*. (2010) confirmed that because of c-axis highly oriented ZSM-5 zeolite nanocrystal bundle of arrays, a novel mesoporous material was synthesized as inter-crystal pores. The improved surface area and mesopore volume in the hierarchical mesoporous ZSM-5 zeolite will improve the reactivity and diffusivity of the reacting molecules (Wang *et al*., 2010).

2.2.3.5 Combined hydrothermal and alkaline leaching synthesis strategy

This is another template free route for hierarchically structured zeolite synthesis, which involves combined effort of hydrothermal and alkaline treatment. This is achievable by steaming of the zeolite material followed by alkaline leaching of the zeolite material followed by steaming. Shi *et al*. (2013) reported that alkaline treatment after heat treatment exhibits triple effects on the synthesized ZSM-5 zeolite, which involves silicate extraction, re-deposition of aluminum atom and aluminum extra-framework removal; while the heat treatment after alkali modification has binary effect, which involves aluminum atom extraction and stabilization. However, heat treatment after alkali modification is more effective in adjusting the zeolites acidity and mesopores creation. The catalyst derived from ZSM-5 zeolite modified through an incorporation of steam and alkali treatment, which exhibits enhanced isomerization activity, better aromatization activity and exceeding stability in the hydro-upgrading of gasoline via fluid catalytic cracking. The details of this scheme are shown below (Figure 2.6 to Figure 2.11).

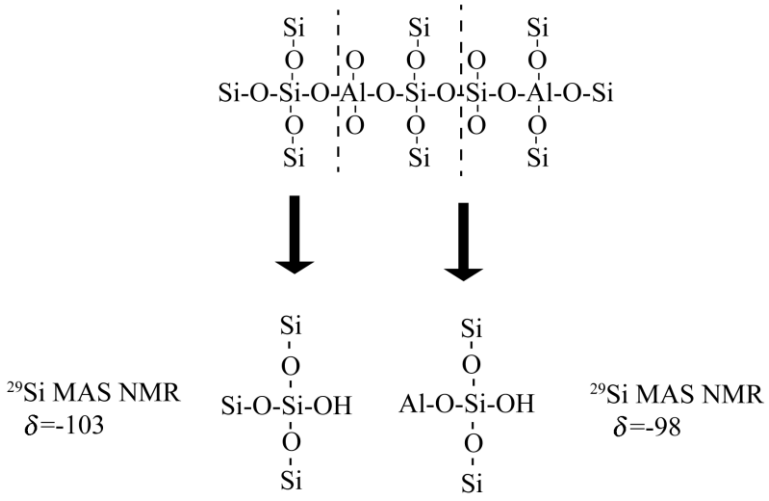

Figure 2.6: Model for alumina extraction and silica extraction of the HZSM-5 zeolite (Zhang et al. 2001).

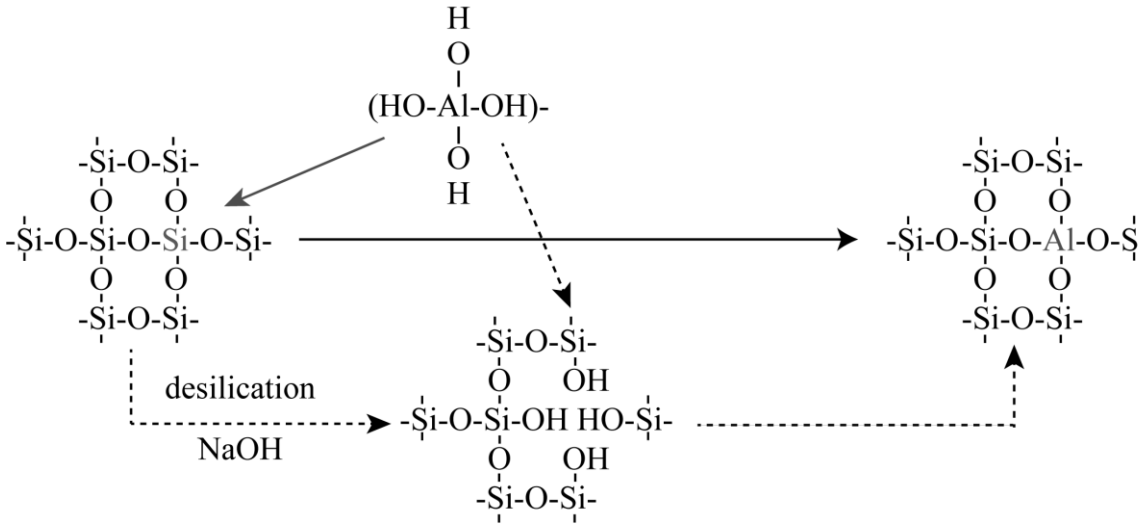

Figure 2.7: Realumination process of the parent HZSM-5 zeolite upon alkali treatment (Shi et al. 2013).

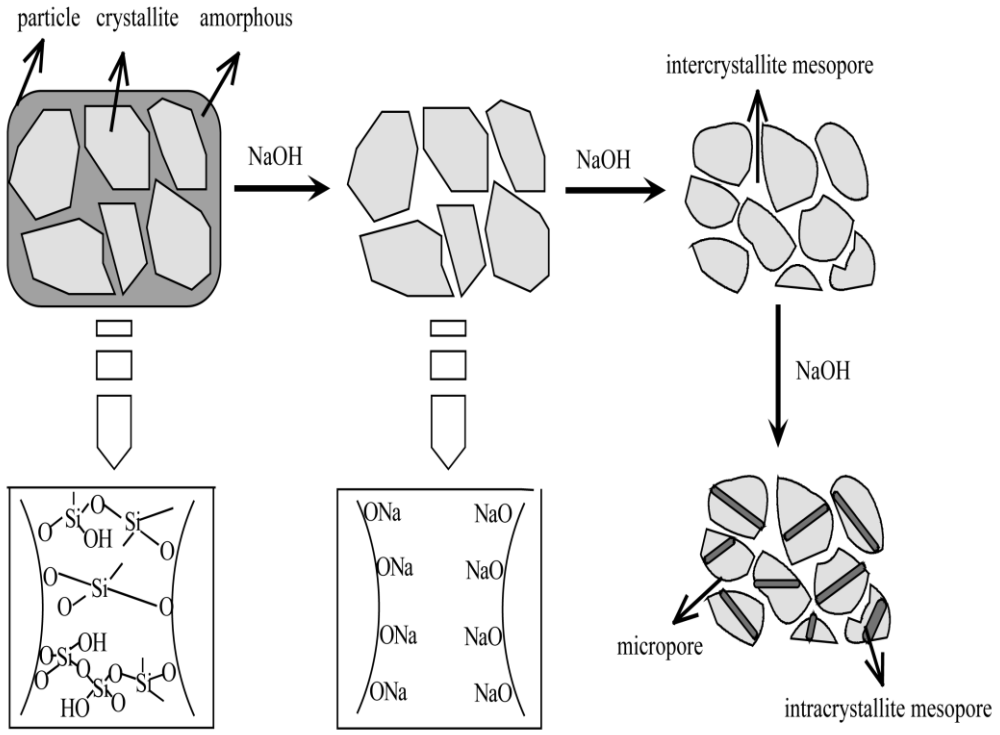

Figure 2.8: Mesopores creation in the HZSM-5 zeolite upon alkali treatment (Shi et al., 2013).

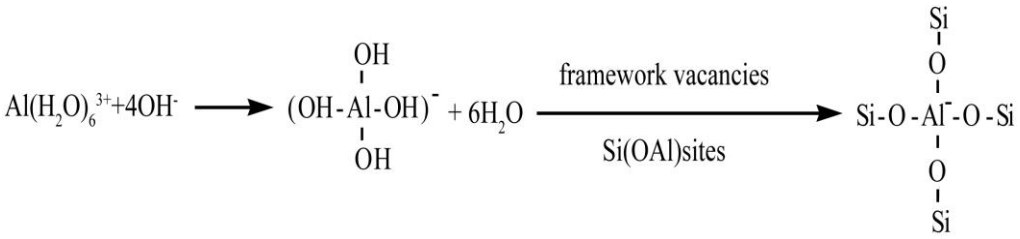

Figure 2.9: Realumination process of the steamed HZSM-5 zeolite upon alkaline treatment (Yang et al., 1997).

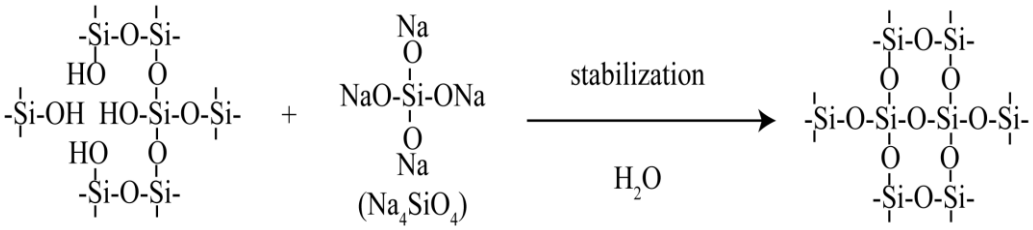

Figure 2.10: Healing process of the desilicated HZSM-5 zeolite upon steaming (Doremieux-Morin et al., 1995).

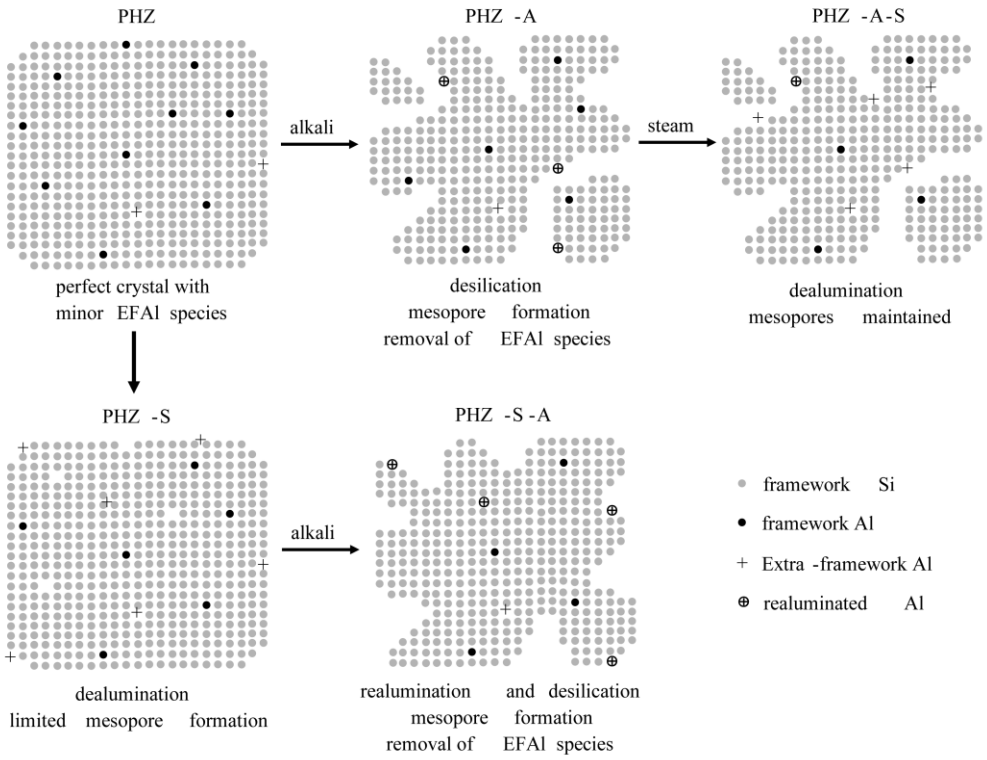

Figure 2.11: Evolution of the porosity and composition of the HZSM-5 zeolite upon the various post-treatments (Shi et al., 2013).

2.3 Metal modification of zeolites

Komvokis *et al*. (2012) examined the metal modification effect of zeolites on product yield and conversion of Fischer-Tropsch (F-T) wax. The results of the catalytic conversion and yields in the cracking of F-T wax by amorphous silica-alumina (ASA), and zeolite catalyst modified by metal are presented in Table 2.1, and the gasoline composition by Paraffins, Isoparaffins, Olefins, Naphthenes, and Aromatics (PIONA) analysis for the same catalyst is shown in Figure 2.12. The dehydrogenation activity was induced by platinum, and tin was used to stabilize the platinum particles by reducing their aggregation-deactivation rate and potassium for adjustment of the number of acid sites of the aluminosilicate supports.

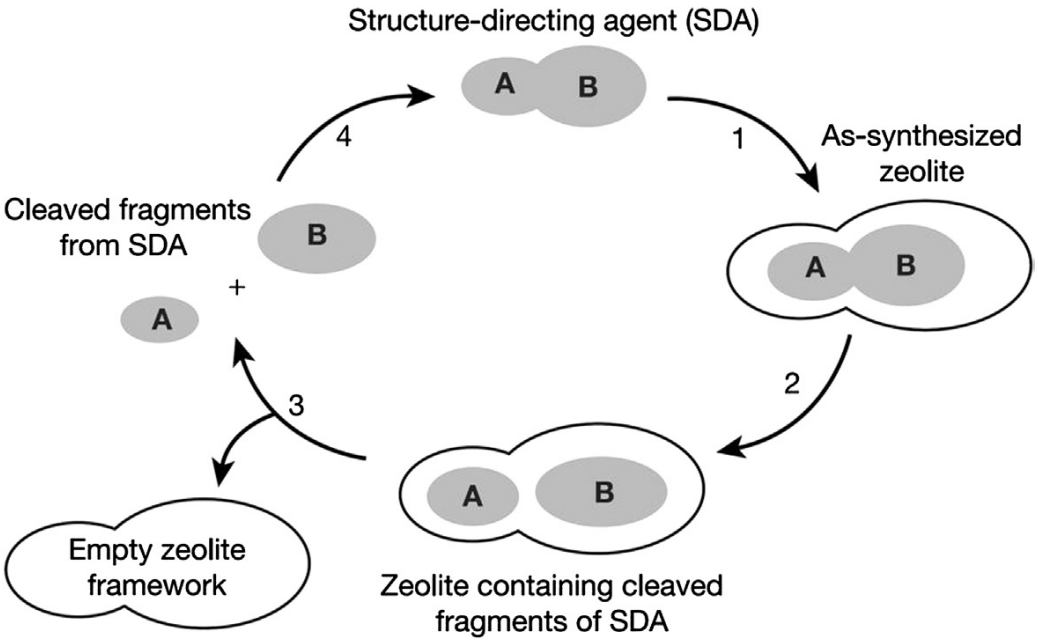

Figure 2.12: Zeolite Synthesis using degradable and recyclable organic template: step 1: organic molecules as template in zeolite synthesis; step 2: organic molecule is cleaved into smaller fragments inside the pores of the zeolite; step 3: the fragments are extracted; and step 4: the template fragments are recombined and recycled back (Eng-Poh, 2013).

Table 2.1: Chemical composition, porosity and acidity characteristics of various types of mesoporous zeolites and other aluminosilicates tested as catalyst in cracking of F-T wax (Komvokis *et al*., 2012).

Samples	Chemical composition		Surface area[a]			Total acid sites[b]	B/L[c]
	Al (wt.%)	Na	Total (m2/g)	Micro (m2/g)	Meso/ macro	(mmol /g)	
H-ZSM-5	1.40	0.01	429	356	73	0.54	5
H-ZSM-5 (3%)[d]	1.55	0.03	193	541	39	0.31	0.8
H-Beta	1.25	0.02	656	343	313	0.49	1.3
H-Beta-st.	1.25	0.02	242	131	111	0.15	0.6
Am-Beta[e]	0.81	0.03	595	125	470	0.22	1.2
H-Y	10.2	0.8	925	874	51	4.39	37
H-Y-st.	10.1	0.82	613	542	71	0.46	0.7
USY-st.	12.5	0.32	565	440	125	0.12	0.6
Pt/USY-st.	12.4	0.29	560	432	128	0.06	0.4
Pt-Sn/USY-st.	12.5	0.29	558	429	129	0.05	0.4
Pt-Sn-K/USY-st.	12.5	0.31	549	425	124	0.03	0.4
Al-MCM-41	1.27	0.04	869	-	869	0.24	0.5
ASA[f]	27.8	0.09	208	-	208	0.21	∞
ASA-st.	27.8	0.09	178	-	178	0.09	-//-

[a] Total surface area was computed using multi-point BET analysis; micro and meso/macropore area using V–t plot analysis.
[b] Computed using TPD-NH3.
[c] Mole ratio of Bronsted acid sites to Lewis computed using FTIR a with in situ pyridine adsorption.
[d] H-ZSM-5 zeolite with very low degree (3%) of crystallinity.
[e] Amorphous Beta-based aluminosilicate.
[f] Amorphous silica–alumina commercial catalyst.

For conventional ASA catalyst, the dispersion of platinum particles shows a little positive effect on reactivity, which yield degree of conversion of ~30 wt.% (Table 2.1) as compared to ~20 wt.% conversion without metal modification. Meanwhile, platinum dispersion on ultra-stable form of zeolite Y (USY-st.) matrix led to significant reduction in wax conversion from 82.56 to 57.54 wt.% with increase in gasoline and LPG (C3 and C4) yields. Tin (0.6 wt.%) was used to moderate the inhibiting effect of platinum on the USY-st. zeolite cracking. This moderation partially recovers the lost conversion to ~62 wt.% and the gasoline yield of ~46 wt.%. Nevertheless, the LPG yield is lower compared

to when only platinum was used. Potassium (0.3 wt.%) dispersion in USY-st. blocks its acid sites thereby leading to significant reduction in the wax conversion.

Komvokis *et al*. (2012) also reported that dispersion of small amounts of platinum (0.5 wt.%) on vigorously steamed zeolite, which was synthesized towards dehydrogenation of n-paraffins to produce olefins. Afterward, it interact with the Bronsted acid sites of the zeolite more swiftly than n-paraffins, according to the initiation reaction step suggested for long chain alkanes hydroisomerization over bifunctional platinum catalysts supported on several zeolite materials (Busto *et al*., 2010; Campelo *et al.*, 2008; Kotrel *et al*., 2000; Scherzer, 1989; Soualah *et al*., 2008). n-paraffins activation by means of dehydrogenation is quite unlike n-paraffins reaction with strong Bronsted acid sites(non-classical penta-coordinated carbonium ion formation by proton addition) or Lewis acid sites (classical carbenium on formation by abstraction of hydride) of zeolites. This can increase the cracking activity of the wax.

Platinum dispersion on the conventional ASA catalyst slight improves wax conversion but because ASA acid sites are mainly Lewis, the cracking activity could not be disseminated by means of formation of carbenium ions as a result of Bronsted acid sites deficiency. Nevertheless, platinum dispersion on steam treated USY zeolite leads to significant increase the cracking performance of the wax, because the remaining Bronsted acid sites on the zeolite are partially blocked (Table 2.1). The presence of both Pt and Sn (Sn, 0.6 wt.%) restored some of the lost cracking activity, whereas subsequent modification with potassium (0.3 wt.%) resulted in very low conversion of wax and lesser acid sites. The hydrogen and coke yield with the samples of steam treated USY zeolite modified with platinum performed better than unmodified USY-st. zeolite. The composition of n- and iso-paraffin decrease upon modification with platinum, whereas

the olefins and aromatics composition increased. This is attributable to the hydrogenation activity of platinum.

2.4 Post synthesis template removal

The organic compound (template) used for preparation of zeolites are removed by combustion performed at high temperature (e.g. ~550 °C) in the air. (Eng-Poh, 2013) reported that during heat treatment, the zeolite framework might be partially destroyed. In addition, a large amount of heat energy are needed for calcinations and organic templates are degraded as CO, CO_2, NOx, and H_2O after calcination, which is environmentally unfavorable.

Template extraction using organic solvent offers another route for detemplating (Jones *et al*., 1998; Lami *et al*., 1993; Takewaki *et al*., 1999a, 1999b). Template removal from zeolites and Beta by extraction using methanol, acetic acid, and dimethylformamide aqueous solution has been carried out (Jones *et al*., 2001). The degree of template extraction was found to depend on the template molecule size and the interaction strength such as electrostatic, van der Waal or hydrogen bond with the framework. Sometimes, liquid solvent extraction is used to remove part of the template from the zeolite framework before the final calcination step (Grudzien *et al*., 2006). Such processes nevertheless, are limited by consumption of large amounts of organic solvents and heat energy.

A novel green route for complete removal and recycling of organic templates used for preparation of ZSM-12, ZSM-11, ZSM-5, VPI-8 zeolites has been proposed (Eng-Poh, 2013; Lee *et al*., 2005). The organic templates used for the preparation of the above zeolites were carefully designed, and easily dismantled within the zeolite pore and thus their fragment removal was possible (Figure 2.12). Moreover, the templates were reassembled and reused for subsequent zeolites synthesis. This later strategy is eco-

friendly and economical since the expensive organic template can be recycled and hence, reducing the cost of zeolite production. However, the method is highly benefited to the zeolite-based low-temperature device manufacturing since the template cleavable from the pore space of the zeolite by altering the reaction conditions.

The use of electromagnetic energy such as microwave radiation for calcination of nanoporous materials was also reported. The rapid and inexpensive method uses the intense heat produced by microwave radiation for the organic template removed from the zeolite matrix (Gallis *et al.*, 2001). For instance, the organic templates from MFI, titanium silicate (TS-1), and BEA zeolites have been effectively removed in very short time, requiring only 5-10 min using microwave energy.

Oxidation of template using ozone or combination of ozone-UV treatment is another promising technique, which can be used for templates removal from zeolites at lower temperatures than the temperature required for conventional calcination (Copperthwaite *et al*., 1985; Heng *et al*., 2004a; Hutchings *et al*., 1989; Li *et al*., 2005). Ozone decomposes into atomic oxygen and radical species, which are strongly reactive oxidants at these temperatures. This strategy is well suited for detemplating of zeolite coatings and membrane deposited on the temperature sensitive substrates due to mild thermal conditions. This strategy has been used for MFI and DDR zeolites (Copperthwaite *et al*., 1985; Heng *et al*., 2004b; Hutchings *et al*., 1989; Li *et al*., 2005). This method is on one side has improved the process of template removal from porous materials and on the other side allows an efficient recovery of the templates and/or more ordered and more stable crystalline structure are obtained.

A new photochemical methods for the removal of the organic template from microporous materials (silicate-1, AlPO-5, ITQ-7) at low temperatures (50-70 °C) have also been

reported (Parikh *et al*., 2004). The strategy is based on the sample exposure to short wavelength UV radiation in air, and as a result, the medium pressure mercury lamp (184-257 nm) generates ozone. This approach is more environmentally friendly because the template can be removed at near room temperature and at the same time, maintaining open inorganic frameworks. In addition, the organic species are converted to CO_2, N, and H_2O, which are non-toxic gasses.

Not only that, non-thermal template removal techniques using cold plasma treatment have been developed (Eng-Poh, 2013). This treatment leads to removal of the organic templates from zeolites within several minutes, without carbon deposition, thereby eliminating both hazardous chemicals usage and high-temperature treatment. Therefore, more economical and environmental benign synthesis is achievable.

2.5 Hierarchy factor

Hierarchy factor is a viable tool for measurement of the degree of structural order of a material. It also helps to correlate and to make quantitative comparison of various zeolite materials produced from different synthesis strategies (Pérez-Ramírez *et al*., 2009; Zheng *et al*., 2011; Zheng *et al*., 2010).

Pérez-Ramírez *et al*. (2009) proposed a model as a tool for classification of hierarchy mesoporous zeolites as derived from the conventional N_2 adsorption analysis. From the effect of the micropore volume on the total pore volume and the effect of the mesopore specific surface area on the total specific surface area of the weighed sample, they defined hierarchy factor (HF) as follows:

$$\mathrm{HF} = \frac{V_{micro} S_{meso}}{V_{Total} S_{BET}} \qquad (2.5)$$

In order to maximize the value of HF, the mesopore surface area needs enhancement without penalizing the micropore volume severely. That is to say, rather than playing a competition role; both porosity levels must complement each other: while the micropores play the active sites, the auxiliary mesopores solved the problem of mass transfer limitation. It is also important to note that two or more different zeolite catalysts prepared through different synthesis strategies but with the same value of hierarchical factor may not necessarily exhibit the same catalytic performance in the same reaction due to varying acid strength and distribution. For instance, the one with the highest number of Brönsted-acid sites will surely exhibit the best performance (Zheng *et al*., 2011).

However, Zheng *et al*. (2013) reported that HF seldom show a linear relationship with catalytic performance as expected when they tested it with catalytic cracking of isopropylbenzene. For instance, sample MFZ-8 with relatively high mesopore volume but low total specific surface area and micropore volume possess a high value of HF (0.13) because HF is defined with respect to total pore volume. In order to make more reasonable quantitative comparison of the degree of structural order of composite materials, (Zheng *et al*., 2013), therefore, revised hierarchy factor as HF' and

$$\mathrm{HF'} = \frac{V_{micro} * S_{meso}}{V_{meso} * S_{BET}} \qquad (2.6)$$

Because

$$\frac{\mathrm{HF'}}{\mathrm{HF}} = \frac{\mathrm{V_{total}}}{\mathrm{V_{meso}}} = \frac{\mathrm{V_{meso}} + \mathrm{V_{micro}}}{\mathrm{V_{meso}}} = 1 + \frac{\mathrm{V_{micro}}}{\mathrm{V_{meso}}} \qquad (2.7)$$

Therefore,

$$HF' = HF * \left(1 + \frac{V_{micro}}{V_{meso}}\right) \quad (2.8)$$

Table 2.5 show several samples of hierarchical mesoporous zeolites and their corresponding HF, HF' Brönsted-acid sites and catalytic cracking performance. It is therefore, clearly seen that HF' is more reasonable in determining degree of hierarchy of composite zeolites that have similar compositions and acidities in reactions with bulky reactants. It is also be noted that crystallization parameters of the synthesized mesoporous materials has effect on the hierarchy factor. Koekkoek *et al*. (2011) synthesized mesoporous zeolites MesoZSM-5(T, y) where T is the crystallization temperature and y is the crystallization time (Table 2.2). From their report, we could see on Table 2.2 that hierarchy factor increase with increase in crystallization temperature and y is the crystallization time.

Table 2.2: Hierarchical factor and Brönsted acidity effect on catalytic performance of mesoporous zeolites.

Zeolite	V_{micro}	V_{meso}	V_{total}	S_{meso}	HF	B site[a]	Reaction				Ref.
	($cm^3\ g^{-1}$)	($cm^3\ g^{-1}$)	($cm^3\ g^{-1}$)	($cm^3\ g^{-1}$)		(mmol/g)	Type	Time (h)	T (°C)	Conv. wt.%	
ZRP-1	0.089	0.131	0.22	128.7	0.1706	1093	n-Heptane cracking	-	650	100.00	(Chen *et al.*, 2012)
H-MFI	0.152	0.034	0.186	52.2	0.1159	197	n-Heptane cracking	-	650	99.79	(Chen *et al.*, 2012)
HZ (10.0) [b]	0.122	0.063	0.185	102.1	0.1991	177	n-Heptane cracking	-	650	99.41	(Chen *et al.*, 2012)
HZ (25.0) [b]	0.113	0.077	0.19	111.7	0.1992	696	n-Heptane cracking	-	650	98.68	(Chen *et al.*, 2012)
HZ (40.0) [b]	0.112	0.133	0.245	109.4	0.1523	836	n-Heptane cracking	-	650	97.91	(Chen *et al.*, 2012)
HZ (50.0) [b]	0.101	0.243	0.344	104.9	0.1009	984	n-Heptane cracking	-	650	97.50	(Chen *et al.*, 2012)
MFZ-17 [e]	0.25	0.11	0.36	91	0.1227	-	isopropylbenzene cracking	0.1	300	100.00	(Zheng *et al.*, 2013)
MFZ-16 [e]	0.26	0.16	0.42	128	0.1376	-	isopropylbenzene cracking	0.1	300	98.79	(Zheng *et al.*, 2013)
MFZ-14	0.26	0.1	0.36	86	0.1138		isopropylbenzene cracking	0.1	300	99.31	(Zheng *et al.*, 2013)
MFZ-12 [e]	0.25	0.07	0.32	45	0.0707		isopropylbenzene cracking	0.1	300	99.00	(Zheng *et al.*, 2013)
MFZ-8 [e]	0.1	0.13	0.23	74	0.1330		isopropylbenzene cracking	0.1	300	98.00	(Zheng *et al.*, 2013)
Y+M [f]	0.25	0.02	0.27	6	0.0106		isopropylbenzene cracking	0.1	300	99.00	(Zheng *et al.*, 2013)
MFZ-17 [e]	0.25	0.11	0.36	91	0.1227		isopropylbenzene cracking	8	300	98.10	(Zheng *et al.*, 2013)
MFZ-16 [e]	0.26	0.16	0.42	128	0.1376		isopropylbenzene cracking	8	300	82.07	(Zheng *et al.*, 2013)
MFZ-14 [e]	0.26	0.1	0.36	86	0.1138		isopropylbenzene cracking	8	300	93.28	(Zheng *et al.*, 2013)
MFZ-12 [e]	0.25	0.07	0.32	45	0.0707		isopropylbenzene cracking	8	300	74.66	(Zheng *et al.*, 2013)
MFZ-8 [e]	0.1	0.13	0.23	74	0.1330		isopropylbenzene cracking	8	300	43.28	(Zheng *et al.*, 2013)
Y+M [f]	0.25	0.02	0.27	6	0.0106		isopropylbenzene cracking	8	300	43.28	(Zheng *et al.*, 2013)
BFZ-1.30 [g]	0.19	0.21	0.4	80	0.0782		Methanol cracking	2	250	77.20	(Zheng *et al.*, 2011)
BFZ-1.35 [g]	0.15	0.22	0.37	112	0.1051		Methanol cracking	2	250	89.70	(Zheng *et al.*, 2011)
BFZ-1.40 [g]	0.18	0.22	0.4	130	0.1289		Methanol cracking	2	250	91.30	(Zheng *et al.*, 2011)
BFZ-1.45 [g]	0.19	0.24	0.43	172	0.1462		Methanol cracking	2	250	97.20	(Zheng *et al.*, 2011)
BFZ-1.45 [g]	0.19	0.24	0.43	172	0.1462		Methanol cracking	72	250	72.00	(Zheng *et al.*, 2011)
BFZ-1.50 [g]	0.19	0.27	0.46	130	0.1045		Methanol cracking	2	250	88.10	(Zheng *et al.*, 2011)
BFZ-s [h]	0.25	0.08	0.33	45	0.0689		Methanol cracking	2	250	17.40	(Zheng *et al.*, 2011)
FAU-BEA [i]	0.19	0.13	0.32	64	0.0717		Methanol cracking	2	250	71.10	(Zheng *et al.*, 2011)
FBZ [j]	0.23	0.11	0.34	72	0.0843		Methanol cracking	2	250	82.10	(Zheng *et al.*, 2011)
BEA	0.18	0.04	0.22	29	0.0459	-	Methanol cracking	2	250	84.70	(Zheng *et al.*, 2011)
FAU	0.36	0.02	0.38	9	0.0116	-	Methanol cracking	2	250	53.60	(Zheng *et al.*, 2011)
Meso-MFI(150, 0) [k]	0.009	0.18	0.189	93	0.0102	3	n-Heptane cracking	2	353	40.00	(Koekkoek *et al.*, 2011)
Meso- MFI (150, 6) [k]	0.034	0.41	0.444	555	0.0621	9	n-Heptane cracking	2	350	40.00	(Koekkoek *et al.*, 2011)
Meso- MFI (150,120) [k]	0.075	0.28	0.355	266	0.1083	80	n-Heptane cracking	2	255	40.00	(Koekkoek *et al.*, 2011)

Zeolite	V_{micro}	V_{meso}	V_{total}	S_{meso}	HF	B site[a]	Reaction				Ref.
	($cm^3\ g^{-1}$)	($cm^3\ g^{-1}$)	($cm^3\ g^{-1}$)	($cm^3\ g^{-1}$)		(mmol/g)	Type	Time (h)	T (^oC)	Conv. wt.%	
Meso- MFI (150, 72)[k]	0.06	0.3	0.36	387	0.1134	51	n-Heptane cracking	2	267	40.00	(Koekkoek *et al.*, 2011)
Meso- MFI (170, 6)[k]	0	0.25	0.25	360	0.0000	6	n-Heptane cracking	2	350	40.00	(Koekkoek *et al.*, 2011)
Meso- MFI (170,120)[k]	0.11	0.11	0.22	90	0.1160	71	n-Heptane cracking	2	252	40.00	(Koekkoek *et al.*, 2011)
BFZ-28[l]	0.23	0.245	0.475	130	0.1042	-	Hydrogenation of benzene	2.964	400	98.46	(Zheng *et al*., 2010)
BFZ-24[l]	0.22	0.21	0.43	101	0.0891	-	Hydrogenation of benzene	-	-	-	(Zheng *et al*., 2010)
BFZ-18[l]	0.2	0.19	0.39	102	0.1032	-	Hydrogenation of benzene	2.964	400	98.46	(Zheng *et al*., 2010)

[a] Brönsted acid site,
[b] HZ (x): composite zeolite prepared from H-MFI and ZRP-1, x stands for percentage of ZRP-1
[c] Hp-Na(x): NaOH treated H-MFI, x refers to the volume (ml) of ethanol in the mixing solution
[d] Ethyl laurate yield in the esterification of lauric acid
[e] MFZ-t: t stands for the hydrothermal treatment time
[f] Y+M: mixture of Y and MFZ zeolites
[g] BFZ-x: a composite zeolite prepared using β zeolite as the core and Y zeolite as the shell (x stands for the concentration of OH- (mol/L) during the second step of the synthesis).
[h] BFZ-s: shaped BFZ
[i] FAU-BEA (a composite zeolite obtained by the overgrowth of zeolite on the core Y crystal)
[j] FBZ (a composite zeolite prepared with Y zeolite as the core as well as the nutrients for β zeolite growth)
[k] MesoZSM-5(T, y): T is the crystallization temperature and y is the crystallization time
[l] BFZ-t: t represents crystallization time (h)

2.6 Hydrothermal stability

Hydrothermal and thermal stability are essential properties of a zeolite catalyst. Several industrial reactions need these essential properties, which are more often than not important for the catalyst life and in determining the selection of the catalytic process.

Hydrothermally stable zeolites are of vital importance in catalysis. It was reported that phosphorous modification or heteroatoms incorporation are effective strategies that can be used to improve zeolites hydrothermal stability (Chen *et al*., 2012; Kaeding *et al*., 1981). Zhao *et al*. (2007) prepared series of catalyst for cracking of C_4 olefin by impregnating HZSM-5 using varying quantities of phosphoric acid then later calcinated in air under high temperature. The introduction of an appropriate amount of phosphorous into the HZSM-5 zeolite matrix is capable of slowing down dealumination and coke deposition, which mainly deactivates HZSM-5 zeolite. There may be synergistic interaction between the Si-O-Al framework and the species of phosphorous oxide and within the pore channels of the zeolite, which greatly helped in optimizing the acid distribution and strength, increasing propylene selectivity and decreasing hydrogen transfer. The description of the exact nature of the new acid site that emerged in P/HZSM-5 during steaming, solid-state 31P and 27Al NMR measurement and D2/OH exchange has also been used in investigating the charge on the acid center before and after phosphorous modification (Liu *et al*., 2012). It was found out that the newly generated acid sites by phosphorous modification seems to be related with phosphorous entering the zeolite matrix at the position stabilized by some extra lattice aluminum and left by dealumination. The residual framework aluminum is protected by the addition of phosphorous to the zeolite lattice against further dealumination. This results in hydrothermal stability of the acid sites in P/HZSM-5 framework and improvement in the

performance of the catalyst towards cracking C_4 olefin after high temperature steaming. In dehydration of methanol to produce olefins, there is a generation of large water quantity in the product mixtures. Therefore, the zeolite catalyst should be able to withstand the steam and high-temperature regeneration. SAPO-34 zeolite has been the catalytic material of choice for the MTO process because of its goodly hydrothermal and thermal stability (Liu *et al*., 2012).

In a Study of Wang *et al*. (2009), the hydrothermal stability of hierarchically porous ZSM-5 was investigated by steam treatment. After steaming for 120 hr, the porous ZSM-5 zeolite maintained the same nitrogen isotherm to the untreated zeolite sample (Figure 2.13), possessing 350 m^2g-1 BET surface area (4% reduction from 363 m^2g-1 to 350 m^2g-1) this proves that the stability of hierarchically porous ZSM-5 zeolite. In order to make a comparison, the hydrothermal stability of commercial mesoporous silica SBA-15 was also investigated (Wang *et al*., 2005). It was steamed for 80 h and the BET surface area decreased by 72% (from 794 m^2g-1 to 220 m^2g-1). This confirms that the hierarchical mesoporosity in porous ZSM-5 is far more stable than the mesoporosity in conventional mesoporous silica SBA-15.

Petrochemical reactions as well as several other refining processes require catalysts that possess goodly hydrothermal and thermal stability. Therefore, it is worthwhile to carrying out a comprehensive study to search for strategies that could lead to improvement of hydrothermal and thermal stability in catalysis.

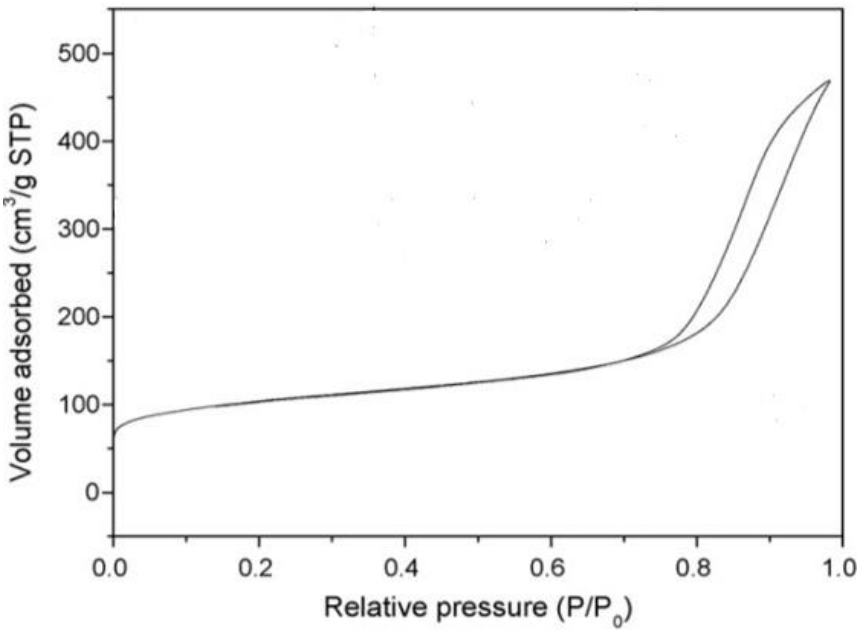

Figure 2.13: Nitrogen isotherm of the hierarchical mesoporous ZSM-5 (Wang et al., 2009).

2.7 Solid acid catalyst from kaolin

Kaolinite is a 1:1 layer phyllosilicate clay mineral that makes up about 10-95% of kaolin mineral. Kaolinite structure possesses a sheet of $Al(OH)_4$ octahedral (gibbsite-like) and a sheet of SiO_4 tetrahedral combined with longitudinal sideline chains forming the dioctahedral structure called 1:1 layer phyllosilicate (Yang *et al*., 2013).. Theoretically, their chemical formula is $Si_2Al_2O_5(OH)_4$ (Al_2O_5 $Si_2.2H_2O$ or $Al_2O_3.2SiO_5.2H_2O$) (Varga, 2007). Other components of kaolin include mica and quartz as well as metal oxides such as K_2O, CaO, TiO_2, Fe_2O_3, Na_2O, MgO, MnO, and P_2O_5 as impurities. It is a versatile hydrated aluminosilicate with wide variety of industrial applications such as catalysis, (Hu *et al*., 2012), ion exchange (Bhattacharyya *et al*., 2011), decolorization (Liu *et al*., 2013), adsorption, catalyst supports and modified catalysts (Vaccari, 1998). Kaolinite catalysts and supports (both modified and unmodified) are regaining attention in catalysis because they are naturally abundant (Panda *et al*., 2011). Other favorable factors include high surface area,

mechanical and chemical stability, Lewis and Brönsted acid sites. The materials are also environmentally benign (do Nascimento *et al*., 2011) with cation-exchange ability (CEC). Reactivity and surface properties have enhanced kaolinite application in the chemical industry based on surface modification. There are various methods as proposed in the open literature for enhancing the properties of kaolinite. These include chemical activation (intercalation, alkali, organic and inorganic acid) (do Nascimento *et al*., 2011), intercalation (Horváth *et al*., 2003), mechanochemical (Makó *et al*., 2006), and thermal treatments (do Nascimento *et al*., 2011).

However, modified kaolinite have received immense attention because of their crystalline structure (Suitch *et al*., 1983) (Figure 2.14) and large pore size, which is advantageous in conversion of bulky molecule (Lenarda *et al*., 2007). Applying mechanochemical techniques have great effects on surface modifications. This is pronounced in Szeg and Zettlitz kaolinite. Mechanochemical activation of these materials improves active centers, surface area, and pore volume (Horváth *et al*., 2003). Kaolinite materials are amenable to alkali, organic and inorganic acid activation. Acid and alkali treatment dissolve external layer and eliminates impurities. Further, dealumination or desilication of kaolinite structure changes the structural and chemical composition (do Nascimento *et al*., 2011a) of the material. Similarly, number of acid sites, surface area and catalytic properties of amorphized kaolin (calcined or grounded), smectic clays (montmorillonite and saponite) and fibrous clays (palygorskite and saponite) (Lenarda *et al*., 2007) increases. The wide range of pore sizes, strong acid sites, and part-amorphous nature, highlight the strong solid acidic properties of modified kaolinite catalysts. These make them viable for dehydration reactions and biomass conversion as well as catalytic cracking (do Nascimento *et al*., 2011b). Modified kaolinite could also act as

meso- and macroporous support for transition metal oxide adsorbent or catalysts in the reacting mixture because of their part-amorphous nature. Modification improves the effectiveness (Hassan *et al*., 2013), reactivity, efficiency as well as the stability of the catalysts via increased aggregation of metal oxide (Liu *et al*., 2013). Instances include pollution control (removal of impurities) (Chen *et al*., 2011; Üzüm *et al*., 2009) especially in wastewater treatment (Liu *et al*., 2013) such as photo-Fenton catalysis (Ayodele, 2013). Others include free fatty acid (FFA) esterification (do Nascimento *et al*., 2011a) and steam gasification (Hassan *et al*., 2013). Interestingly, kaolinite is impervious to microbial attack; they are thermally stable, hydrophilic in nature and easily regenerated. Some authors reported the suitability of kaolinite as inorganic supports for enzymatic (organic) catalysts (Huang *et al*., 2008). Furthermore, several researchers highlighted these materials as economic precursors in synthesizing microspherical zeolitic molecular sieves such as Y and X zeolites.

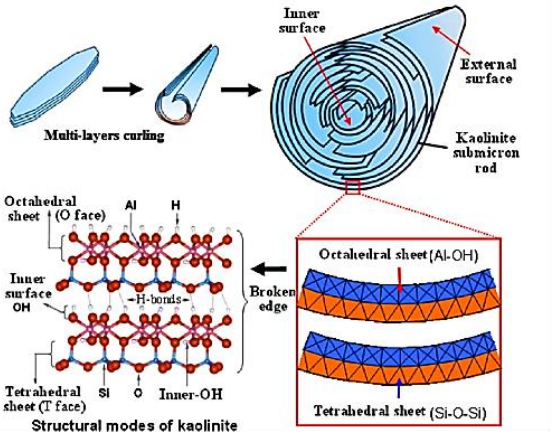

Figure 2.14: Schematic diagram of kaolinte proposed by Hu et al. (2002).

Despite extensive researches on catalytic applications of these materials, the advent of synthetic silica/aluminas and zeolite Y has seemingly overshadowed their popularity. Moreover, fast expanding FCC units led to increased catalyst consumption. This created a

dearth of high quality starting materials for in situ synthesis. Therefore, we explore the physicochemical properties of kaolinite that make them suitable for catalysis. To achieve this aim seamlessly, the section reviewed the physicochemistry of kaolin, and effect of their amenability to modification on their catalytic performance. The review comprises five sections: Section 1 gives a general discussion on physicochemical properties of kaolin. Section 2 reviews the different types of modifications while section 3 presents instances that discuss the applicability of kaolinite as a precursor in synthesizing microspherical zeolites. To stimulate further researches, section 3 also gives in-depth analyzes of kaolinite as catalyst supports. The discussion concludes by proffering promising solutions that will ensure the prominence of kaolinite in catalysis. These include recent advances in improving the development of new materials.

2.7.1 Physicochemical properties

The physicochemical properties of kaolinite determine their industrial applications in catalysis. Manipulating these properties increases the industrial applicability of these materials by enhancing activity and product selectivity (Sani *et al*., 2014). Therefore, this section highlights how analyzes such as XRD, TGA, DSC and FTIR reveal modifications on kaolinite. The section also discussed instances how thermal activation and surface charge heterogeneity affect these physicochemical properties. Table 2.3 shows the chemical composition of different kaolin samples with Si/Al ratio ranging from 1.1 to 1.78. The Table also highlights impurities such as K_2O, CaO, TiO_2, Fe_2O_3, Na_2O, MgO, MnO, and P_2O_5.

Table 2.3: Physicochemical properties of some kaolinite sample.

Kaolinite Notation	Sample Origin	Si/Al	K_2O	CaO	TiO_2	Fe_2O_3	Na_2O	MgO	MnO	P_2O_5	H_2O/LOI [a]	Ref.
A	Unknown	1.2	0.9	-	0.4	0.4	-	-	-	-	-	(Castellano *et al.*, 2010)
B	Brittany (F)	1.3	2.5	-		0.5	-	-	-	-	-	(Castellano *et al.*, 2010)
C	Unknown	1.2	1	-	0.4	0.4	-	-	-	-	-	(Castellano *et al.*, 2010)
D	Charentes basin (F)	1.1	0.5	0.4	0.7	0.8	-	-	-	-	-	(Castellano *et al.*, 2010)
MK	Mahoming China	1.24	0.12	0.15	0.25	0.41	0.18	0.22	-	-	14	(Hu *et al.*, 2012)
BK	Beihai China	1.26	0.9	0.01	0.05	0.32	0.2	0.12	-	-	13.47	(Hu *et al.*, 2012)
HK	Hanpu, China	1.34	1.26	0.01	0.06	0.39	0.03	0.15	-	-	12.51	(Hu *et al.*, 2012)
LK	Longyan China	1.24	0.19	0.1	0.12	0.74	0.03	0.04	0.01	-	14.68	(Hu *et al.*, 2012)
KK	Zhangjiakou China	1.3	0.01	0.47	1.38	0.4	0.08	0.01	0	0.1	13.93	(Cheng *et al.*, 2010)

[a] LOI: loss on ignition.
[b] XRD at 001 position (Å).

2.7.1.1 Crystallinity assessment

Kaolinites XRD patterns exhibit broadband between 2θ = ~12.2-35^{o} with 4 peaks, which have basal spacing of about 0.71, 0.446, 0.358 and 0.256 nm respectively (Vizcayno *et al*., 2010). XRD diffractograms reveal structural defects in kaolinite because of variability in peak positions and intensity modulation of kaolinite XRD patterns (Chmielová *et al*., 2002). XRD identification of order-disorder is challenging because of overlapping peaks and interferences in kaolinites. Hinckley index (HI) (Stoch, 1974) measures the degree of structural order of kaolinite crystal structure. Other techniques include weighting intensity ratio index (WIRI) for analyzing kaolitic rock consisting of not less than 20 wt% kaolinite (Aparicio *et al*., 1999; Plançon *et al*., 1990) and Aparicio-Galan-Ferrell index (AGFI) (Chmielová *et al*., 2002). It is possible to obtain HI value using (02, 11) band which composes of 02*l* and 11*l* sequence (20 to 23° 2θ CuKα) because it is sensitive to random and interlayer displacements of type b/3 and 2 (Aparicio *et al*., 1999). This index value is:

$$\mathrm{HI} = \frac{\mathrm{A} + \mathrm{B}}{\mathrm{A_h}} \qquad (2.9)$$

where A is the$1\bar{1}0$ reflection height above the band of overlapping peak; B is the$11\bar{1}$ reflection height above the band of overlapping peak and A_h is the overall reflection height $1\bar{1}0$ peak above the background as shown in Figure 2.15 below (Chmielová *et al*., 2002). HI values range from 0.3 to 1.8; the higher the HI value the higher the degree of structural order (Stoch, 1974). For ordered kaolinites, the HI value is greater than 1.0 while the HI is below 1.0 for disordered kaolinites, (Chmielová *et al*., 2002).

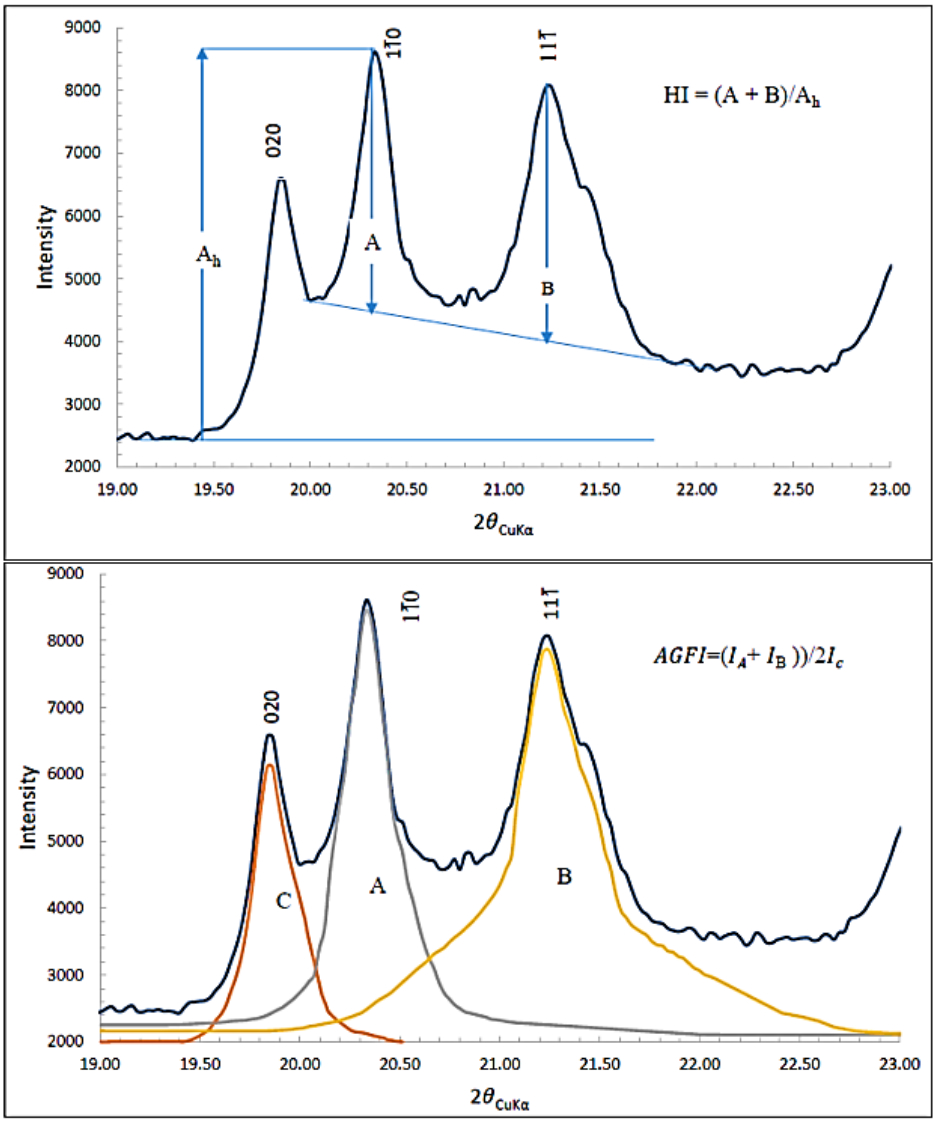

Figure 2.15: Fitting procedure for HI and AGFI parameter on (02, 11) band.

It is appropriate to obtain AGFI value from (02, 11) band. Weighting peak intensity ratio of 020, 1$\bar{1}$0, 11$\bar{1}$ peak reflection estimates AGFI value thus (Chmielová *et al*., 2002):

$$\mathrm{AGFI} = \frac{\mathrm{I}(1\,\bar{1}\,0) + \mathrm{I}(11\,\bar{1})}{\mathrm{wI}(020)} \qquad (2.10)$$

For 1$\bar{1}$0 and 11$\bar{1}$ peak intensities (I_A and I_B), the weighting coefficient is 1, while for 020 intensity, I_C, the weighting coefficient, w = 2. Therefore,

$$\mathrm{AGFI} = \frac{\mathrm{I_A} + \mathrm{I_B}}{2\mathrm{I_C}} \qquad (2.11)$$

Where IA is the $1\bar{1}0$ peak reflection intensity; IB is the $11\bar{1}$ peak reflection intensity and IC is the 020 peak reflection intensity, as shown in Figure 2.2 (Chmielová *et al*., 2002). It is appropriate to compute the peak intensities value for IA, IB and IC using DIFPATAN (computer program developed by Kuzel, 1991) (Valášková *et al*., 2007). WIRI is a function of the peak intensities of (02, 11) band and full width half maximum (FWHM) of the corresponding 020, $1\bar{1}0$, $11\bar{1}$ and $1\bar{1}\bar{1}$ reflections resulting from decomposition of the same band. We can obtain the values of FWHM and corresponding intensities using DIFPATAN (Chmielová *et al*., 2002).

$$WIRI = 1 - e^{-\left(\frac{w_1 I(1\bar{1}0) + w_2 I(11\bar{1}) + w_3 I(1\bar{1}\bar{1})}{w_4 I(020)}\right)} \qquad (2.12)$$

where weighting coefficients w_1, w_2, w_3 and w_4 are the reciprocal of FWHM of $1\bar{1}0$, $11\bar{1}$, $1\bar{1}\bar{1}$ and 020 peak respectively (Ptáček *et al*., 2013). Chmielova *et al*. (2002), modeled the relationship between HI and WIRI was as HI = 0.10 + 1.44WIRI with R = 0.989. The relation: AGFI = 0.7 – 0.65WIRI + 1.86WIRI^2 with R = 0.992 provides modeled relationship between AGFI and WIRI. The value of WIRI ranges between 0 and 1. For low degree order, WIRI ≤ 0.4, for medium order, 0.4 < WIRI ≤ 0.7 and > 0.7 for high order WIRI (Chmielová *et al*., 2002; Ptáček *et al*., 2013).

2.7.1.2 Surface charge heterogeneity

Hydrogen bond binds the tetrahedral sheet and the gibbsite-like sheet of the 1:1 layers silicate structure of kaolinite. The bond is between the electronegative oxygen of the tetrahedral sheet and the hydroxyl group of the octahedral sheet in c-axis (Liu *et al*., 2013; Yang *et al*., 2013). Consequently, kaolinite particles possess oppositely charged surface parts in an aqueous medium. One is negative charge permanently on the T (tetrahedral)

faces. This arises from minor isomorphic substitution in the tetrahedral layer. The second is a variable charge on the O faces (hydroxyl-terminated planes) because of proton donation or acceptance of the edge groups (Hu *et al*., 2012). Depending on the pH in the protonation/deprotonation reaction in an aqueous phase, the charge on the amphoteric sites develops on the edges and faces of the octahedral (O) sheet. This causes charge heterogeneity (Brady *et al*., 1996; Tombácz *et al*., 2006). Protonation of aluminol group occurs when kaolinite in aqueous medium possesses pH value below the point of zero net proton charge (PZNPC) of the main edge (amphoteric) site. Conversely, deprotonation of silanol and aluminol group occur when the pH value of kaolinite in an aqueous medium is greater than PZNPC of the main edge (amphoteric) site. Both gibbsite planes and broken edges of aluminol (Al-OH) sites accept proton at pH below the PZNPC of amphoteric sites (~6.0-6.5). Therefore, increasing the pH above the PZNPC value results in formation of negative charge on the gibbsite planes and the broken edges, which leads to decrease in zeta potential (Hu *et al*., 2012). This makes the aluminol (Al-OH) groups and broken edges reactive. Conversely, silanol (Si-OH) on the broken edges are only reactive at abnormal (above PZNPC) pH values (Brady *et al*., 1996). However, the hydroxyl groups on the O faces are less reactive than those on the aluminols and the silanols on the broken edges (Brady *et al*., 1996). The following reactions occur at gibbsite planes and the broken edges leading to formation of positive charges:

$$Al\text{-}OH + OH^- \rightarrow Al\text{-}O^- \qquad (2.13)$$

The following reactions occur at the gibbsite planes and the broken edges leading to formation of negative charges:

$$Si\text{-}OH + OH^- \rightarrow Si\text{-}O^- . \qquad (2.14)$$

$$Al\text{-}OH + H+ \rightarrow Al\text{-}OH^{2}+. \qquad (2.15)$$

2.7.1.3 Thermal properties of Kaolinites

Comprehensive understanding of kaolinite thermal behavior is essential for deducing results of the thermal analysis. Thermal analysis gives information on weight loss, recrystallization, decomposition and phase transformation (Hussin *et al*., 2011).

Thermogravimetry/differential thermal analysis (TG/DTA) or differential scanning calorimetry (DSC) analyzes reveal the thermal behavior of the kaolinite structure (Cheng *et al.*, 2012). Kaolinites exhibit two endothermic peaks (at ~55 to 80 °C and ~450 to 600 °C) and one exothermic peak (at ~980 to 1000 °C) (Figure 2.16a). The first endothermic peak is of low intensity with associated weight loss of ~0.85 wt% which is due to water absorbed physically from the atmosphere held within the particle defects. The second endothermic peak with higher intensity is because of weight loss of ~11.2 to14.2 wt.% (Konan *et al*., 2009). This water loss is from coordinated molecules at the surface of kaolinite particles arising from the interaction between the released OH units from the gibbsite-like sheets (Horváth *et al*., 2003). Theoretically, the weight loss for dehydroxylation of kaolinite is 13.96 wt.% (Gasparini *et al*., 2013; Ptáček *et al*., 2010). Dehydroxylation is important because it results to the formation of metakaolin as shown in the reaction below:

$$Al_2Si_2O_5(OH)_4 \rightarrow Al_2O_3.2SiO_2 + 2H_2O \qquad (2.16)$$

Dehydroxylation occurs simultaneously in homogeneous and heterogeneous mechanisms. Two neighboring OH-groups with different (lower and greater than PZNPC) pH values interact in a homogeneous mechanism. The proton of the OH unit with pH value lower than PZNPC reacts with that with pH value greater than PZNPC to release water through the interlayer spaces of the kaolinite particles. The increase in electrical conductivity of dehydroxylation temperature (Cheng *et al*., 2012) during

heterogeneous mechanism induces migration of protons produced in the kaolinite structure to the elimination region. This enhances interaction with the OH units and subsequent water formation. Plausibly, these explain the variation in the peak temperatures. This is because of variation in the degree of structural order, pressure, water vapor partial pressure, ultrasound processing, heating rate and degree of mechanochemical activation. A Higher degree of structural order produces higher endothermic peak while smaller particle size leads to lower endothermic peak (Horváth *et al*., 2003).

The exothermic transformation from endothermic peak to takes place at ~700 °C and subsequently another exothermic peak appears at ~980 to 1000 °C. These are attributed to a transformation of metakaoline to spinel or -alumina and amorphous silica. The latter transformation started at ~920 °C and lasted until ~1100 °C. However, the precise product obtained from this transformation is still under investigation (Ghorbel *et al*., 2008):

$$2(Al_2O_3.2SiO_2) \rightarrow 2Al_2O_3.3SiO_2\,(\text{spinel}) + SiO_2 \qquad (2.17)$$

$$Al_2O_3.2SiO_2 \rightarrow Al_2O_3\,(\gamma\text{-alumina}) + 2SiO_2 \qquad (2.18)$$

Mullite phase starts to form at ~1100 °C and it increases with heating until 1300 °C. Subsequently, crystalline cristobalite emerges from the amorphous silica (Eq. 2.19).

$$3(2Al_2O_3.3SiO_2) \rightarrow 2(3Al_2O_3.2SiO_2)\,(\text{mullite}) + 5SiO_2 \qquad (2.19)$$

$$SiO_2\,(\text{amorphous}) \rightarrow SiO_2\,(\text{cristabalite}) \qquad (2.20)$$

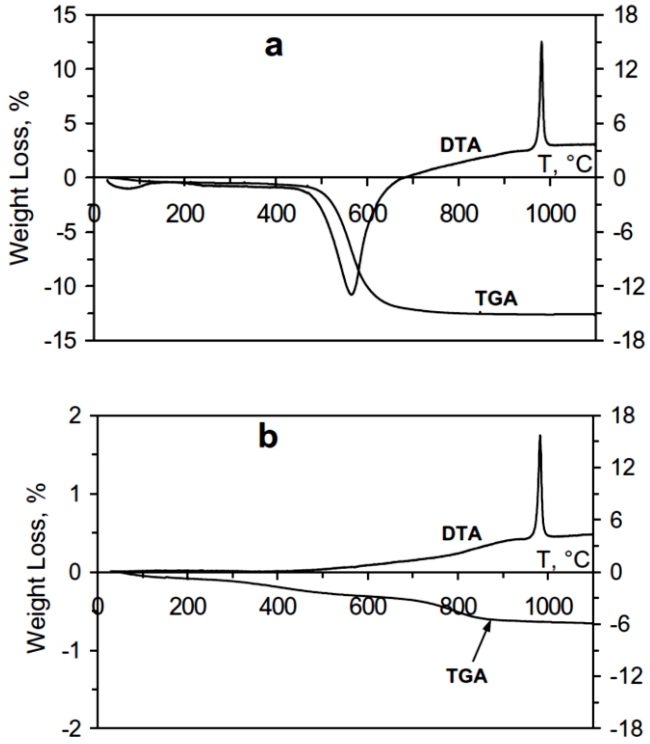

Figure 2.16: TG/TDA of (a) kaolinite and (b) metakaolin (Konan et al., 2009).

2.7.2 Modification methods

As we alluded above, manipulating the physicochemical properties of catalytic materials is one of the surest means of enhancing activity and product selectivity. Hence, this section provides specific instances on different modification methods for improving kaolinite properties such as surface area, porosity, and acidity.

2.7.2.1 Mechanochemical activation

This modification route entails particle size reduction and helps to increase the pore volume and surface area of kaolinite materials. It culminates in improved surface reactivity as well as a higher capacity for ion exchange (Horváth *et al.*, 2003). The mechanochemical modification can be via specific micronization processes or industrial grinding (Dellisanti *et al.*, 2012). However, mechanochemical modification leads to delamination of kaolinite particles and agglomeration of the delaminated particles to form

huge spheroidal particles. The delaminated product is a randomly structured wet xerogel in which the hydroxyl units react to form coordinated water molecules attached to the active sites on the surface of the modified kaolinite. This is because of water molecules formed from the interaction between two -OH units (Eq. 2.22) by proton migration in a process called prototropy (Horváth *et al*., 2003).

$$OH^- \leftrightarrow H^+ + O^{2-} \quad (2.21)$$

$$H^+ + O\,H^- \leftrightarrow H_2O \quad (2.22)$$

Expectedly, grinding decreases structurally ordered kaolinite that coexist with the disordered materials. This affects the degree of structural order in the delaminated precursor, which determines the physicochemical properties of the mechanochemically activated kaolinite. Moreover, excess grinding alters kaolinite crystal structure and turns it into an amorphous material with decreased surface area and pore volume (Sánchez *et al*., 1999) reported that delamination results in alumination of the kaolinite surface due to the formation of a coating of $Al2O_3$ generated from the grinding process. This leads to enrichment in the octahedral layer of the kaolinite and a corresponding increase in the PZNPC (Gasparini *et al*., 2013). (Dellisanti *et al*., 2012) reported no appreciable change until after ~5 h grinding at low spinning velocity, which corresponds to 0.25 h at a high speed spinning velocity. A bimodal particle size distribution appeared and increased appreciably with a great decrease in frequency volume. This bimodal distribution after 5 h of grinding gradually transforms into a modal particle diameter after 10 to 20 h of grinding. This is because of the agglomeration of delaminated particles to form huge spheroidal particles (Vaccari, 1998). Dellisanti *et al*. (2012) reported that mild grinding at low spinning velocity for 1 h does not affect the coherent scattering domain (CSD) and there is no accumulation of microstrain in the kaolinite structure. However, grinding at a low spinning velocity (corresponding to 0.25 to 1 h, at high-speed) for 5 to 10 h decreases

the value of CSD with an associated increase in the kaolinite's microstrain structure. This is because of an increase in the FWHM value of the (001) diffraction peak resulting from a reduction in crystal size (Dellisanti *et al*., 2012; Makó *et al*., 2006). Average crystal deformation are represented by microstrain measured along the c-direction (001). Further grinding above 10 h increases the amorphousness of the kaolinite structure slightly but microstrain and CSD values remain constant (Dellisanti *et al*., 2012). Table 2.7 presents kaolinite FTIR results investigated by several authors.

Table 2.4: Recorded FTIR vibrations assignments for kaolinite samples (Belver *et al*., 2002; Castellano *et al*., 2010; Cheng *et al*., 2010; Dudkin *et al*., 2004; Hu *et al*., 2012; Konan *et al*., 2009; Panda *et al*., 2010).

Suggested assignments	Wave numbers (cm^{-1})							
A	MK	BK	HK	LK	AK	FK	EK	DK
Si-OH stretching vibration	3740	-	-	3739	-	-	-	-
Inner surface -OH in-phase stretching(strong) vibration	3695	3703	3701	3696	3695	3695	3696	3695
Inner surface -OH out-phase stretching (medium) vibration	3660	3650	3650	3661	3669	3669	3669	3669
	-	-	-	-	3652	3652	3652	3653
Inner surface -OH stretching (strong) vibration	3622	3619	3620	3620	3619	3619	3619	3619
Inner layer water -OH vibration	-	-	-	3566	-	-	-	-
Physical absorbed water -OH vibration	1629	1624	1624	1625	-	-	-	-
Apical Si-O in-plane stretching vibration	1107	1113	1118	-	1114	1114	1114	1112
Skeleton Si-O-Si in-plane stretching vibration	1014	1031	1032	1033	1031	1031	1031	1031
Al-OH bending vibration	918	912	912	913	938	938	938	936
AL-OH ("gibbsite-like" layer) translational vibration	792	795	796	794	792	792	792	794
	755	755	754	754	755	755	756	755
	695	697	696	689	699	698	699	698
Si-O-Al bending vibration	541	538	536	538	537	539	537	537
Si-O bending vibration	471	468	469	470	469	469	469	469
	426	429	430	432	429	429	429	429

FTIR spectral changes occur after 5 to 10 h of grinding. These changes include peak broadening, reduction in peak intensity, and the emergence of two broadband associated with water molecules absorbed by ground samples. These bands faded or likely disappeared with increase in grinding time (Dellisanti *et al*., 2012). Consequently, longer

grinding time reduces surface structural variations. Further, it increases the number of acidic centers significantly. However, further grinding of the super-active centers increases basicity (Horváth *et al*., 2005; Sun *et al*., 2011).

2.7.2.2 Thermal activation

Calcination at the temperature range of 550 to 950 °C modifies kaolinite to metakaolin. The aim of this modification route is to improve the thermal stability of the kaolinite material and to prepare it for further modification such as intercalation and chemical activation (Belver *et al*., 2002). In addition, thermal activation breaks the hydrogen bonds between the layers of the 1:1 phyllosilicate material. This leads to evolution of alumina coordinate towards AlVI-O, separation into alumina-rich and silicon-rich domains and formation of spinel phase (Konan *et al*., 2009). In the TG/DTA analysis, metakaolin exhibits only a peak. This is an exothermic peak at ~980 to 1000 °C (Figure 2.16b) (Konan *et al*., 2009). However, no weight loss is associated with the exotherm. This is because of germination of mullite and amorphous silica extraction from metakaolin. The product of this synthesis is amorphous aluminosilicate, which is more reactive than kaolinite. The formed metakaolin is a cementitious material used as a pozzolan (Vizcayno *et al*., 2010). It is also a better-starting material for chemical lixiviation (Belver *et al*., 2002).

Vizcayno *et al*. (2010) studied the XRD pattern of metakaolin and showed a reduction pattern in peak intensity of 001 basal planes (2). This is due to breakage of the hydrogen bonds between the layers of kaolinite. This modification affects the basal plane peaks. Thermal activation at 700 °C leads to dehydroxylation of all the moisture content of kaolinite. However, mica and quartz moisture contents remain unaltered in the solid material. FTIR spectral reveals emergence of another band at ~820 cm^{-1}. This is because of the evolution of coordinate alumina towards AlVI-O. Furthermore, the Si-O-Al

bending vibration vanishes because of deformation of the 1:1 dioctahedral layers. This alters the Si-O and Si-O-S stretching vibrations at ~1030, ~1039 and ~1113 cm^{-1} (Tironi *et al*., 2012; Vizcayno *et al.*, 2010).

2.7.2.3 Intercalation

Intercalation is the effective insertion of a neutral polar organic substance into the interlamellar spaces of an inorganic host lattice in a regularly spaced stack to produce nano-sized composite materials. Wide interlamellar spaces prevent interactions between randomly dispersed layers in a consistent polymer matrix. This tends to facilitate exfoliation of the synthesized material. Kaolinite is unique; remarkably, the noncentrosymmetric structure is a suitable host for intercalation (Elbokl & Detellier, 2006). Factors affecting intercalation include crystallinity and the particle size of the host material. Greater crystallinity induces a higher rate of intercalation while smaller particle size causes lower intercalation rate. This is because the degree of structural order declines with a reduced particle size (Deng *et al*., 2002). Intercalated kaolinite are efficient adsorbents (DA Silva *et al*., 2013), catalysts, catalyst supports and ion exchange agents (Lopes *et al*., 2003).

However, the main obstacle hindering kaolinite application as a host is the rigidity of its interlamellar space and lack of charge. Therefore, only a few guest compounds like methanol, acetamide, octadecyl amine, dimethylformamide, potassium acetate, N-methylformamide, deuterated dimethylsulfoxide and dimethylsulfoxide (DMSO) can intercalate directly into kaolinite layer. The most commonly used starting guest material is DMSO because it possesses high thermal stability (Lopes *et al*., 2003). However, the obtained intercalates after introducing guest compounds could undergo further intercalation of organic guests that cannot intercalate directly (Matusik *et al*., 2013; Sun *et al*., 2011). Covalent grafting of small polar molecules such as DMSO or methanol

achieves this modification. The guest compound migrates to the interlamellar aluminol basal plane of the kaolinite to generate Al-O-C bonds and expand space. Subsequently, the second guest can then displace the first guest (Letaief *et al*., 2008). Another intercalation method is co-grinding of solid organic guest and inorganic host. This method is called mechanochemical intercalation (Makó *et al.*, 2013; Sun *et al.*, 2011).

Several authors (Elbokl & Detellier, 2006; Song *et al*., 2013; Sun *et al*., 2011) have studied kaolinite-DMSO intercalation XRD patterns. They reported the formation of Kaolinite-DMSO intercalates results in a basal spacing increment of approximately 0.4 nm. The percentage DMSO intercalation is greater than 90%. This is possible because DMSO aggregates in aqueous solution and become more amorphous because of its large dipole moment. The presence of a large amount of free substratum under hydrothermal conditions results in a high rate of intercalation (Lopes *et al*., 2003). Intercalating potassium acetate (KAc) into kaolinite with DSMO as the starting guest material results in ~0.71 nm expansion. Furthermore, two small peaks emerge at ~ 8.7 and ~ 9.8° 2θ. This is because DSMO deintercalated after drying under vacuum (Cheng *et al*., 2010; Johnston *et al*., 1990).

Several FTIR spectra studies have shown the emergence of additional bands at 3663 and 905 cm^{-1}, a reduction in the intensity of the 3696 cm^{-1} band with no changes to the 3622 cm^{-1} band. The 3663 cm^{-1} band is due to the vibration of inner surface hydroxyl stretching attached to the DMSO with hydrogen bonds. Conversely, the band at 905 cm^{-1} is due to the deformation of inner surface hydroxyl units attached to DMSO S=O units with hydrogen bonds. The vibration of the in-plane bending and out-plane bending of C-H bonds produces the 3023 and 2937 cm^{-1} bands. However, the 3669 and 3654 cm^{-1} bands disappear after intercalating DMSO into kaolinite. Studies have also shown the subsequent disappearance of the 3663 cm^{-1} band and emergence of bands at 3698 and

3610 cm^{-1} when KAc is intercalated with kaolinite. Similarly, deintercalating DMSO in KAc solution leads to resurfacing of the pleochroic band at 3698 cm^{-1}.

Consequently, the presence of the 3610 cm^{-1} band shows the successful intercalation of KAc into the kaolinite structure (Lopes *et al.*, 2003; Zhang *et al.*, 2013). Table 2.5 presents the details of numerous FTIR assignments highlighting the effects of intercalation. Similarly, intercalating kaolinite with methanol causes space expansion of ~0.37 to 0.4 nm. This expansion is the same as the molecular diameter of methanol. This indicates the presence of methanol and weak interaction between the methanol and kaolinite. However, the percentage intercalation of methanol is ~93.7 (Zhang *et al.*, 2013).

Table 2.5: FTIR assignments for crude kaolinite and kaolinite intercalates (Elbokl *et al.*, 2006; Lopes *et al*., 2003; Zhang *et al.*, 2007; Zhang *et al.*, 2013).

Suggested assignments	Wave numbers (c m^{-1})			
	Crude-Kaolinite	Kaolinite -DSMO	Kaolinite -Kac	Kaolinite -MeOH
Inner surface -OH in-phase stretching(strong) vibration	3696	3697	3698	3700
Inner surface -OH out-phase stretching (medium) vibration	3669	3663		3660
	-	-	-	
Inner surface -OH stretching (strong) vibration	3622	3621	3610	3620
		3540		3540
		3500		
In-plane bending of the vibration of C-H		3023		3031
Out-plane bending of the vibration of C-H	-	2937	-	2969
Physical absorbed water -OH vibration	1629	1635	1640	1630
Apical Si-O in-plane stretching vibration	1107	1103		1107
Skeleton Si-O-Si in-plane stretching vibration	1034	1032	1035	1031
Al-OH bending vibration	913	908	899	913
AL-OH ("gibbsite-like" layer) translational vibration	753	746	785	794
	695	689	698	692
	539	544	555	689
Si-O-Al bending vibration	470	467	478	469
Si-O bending vibration	431	433	438	430

There have been several studies on thermal analysis of intercalates (Elbokl *et al*., 2008; Letaief *et al*., 2008; Zhang *et al*., 2013) such as kaolinite-DMSO, kaolinite-polystyrene, and kaolinite-[bmim]Br using TG-DSC. The first weight loss similar to that of crude kaolinite appears at ~80 °C. This is because of the loss of externally absorbed water. Subsequent partial deintercalation of DMSO occurs at 190 °C while dehydrolysis of kaolinite DMSO intercalate occurs at ~479 °C.

The dehydroxylation temperature of crude kaolinite is slightly higher than that of kaolinite-DMSO. Similarly, there is partial deintercalation of 1-butyl-3 methylimidazolium bromine [brmim]Br at 277 °C followed by simultaneous decomposition of [brmim]Br and dehydroxylation of kaolinite at ~470 and 545 °C respectively. This shows the presence of stronger hydrogen bond between the kaolinite hydroxyl layer and [brmim]Br than the bond between kaolinite layers. This culminates to increase in thermal stability of the kaolinite material (Zhang *et al*., 2013). Ovramenko *et al.* (1994) showed that combined effect of intercalation and mechanochemical activation decreases the surface acidity of kaolinite. This is because longer grinding time destroys the structural OH groups and the kaolinite structural order. This decreases the degree of intercalation and forms super-active centers on the kaolinite surface (Horváth *et al*., 2005). In situ decomposition of formamide bonded to these centers at 200 to 350 ^{o}C forms CO and NH_3 (Horváth *et al*., 2005) Hence, the significant effect that intercalation has on the acid-base properties of kaolinite super-active centers.

2.7.2.4 Chemical activation

(a) ***Activation by alkali***

Alkali activation adjusts the acidity, surface area, pore size, and volume as well as its adsorption strength. This makes it a suitable precursor for solid basic catalyst (Colina *et al*., 2002; Slaty *et al*., 2013). Alkali activation technique deprotonates aluminol and

silanol groups from kaolinite. This leads to simultaneous dealumination and desilication of the kaolinite material (Hu *et al*., 2012). However, the extent of dealumination is always low or insignificant (Serrano *et al.*, 2013). Kumar *et al*. (2013a) reported that kaolinite treated with 3 M of NaOH at 110 °C exhibits significant changes. This change includes surface area (23 to 76 m^2/g), pore volume (0.361to 0.591 cm^3/g). Further, Si/Al ratio (0.82 to 1.688) and acidity (0.049 to 0.112 mmol/g). While Belver *et al*. (2002) reported that kaolinite treated with 5 M of KOH at 90 °C after calcination at 600 °C for 6 h exhibits an adverse effect. The affected parameters are surface area (18 to 4.1 m^2/g), pore volume (80 to 7.9 cm^3/g), Si/Al ratio (1.783 to 1.74) and acidity (0.1049 to 0.1302 mmol/g). However, 24 h treatment reduces the acidity to 0.0872 mmol/g because of neutralization of acid sites formed due to excessive leaching. Alkali activation is also the suitable method for developing a variety of basic zeolites with low Si/Al ratios. These includes K-F zeolite, 13X zeolite (Ma *et al*., 2013), A and X zeolite (Belviso *et al.*, 2013), zeolite N (Mackinnon *et al*., 2012), Na-Y zeolite (EL-Mekkawi *et al*., 2013), MCM-41 (Du *et al*., 2011) and Zeolite NaA (Loiola *et al.*, 2012). Furthermore, acid activation followed by alkali activation is another technique for synthesizing ZSM-5 zeolite via a template or template-free synthesis (Pan *et al*., 2014a, 2014b). It is important to note that at ~1000 °C, alkali-activated kaolinite exhibit an endothermic peak while crude kaolinite exhibit an exothermic peak at the same temperature (Slaty *et al*., 2013; Wang *et al*., 2007). Results obtained from XRD studies show a progressive decrease in peak intensity of kaolinite structure. Similarly, FTIR studies show extreme weakness in the structural hydroxyl vibration bands of kaolinite (Kumar *et al*., 2013a). The DTA profile shows an increase in the endothermic peak from ~200 to 600 °C. The dehydroxilation is because of deformation of some layers in the matrix of the synthesized material.

*(b) **Activation by acid***

Acid activated kaolinite are popular in adsorption, ion exchange and silica-alumina-phosphate such as SAPO-34 and SAPO-5. Acid activation enhances kaolinite acidity, surface area, pore size, and volume as well as its catalytic properties. This makes it a suitable precursor for a solid acid catalyst for petrochemical processes (Lenarda *et al*., 2007). Organic and inorganic acid activate kaolinite chemically (Hussin *et al*., 2011). Acid activation leads to dealumination, removal of mineral impurities, disaggregation of kaolinite particles, and external layer dissolution. This changes the structure and chemical composition of the kaolinite materials (Panda *et al*., 2010). Recently, synthesizing solid acid catalysts from zeolites for petrochemical industries has received great attention from numerous consortia. These interests highlight the importance of acid activated kaolinite for heavy molecule conversions. This is because it is cheaper, and its pore size and structure are more suitable than that of zeolites (Lenarda *et al*., 2007). However, for effective chemical activation, ~ 550 to 950 °C is the calcination temperature range for forming metakaolin from kaolinite. This is because of the presence of strong hydrogen bond between its layers, making it resistance to chemical attack (Belver *et al*., 2002; Dudkin *et al*., 2004). Aside increasing kaolinite porosity, acid activation also enhances acid center and surface area. Further, kaolinite is suitable as an inorganic host for intercalation and exfoliation (Valášková *et al*., 2011).

Acid activation protonates the aluminol (AlOH) group using the hydrogen ion from aqueous acid medium and this leads to dealumination and increasing the Si/Al ratio of the synthesis materials (Hu *et al*., 2012). The synthesized material is a mixture of inactivated kaolinite, amorphous and hydrous aluminosilicate as well as some partially protonated silica lamellae (Belver *et al*., 2002). The solubility of kaolinite varies from acid to acid, ratio of kaolinite to acid, operating temperature, leaching period, kaolinite

particle size as well as the concentration of the acid. Kaolinite solubility increases with acid concentration and leaching period, but excessive leaching leads to decrease in surface area (Panda *et al.*, 2010).

Activation with inorganic acids is more effective in generating new surface acid sites. This leads to a collapse of the kaolinite structure because of excessive leaching of the octahedral layer. On the other hand, organic acids do not generate new acid sites as effective as the mineral acids. Meanwhile, they preserve the kaolinite structure because of their low activation power. Table 2.6 presents a detailed comparison between organic and inorganic acid activation. It also shows the textural properties of some kaolinite samples before and after modification. Evidently, specific surface area and pore volumes increase with an increase in the molarity of the activator and activation time. (Panda *et al.*, 2010) proposed that under the same condition, solubility of kaolinite in HCl is lesser than in H_2SO_4. Further, the order of kaolinite solubility and subsequent increase in surface area (Table 2.9) from acid activation is: $CH_3COOH < H_3PO_4 < HCl < H_2SO_4 < HClO_4 < HNO_3$. Equations (2.23 and 2.24) express the dealumination process of Al/Si stoichiometry of kaolinite in an aqueous acidic medium.

$$3H_2SO_4 + Al_2Si_2O_5(OH)_4 \leftrightarrow Al_2(SO_4)_3 + 2H_4SiO_4 + 3H_2O \qquad (2.23)$$

$$3SO_3 + Al_2O_3 \leftrightarrow Al_2(SO_4)_3 \qquad (2.24)$$

From XRD structural analysis, several reports showed that all the peaks of the acid activated kaolinite correspond with the peaks of the original kaolinite material. However, acid activation reduces kaolinite peaks intensity because of decrease in the degree of structural order. Meanwhile, mild acid activation increases the structural order because of increase in crystal size. This is due to decrease in the peak FWHM value. At higher acid concentration, the peak in the XRD becomes blurred. This indicates the low degree

of structural order and amorphous nature of the synthesized material (Ayodele, 2013; Panda *et al*., 2010). FTIR spectral analysis shows the inner OH stretching vibration at ~3620 cm^{-1} had little or negligible weakness at mild acid activation. However, as the acid strength increases, the rate of weakness of this band increases. This shows that protonation increases with increase in acid concentration. It also leads to increase in the rate of dealumination and dehydroxylation. In the OH bending vibration region, all the bands show little or no weakness at mild acid activation.

However, at moderate acid concentration of ~5 M, the bands show drastic reduction while at high concentration of ~10 M, all the bands at the region disappear. This is because of transformation of kaolinite from crystalline phase to amorphous phase due to the gibbsite-like layer deformation (Ayodele, 2013). Moreover, there is emergence of Lewis site-bonded pyridine near 1446 and 1595 cm^{-1} and Brönsted acid site-bonded pyridine at 1489, 1546 and 1633 cm^{-1}. This is owing to the weak H bond to the pyridine molecules surface (do Nascimento *et al*., 2011; Perissinotto *et al*., 1997). Acid activation increases the surface area of the materials, giving room to physical absorption of water. The physically absorbed water on the kaolinite material increases. Conversely, structural and coordinated water decrease with increase in concentration of acid used in the activation. This results in increase in the endothermic peaks of the synthesized material. The endotherm increase attributed to increase in recrystallization and dehydroxilation temperature (Ayodele, 2013). The endotherms are higher in kaolinites with high degree of structural order than the ones with low order (Valášková *et al*., 2011).

Table 2.6: Textural properties of some modified kaolinites before and after activation.

Kaolin	sample	Properties before activation				Activation		Mol[f]	Temp	Time	Properties after activation					Ref
Notation	Origin	SSA[a]	Pvol[b]	Si/Al	Ac[c]	Calc[d] T (°C)	Chem[e]	(M)	(°C)	(h)	SSA[a]	Pvol[b]	Si/Al	Ac[c]	Acs[g]	
K1	China	19.4	0.1	1.1			H_3PO_4	10	110	2	166	0.59	16.63			(Ayodele, 2013)
K1	China	19.4	0.1	1.1			H_3PO_4	5	110	2	45.3	0.17	1.76			(Ayodele, 2013)
K2	Kolkata India	23	0.36	0.65			H_2SO_4	10	110	4	143	1.18	8.09			(Panda *et al.*, 2010)
K2	Kolkata India	23	0.36	0.65			H_2SO_4	5	110	4	107	0.967	1.63			(Panda *et al.*, 2010)
K2	Kolkata India	23	0.36	0.65			H_2SO_4	3	110	4	83	0.67	1.3			(Panda *et al.*, 2010)
KGa-1b	Georgia	9.8	-				HCL	2	80	14	34.2	-				(Valášková *et al.*, 2011)
Kga-2	Georgia	20.5	-				HCL	2	80	14	45	-				(Valášková *et al.*, 2011)
KGa-1b	Georgia	3.8	-				H_2SO_4	0.25	100	3	15.6	-				(Bhattacharyya *et al.*, 2011)
K3	Unknown	9	0.08			950	H_2SO_4	12	90	4	112	0.13			106	(Lenarda *et al.*, 2007)
K3	Unknown	9	0.08			850	H_2SO_4	12	90	20	288	0.22			114	(Lenarda *et al.*, 2007)
K3	Unknown	9	0.08			850	H_2SO_4	12	90	4	239	0.17			312	(Lenarda *et al.*, 2007)
K3	Unknown	9	0.08			950	H_2SO_4	12	90	20	110	0.13			87	(Lenarda *et al.*, 2007)
K4	China		-	2.38			NaOH	-	200	4	326	-				(Ma *et al.*, 2013)
Kflint	Para-Brazil	24	-			950	H_2SO_4	4	90	1	406	-			237.7	(do Nascimento, Tito, *et al.*, 2011)
Kflint	Para-Brazil	24				950	H_2SO_4	1	90	1	76				72	(do Nascimento, Tito, *et al.*, 2011)
Kflint	Para-Brazil	24				850	H_2SO_4	4	90	1	341				147.4	(do Nascimento, Tito, *et al.*, 2011)
K8	Jiangsu, china	41.1	-	2.00			Washing			-	41.1	-	2.00			(Rong *et al.*, 2002)

Kaolin	sample	Properties before activation				Activation		Mol[f]	Temp	Time	Properties after activation					Ref
Notation	Origin	SSA[a]	Pvol[b]	Si/Al	Ac[c]	Calc[d] T (°C)	Chem[e]	(M)	(°C)	(h)	SSA[a]	Pvol[b]	Si/Al	Ac[c]	Acs[g]	
Kflint	Para-Brazil	24				850	H_2SO_4	1	90	1	27				35.5	(do Nascimento, Tito, *et al.*, 2011)
Kflint	Para-Brazil	-	-			960	HCl and 20% TPW[h]	0.1	200	4	-	-	5.57			(da Silva Lacerda Junior *et al.*, 2013)
KC	South Africa					960	HCl and 20% TPW[h]	0.1	200	4			1.06			(da Silva Lacerda Junior *et al.*, 2013)
KC	South Africa					960	HCl and 20% TPW[h]	0.5	200	4			0.901			(da Silva Lacerda Junior *et al.*, 2013)
KGa-1b	Para-Brazil	12	-	1.90		950	H_2SO_4	4	90	1	138	-			163.4	(do Nascimento, Angélica, *et al.*, 2011)
Kga-2	Para-Brazil	20	-	1.93		950	H_2SO_4	4	90	1	65	-			147.4	(do Nascimento, Angélica, *et al.*, 2011)
Kflint	Para-Brazil	24	-	193		950	H_2SO_4	4	90	1	406	-			237.7	(do Nascimento, Angélica, *et al.*, 2011)
KC	South Africa	9	-	1.96		950	H_2SO_4	4	90	1	233	-			250.5	(do Nascimento, Angélica, *et al.*, 2011)
K5	Kolkata, India	23	0.36	0.65			H_2SO_4	10	110	4	143	1.18	8.09			(Panda *et al.*, 2011)
K5	Kolkata, India	23	0.36	0.65			H_2SO_4	5	110	4	107	0.967	1.63			(Panda *et al.*, 2011)
K7	Beijing, China		-	1.3		850	H_2SO_4	-	180	24	198	0.168			83	(P Wang *et al.*, 2007)
K2µm	Navalacruz, Spain	18.2	80		0.105	700	KOH	5	90	6	3.7	8.1				(Belver *et al.*, 2002)

Kaolin	sample	Properties before activation				Activation		Mol[f]	Temp	Time	Properties after activation					Ref
Notation	Origin	SSA[a]	Pvol[b]	Si/Al	Ac[c]	Calc[d] T (°C)	Chem[e]	(M)	(°C)	(h)	SSA[a]	Pvol[b]	Si/Al	Ac[c]	Acs[g]	
K5	Kolkata, India	23	0.36	0.65			H_2SO_4	3	110	4	83	0.67	1.3			(Panda *et al.*, 2011)
K5	Kolkata, India	23	0.36	0.65			H_2SO_4	1	110	4	69	0.489	0.81			(Panda *et al.*, 2011)
K6	Beijing, China		-	1.62			NaOH	-	-	-	364	0.47		0.57		(Tan *et al.*, 2007)
K5	Kolkata, India	23	0.36	0.82	0.049	-	CH_3COOH	3	110	4	38	0.504	0.885	0.11		(Kumar *et al.*, 2013)
K5	Kolkata, India	23	0.36	0.82	0.049	-	H_3PO_4	3	110	4	42	0.658	0.972	0.11		(Kumar *et al.*, 2013)
K5	Kolkata, India	23	0.36	0.82	0.049	-	HCl	3	110	4	78	1.083	1.144	0.23		(Kumar *et al.*, 2013)
K5	Kolkata, India	23	0.36	0.82	0.049	-	HNO_3	3	110	4	86	1.124	1.782	0.34		(Kumar *et al.*, 2013)
K5	Kolkata, India	23	0.36	0.82	0.049	-	NaOH	3	110	4	76	0.591	1.688	0.11		(Kumar *et al.*, 2013)
K2µm	Navalacruz, Spain	18.2	80		0.105	600	HCl	6	90	6	219	146		0.19		(Belver *et al.*, 2002)
K2µm	Navalacruz, Spain	18.2	80		0.105	700	HCl	6	90	6	172	141				(Belver *et al.*, 2002)
K2µm	Navalacruz, Spain	18.2	80		0.105	800	HCl	6	90	6	209	145		0.19		(Belver *et al.*, 2002)
K2µm	Navalacruz, Spain	18.2	80		0.105	900	HCl	6	90	6	50.7	71				(Belver *et al.*, 2002)
K2µm	Navalacruz, Spain	18.2	80		0.105	700	HCl	6	90	24	21.9			0.14		(Belver *et al.*, 2002)
K2µm	Navalacruz, Spain	18.2	80		0.105	700	KOH	1	90	6	8.5					(Belver *et al.*, 2002)
K2µm	Navalacruz, Spain	18.2	80		0.105	600	KOH	1	90	6	9.2					(Belver *et al.*, 2002)
K10	Leghorn, Italy..	17		2.02		600	HCl	6	80	4	318		17.7			(Perissinotto *et al.*, 1997)
K2µm	Navalacruz, Spain	18.2	80		0.105	600	KOH	5	90	6	4.1	7.9		0.11		(Belver *et al.*, 2002)

Kaolin	sample	Properties before activation				Activation		Mol[f]	Temp	Time	Properties after activation					Ref.
Notation	Origin	SSA[a]	Pvol[b]	Si/Al	Ac[c]	Calc[d] T (°C)	Chem[e]	(M)	(°C)	(h)	SSA[a]	Pvol[b]	Si/Al	Ac[c]	Acs[g]	
K2µm	Navalacruz, Spain	18.2	80		0.105	600	KOH	6	90	24	2.4			0.09		(Belver *et al.*, 2002)
K10	Leghorn, Italy..	17		2.02		600	HCl	2	80	4	185		16.67			(Perissinotto *et al.*, 1997)
K10	Leghorn, Italy..	17		2.02		600	H_2SO_4	3	80	4	250		21.86			(Perissinotto *et al.*, 1997)
PBK-K	Unknown	26.6	-			550	H_2SO_4	4	100	0.75	70.4	-				(Sabu *et al.*, 1999)
PBK-K	Unknown	26.6	-			550	HNO_3	4	100	0.75	101	-				(Sabu *et al.*, 1999)
PBK-K	Unknown	26.6	-			550	$HClO_4$	4	100	0.75	79.7	-				(Sabu *et al.*, 1999)
KS 1	Ukraina	25	-			500	HCl	3	105	5	29.6	-				(Koyuncu *et al.*, 2007)
Kflint	Para-Brazil	17	-			850	H_2SO_4	4	130	0.25	187	-		4.32		(de Oliveira *et al.*, 2012)
Kflint	Para-Brazil	17	-			850	H_2SO_4	4	130	0.13	150	-		0.84		(de Oliveira *et al.*, 2012)
Kflint	Para-Brazil	17	-			850	H_2SO_4	4	130	0.25	285	-		1.44		(de Oliveira *et al.*, 2012)
Kflint	Para-Brazil	17	-			850	H_2SO_4	4	130	0.13	246	-		0.57		(de Oliveira *et al.*, 2012)
Kflint	Para-Brazil	17				950	H_2SO_5	4	130	0.25						(de Oliveira *et al.*, 2012)
Ka	Southwestern	19	0.103				Kaolinite-Porphyrin intercalate	-	150	315	10	0.068				(Bizaia *et al.*, 2009)

[a] SSA: BET specific surface area (m^2/g). [b] Pvol: pore volume (cm3/g). [c] Ac: acidity (mmol/g). [d] Calc: calcination temperature (°C). [e] Chem: chemical activation
[f] Mol: Molarity (M). [g] Acs: acid sites (µmol/g). [h] TPW: 12- Tungstop-hosphoric acid.

2.7.3 Catalytic application of modified kaolinites

2.7.3.1 As catalyst support

Modified kaolinite have proved to be efficient solid catalysts and catalyst supports in various reactions. These include cracking, esterification, aromatization, alkylation, adsorption, oxidation and isomerization. This is because of their robust enhancement in surface area, thermal stability and acidity. This has led to improved conversion, yield and selectivity in several reactions. It is apparent from the table that under the same activation conditions, conversion increases with increasing specific surface area (Sabu *et al*., 1999, de Oliveira *et al*., 2012). However, dehydration of 2- propanol with H_2SO_4-treated kaolinite exhibited a contrary trend (Perissinotto *et al*., 1997). This is probably because of the disappearance of all of the strong acid sites from the synthesized solid acid catalyst at higher acid concentrations, despite the overall higher surface area.

2.7.3.2 Support for fluid cracking catalyst

Due to lower price and availability, modified kaolinite constitutes a suitable support for FCC catalysts. Fortification of FCC catalysts with modified kaolinite inculcates porosity on the catalyst structure (Haden Jr *et al*., 1972). This could help to improve the cracking activity towards production of gasoline with high octane number as well as enhance the yield of lower olefins such as butylene and propylene (Shi *et al*., 1998). Speronello (1986) invented a novel porous mullite via calcination of kaolinite at 1200 ^{o}C. They reported that the synthesized mullite were resistant to attrition due to formation of strong inter-crystalline bonds between the mullite crystals. The mullite was impregnated with a chloroplatinic acid solution by incipient wetness. The resulting catalyst was used in FCC unit for CO oxidation. Absil *et al*. (1994) invented phosphorous modified kaolinite blended with ZSM-5 zeolites. The catalyst

blend with 40 wt% of ZSM-5 and about 2.3-2.5 wt% phosphorous composition shows good attrition resistance (4-5). It was used in cracking of Joliet sour heavy gas oil in a fixed fluidized bed unit. The catalyst blend showed significant improvement in the butylene and propylene yield compared to the base catalyst. This report corroborated with an earlier study (Absil *et al*., 1993).

2.7.3.3 As stand-alone catalyst

Modified kaolinite have proved to be efficient solid catalysts and catalyst supports in various reactions. These include cracking, esterification, aromatization, alkylation, adsorption, oxidation and isomerization. This improved conversion, yield and selectivity in several reactions, as shown in Table 2.7 is attributed to their robust enhancement in surface area, thermal stability and acidity. It is was reported that under the same activation conditions, conversion increases with increasing specific surface area (de Oliveira *et al*., 2013; Sabu *et al*., 1999b). However, dehydration of 2-propanol with H_2SO_4-treated kaolinite exhibited a contrary trend (Perissinotto *et al*., 1997). This is probably because of the disappearance of all of the strong acid sites from the synthesized solid acid catalyst at higher acid concentrations, despite the overall higher surface area.

Table 2.7: Various application of modified kaolinite, XRD and FTIR analysis, number of acid sites and the conversion and yield of the reaction (do Nascimento *et al.*, 2011; Panda *et al.* 2011; Lenarda *et al.*, 2007; Rong and Xiao, 2011; Uzum et al., 2009, Wang *et al.*, 2007; Mahmoud and Saleh, 1999; Shen *et al.*, 2009; de Oliveira *et al.*, 2012; Perissinotto *et al.*, 1999; Jose and de Janeiro, 1992).

Kaolinite sample		Modification			Application	SSA[b]	Reaction		Conv[c]	Yeild	Acs[e]
Notation	Origin	strategy	Mol[a] (M)	time (h)		(m2/g)	temp. (°C)	time (h)	(wt.%)	(wt.%)	
Kflint	Para-Brazil	H_2SO_4 activation	4	1	Esterification of oleic acid	408	160	4	98.9	-	237.7
Kflint	Para-Brazil	H_2SO_4 activation	4	1	Esterification of oleic acid	341	130	4	84.2		237.7
Kflint	Para-Brazil	H_2SO_4 activation	4	0.25	Esterification of oleic acid	187	100	0.5	95.2		
Kflint	Para-Brazil	H_2SO_4 activation	4	0.13	Esterification of oleic acid	150	100	0.5	56.4		
Kflint	Para-Brazil	H_2SO_4 activation	4	0.25	Esterification of oleic acid	285	100	0.5	83.3		
Kflint	Para-Brazil	H_2SO_4 activation	4	0.13	Esterification of oleic acid	246	100	0.5	13.5		
K8	Jiangsu, china	washing			cracking	41.1	460		13.4	-	-
Kflint		HCl and 20% TPW[f]	0.1	4	Esterification of oleic acid		100	2		97.21	-
KGa-1b	Georgia	H_2SO_4 activation	4	1	Esterification of oleic acid	138	160	4	94.8	-	163.4
Kga-2	Georgia	H_2SO_4 activation	4	1	Esterification of oleic acid	65	160	4	72	-	22.9
Kflint	Para-Brazil	H_2SO_4 activation	4	1	Esterification of oleic acid	406	160	4	98.9	-	237.7
KC	South Africa	H_2SO_4 activation	4	1	Esterification of oleic acid	335	160	4	98.8	-	250.5
K5	Kolkata, India	No activation	10	4	Cracking of polypropylene	143	450	0.33	-	89.5	-
K6	Beijing, China	NaOH activation			Cracking of heavy crude oil	364	500	-	-	74.4	37.3
K7	Beijing, China	H_2SO_4 activation		24	FCC naphtha aromatization	198.3	550	-	-	73.93	83
K9	A1-Azraq, Jordan	HCl activation	2		Debuytlation of 2-tert-butylphenol		230	0.5	94		

Kaolinite sample Notation	Origin	Modification strategy	Mol[a] (M)	time (h)	Application	SSA[b] (m2/g)	Reaction temp. (°C)	time (h)	Conv[c] (wt.%)	Yeild (wt.%)	Acs[e]
K9	A1-Azraq, Jordan	HCl activation	1		Debuytlation of 2-tert-butylphenol		230	0.5	97		
K9	A1-Azraq, Jordan	HCl activation	0.5		Debuytlation of 2-tert-butylphenol		230	0.5	96		
K9	A1-Azraq, Jordan	H_3PO_4 activation	1		Debuytlation of 2-tert-butylphenol		230	0.5	97		
K9	A1-Azraq, Jordan	CH_3COOH activation	1		Debuytlation of 2-tert-butylphenol		230	0.5	92		
K10	Leghorn, Italy	HCl activation	2	4	2-propanol dehydratation	185	120		26.1		
K10	Leghorn, Italy	HCl activation	6	4	2-propanol dehydratation	318	120		40.8		
K10	Leghorn, Italy	H_2SO_4 activation	1	4	2-propanol dehydratation	164	120		99.4		
K10	Leghorn, Italy	H_2SO_4 activation	3	4	2-propanol dehydratation	250	120		55.8		
PBK-K		H_2SO_4 activation	4	0.75	Friedel Crafts alkylation	70.42	80	0.5	86.12	-	-
PBK-K		HNO_3 activation	4	0.75	Friedel Crafts alkylation	100.9	80	0.5	87	-	-
PBK-K		$HClO_4$ activation	4	0.75	Friedel Crafts alkylation	79.69	80	0.5	86.5	-	-
KS 1	Ukraina	HCl activation	3	5	absorption 3-methoxybenzaldehyde	24.95	60	3	80	-	-
Kflint	Para-Brazil	H_2SO_4 activation	4	0.25	Esterification of oleic acid	187	115	0.67	96.5	-	4.32
Kflint	Para-Brazil	H_2SO_4 activation	4	0.13	Esterification of oleic acid	150	100	0.5	56.4	-	-
Kflint	Para-Brazil	H_2SO_4 activation	4	0.25	Esterification of oleic acid	285	100	0.5	83.3	-	
Kflint	Para-Brazil	H_2SO_4 activation	4	0.13	Esterification of oleic acid	246	100	0.5	13.5	-	
Ka	Southwestern Brazil	Kaolinite-Porphyrin intercalate		315	Oxidation of cyclohexanone	10	80	24	85	100	87
K3			12	20	isomerization of 1-butene	110			6.1		114

Kaolinite sample		Modification			Application	SSA[b]	Reaction		Conv[c]	Yeild	Acs[e]
Notation	Origin	strategy	Mol[a] (M)	time (h)		(m2/g)	temp. (°C)	time (h)	(wt.%)	(wt.%)	
K3	Unknown	H_2SO_4 activation	12	20	isomerization of 1-butene	288	-	-	18		106
K3	Unknown	H_2SO_4 activation	12	4	isomerization of 1-butene	112	-	-	7.5		

[a] M: Molarity (M)
[b] SSA: BET specific surface area (m^2/g)
[c] Conv: Conversion
[d] Sel: Selectivity
[e] Acs: acid sites (μmol/g)
[f] TPW: 12-Tungstop-hosphoric acid activation
[g] isobutene selectivity
[h] debutilation selectivity

2.7.3.4 Synthesis of microspherical zeolitic molecular sieves

Several studies have shown the viability of kaolinite as starting materials for synthesizing microspherical zeolitic materials. This is because they are resistant to attrition, thermally and hydrothermally stable, cheap and readily available (Atta *et al*., 2007; Brown *et al*., 1979; Chang *et al*., 2006). A standard way of synthesizing microspheres is by mixing metakaolin (obtained from kaolinite), raw kaolinite, sodium silicate and water. A spray drying technique dries the mixture before calcination to form the required fluid microspheres. Mixing the microspheres with an aqueous solution of NaOH to form slurry enhances stirring. Hydrothermal treatment of the slurry with continuous stirring crystallizes into faujasite zeolite. Proper monitoring of the crystallization process minimizes the formation of unwanted B zeolite. The composite material synthesized from this process may be more than 15% faujasite zeolite with Si/Al ratio greater than 4. For instance, Haden *et al*. (1970) and Brown *et al*. (1980) have synthesized and patented catalytic cracking catalysts such as crystalline faujasite, X and Y zeolites.

Haden *et al.* (1970) used this procedure to synthesize 22.6% NaY zeolite with Si/Al ratio of 4.53. To improve the faujasitic zeolite yield, Haden *et al*. (1972) proposed the application of deflocculating agent to slurries of hydrated kaolin with higher levels of solids to aid spray drying. The authors separated the resulting microspheres into two (10/90) fractions by weight prior to calcination and alkali treatment. The calcination temperatures employed for the 10 and 90 fractions were below and above the clay exotherms respectively. To obtain Y zeolite with improved resistance to attrition and higher yield of 52% within shorter crystallization time, the authors posit mixing the two fractions before treating with caustic soda solution. In a recent study Atta *et al*. (2007), dealuminated metakaolin with an inorganic acid in

synthesizing X zeolite. This increased the Si/Al ratio to the expected value rather than using sodium silicate as reported by Haden *et al* (1972).

Interestingly, the authors obtained 57% faujasitic zeolite comprised of 34% X zeolite and 23% Y zeolite. They attributed this to the similar synthesis conditions for both zeolites such as Si/Al ratio, pH value, aging, reaction temperature, and time. This seems improbable because (Haden Jr *et al*., 1972) used 22 h aging period to achieve 52% Y zeolite while (Brown *et al*., 1980) used 72 h. However, Chandrasekhar and Pramada (2004) gave the plausible explanation. They proposed that purity and crystallinity of Y zeolite increase with longer aging periods. Hence, Haden *et al*. (1972) would have generated a higher percentage of Y zeolite if they had increased the aging period.

2.7.3.5 In Synthesis of silicoaluminophosphate (SAPO) sieve

SAPOs are microporous zeolitic materials with high amount of strong acidity, which favor them in process such as olefins production (Cui *et al*., 2013; Fatourehchi *et al*., 2011; Wang *et al*., 2011). The conventional SAPOs are synthesized hydrothermally from natural compounds containing silica, alumina and phosphorus individually or lamella aluminophosphates developed from related compounds (Pastore *et al*., 2008; Yang *et al*., 2013), which make them expensive. Thermally modified raw kaolinite (metakaolin) can serve as a cheap source of both silica and alumina in synthesis of SAPO molecular sieves such as SAPO-5, SAPO-11, SAPO-20, SAPO-34, SAPO-44, and SAPO-47. This is because the silica and alumina atom in the metakaolin are capable of coordinating well with related ligands (Wang *et al*., 2010). However, Wang *et al.* (2010) revealed that from previous research, not all the silica and alumina atom in metakaolin partake in the development of SAPO framework. The extra framework silica and alumina constitute impurity in SAPO,

which does not favor their catalytic application. To proffer solution to this drawback, they investigated the synthesis of SAPO-34 in a three steps crystallization process. The first step is transformation of kaolinite to metakaolin at 800 °C to make it active for further treatment. The second step involves transformation of the metakaolin to primary building units (PBU) by aging and initial heating. The final stage is crystallization at 150 °C. The steps produced SAPOs void of contaminating phases using kaolinite as a cheap precursor. Meanwhile, SAPOs being microporous molecular sieve with a high density of acid sites, they are prone to rapid deactivation by coking, which decrease their catalytic activity (Wang *et al*., 2011).This informs the need to develop SAPOs that are capable of coke suppression.

Recently, several author had studied synthesis of hierarchical mesoporous SAPOs with mild acidity to solve the problem of rapid deactivation (Cui *et al*., 2013; Yang *et al*., 2012). Zhu *et al*. (2009) synthesized hierarchical SAPO-34 composed of decussate zeolite slice units by using raw kaolin as a special silica and alumina source. The improved reactivity and selectivity of olefin in conversion dimethyl ether to olefin reaction are credited to the distinctive hierarchical network. Cui *et al*. (2013) also reported the efficiency of hierarchical cross-like SAPO-34 developed through hydrothermal process using polyethylene glycol as the mesostructure directing agent. The catalyst performed excellently achieving up to 96% olefins selectivity, which was ascribed to ease of diffusion of both reactants and product through the well-connected pore channels.

2.8 Functionalized heterogeneous catalysts

Functionalized heterogeneous catalysts such as clays, carbons, zeolites, mesoporous silica and metal oxide has become an active research area over several decades due to their interesting catalytic performance (Hino *et al*., 1979; Narkhede *et al.,* 2015). Although, the

metal oxides themselves possess both the Lewis and Bronsted sites that are capable of biodiesel production, their Bronsted acidity could be enhanced by functionalization with proton-donating inorganic compound (Jin *et al.*, 1986). The inorganic compounds include sulfonic group, sulfuric acid, ammonium sulfate, aqueous ammonium metatungstate solution and tungstophosphoric acid (Lee *et al*., 2014; Narkhede *et al.*, 2015; Ropero-Vega *et al.*, 2010; Srilatha *et al*., 2011). Prominent of these are the sulfate precursors because of the super acid attribute of sulfate ions, which is capable of inducing polarization of the OH groups nearby. This sulfate structure shows that each sulfur atom is bonded to the lattice via two tri-coordinated oxygen atoms in a special scheme (Yamaguchi *et al.,* 1986). This exhibits C2v symmetry which forms a bridge and chelate structure (Figure 2.18) (Ropero-Vega *et al.*, 2010).

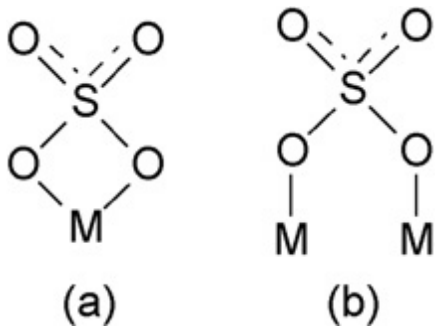

Figure 2.17: Sulfate structures: (a) coordinated with C2v chelate and (b) C2v bridge.

The S-O-M bonds shows the presence of Bronsted acid sites due to cleavage with water as in the chelate structure, while the bridge structure ((M-O)2S(=O)-OH) indicates that S(V) is the oxidation level of sulfur (Yang *et al.,* 2003).

Metal oxide such as TiO_2 (de Almeida *et al.*, 2008) SiO2, (Testa *et al*., 2010), Nb_2O_5 (Peters *et al.*, 2006), ZrO_2 (Peters *et al*., 2006), SnO_2 (Furuta *et al.*, 2004) Al_2O_3 (Yang *et al.*, 2003); mixed oxides such as SnO_2-Al_2O_3 (H-F Guo *et al*., 2008), TiO_2-SiO_2 , (Yang *et al.*, 2003), ZrO_2-Al_2O_3 (Yang *et al.*, 2003); hybrid silica such as amorphous, HMS, SBA-15, MCM-41 (Testa *et al.*, 2014), and aluminosilicates such as have been functionalized successfully with sulfate groups. These have shown remarkable performance in production of biodiesel and specialty chemicals. Testa *et al.* (2010) studied the catalytic performance of sulfated hybrid silicas for acetic acid esterification with butanol. The report shows that the samples produced exhibit splendid catalytic activity and are remarkably stable despite the decrease of sulfate ion concentration upon recycling. The catalytic performance of sulfated metal oxide is a major function of the quantity of sulfate ions deposited on the surface of the oxide. The increase in the sulfate ion content leads to increase in the acid strength. Factors such as sulfate ion precursor, amount, calcination temperature and preparation method can influence the deposition of sulfate ions on the metal oxide.

de Almeida *et al.* (2008) investigated the effect of sulfate concentration used in preparation on sulfated titania on its catalytic performance. They reported that increase in sulfate concentration enhanced the textural properties such as pore volume and average pore diameter, specific surface area and the sulfate ion incorporation.

Ropero-Vega *et al*. (2010) comparatively studied synthesis of sulfated Titania using ammonium sulfate and sulfuric acid as sulfate precursors and evaluated their performance in the esterification of oleic acid. Their report showed that larger amount of sulfate ions were

linked to the surface the Titania with ammonium sulfate than with sulfuric acid. This is because salvation with ammonium sulfate incorporated both Lewis and Bronzed acid sites, while sulfuric acid deposited only Lewis sites. Consequently, sulfation with ammonium sulfate gives a superior catalytic performance. Figure 2.19 presents the model for the development of Lewis and Bronsted acid sites on sulfated Titania. The inductive effect on S=O bonds could remarkably increase the acid strength.

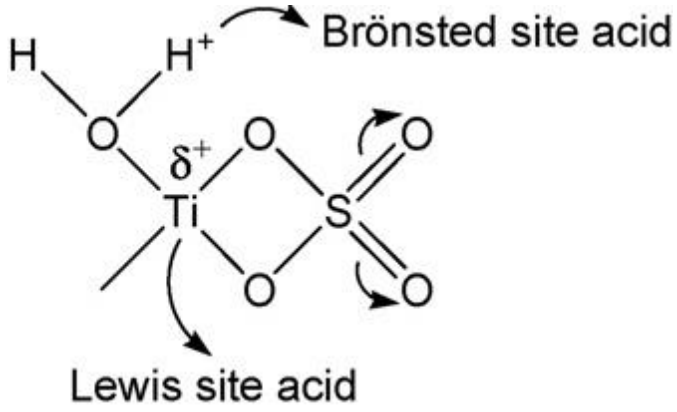

Figure 2.19: Schematic representation of the Brönsted and Lewis acid sites present in the sulfated Titania in form of chelate (Ropero-Vega et al., 2010).

Usai *et al*. (2013) compared the effect of two different organic sulfate precursors (propyl-sulfonic acid and phenyl-sulfonic acid) on mesoporous silica (SBA-15) for interesterification of a vegetable oil. They observed that phenyl-sulfonic acid functionalized SBA-15 showed outstanding catalytic performance due to its remarkably higher acidity compared to propyl-sulfonic acid. This report corroborates with previous findings (Melero *et al*., 2002).

The calcination temperature is of vital importance in the synthesis of sulfated oxides because calcination stabilizes the properties and produce the active sites of the materials. The optimum calcination temperature varies from one metal oxide to another. Khder *et al*. (2008) studied the effect of calcination temperature on the formation of sulfated tin oxide for acetic

acid esterification with amyl alcohol. Their report showed that increase in calcination temperature up to 550 °C leads to increase in sulfate content and a corresponding increase in acidity, which culminated in increased catalytic activity. However, a further increase in calcination temperature up to 750 °C resulted in decreased catalytic performance due to a decrease in acidity. This could be attributed to the removal of Bronsted acid sites and addition of Lewis acid site at a temperature above the optimum since better activity is essentially promoted by Bronsted acid sites. Meanwhile, Yang *et al*. (2003) reported 450 °C as the optimum calcination temperature for sulfated titanium-silicon for acetic acid conversion. This is attributed to the highest number of acid sites and specific surface area produced at the said optimum temperature.

Similarly, the acid strength of sulfated metal oxide depends on the electronegativity of the metal element. Protons release is more facile for metal elements with lower electronegativity. Considering Zr, Ta, Ti and Nb, their electronegativity are 1.33, 1.50, 1.54 and 1.6 respectively. This corroborates with the report of Li *et al*. (2011), which shows that the order of the Bronsted acidity of the metal oxides as $SO_{42}-/ZrO_2 > SO_{42}-/Ta_2O_5 > SO_{42}-/Nb_2O_5 > SO_{42}-/TiO_2$. Furuta *et al.* (2004) investigated the efficiency of sulfated tin oxide and zirconia for n-octanoic acid esterification with methanol. They reported that the acid strength of sulfated zirconia is lower than that of sulfated tin oxide, which enables sulfated tin oxide for better catalytic activities. This report is concomitant with previous findings (Furuta *et al*., 2004; Matsuhashi *et al.,* 2001; Tatsumi *et al.,* 1996).

Mesoporous silica could also serve as a support for superacid catalyst because their mesostructure is adjustable and hydrophobic/hydrophilic balance can be improved by functionalizing with diverse groups of sulfonic acid (Avhad *et al*., 2015; Melero *et al*., 2010).

2.9 Acidity characterization

Solid superacids are characterized by various techniques such as X-ray diffraction (XRD), ammonia temperature program desorption (NH3-TPD), infrared spectroscopy (FTIR) pyridine adsorption. In addition, titration method with a probe using Hammett Indicators and Potentiometric titration are used (Ropero-Vega *et al.*, 2010).

Titration method with a probe using Hammett indicators also determines the acid strength distribution and surface acidity of heterogeneous catalysts. Hammett indicators are uncharged bases that can be converted to conjugate acids by proton transfer. The probe reagent for the titration includes water, pyridine, ethyl alcohol and n-butylamine. While n-butylamine ($pKa \leq +10.6$) and pyridine ($pKa \leq +5.3$) are easily absorbed on the active sites, ethyl alcohol ($pKa \leq -2$) and water ($pKa \leq -1.7$) are scarcely absorbed (Matsuzaki *et al.*, 1969). The popularly used of these probe reagents is n-butylamine because of it possesses the highest pKa value. The degree of hydration and exchangeable cations of a sample strongly determines its surface acidity. Touillaux *et al*. (1968) discovered that the water molecule absorbed on montmorillonite dissociates 107 times faster than ordinary water. This is traceable to the acidic nature of the exchangeable cation in the absorbed water, which donated proton as follows (Frenkel, 1974):

$$M^n(H_2O) \longrightarrow (M - OH)^{n-1} + H^+. \qquad (2.25)$$

The ability of a solid sample to donate proton (pKa) is expressed by Hammett and Deyrup as:

$$H_0 = pKa + \frac{\log[B]}{[BH^+]} \quad (2.26)$$

Where pKa represents the activity of the hydrogen ion from the surface acid, [BH+] and [B] is the activity coefficients of the acid and basic sites formed by the indicator, respectively (Yurdakoc *et al*., 1999). If the reaction proceeds by transfer of electron pair to the surface then the activity function is given by:

$$H_0 = pKa + \frac{\log[B]}{[AB]} \quad (2.27)$$

Where [*AB*] represents the neutral base concentration that reacted with the electron pair acceptor, A or Lewis acid.

Prior to the titration, the sample is to be prepared by heating at 200 ^{o}C for 1 h under vacuum condition according to Yang *et al.* (2003). Ropero-Vega *et al.* (2010) proposed preparation by dispersing the sample in dry benzene. After preparation, the sample is to be titrated with a probe prior to addition of Hammett indicators vapor. The amount of acid sites for both Lewis and Bronsted sites can be determined by the mole of the sites per gram of the sample after the validation of acid strength. The acid strength for solid acid is in the range of H_0 = 6.8 to as low as below -8.2. Samples with acid strength estimated to be greater than H_0 = -11.93 are said to be superacids. This corresponds to the strength of H_2SO_4 (100%). However, titration using Hammett indicators is not suitable for dark or colored samples due to difficulty in observing color change.

On the other hand, FTIR-pyridine adsorption is said to be more reliable in classifying and quantifying the acidity properties of solid acids because of it is has good resolution, sensitive

and ability to determine chemical species (Wang *et al.,* 2006; Yurdakoc *et al.,* 1999). It classified the acid sites into Brönsted and/or Lewis and based on acid strength as well. The samples are prepared by annealing and pressing it into a thin self-supporting wafer. This is followed by evacuation at 400 °C for 2 h in a vacuum to purge the species that are strongly bonded to the sample and activate it prior to absorption. Further, pyridine adsorption takes place at room temperature for like 10 min after which the sample is desorbed at 200, 300, 400 and 700 °C. The desorption temperature corresponds to weak, mild, strong and super acidity respectively. The bands intensity at 1450 cm^{-1} 1540 cm^{-1} and 1438 cm^{-1} which corresponds to Lewis and Brönsted acid sites and surface hydroxyl respectively determine the concentration of each sites (Cardona-Martínez *et al.,* 1990; Li *et al.*, 2014; Yang *et al.,* 2003). Further, the band at 1488 cm^{-1} represents a mixture of Lewis and Brönsted acid sites (Saravanan *et al.,* 2012).

NH_3-TPD determines the acid strength distribution and amount of acid sites of solid acid samples. In comparison with other analytical methods available, NH_3-TPD is becoming popular in probing surface acidity of solidacid samples (Gorgulho *et al*., 2008). However, the technique is somehow tedious and wastes time towards repeated operation for more sample analysis. Meanwhile, Wang *et al.* (2004) developed a high-throughput strategy using multistream mass spectrometer screening (MSMSS) procedure. This technique shows outstanding improvement over the conventional method because it can be used to analyze up to 10 samples in almost 6 h. Gorgulho *et al.* (2008) comparatively studied the effectiveness of titration and TPD techniques. They reported that both methods give closely related results, but the quantitative results of TPD are closer to that of the elemental analysis. Titration method is less effective in quantifying weak acid sites. Prior to the NH_3 adsorption, the

sample must be degassed in helium at 100 °C for 1 h to remove physically absorbed moisture. The sample was further pretreated at 500 °C with 10 °C/min ramp for 2 h to eliminate strongly bound species and activate the sample and subsequently cooled to 120 °C. Adsorption proceeds by saturating the sample with NH_3 at 120 °C and purge in helium for 1 h. NH_3 desorption takes place by ramping the sample to 1000 °C at 10 °C/min. The volume per gram of NH_3 desorbed can be measured by thermal conductivity detector (TCD).

2.10 Thermal decomposition kinetics of biodiesel

Thermogravimetric analysis (TG/DTG) has been used extensively to determine the devolatilization behavior and kinetic parameters of biomass (Fasina and Littlefield, 2012; Biswas and Sharma, 2013; Aboyade *et al,.* 2011). Thermal methods provide ample information of net weight loss which are used in determining the kinetic parameters. The technology presents a more excellent way to utilize biomass and make them more attractive as an alternative energy source. Biomass molecules are decomposed into volatiles, liquids and chars via pyrolysis. The liquid as well as gaseous products exhibit high calorific value which makes them suitable fuel (Di Blasi, 2008). Final temperature, heating rate and physicochemical properties of the biomass play a vital role in determining biomass pyrolysis behavior (Ounas *et al.*, 2011). According to literature, the main chemical event in vegetable oil pyrolysis is dehydration and devolatilization. Dehydration starts from 100 °C while devolatilization of unsaturated ester molecules starts around 220 °C and evolution of the remaining materials starts around 320 °C (Biswas and Sharma, 2013).

Moreover, to have detail understanding of pyrolysis kinetic of biomass, it is essential to use accurate kinetic model. This is based on the closeness of simulated data to the experimental data using correlation coefficient.

2.10.1 Determination of Kinetic parameters

The thermal decomposition of biodiesel relates to the experimental data as follows:

$$\frac{dx}{dt} = K(T)(1-x)^n \quad (2.8)$$

Where x is the extent of conversion, T is temperature, K, the specific rate constant, n, the reaction order and t is time. The conversion rate $\frac{dx}{dt}$ for non-isothermal pyrolysis at constant heating rate,

$\beta = \frac{dT}{dt}$, could be written as;

$$\frac{dx}{dt} = \beta \frac{dx}{dT} = K(T)(1-x)^n \quad (2.9)$$

Also, the degree of advance, x is;

$$x = \frac{w_0 - w}{w_0 - w_f} \quad (2.10)$$

Where w_o, w_f and w refers to the weight of samples at the beginning, end and time t respectively. Since weight loss is temperature dependent, K(T) is often modeled by Arrhenius equation (Aboulkas et al., 2009).

$$K(T) = Aexp(-\frac{E}{RT}) \quad (2.11)$$

where R is the gas constant (8.314 J/mole K), A is the frequency factor (min-1), EA is the activation energy (kJ/mol) and T is the absolute temperature (K). Combination of equation (1) and (2) gives;

$$\beta \frac{dx}{dT} = Aexp(-\frac{E}{RT})(1-x)^n \quad (2.12)$$

Differential model combine Eq. (1) and (4) to give

$$\ln((\frac{\mathrm{dx}}{\mathrm{dt}})/(1-x)^n) = \ln A - E/(RT) \quad (2.13)$$

The graph of ln((*dx/dt*)/ *(1-x)*^{n}*)* vs. *1/T* offers a linear plot whose slope corresponds to -E_A/R and the intercept gives ln *A*.

Rearranging equation 2 gives:

$$\frac{dx}{(1-x)^n} = \frac{A}{\beta} e^{\frac{-E}{RT}} dT \quad (2.14)$$

Integral method is generally accepted model which is based on temperature integral approximation by Coats and Redfern (Apaydin-Varol *et al.*, 2014). Therefore, Eq. (2.14) becomes:

$$\int_0^x \frac{dx}{(1-x)^n} = \frac{A}{\beta} \int_{T_0}^T e^{\frac{-E}{RT}} dT \quad (2.15)$$

The left side of Eq. (8) gives:

$$\int_0^x \frac{dx}{(1-x)^n} = \frac{(1-(1-x)^{(1-n)}}{1-n} \quad (2.16)$$

The right-hand side of Eq. (2.15) could be simplified using asymptotic series. The integration gives:

$$\frac{A}{\beta} \int_{T_0}^T e^{\frac{-E}{RT}} dT = T^2 \left\{\frac{AR}{\beta E}\left[1 - \frac{2RT}{E}\right]\right\} e^{\frac{-E}{RT}} \quad (2.17)$$

Substitution of Eqs. (9) and (10) into (8) gives:

$$\frac{(1-(1-x)^{(1-n)}}{T^2(1-n)} = \left\{\frac{AR}{\beta E}\left[1 - \frac{2RT}{E}\right]\right\} e^{\frac{-E}{RT}} \quad (2.18)$$

The natural logarithm of both sides assuming E >> 2RTgives:

$$ln\left[\frac{(1-(1-x)^{(1-n)}}{T^2(1-n)}\right] = ln\frac{AR}{\beta E} - \frac{E}{RT} \quad (2.19)$$

The graph of left-hand side vs. *1/T* offers a straight line plot whose slope corresponds to -*E/R* and the intercept gives ln *AR/βE*.

Ingraham and Marrier (Kök *et al.,* 2000) expressed rate constant K as *dw/dt* for the linear kinetics of the heterogeneous reaction. Where *dw* is the weight loss per unit area at *dt* period. Therefore, Eq. (2.12) becomes:

$$\log\left(\frac{dw}{\mathrm{dT}}\right) = -\log \mathrm{T} - \log\beta + \log A - E/(2.303RT) \quad (2.20)$$

The graph of log*(dw/dT*) + *log T* + *log β* vs. *1/T* offers a linear plot whose slope corresponds to -*E/ 2.303R* and the intercept gives log *A*. This gives the value of activation energy and Arrhenius constant/frequency factor.

2.11 Summary

In summary, the study discussed catalyst development towards efficient biodiesel production. The scope of the study is limited to development of a viable solidacid catalyst suitable for biodiesel production from shea butter. To ensure economical process, cheap and abundant kaolin is investigated as starting material for the synthesis of solidacid catalyst. This was done by examining the physicochemical properties and possible modification strategies. The strategies envisaged is chemical (acid and alkali) activation method. The modifications took advantage of heterogeneity of kaolinite surface in acid dealumination and alkali desilication procedures. Moreover, combination acid and alkali activations formed a synthesis route for hierarchical nanoporous HY zeolite. Further, functionalization of the synthesized hierarchical nanoporous HY zeolite with sulfate group and its activity in biodiesel production will be investigated. Hierarchical mesoporous ZSM-5 zeolites were also

envisaged by desilication of commercial ZSM-5. Finally, it is worthy to note that this advances in solidacid catalysts synthesis for biodiesel production could essentially lead to an industrial-scale application.

CHAPTER 3: SYNTHESIS AND CHARACTERIZATION OF HIGHLY ORDERED SOLIDACID CATALYST FROM KAOLIN

3.1 Introduction

Biodiesel is renewable, sustainable and non-fossil based fuel with various advantages such as renewability; sustainability, biodegradability, lower GHG-emissions and enhanced lubricity (do Nascimento *et al.,* 2011). Further, the prospect of producing biodiesel from existing refineries is promising. However, robust and active solidacid catalysts are essential for ensuring smooth transition into the refineries for commercial productions. Evidently, solidacid catalysts have gained wide acceptance in catalytic conversion processes such as bulk chemistry and petrochemical processes (do Nascimento *et al.*, 2011; Perissinotto *et al.*, 1997). However, the cost of producing such catalysts remains major challenge hindering catalysis from ensuring the prominence of biodiesel. Hence, cheaper starting materials with equally high catalytic properties will help in alleviating the economic constraints. Interestingly, kaolinite clay minerals catalysts found industrial applications since the early 1930s. Significant progress in several industrial processes such as petrochemistry; especially catalytic refining and bulk chemistry became possible with kaolinite as a precursor in active catalyst synthesis. This is because of the unique structure and pore size, which are suitable for conversion of bulky molecules (Lenarda *et al.,* 2007). These explain the renewed interests that aluminosilicates from clay are receiving towards solidacid catalyst synthesis. However, kaolinite resist acid attack during activation because of higher octahedral alumina contents. Calcining at temperatures between 550 and 950 °C subdues this resistance by transforming the clay to metakaolin. Nonetheless, this transformation deforms the crystalline structure of the clay material.

A process for alleviating these issues is acid leaching of metakaolin. Development of porosity, acidity and surface area are the major significance of acid leaching. The process also dealuminates and purifies the octahedral layers to facilitate the formation of surface structure. However, materials synthesized by this procedure are amorphous in nature. Therefore, there is a need to make the catalytic material crystalline for higher catalytic performances. This is because crystalline materials exhibit higher catalytic activity, high yields of gasoline, paraffinic and aromatic components because of their high hydrothermal stability. They also exhibit lower deactivation rates compared with synthetic amorphous aluminosilicates (Corma *et al.,* 1996; Tan *et al.,* 2007). Initially, researchers synthesized solidacid catalysts for catalytic cracking for by lixiviation of kaolinite and bentonite clay (Perissinotto *et al.,* 1997). Moreover, recent reports exhibited promising potentials of solidacid catalysts from clay for biodiesel production by esterification (da Silva Jr *et al.,* 2013; de Oliveira *et al.,* 2012; Patel *et al.,* 2013). Similarly, Dang *et al.* (2013) obtained encouraging results from transesterifying vegetable oil in excess methanol to produce biodiesel. The plausible reason to these is that solidacid catalysts catalyst enhance free fatty acids (FFA) conversion during biodiesel production (Boz *et al.,* 2009).

Moreover, Faujasitic (FAU) zeolites, which can also be made from kaolin have gained immense popularity within the research community and commercially as a solid acid catalyst. This is because they possess uniform pore size, high specific surface area and thermal stability (Karami *et al.,* 2009). They also possess tunable pore and acidity, which endowed them to be useful for several petrochemical processes (Shen *et al.,* 2007). However, their average pore size is relatively low, which limits their utilization in processes that involve bulky molecules. Such processes include organic waste treatment,

heavy crude oil and bio-oil upgrading. This is because of their mass transfer hurdle in bulky chemical reaction (Verhoef *et al.*, 2001). Several researchers reported strategies for overcoming this transport limitation of bulky molecules. These include dealumination, desilication, synthesis of mesoporous zeolites and microporous zeolites, and use of structural directing agents (Groen *et al.*, 2006). Further, other aspects investigated include commercially available dual pore materials from crystalline composite materials and crystalline physical mixtures (Guo *et al*., 2001; Huang *et al.*, 2000).

However, these strategies do not offer satisfactory result for acidity, structural, thermal, and hydrothermal stability (Tan *et al*., 2007). Recently, one of the most potent strategies is the synthesis of nano crystal materials with more than one porosity level termed "hierarchical nanoporous". This synergistically combines the outstanding properties of mesoporous and microporous zeolites (Jacobsen *et al.*, 2000b; Ogura *et al.*, 2001). Hierarchical nanoporous materials exhibit high thermal and hydrothermal stability and possess unique pore channel with bimodal pore system (micro- and meso-pores) (Han *et al.*, 2002; Tan *et al.*, 2007). The connection of microporous and mesoporous channels in a highly ordered manner enables the microporous channels to reside in the matrix. This enables the reactant molecules to travel a shorter diffusion path (Van Donk *et al.*, 2003).

Several researchers have worked on synthesis of these bimodal materials (Rong *et al.*, 2002; Tan *et al.*, 2007; Xu *et al.*, 2000). Tan *et al.* (2007) investigated synthesis of MY/kaolin composites with hierarchical mesoporous structure by overgrowth of mesoporous Y zeolite on kaolin. The synthesized MY/kaolin composites possess short diffusion path length high hydrothermal stability and moderate acidity. However, they exhibit low hierarchical factor and the starting materials for the synthesis are not

economical. Therefore, it is imperative to investigate the possibility of synthesizing hierarchical nanoporous zeolites from cheaper starting materials.

Liu *et al* (2003) investigated synthesis of NaY zeolite from coal-based kaolin. They reported that the optimum crystallization temperature is 107 °C. This gives higher specific surface area (SSA) and crystallinity.

Many variables influence formation of these faujasitic materials (Köroğlu *et al.,* 2002). This informs the need to employ multivariate experimental design to scrutinize the statistically significant independent variables (Karami *et al.,* 2009). In this case, response surface methodology (RSM) is a viable optimization tool. This methodology employs central composite design (CCD) as one of the design tools for model fitting through least square method (Ahmadi *et al.,* 2005). To investigate the suitability of the proposed model equation, analysis of variance (ANOVA) is a vital tool (Vining *et al.,* 2010). This provides diagnostic checking test for the model by the use of Fisher's statistical test (F-test). Response surface plots helps to provide the location of optimal response and surfaces study. RSM also offers robust evaluation of operation results and efficiency (Vining *et al.,* 2010). Several work has been done on Y zeolite synthesis (Chandrasekhar & Pramada (2004); Karami and Rohani, 2009; Liu *et al.,* 2003), but few actually conducted optimization studies. Karami and Rohani (2009) conducted optimization study for synthesis of Y zeolite using soluble silicate and aluminum sulfate as silica and alumina source respectively in a two-level factorial design. However, the zeolite precursors are expensive. Chandrasekhar and Pramada (2004) showed the prospect of producing Y zeolite from kaolin being a cheap source for both silica and alumina but the process variables are not systematically optimized.

Therefore, this study investigated the nature of Brönsted acid sites effect of and crystallization of thermal and acid treated amorphous aluminosilicates in synthesizing solidacid catalyst. An optimization study was conducted for synthesis of hierarchical nanoporous HY zeolite from kaolin in a two-level full factorial design using CCD. The mathematical models were developed in terms of aging, crystallization and NaOH solution to kaolin ratio (NaS). This is to provide a quantitative evaluation of hierarchical factor (HF), crystallinity and specific surface area (SSA). The experimental design is made up of 20 run with the center point repeated 6 times. This is to ensure accurate measurement and satisfactory reproducibility towards producing pure hierarchical nanoporous HY zeolites.

3.2 Experimental

3.2.1 Materials

The kaolin used for this investigation was purchased from R&M Chemicals Sdn. Bhd., Malaysia. It is an ordered kaolinite with weighted intensity ratio index (WIRI) of 0.9151. The study utilized the reagents without further purification. R&M Chemicals Sdn. Bhd., Malaysia also supplied the NaOH and H_3PO_4 (85% pure), while the reference Y zeolite was purchased from Sigma Aldrich Sdn. Bhd., Malaysia.

3.2.2 Methods

3.2.2.1 Ordered solidacid catalyst

The kaolin was transformed into metakaolin by calcination at 850 °C. This thermal process made the material more susceptible to dealumination and removal of impurities. 6M H_3PO_4 leached the metakaolin sample at 90 °C for 4 h. The resulting solution was divided into two parts after quenching with distilled water. A repetitive washing step on the first portion with distilled water achieved a pH value of 5. Conversely, mixing with

predetermined amount of aqueous NaOH facilitated attaining same pH value of 5 on the second portion. Both solutions were filtered separately with vacuum pump and dried them overnight at 120 °C. The samples obtained from distilled water and NaOH solution pH adjustment were designated as PLK8-6M4h and NaPLK8-6M4h respectively. The NaPLK8-6M4h samples were ion exchanged with 0.1 M NH_4NO_3 for 24 h. The resulting solution was filtered and dried overnight at 120 °C and designated HPLK8-6M4h. The calcination condition for all synthesized materials is 550 °C for 2 h.

3.2.2.2 Hierarchical nanoporous HY zeolite

The HY zeolites precursor were obtained by thermal activation at 850 °C for 2 h and subsequent activation with 4M H_2SO_4 at 90 °C for 3 h to produce amorphous aluminosilicate. After drying and calcination at 550 °C for 2 h, the precursor was added to an aqueous NaOH solution (14%) at ratio 1:9 (solute/solution). The solution was aged at room temperature from 24 to 72 h and subsequently crystallized at 100 °C for 16 and 24 h. The resulting mixture was washed and filtered with distilled water using vacuum pump until pH between 9 and 10. Further, the sample was dried at 110 °C overnight, and subsequently soaked in a solution saturated with NaCl to their equilibrium water content (Chandrasekhar & Pramada, 2004). Further, it was placed in a fume cupboard to remove excess water and dried. The sample was transformed into hydronium form in 0.2 M ammonium nitrate solution for 24 h. The filtering and drying of the resulting solution took place at 110 °C overnight and then calcination followed at 550 °C for 2 h. The obtained samples are designated HY-x-y, where x represents aging period (d), and y represents the crystallization time (h). For instance the sample aged for 1 d and crystallized for 16 h is HY-1-16 and for sample without salt, HY-1-16_ns.

3.2.3 Characterization

The study employed X-ray diffraction analysis (XRD), FTIR, and N_2 adsorption–desorption isotherms for characterizing the synthesized materials. PANanalytical X'pert Empyrean X-ray diffractometer with CuKα radiation at 40 kV and 40 mA performed the XRD analysis. The peak reflections at (511), (440), (533), and (642) helped to determine the average crystal size and relative crystallinity of the samples (Hosseinpour *et al.*, 2009).

$$Rel.Crystallinity\ (\%) = \frac{Sum\ of sample\ characteristic\ peak\ area}{Sum\ of\ \ the\ reference\ characteristic\ peak\ area} \times 100 \quad (3.1)$$

The crystallite size of the aforementioned peaks were computed with the aid of PANalytical X'Pert HighScore software (Frunz *et al.,* 2006). Further, we compared the crystallinity of the samples with that of conventional Y zeolite to obtain the values of relative crystallinity.

Perkin Elmer Spectrum RX FT-IR was used to for the infrared spectroscopy (IR) to confirm Y zeolite fingerprint. Surface area and porosity analyzer (Micrometrics ASAP 2020) gave the nitrogen adsorption/desorption analysis using analysis bath temperature of 77.350 K.

The morphology of the synthesized HY zeolites were visualized by Scanning electron microscopy (SEM, FEI Quanta 400 FE-SEM) using 20 kV as the accelerating voltage. The HY zeolites samples were coated with gold, prior to examination, to enhance the electrical conductivity.

Similarly, Quantachrome Nova 1200 apparatus analyzed the N2 adsorption–desorption isotherms at liquid nitrogen temperature. Outgassing at 130 °C for 2 h before each

measurement ensured accurate results on all the samples. We employed t-plot methods and Brunauer–Emmett–Teller (BET) to analyze the specific surface area, microporous area, microporous volume and pore-size distribution, specific surface area respectively.

Chemisorp 2720 was used to perform ammonia temperature programmed desorption (NH_3-TPD) analysis. The equipment consists of TPx Quartz sample tube micro-reactor installed in a vertical furnace. An online thermal conductivity detector (TCD) recorded the desorption signal. About 0.2 g of sample was placed in the micro reactor with the support of quartz wool. The sample purging took place under 20 ml/min flow of helium at 550 ℃ for 2 h. Then the physisorbed ammonia was flushed out with 20 ml/min flow of helium at 110 rt of quartz wool. The sample purging took place under 20 ml/min flow of helium at 550 °C for 1 h followed. Further, record of the ammonia desorption was taken from 70 to 500 rt of quartz wool. The sample purging took place under 20 ml/min flow of helium at 550 °C in 20 ml/min flow of helium at 10 rt of quartz wool. The sample purging took place under 20 ml/min flow of helium at 550 °C/min and TCD helped in continuous monitoring of the desorbed ammonia.

3.2.3.1 Crystallinity assessment of ordered solidacid catalyst

3.2.3.2 XRD method

Crystallinity is a function of the physical nature of the characteristic peaks. Broad peaks indicate low crystallinity while sharp X-ray peaks indicate high crystallinity. Therefore, to assess crystallinity index of the materials, the XRD patterns was analyzed. We employed the Aparicio-Galán-Ferrell (AGFI), Hinckley (HI) represented by Eq. 3.2 and 3.3; and weighted intensity ratio index (WIRI) with weighted intensity of (0 2 1 1) band in computing the indices.

$$\mathrm{AGFI} = \frac{\mathrm{I_A} + \mathrm{I_B}}{2\mathrm{I_C}} \qquad (3.2)$$

However, HI (Eq. 3.2) is only applicable where the kaolinite content in the material is more than 20 wt%. For highly crystalline kaolinite, the HI value is greater than 1.0 while it is below 1.0 for kaolinite with low crystallinity (Chmielová *et al*., 2002). Figure 3.1 illustrates the values of the individual peaks obtained from the XRD patterns.

$$\mathrm{HI} = \frac{\mathrm{A} + \mathrm{B}}{\mathrm{A_h}} \qquad (3.3)$$

In contrast, WIRI (Eq. 3) defines crystallinity as function of peak intensities of (02, 11) band and full width half maximum (FWHM) of the corresponding 020, $1\bar{1}0$, $11\bar{1}$ and $1\bar{1}\bar{1}$ reflections resulting from decomposition of the same band (Chmielová *et al.,* 2002; Ptáček *et al.,* 2013). The weighting coefficients w_1, w_2, w_3 and w_4 in Eq. 3.4 are the reciprocal of FWHM of $1\bar{1}0$, $11\bar{1}$, $1\bar{1}\bar{1}$ and 020 peaks respectively (Ptáček *et al.*, 2013). The value of WIRI ranges between 0 and 1. It is ≤ 0.4, 0.4<WIRI≤ 0.7 and 0.7 for low crystallinity, medium crystallinity and for high crystallinity respectively.

$$WIRI = 1 - e^{-\left(\frac{w_1 I(1\bar{1}0) + w_2 I(11\bar{1}) + w_3 I(1\bar{1}\bar{1})}{w_4 I(020)}\right)} \qquad (3.4)$$

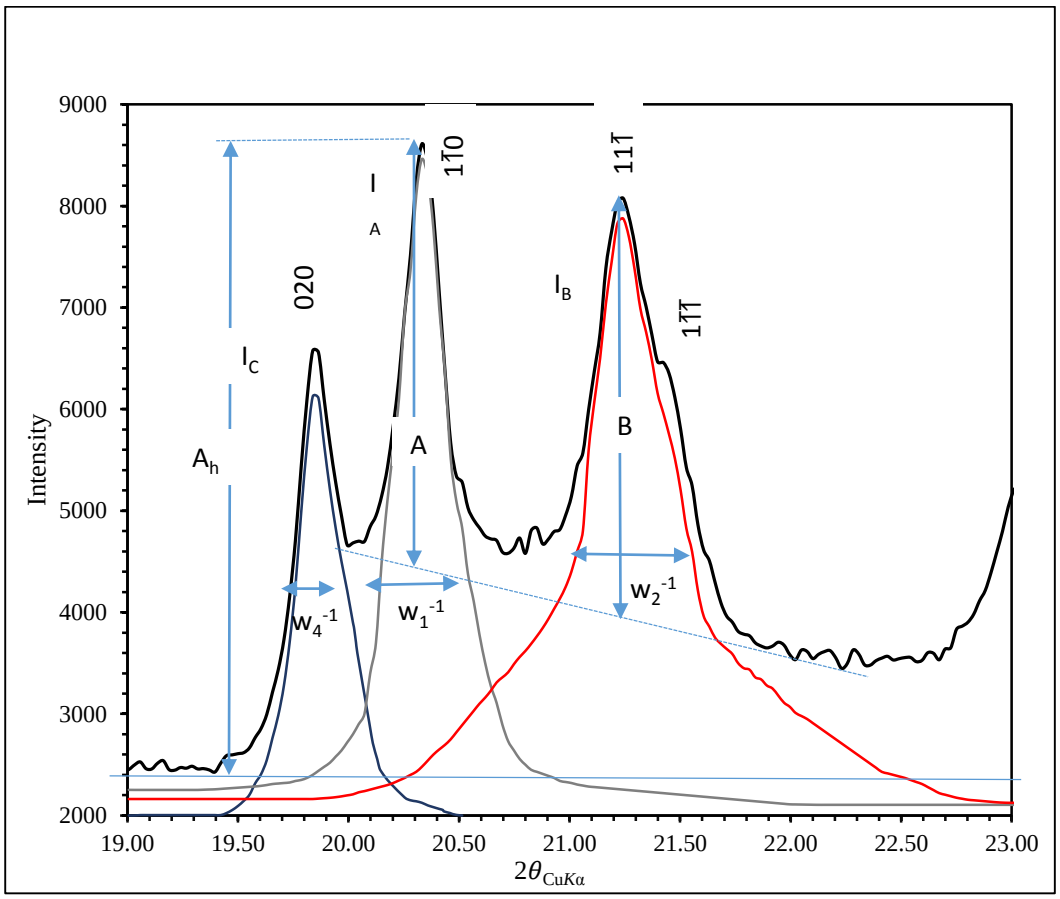

Figure 3.1: Computation of HI, AGFI and WIRI indices values from kaolin XRD data.

3.2.4 Hierarchy factor of HY zeolite

Hierarchy factor is a viable tool for categorizing the degree of structural order of porous materials. This estimates how less mesopore formation penalize the micropore formation of the synthesized zeolite sample (Pérez-Ramıīrez *et al.*, 2009; Zheng *et al.*, 2010, 2011, 2013).

Zheng *et al*. (2013) proposed a model as a model for classification of hierarchy mesoporous zeolites as derived from the conventional N_2 adsorption/desorption analysis. From the ratio of micropore volume to mesopore volume (Vmicro/Vmeso) and relative mesopore specific surface area (S_{meso}/S_{BET}) of the weighed sample, they defined HF as follows:

$$\mathrm{HF} = \frac{V_{micro} S_{meso}}{V_{Total} S_{BET}} \quad (3.5)$$

3.2.5 Central composite design optimization study of HY zeolites

3.2.5.1 Experimental design and data analysis

Table 3.1 presents a two-level full factorial design by CCD in which three process parameters: ageing, crystallization and NaOH solution to kaolin ratio were expressed as dimensionless (X_1, X_2, and X_3 respectively). The coded values are -1, 0, 1 for low, center and high level respectively. The process parameter levels selection was centered on the results of our earlier works.

Minitab® 16.2.2 was used for the regression and statistical analysis of the experimental data. The total number of runs is 20 which entails 8 cube point, 4 center points in cube, 6 axial points and 2 center points in axial. The distance between the center point and axial point, α of one factor's low/high level while the remaining factors maintained their center values. That is, the axial points are situated at (0, 0, ±α), (0, ±α, 0) and (±α, 0, 0). Generally, α is a function of a number of factor, k and is given as (2k) 0.25. Nevertheless, Minitab® 16.2.2 provides user an option of choosing the value of α. The value of α used in this work is 1.633. The number of runs replicated at the center point served as materials for experimental error determination. The responses chosen for RSM study are crystallinity, SSA and HF that were designated as Y_1, Y_2 and Y_3 respectively.

Table 3.1: Levels of HY zeolites Independent variables for the CCD

Variable	Symbol	Coded variable levels		
		-1	**0**	**1**
Ageing time (h)	X_1	12	24	36
Crystallization time (h)	X_2	24	48	72
NaOH to sample ratio (ml/g)	X_3	6	9	12

The CCD was arranged in a manner that permits modelling of suitable empirical model (second order polynomial equation). The simplified form of this model are used to obtain the desired responses generally as:

$$Y = \beta_0 + \sum_{i=1}^{n} \beta_i X_i + \sum_{i=1}^{n} \beta_{ii} {X_i}^2 + \sum_{i=1}^{n} \sum_{j=1}^{n} \beta_{ij} X_i X_j + e \qquad (3.6)$$

Where X stands for the independent variables, β for the regression coefficients, e is the error and Y stand for modeled responses. β_0 is the offset term while βiXi and βiiXi2 are the linear effect and quadratic effect respectively, and βijXiXj is the second order term.

The suitability of the proposed model was analyzed by ANOVA. ANOVA determines which of the operating parameters affect the responses significantly using *F*-test for diagnosis (Ahmadi *et al.*, 2005). This determines the effects estimates of each parameter with respect to their magnitude and significance. Further, possible response models were obtained. The effect estimate is the anticipated improvement in the response as the process variables were varied from low to high. Terms with a p-value greater than 0.05 were discarded and regarded as 'residual error'. This was followed by a new ANOVA

check. Note, p-value is an index that measures the unreliability of a result (Platz *et al*., 2005).

Either *p*-value or *F*-value of the model and lack-of-fit are suitable for determination of model significance (Rosa *et al.,* 2007). The ratio of the mean square (MS) of the process variable to the MS of the error terms gives the *F*-value while the *p*-value is obtained from F distribution using the degree of freedom and the *F*-value of the process variable and that of the error term. The model shows significant lack-of-fit if the pure error is significantly lower than the residual. In this case, pure error rather than the residual error is suitable for determination of *F*-value (Rosa *et al.,* 2007).

The critical value of F for the model as well as the lack-of-it are function of the degree of freedom of each term and that of their associated error terms (Barker, 2005; Box *et al.,* 1978). If the *F*-value of the model is higher than its critical value and lack of fit *F*-value is less than its critical value, the regression model is acceptable. The model is also acceptable if its *p*-value is less than 0.05 and its lack-of-fit is greater than 0.05. Else, the model is acceptable if not less than 95% of the data fit into the model (correlation coefficient, $R2 > 0.95$).

For further evaluation of the effectiveness of the models, margin of error was estimated for a two-sided confident interval at 95% confidence level using standard deviation (normal). Margin of error expresses the random error that emanates from uncertainties or discrepancies between the measured and the predicted value of a parameter (Garrett *et al.,* 1985). This will enable appropriate interpretation of the result. The magnitude of this error by standard error estimate and solely depends on factors like the sample size, the amount of variation in the responses, and the subgroup size for which the estimate was

made (Aud *et al.*, 2011). For a two-sided alternative hypothesis, the margin of error is the distance from the estimated statistic to each confidence interval value. Wider confidence level gives a larger margin of error, and lesser reliability of the model (Meyer *et al.*, 2013). Moreover, we assessed the quality of the synthesized samples by computing the tolerance interval. Tolerance interval has gained immense popularity among various statistical intervals especially in manufacturing industries because it confidently satisfies the expectation of the manufacturers (Lai *et al.*, 2012; Nourmohammadi *et al.*, 2015). The intervals are wider than other statistical intervals such as confidence and prediction intervals. This enables it to provide limits of quantification and detection estimates (Zorn *et al.*, 1999).

3.3 Results and discussion

3.3.1 Ordered solidacid catalyst

3.3.1.1 FTIR analysis

Figure 3.2 illustrates FTIR assignments of untreated kaolin and that of synthesized kaolinitic samples. Markedly, untreated kaolin spectrum exhibits unique bands at 3687, 3632 and 3620 cm^{-1} in the O-H stretching region (Figure 3.2a). This corresponds to the octahedral hydroxyl units (Al-OHstr) (Ayodele, 2013; Hu *et al*., 2012). The band at 3687 cm^{-1} displayed strong inner surface O-H in-phase stretching vibration. Similarly, the absorption band at 3620 cm^{-1} showed strong inner surface O-H stretching vibration between the tetrahedral and octahedral lamella of kaolin (Ayodele, 2013; Panda *et al*., 2010). Conversely, the inner surface OH out-phase stretching vibration found at 3632 cm-1 exhibited medium strength. Interestingly, these unique bands disappeared after calcining at 850 °C. We attributed this phenomenon to hydrogen bonds breakage between the layers of the kaolin because of thermal effect on the structural hydroxyl units. This

paves way for a more severe acid leaching of the material. Equally, kaolinite-bending regions at 914, 789, 750, 684 and 530 cm^{-1} disappeared after calcination and acid leaching (Figure 3.2b).

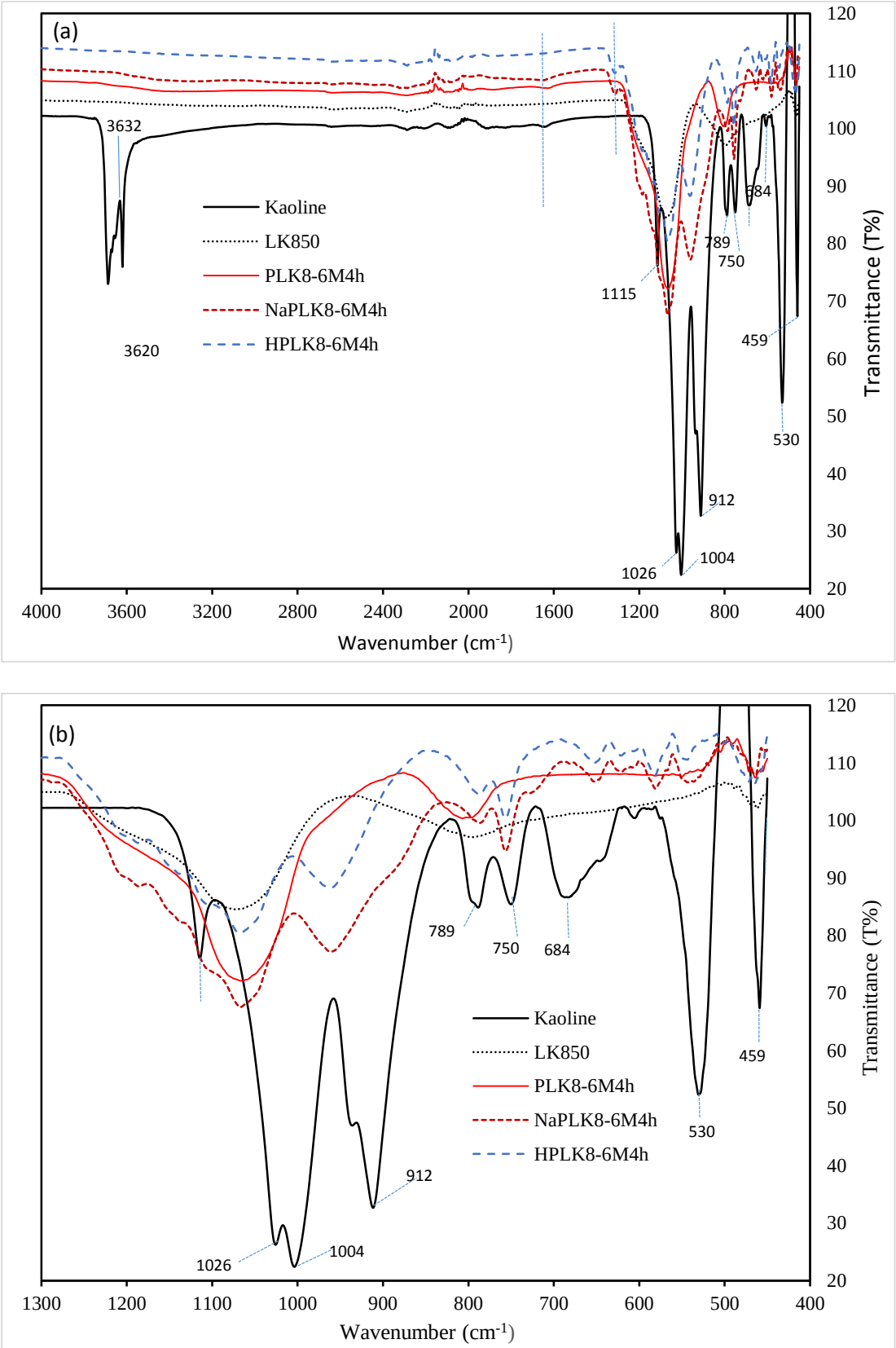

Figure 3.2: FTIR spectra of untreated kaolin and synthesized kaolinites.

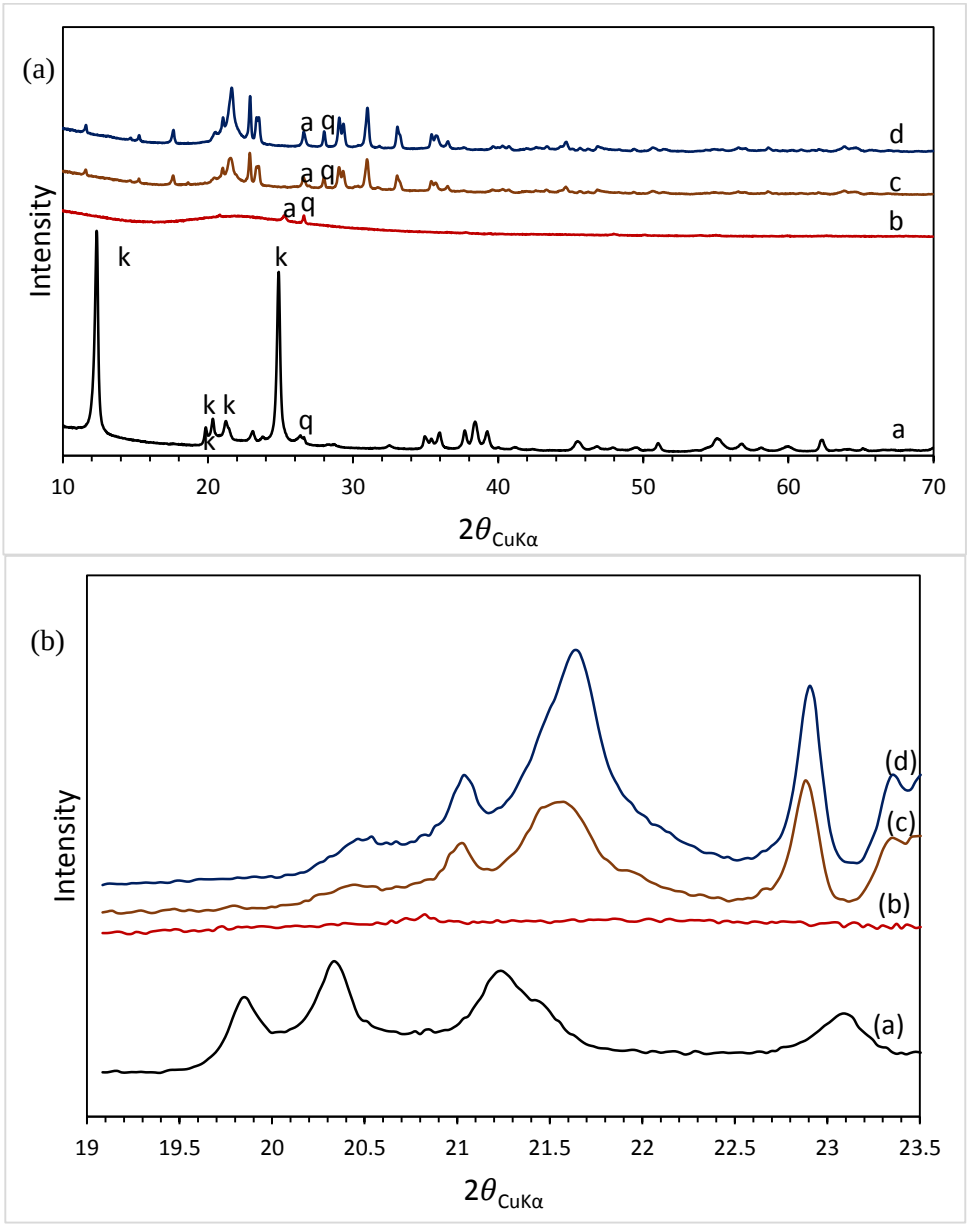

Figure 3.3: XRD pattern for kaolinite (a), PLk8-6M4h (b), NaPLk8-6M4h (c) and HPLk8-6M4h (d).

This leads to structural deformation of the material from crystalline to an amorphous structure. This is consistent with the results revealed by XRD illustrated in (Figure 3.3). The disappearance is despite different vibrational directions of 914 and 530 cm-1 bands (Al-OH and Si-OH bending vibrations respectively) and 789, 750 and 684 cm-1 bands representing Al-OH ("gibbsite-like" layer) translational vibrations. These bands reappeared at the bending region (Figure 3.2b) as exhibited by synthesized NaPLK8-

6M4h samples. We ascribed this transformation to crystalline structure restoration in the catalytic material. However, because of increase in Si/Al ratio, the peak intensities of NaPLK8-6M4h samples were lower than that of the untreated kaolin.

3.3.1.2 N_2 adsorption–desorption

Table 3.2 presents the textural properties of the catalyst samples. Incipient wetness impregnation of NaOH on PK8-6M-4h leads to drastic decrease in the specific surface area (SSA) and pore volume. This is could be attributed to collapse of the mesopore walls which greatly increase the pore size. Further, ion exchanged with 0.1 M NH_4NO_3 further decrease the SSA and pore volume.

Table 3.2: Textural properties of the samples

Sample	S_{BET}	S_{micro}[a]	S_{meso}[a]	V_{total}[a]	V_{mic}[a]	D_{meso}[b]
	m^2/g	m^2/g	m^2/g	cm^3/g	cm^3/g	(nm)
PK8-6M-4h	408.19	33.21	374.98	0.348	0.0088	4.96
HPK8-6M-4h	1.81	0.35	1.45	0.006	0.0001	30.38
NaPK8-6M-4h	2.75	0.39	2.36	0.010	0.0001	24.51

[a] Calculated from the t-plot curve.
[b] BJH method.

3.3.1.3 X-ray diffractograms analysis

Several studies (Chmielová *et al.*, 2002; Lenarda *et al.*, 2007; Ptáček *et al*., 2013) have shown the possibility of detecting major variances such as crystallinity index for different kaolinitic materials within the range of $20°<2\theta>24°$. Transformation of kaolin to metakaolin at 850°C for 2 h leads to water loss and disappearance of all the kaolinite peaks. However, attaching anatase (TiO_2) and quartz replaces the peaks with a broadband peak in the range of $20°<2\theta>30°$. This is associated with the presence of amorphous SiO_2 (Lenarda *et al*., 2007) and increase in anatase composition. This is represented by the appearance of three peaks at 26.61°, 48°and 55° (Figure 3.3a). Conversely, the disappearance of the peak at 001 basal plane (2) is traceable to hydrogen bonds breakage

between the layers of kaolinite. This structural water loss transformed the octahedral alumina unit into penta- and tetrahedral coordinated alumina unit (do Nascimento *et al*., 2011; Massiot *et al.*, 1995). Further, it exposed the material to acid attack by partial dissolution of Al^{3+}. Consequently, the acid treated metakaolin (PLK8-6M4h) exhibited similar XRD pattern to that of the metakaolin but with increased amorphous phase. Nonetheless, XRD pattern for the commercial kaolin showed characteristic peaks at 2θ values of 12.34° and 24.87° (Figure 3a). The XRD pattern of NaOH-adjusted material (NaPLK8-6M4h) displayed reemergence of the peak at 001 basal plane (2) but with a very low intensity. We ascribed this to bonding of hydrogen bonds between the layers of the materials. Interestingly, the process of ion exchange increased the intensity of all the peaks as exhibited by samples designated HPLK8-6M4h. Further, intensity of peaks in the range of 20°<2θ>24° was restored.

3.3.1.4 Crystallinity assessment

Figure 3.3b illustrates the variances in the X-ray diffractograms of untreated commercial kaolinite and synthesized materials. The complete disappearance of kaolinite peaks was evident from PLk8-6M4h diffractograms except for the peak in the range of 20°<2θ>24°. Therefore, to determine crystallinity indices, we analyzed the diffraction (02, 11) intensities in this range. Table 3.3 presents the results of the crystallinity indices as computed according to Eq (3.2) to (3.4).

Table 3.3: Crystallinity indices of the kaolinite materials.

Samples	Indices		
	HI	**AGFI**	**WIRI**
Kaolinite	1.328	1.429	0.9151
LK8	-	-	-
PLk8-6M4h	-	-	-
NaPLk8-6M4h	2.000	2.845	0.9999
HPLK8-6M4h	2.490	3.892	0.9997

The result shows that the expected product (HPLK8-6M4h) has higher crystallinity index than kaolin. From the result, it was also discovered that WIRI is the most appropriate crystallinity index for kaolinites. This is because theoretically, HPLK8-6M4h is expected to have lower crystallinity than NaPLk8-6M4h due to ion exchange. This observation corroborates the report of Sato *et al.* (2003) that ion exchange reduces crystallinity of sodium aluminosilicates.

3.3.2 Hierarchical nanoporous HY zeolite

Table 3.4 presents the silica and alumina compositions and Si/Al molar ratio of the HY zeolites produced from acid activated metakaolin and Figure 3.4 gives the XRD patterns of the synthesized catalysts with standard XRD peak positions. The results showed slight decrease in Si/Al molar ratio as the ageing increase from 24 to 48 h but rather rapid decrease upon increase to 72 h. However, as the crystallization time increased from 16 to 24 h, the Si/Al molar ratio increased from 1.55 to 1.61. The samples XRD spectrum show purely Y zeolite characteristic peaks ((511), (440), (533), and (642)) without the competitive presence of 4A, P and MOR zeolite peaks. The results showed that all the samples exhibit characteristic peaks of Y zeolite but with lower intensity. The sample HY-3-16 has the lowest intensity of Y zeolite characteristic peaks.

Table 3.4: Silica and alumina content of the samples.

Sample	Si (wt%)	Al (wt%)	Si/Al
HY-1-16	44.49	25.17	1.57
HY-1-16_ns	43.74	27.60	1.39
H-2-16	45.46	25.84	1.55
HY-2-24	47.00	25.70	1.61
HY-3-16	42.69	26.99	1.39

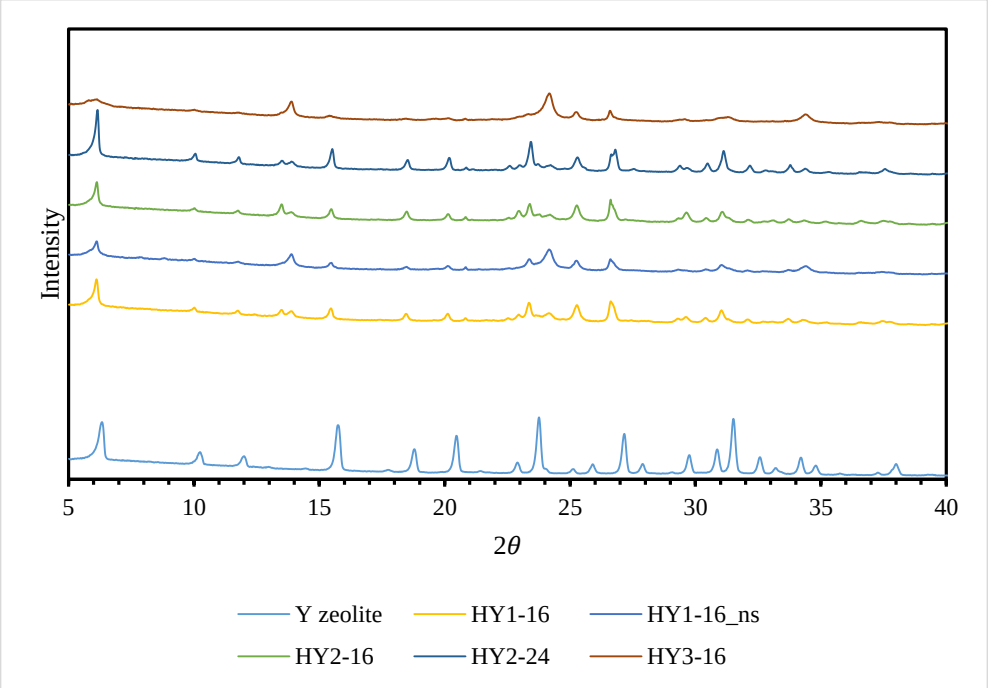

Figure 3.4: XRD pattern for the synthesized HY zeolites.

The characteristic peaks at (511), (440) and (533) are relatively too low compared to the other samples, which makes them nearly invisible in Figure 3.5. A closer look is shown in Figure 3.5. This is because excess aging impedes crystallization. Table 3.5 illustrates the relative crystallinity and average crystal size of the catalysts as computed using PANalytical X'Pert HighScore software on reflection peaks (511), (440), (533), and (642). The optimum aging time was observed to be 48 h, while the optimum

crystallization time is 16 h. This shows that excess aging and crystallization is detrimental to the crystallinity of HY zeolite. The sample without salt incorporation exhibits lower relative crystallinity than the sample incorporated with salt. Further, the average crystal size of all the samples confirms the nanoporosity of the synthesized samples. This confirms the hierarchical nanoporosity of the synthesized HY zeolites.

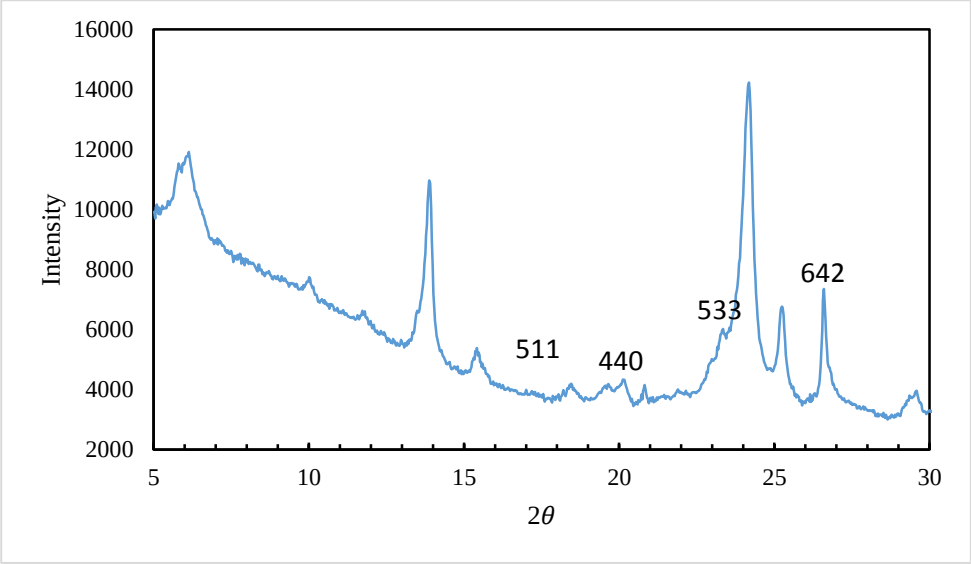

Figure 3.5: XRD pattern for the synthesized HY-3-16 zeolite.

Table 3.5: Relative crystallinity and average crystal size of the synthesized nanoporous HY zeolites from XRD data.

Sample	Total rel. Intensity	Relative crystallinity[a]	Ave. Crystal Size (nm)
Y ZEOLITE	288.90		
HY-1-16	181.24	62.73	74.72
HY-1-16_ns	143.75	49.76	70.29
HY-2-16	199.66	69.11	90.60
HY-2-24	147.08	50.91	82.58
HY-3-16	76.29	26.41	68.57

[a]Computed using the relative intensity of the samples relative to the relative intensity of conventional Y zeolite.

Table 3.6 presents the results of the surface area and porosity analysis with N_2 adsorption-desorption isotherms at p/po =0.98. BET model gave the specific surface area (SSA) and pore size distribution of the isotherms. The table also includes the computed HF values.

Moreover, Figure 3.6 shows the absorption/desorption isotherm of the HY zeolite samples. At relative pressure (p/po) 0.7 the samples exhibits a substantial increase in adsorption while desorption curve shows hysteresis loops.

Table 3.6: Textural parameters of the synthesized HY zeolites.

Sample	S_{BET}	S_{micro}[a]	S_{meso}[a]	V_{total}[a]	V_{mic}[a]	D_{meso}[b]	HF[c]	Acid sites
	m^2/g	m^2/g	m^2/g	cm^3/g	cm^3/g	(nm)		(mmol/g)
HY-1-16	248.73	222.54	26.19	0.18	0.10	4.87	0.147	1.43
HY-1-16_ns	181.67	147.86	38.80	0.19	0.07	4.12	0.108	0.94
HY-2-16	199.98	175.28	24.69	0.15	0.08	3.05	0.142	1.26
HY-2-24	316.50	287.62	28.88	0.19	0.13	2.42	0.214	2.06
HY-3-16	167.98	126.63	41.36	0.20	0.06	4.87	0.099	0.83

[a]Calculated from the t-plot curve.
[b]BET method.
[c]HF = V_{micro} x S_{meso}/(V_{meso} x S_{BET}).

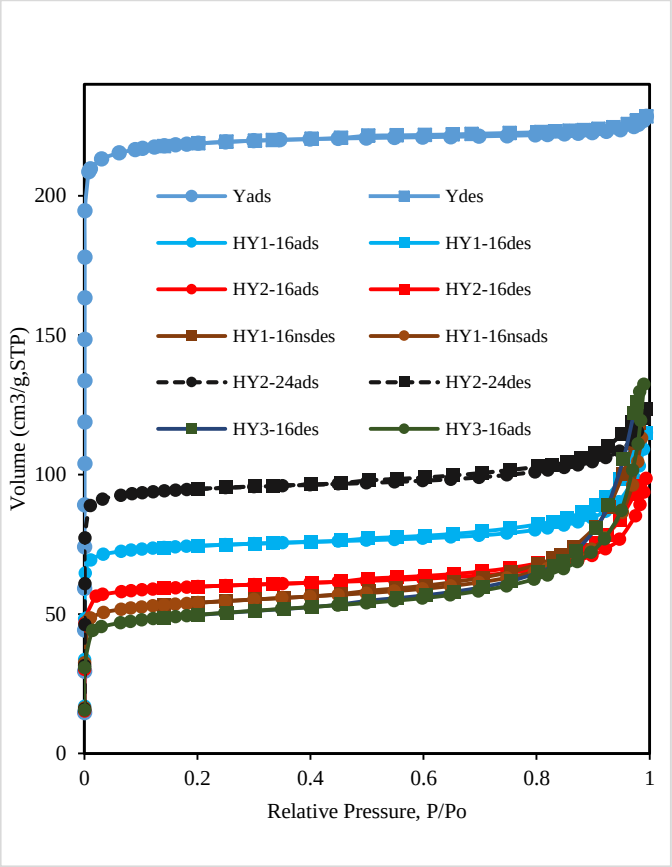

Figure 3.6: Nitrogen adsorption/desorption isotherms of HY zeolites samples.

Figure 3.7 presents the NH_3-TPD spectra of the synthesized HY zeolite samples. This enables us to determine the acid number and the acid strength distribution of the acid site. The samples exhibited well resolved symmetric peak at about 180 °C and a shoulder at about 300 °C. This shows that the HY zeolite samples exhibit mild acid strength high number of acid sites. Table 3.7 illustrates the total amount of acid sites from the NH_3-TPD peak area of the samples. The results show that as aging increased from 24 to 72 h, acid sites decreased from 1.43 to 0.83 mmol/g after 16 h crystallization. However, the increase in crystallization time from 16 to 24 h increased the acid sites from 1.26 to 2.06 mmol/g. Further, incorporation of NaCl also improve the acidity.

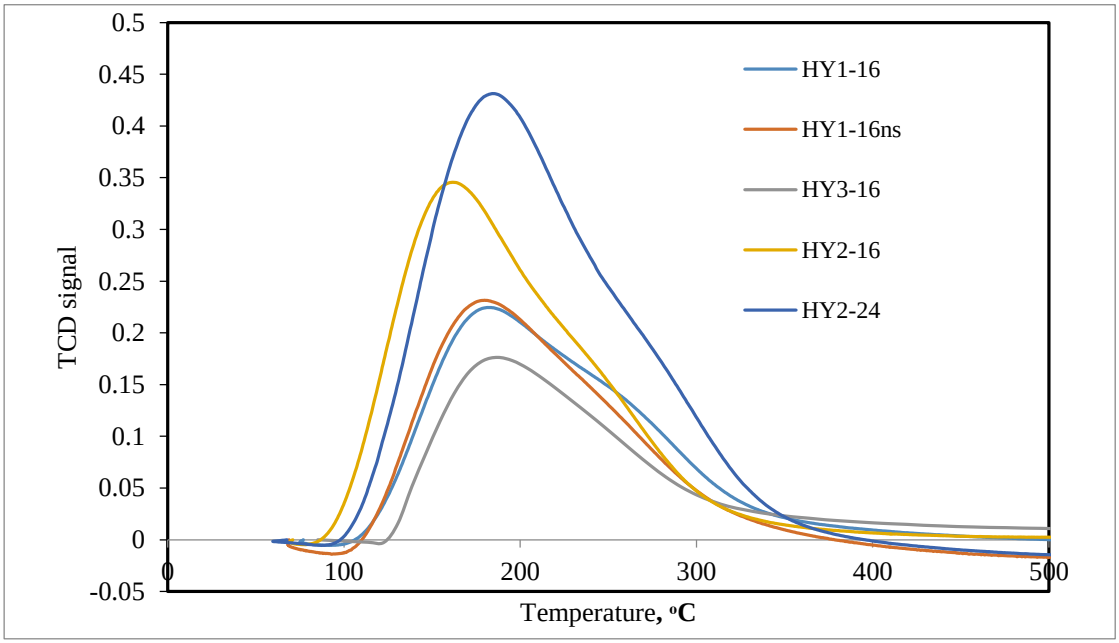

Figure 3.7: Ammonia-TPD curves of the synthesized nanoporous HY zeolite.

3.3.2.1 Effect of ageing period on formation of HY zeolite

The effect of aging in zeolite synthesis is of utmost importance. Table 3.5 and Table 3.6 present aging effects on crystallinity, SSA, HF, and acidity. The most appropriate aging time is 24 h because it gave the highest SSA for all samples hydrothermally crystallized for 16 h. Further increase in the aging period is detrimental to HY zeolites synthesis

because it leads to reduction in HF, SSA, crystallinity, micropore volume and number of acid sites of the samples.

3.3.2.2 Effect of crystallization period on formation of HY zeolite

Crystallization effect is also essential in the synthesis of HY zeolite. Table 3.5 shows that 16 h crystallization gives the highest relative crystallinity. It is worthy to know that increase from 16 to 24 h crystallization of the sample aged for 48 h greatly reduce the pore size and crystal size. However, there is an enhancement in the number of acid sites, SSA, total pore volume, micropore volume and HF value as shown in Table 3.6.

3.3.2.3 Effect of NaCl imbibement

The essence of NaCl imbibement is to enhance the crystallinity and hydrothermal stability and maintain the initial porous structure. However, excess salt collapse the mesopore wall of mesoporous materials (Chandrasekhar & Pramada, 2004; Yu *et al.,* 2001). Figure 3.8 presents XRD pattern for nanoporous HY zeolites with and without NaCl incorporation. The intensities of XRD reflection peaks (511), (440), (533), and (642) of samples with salts exhibits higher order resolution than sample without. The presence of the non-faujasitic peak at (622), which is more pronounced in the non-salted sample XRD pattern, may be responsible for its lower crystallinity. This indicates the proposed salt incorporation method by Chandrasekhar and Pramada (2004) used in this work is appropriate. Moreover, not only did salt incorporation enhance relative crystallinity, SSA, pore size, and HF, it also increase the number of acid sites of the sample.

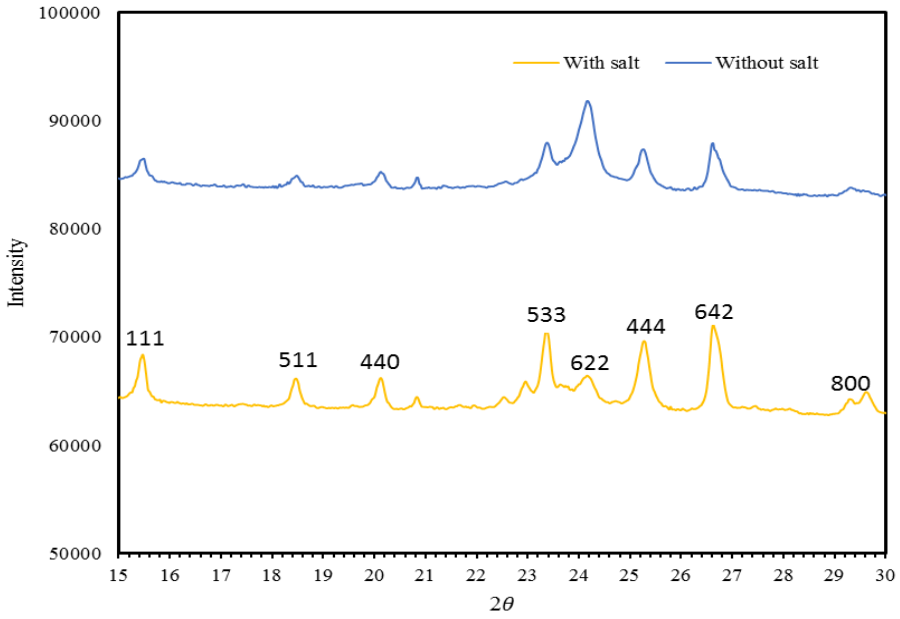

Figure 3.8: XRD pattern for samples with salt, and sample without salt aged for 1day and crystalized for 16 h.

3.3.3 Central composite design optimization study of HY zeolites

3.3.4 Hierarchical nanoporous HY zeolite characterization

The results of the textural properties, Si/Al molar ratio and XRD peak areas are presented in the Tables 3.7, Figure 3.9 to Figure 3.11. The table shows samples textural parameters of the samples with respect to their operating conditions. It is evident from here that crystallinity, Si/Al ratio and SSA increase with an increase in aging time from 24 to 43.6 h. The relative crystallinity of HY36-24-6 is greater than 100% probably because the reference Y zeolite composes of a little amorphous part. Crystallization time also improves the textural properties of the samples, but severe crystallization proved detrimental. Likewise, increase in NaOH/Solid from 6 to 9 ml/g leads to decrease in SSA, HF, Si/Al ratio and crystallinity of the sample.

Table 3.7: Textural properties and composition of some selected HY zeolite samples.

Sample	X_1 (h)	X_2 (h)	X_3 (ml/g)	Y_1 (%)	BJH pore Size (nm)	Si/Al	Y_2 (cm^2/g)	Y_3
HY12-24-12	12.00	24.00	12.00	74.93	8.98	1.59	366.90	0.20
HY24-48-9	24.00	48.00	9.00	76.62	8.61	1.52	359.06	0.23
HY36-24-6	36.00	24.00	6.00	106.86	8.03	1.88	443.78	0.30
HY36-24-12	36.00	24.00	12.00	63.79	8.46	1.53	394.84	0.18
HY36-72-6	36.00	72.00	6.00	87.29	6.81	1.83	367.34	0.32
HY43.6-48-9	43.60	48.00	9.00	85.64	7.15	1.67	406.14	0.23
HY12-72-12	12.00	72.00	12.00	31.32	14.66	1.43	133.24	0.11

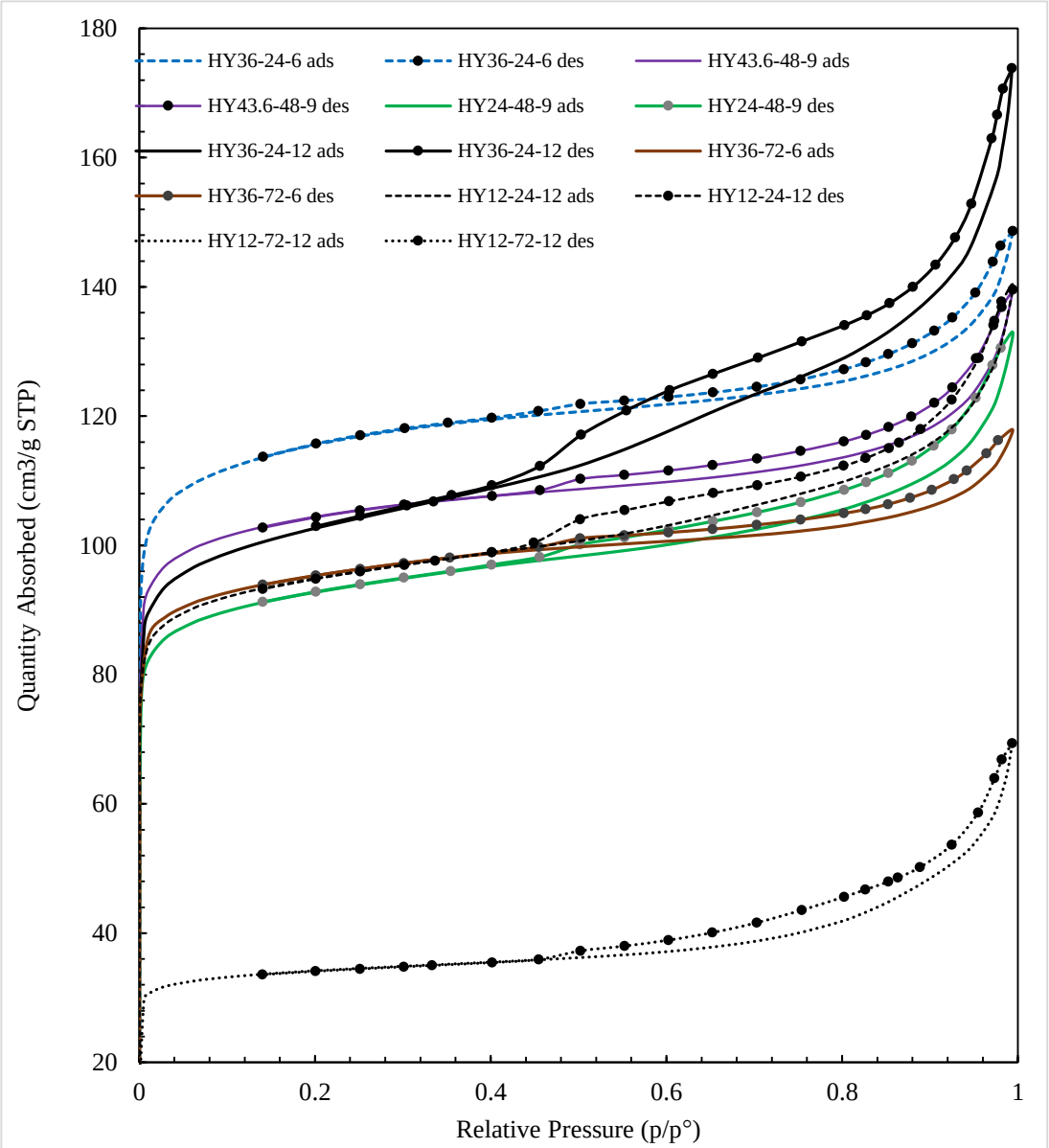

Figure 3.9: Nitrogen adsorption/desorption isotherms of some selected HY zeolites samples.

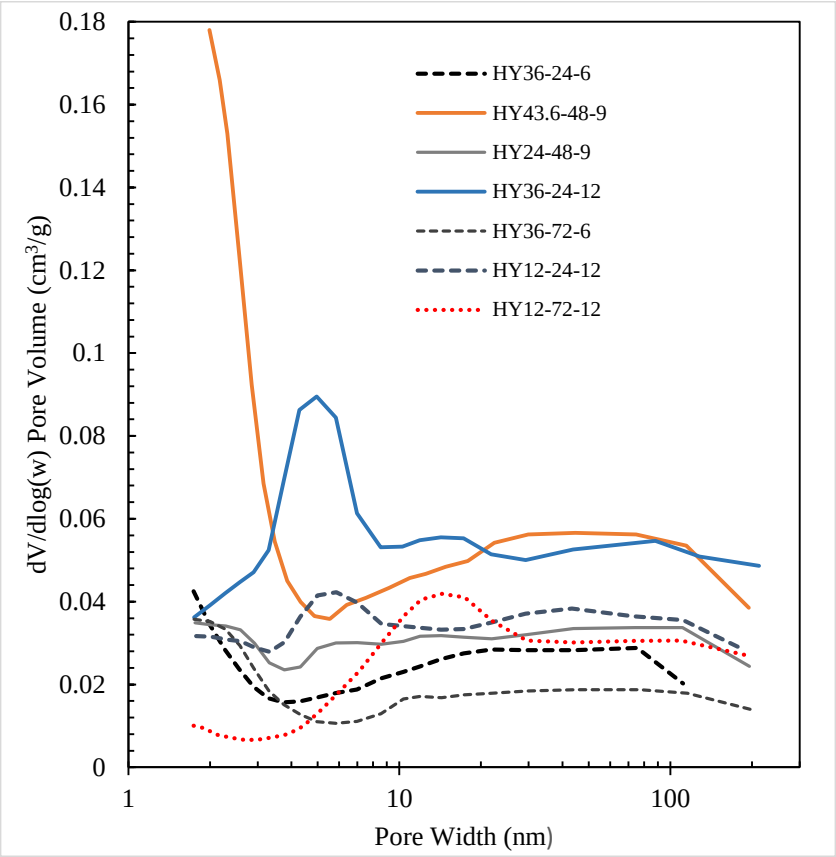

Figure 3.10: Pore size distribution of some selected HY zeolites samples.

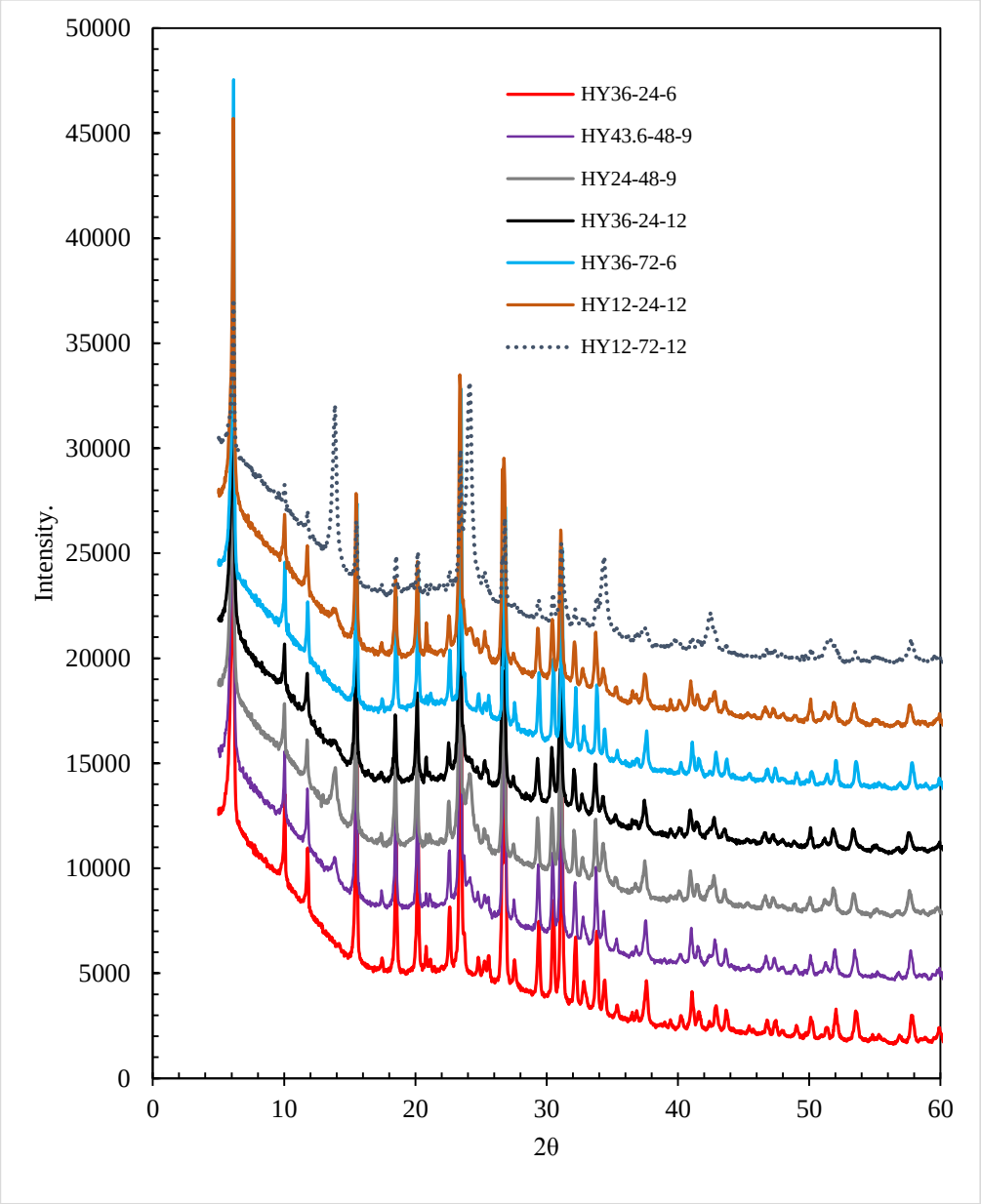

Figure 3.11: Powder XRD pattern of some selected HY zeolites samples.

The N_2 adsorption/desorption isotherms show that the synthesized samples possess uniform mesoporosity, which are evident by sharp steps at p/p° in the range of 0.4-0.45. The average pore size of the samples are shown in Table 5.3. Figure 3.10 shows the pore size distribution using BJH model. The results show that all the samples exhibit hierarchical pore structure with mesoporosity range of 2-50 nm, and macroporosity range of 50- 200 nm. The hierarchy factors of the samples are shown in Table 5.3. The XRD

patterns show the characteristics of Y zeolite without the competing presence of any impurities. Further, the intensity of the characteristic peaks informs their crystallinity (Table 3.7). The formation of hierarchical nanoporous HY zeolite was also confirmed by FT-IR spectroscopy, as shown in Figure 3.12. All the samples possess the characteristic peaks of Y zeolite at around 1002 and 460 cm^{-1}. The band 455–476 cm^{-1} are attributed to the O–T (Si or Al) bending vibrations (Zhang *et al.*, 2010), and the broad bands around 1000 cm^{-1} are attributed to the internal tetrahedral asymmetrical stretching vibration. Further, the bands at 558–572 cm^{-1} are ascribed to the hexatomic ring vibrations of Y zeolite (Holmberg *et al.*, 2003; Kosanović *et al.*, 2011), and the bands at 760–790 cm^{-1} are assigned to the external linkage symmetrical stretching vibrations.

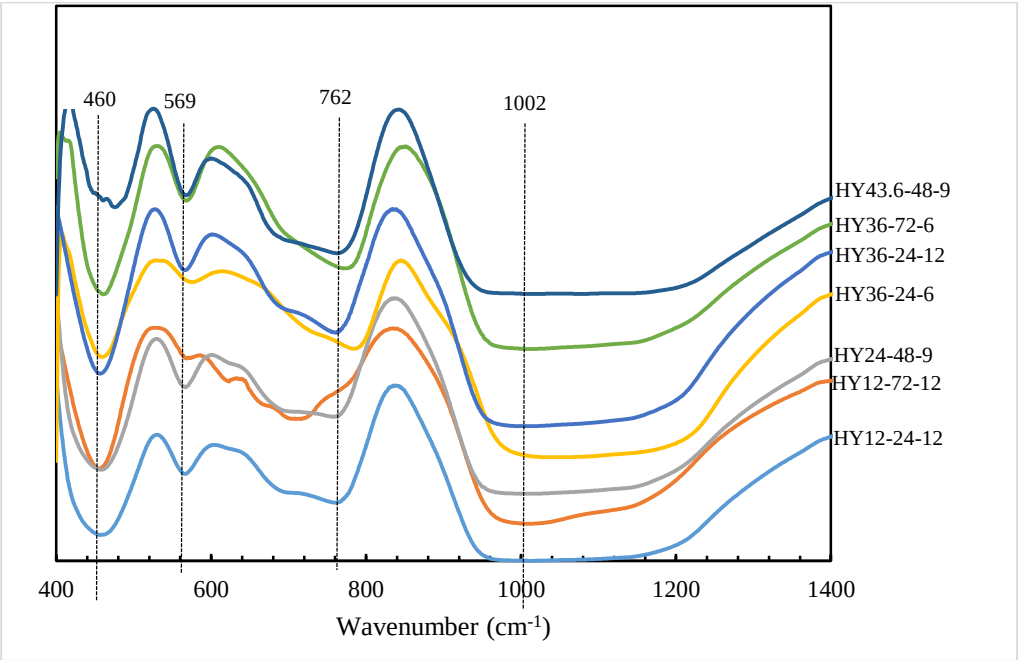

Figure 3.12: FT-IR spectra of some selected HY zeolites samples.

SEM was employed to observe the morphology of synthesized HY zeolites as illustrated in Figure 3.13. All the samples show both the octahedral morphology attributed to conventional Y zeolite and globular particles with rugged surfaces, which confirms the mesoporosity of the samples (Qin *et al.*, 2013).

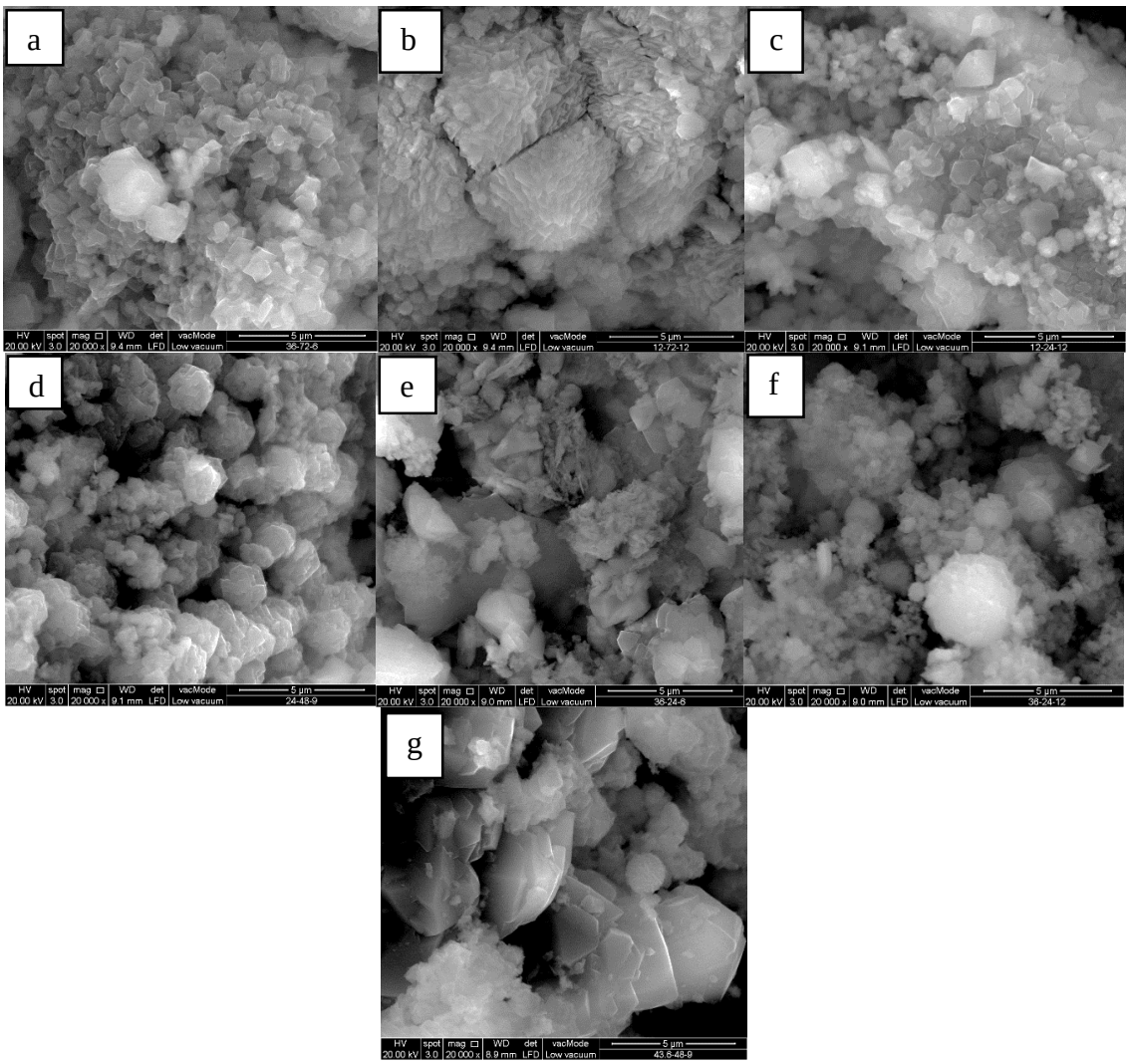

Figure 3.13: SEM images of some selected HY zeolites samples. (a): HY36-72-6; (b): HY12-72-12; (c): HY12-24-12; (d): HY24-48-9; (e): HY36-24-6; (f): HY36-24-12; (g): HY43.6-48-9.

Table 3.8: Results of the response variables.

Run	Aging (h)	Crystalzation (h)	NaOH/Solid (ml/g)	Crystalinity (%)	SSA cm^2/g	HF
1	24	8.8	9	42.55	130.26	0.07
2	24	48	4.1	20.78	33.16	0.07
3	24	48	13.9	5.3143	22.79	0.02
4	24	48	9	74.07	349.45	0.24
5	24	48	9	75.09	350.21	0.24
6	43.6	48	9	85.64	406.14	0.23
7	24	87.2	9	16.09	80.46	0.13
8	4.4	48	9	73.61	325.08	0.21
9	36	24	6	106.86	443.78	0.30
10	36	72	12	40.57	165.72	0.17
11	24	48	9	78.15	366.62	0.22
12	24	48	9	74.94	353.34	0.22
13	12	72	6	83.19	319.98	0.29
14	12	72	12	31.32	133.24	0.11
15	12	24	6	84.41	363.82	0.21
16	36	24	12	63.79	394.84	0.18
17	12	24	12	74.93	366.90	0.20
18	24	48	9	76.62	359.06	0.23
19	24	48	9	77.98	361.46	0.22
20	36	72	6	87.29	367.34	0.32

3.3.5 Statistical analysis

The CCD arrangement of the three process variables enables development of mathematical model presenting each response as a function of ageing time (X_1), crystallization time (X_2) and NaOH/solid ratio (X_3). Each response was computed as a function of the sum of a constant, three second-order effects, three first-order effects and three interaction effects of the process variables (Eq. (3.6)). Six replicated runs at the center point (runs 4, 5, 11, 12, 18 and 19) determined the residual error associated with the experiment. This error is an inexplicable variance in the experiment that significantly affects the reliability of the experiment as well as the mathematical model. ANOVA helped to analyze the suitability of the proposed model.

The experimental data were modeled into second-order quadratic equation. Table 5.5 presents the model coefficients with their respective F-value and p-values. Below are the full models for crystallinity (Y_1), SSA (Y_2) and HF (Y_3):

$$Y_1 = -70.028 - 2.028X_1 + 1.857X_2 + 32.818X_3 + 0.066{X_1}^2 - 0.016{X_2}^2 - 1.723{X_3}^2 + 0.001X_1X_2 - 0.099X_1X_3 - 0.08X_2X_3 \quad (3.7)$$

$$Y_2 = -613.107 - 10.05X_1 + 12.471X_2 + 187.713X_3 + 0.307{X_1}^2 - 0.093{X_2}^2 - 9.16{X_3}^2 - 0.012X_1X_2 - 0.232X_1X_3 - 0.595X_2X_3 \quad (3.8)$$

$$Y_3 = -0.278 - 0.0044X_1 + 0.0069X_2 + 0.0927X_3 + 0.0002{X_1}^2 - 0.0000{X_2}^2 - 0.0047{X_3}^2 + 0.000X_1X_2 - 0.0003X_1X_3 - 0.0003X_2X_3 \quad (3.9)$$

Table 3.9: Proposed model for crystallinity, SSA and HF for hierarchical nanoporous HY zeolite formulation.

Term	Crystallinity		SSA		HF	
	Coeff	**p-value**	**Coeff**	**p-value**	**Coeff**	**p-value**
β_0	-70.028	0.29	-613.107	0.075	-0.277947	0.251
Blocks	12.0976	0.004	60.408	0.004	0.035471	0.013
X_1	-2.0288	0.332	-10.05	0.327	-0.0044	0.556
X_2	1.8573	0.093	12.471	0.03	0.006919	0.087
X_3	32.8179	0.006	187.713	0.002	0.092658	0.02
X_1^2	0.0657	0.036	0.307	0.043	0.000165	0.123
X_2^2	-0.0163	0.036	-0.093	0.019	-0.000038	0.147
X_3^2	-1.7234	0.003	-9.16	0.002	-0.004646	0.015
X_1X_2	0.0009	0.96	-0.012	0.888	0.000005	0.941
X_1X_3	-0.0987	0.489	-0.232	0.737	-0.000271	0.6
X_2X_3	-0.0799	0.272	-0.595	0.109	-0.000338	0.207
R^2	87.91		87.73		81.49	

The significances of the terms in the model were measured by their p-values and F-values. A process variable has significance on a response only if the p-value is less than 0.05, or if the F-value is greater than its critical value. F- statistic can be written as

$$F = \frac{MSR}{MSE} \tag{3.10}$$

$$MSE = \frac{SSE}{DF} \tag{3.11}$$

Where MSR and MSE are the mean squares for models and residuals respectively, SSE is the sum of square for residuals and DF is the degree of freedom.

From Table 5.5, It could be seen that all the square terms significantly affects crystallinity and SSA; only X_3 is significant for crystallinity linearly while X_1 and X_3 affect SSA significantly; and X_3 and X_2 significantly affect the HF of the samples. It is clear that none of the interactions between the process variables affect any of the response.

3.3.6 Model Significance Check

The acceptability of the proposed models are investigated with ANOVA using 95% confidence level (Table 5.6). This analysis was performed using Minitab statistical software, which used mean square, based on residual error (MSE) to compute F-value. The F-value for crystallinity, SSA, and HF models are 5.66, 5.48 and 3.05, respectively and the critical $F_{0.05,\,9,\,9}$ is 3.18. Also, the p-value the model of crystallinity, SSA and HF are 0.008, 0.009 and 0.054, respectively. Therefore, it is clear that the F-values and p-values of the entire response model show that all the models are significant except that of HF. However, since the pure error is significantly lower than residual error, then the model shows significant lack-of-fit (0.00). Therefore, we use the mean square for pure error rather than MSE to re-compute *F*-value, then *F*-value of HF becomes 312.92 which is greater than the critical $F_{0.05,9,4}$ (6.00). This shows that HF model is also significant based on pure error due to significant lack-of-fit.

Table 3.10: ANOVA for the predicted response models.

Source	DF	Seq SS	Adj SS	Adj MS	F-test	F-critical	P-value
Crystallinity							
Blocks	1	2810	2809.96	2809.96	14.5		0.004
Model	9	9870.8	9870.81	1096.76	5.66	3.188	0.008
Linear	3	3764.6	3675.71	1225.24	6.32		0.014
Square	3	5739.7	5739.65	1913.22	9.87		0.003
Interaction	3	366.6	366.58	122.19	0.63		0.614
Residual Error	9	1744.7	1744.67	193.85	0		
Lack-of-Fit	5	1737.5	1737.49	347.5	193.54	6	0
Pure Error	4	7.2	7.18	1.8			
Total	19	14425.5					
SSA							
Blocks	1	70063	70062	70062.1	15.08		0.004
Model	9	228900	228900	25433.4	5.48	3.188	0.009
Linear	3	56057	122438	40812.5	8.79		0.005
Square	3	157522	157522	52507.4	11.3		0.002
Interaction	3	15321	15321	5107.2	1.1		0.399
Residual Error	9	41808	41808	41808	4645.4		
Lack-of-Fit	5	41717	41717	41717	8343.4	6	0
Pure Error	4	91	91	91	22.9		
Total	19	340771					
HF							
Blocks	1	0.024158	0.024157	0.024157	9.41		0.013
Model	9	0.070404	0.070404	0.007823	3.05		0.056
Linear	3	0.026473	0.030668	0.010223	3.98		0.046
Square	3	0.03841	0.03841	0.012803	4.99		0.026
Interaction	3	0.00552	0.00552	0.00184	0.66		0.566
Residual Error	9	0.023101	0.023101	0.002567	0		
Lack-of-Fit	5	0.023001	0.023001	0.0046	183.42	6	0
Pure Error	4	0.0001	0.0001	0.000025			
Total	19	0.117662					

Table 3.11 shows the margin of error for the models. The lower bound is almost half of the upper bound. The observed discrepancies as shown in the table could be associated with measurement position estimate and clerical error (Benoit *et al.*, 2009; Volkens,

2001). This gives statistically relaxed error margins, which engenders successful alignment in each group according to the report of Maniar *et al.* (2011).

Table 3.11: Margin of error for the response parameters at 95% confidence level.

Sample	Y_1	Y_2	Y_3
Standard deviation	27.55	133.92	0.079
Upper bound	12.69	61.68	0.036
Lower bound	-6.6	-32.08	-0.019

To further, evaluate the effectiveness of the models with respect to sample quality, we compute the tolerance interval at 95% confidence level for each model as shown in Figure 3.14. This gives us the range of expected response from the each model in the nonparametric region of normal distribution. The normality test shows that the sample data are normally distributed. Therefore, we can use the normal interval (-12.47-139.79% for Y_1; -85.35-654.71cm^2/g for Y_2 and -0.024 to 0.411 for Y_3). However, the lower limits are lower than the expected value range, which makes the range too wide. Consequently, the nonparametric (distribution-free) method becomes more appropriate. This gives interval 5.31-106.86% for Y_1; 22.79-443.78 cm^2/g for Y_2 and 0.019-0.319 for Y_3.

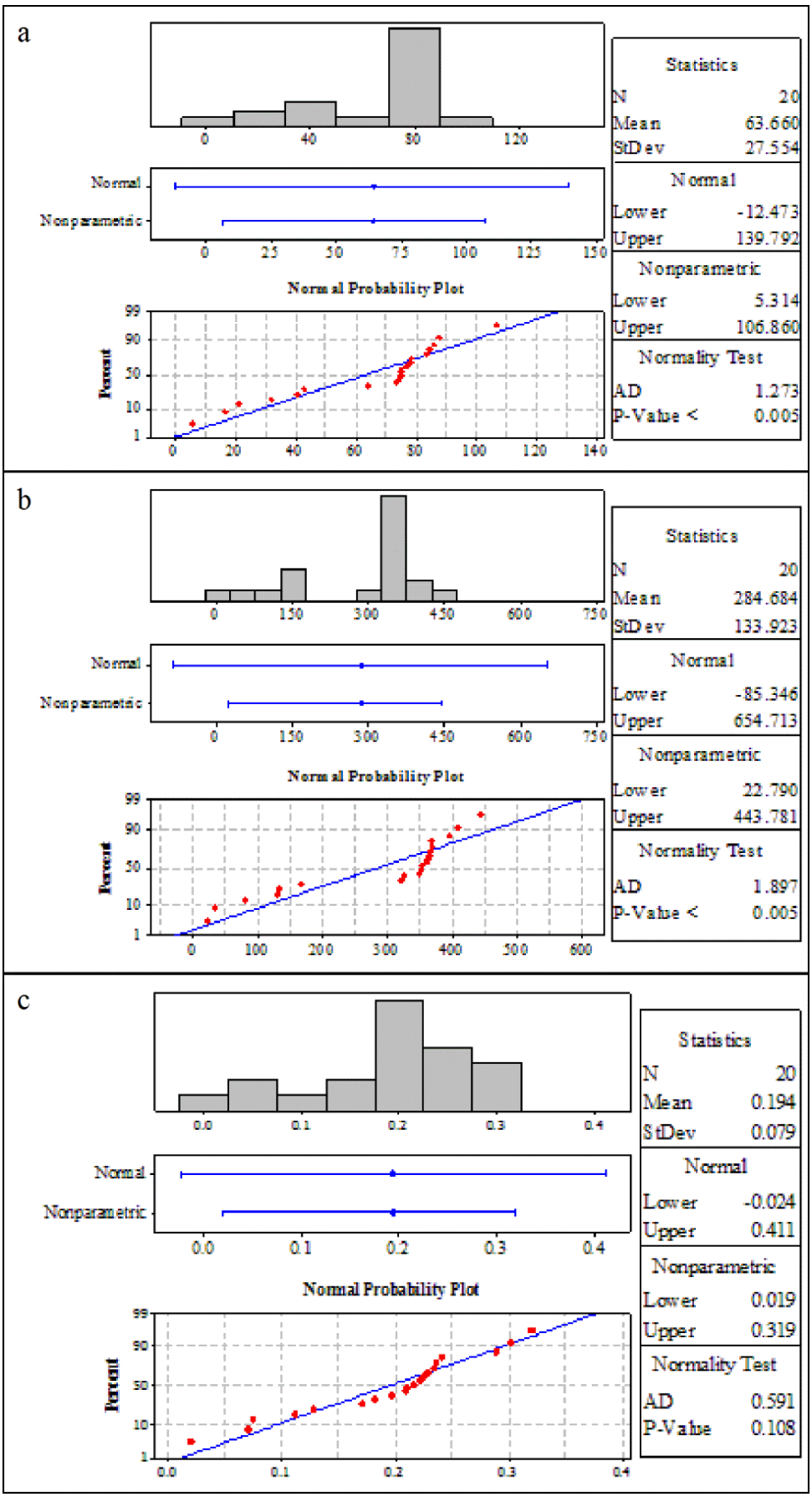

Figure 3.14: Tolerance interval plot for (a) Crystallinity, (b) SSA; and (c) HF.

3.3.7 Effect of process variables

Figures 3.15-3.17 show the surface plots of sets of combination of two process variables, fixing the other variable for crystallinity, SSA and HF model. In the model for all the response variables, X_3 is the most significant process variable. This is because it exhibits the highest coefficient in the response models. However, X_3 shows no significant interaction with other process variable. Figure 3.15 illustrates the dependence of crystallinity (Y_1) on the process variables. The plots exhibit robust curvature of three-dimensional faces. The crystallinity increases as the NaOH/solid ratio (X_3) decreases to its low level (6 ml/g). Y_1 also increase with crystallization time (X_2) towards the central level and latter decrease as X_2 increases. Conversely, Y_1 sparingly decreases with increase in aging time (X_1) towards the center level and thereafter increases with X_1 to its high level. This indicates that the stronger effect of aging occurs at its high level meaning that aging is crucial to obtaining high purity Y zeolite. The surface plots of the effect of the process variables in Figure 3.16 reveals that all the process variables significantly influenced SSA (Y_2). Initially, at the lowest X_1 (4.04 h) towards the center level, there is no significant change in the value of Y_2. As X_1 increased to the high level, Y_2 increases meaning that micropore volume increases with aging. At the lowest level of X_2, Y_2 is low but an increase in X_2 to the low level leads to slight decrease in Y_2 towards high level and subsequent rapid decrease towards the highest level. Y_2 increased as X_3 increases to the lower level (6 ml/g) but further increase in X_3 leads to decrease in Y_2. Further, the effect of process variables in Figure 3.17 indicates that all the factors affect the HF (Y_3). Y_3 increases with increase in X_1 and X_2, but an increase in X_2 towards its high level leads to decrease in Y_3. At the lowest level of X_3, Y_3 is low. However, increase in X_3 to the low-level increases Y_3. Meanwhile, a further increase in X_3 is detrimental to Y_3.

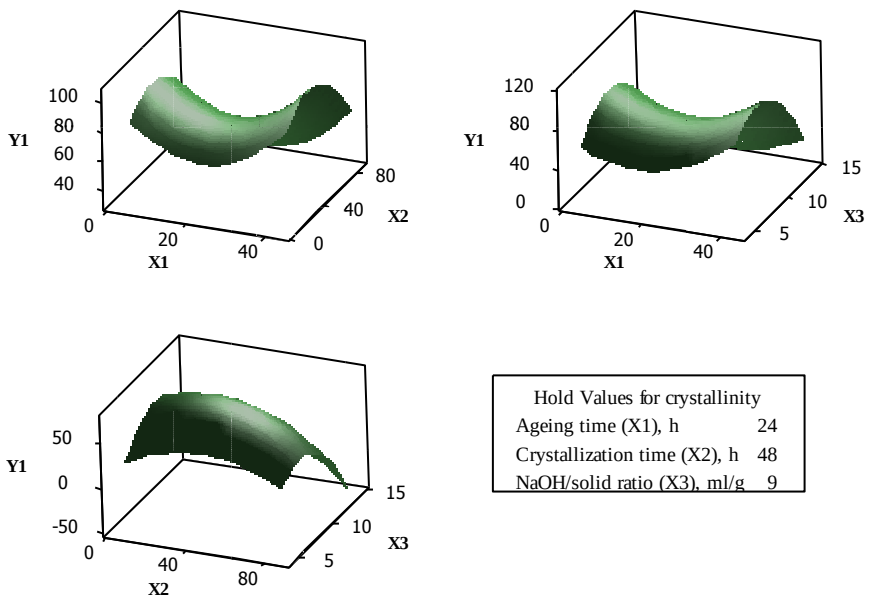

Figure 3.15: Response surface plot showing the effect of process variables on crystallinity.

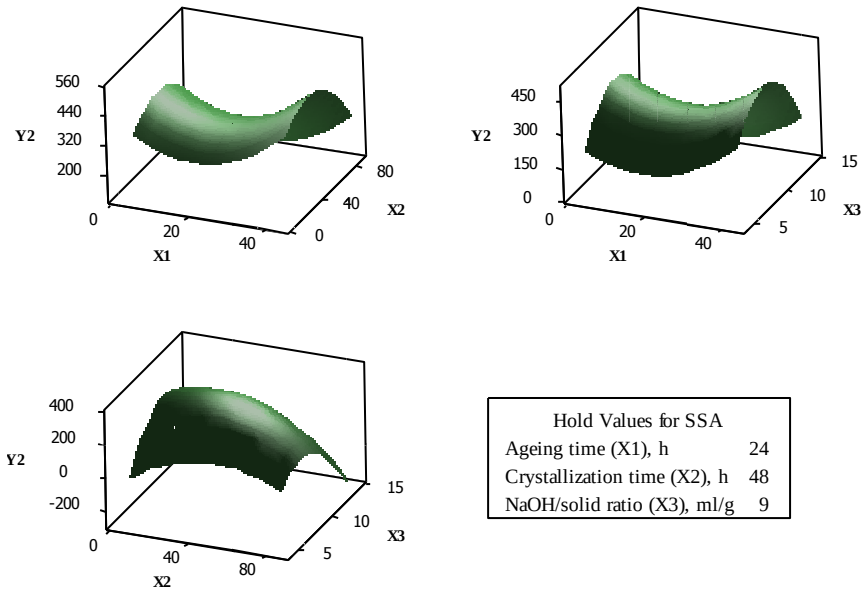

Figure 3.16: Response surface plot showing the effect of process variables on specific surface area.

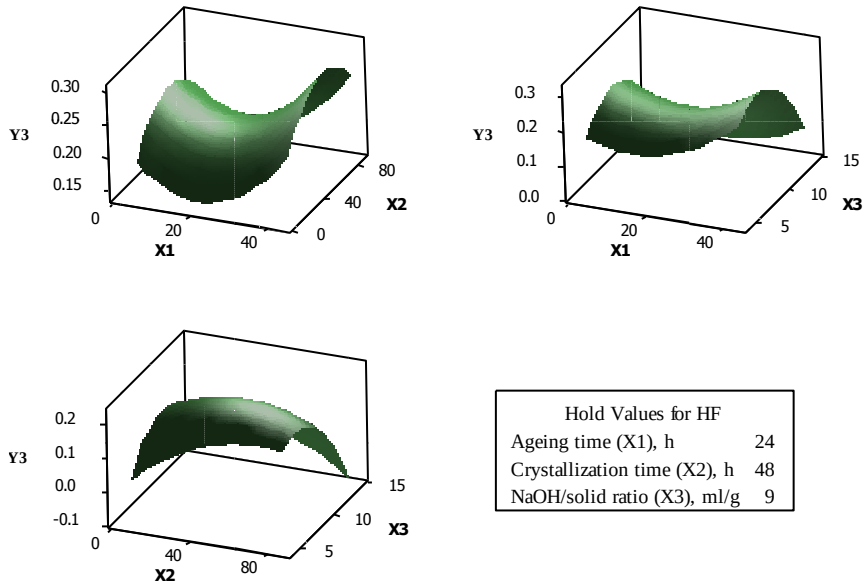

Figure 3.17: Response surface plot showing the effect of process variables on hierarchy factor.

3.3.8 Optimization of process variables

Response optimizer helps in identification of a set of independent variable values that could jointly optimize the response variables. The suitability of the set of independent variables in satisfying the requirements of the targeted responses was measured by the term called composite desirability (D). The value of D was obtained from the predetermined individual desirability (d) for each response. To maximize the composite desirability, multiple starting points reduced gradient algorithm was used. This helps to determine the optimal value of the process variables.

Figure 3.18 presents the plots of all the responses and the sets of process variables and responses. It also includes the individual desirability of the process variables as well as the composite desirability. The optimum set of operating parameter for hierarchical nanoporous HY zeolites synthesis is; Aging time = 43.60 h, crystallization time = 64.23 h and NaOH/solid ratio = 6.97 ml/g. The predicted responses are crystallinity = 99.95%, SSA = 442.73, HF = 0.33. This is in consonant with the report of Karami and Rohani

(2009) which states that the aging time varies from 40-120 h depending on the silica and alumina source. The value of composite desirability ranges from 0 to 1. For ideal case, the value tends towards 1, while zero means one or more dependent variables are not within their acceptable limit. The value of the composite desirability obtained is 0.9021. This value is well acceptable because of its closeness to the ideal case.

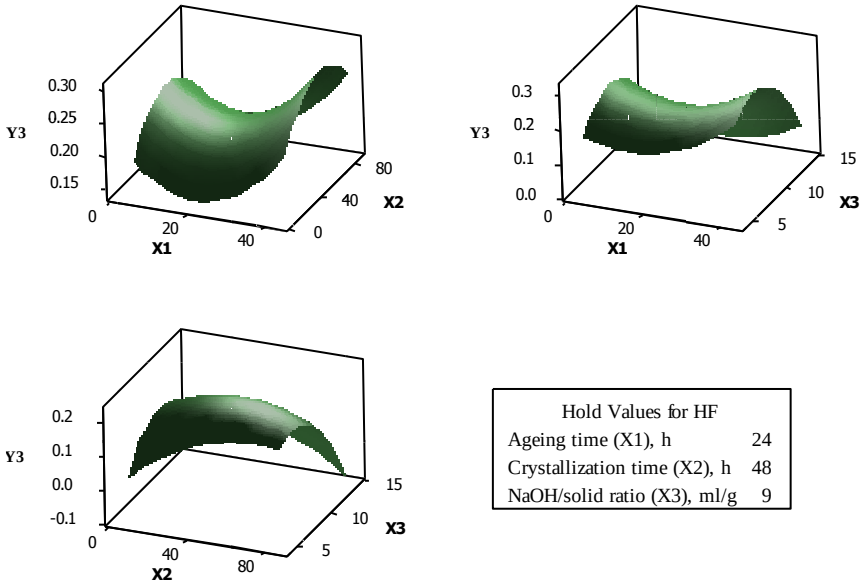

Figure 3.18: Optimization plots for crystallinity, SSA and HF. (where D = composite desirability, d = individual desirability, Targ = target, cur = position of the cursor, y = value of response variables at optimal process variables, High and Low means high and low levels of process variable in the DoE).

3.4 Summary

A novel highly ordered crystalline solid acid catalyst was synthesized from kaolin. This was achieved by thermal activation followed by acid treatment and subsequent NaOH impregnation. The synthesized catalyst exhibits kaolinite with higher XRD peak intensity than the starting kaolin. This shows that its crystallinity is higher than that of the starting kaolin. The value of the crystallinity indices (HI, AGFI and WIRI also attests to this claim. Among all the crystallinity index, WIRI proves the most appropriate because

HPLK8-6M4h is expected to have lower crystallinity than NaPLk8-6M4h. The crystallinity of the product was confirmed by the FTIR spectra because all the disappeared bands after thermal and acid activation reappeared.

Synthesis hierarchical nanoporous HY zeolite was attained by maximizing the hierarchical factor (HF). This is accomplished by varying the aging and crystallization time. The crystallite size of about 68-91 nm and Si/Al ratio ranging from 1.39 to 1.61 were obtained. The aging was varied from 24 – 72 h, and the best aging period is 24 h. Comparative crystallization was done for 16 and 24 h for sample aged for 48 h. Sample HY-2-24 gives lower relative crystallinity but a higher number of acid sites, Si/Al ratio, surface area and HF. Salt incorporation after crystallization also enhanced HF, number of acid sites, relative crystallinity, and preserve the mesopore structure. Therefore, crystalline, mild acid, hierarchical nanoporous HY zeolite with enhanced surface area is achievable by varying the aging and crystallization time.

To describe the effect of aging time (X_1), crystallization time (X_2) and f NaOH solution to kaolin ratio (X_3) on the properties of hierarchical nanoporous HY zeolite, RSM models based on CCD were developed. The responses under consideration are crystallinity (Y_1), SSA (Y_2) and HF (Y_3). X_3 was discovered to be the most significant 0-variance (ANOVA) and optimization study using response surface methodology (RSM) authenticated this observation. All the response models obtained for the HY zeolite synthesis showed *p*-value less than 0.05 and *F*-value higher than the critical value of F except HF. However, the *F*-value for HF was re-computed using mean square based on pure error rather than MSE. This gives *F*-value greater than its critical value. This reveals that the HF model is adequate but showed significant lack-of-fit. The optimum formulation for 99.95% crystallinity, 442.73 m^3/g BET surface area, and 0.33 hierarchy

factor (HF) was 43.60 h aging time, 64.23 h crystallization and 6.97 ml/g NaOH solution to kaolin ratio. Therefore, it is possible to develop an empirical model to predict the formulation for the synthesis of hierarchical nanoporous HY zeolite. Adjustment of all the process variables was found to be significant for C% and SSA while only X_3 has a significant effect on HF.

CHAPTER 4: SYNTHESIS AND APPLICATION OF HIERARCHICAL MESOPOROUS HZSM-5 FOR BIODIESEL PRODUCTION FROM SHEA BUTTER

4.1 Introduction

Depleting global petroleum reserves, greenhouse gas (GHG) emissions and health-related issues are increasing the demand for alternative energy resources. Incidentally, the benign nature, renewability and economic prospects of biodiesel is gaining attention (Ramos *et al*., 2008). This makes biodiesel more advantageous than fossil-diesel. Moreover, it exhibits superior lubricating property, flash point and cetane number thereby, prolonging engine life (Farag *et al*., 2012; Reinoso *et al*., 2014). Biodiesel is obtained from lipid feedstock derived long-chain fatty acid mono-alkyl esters such as algae-derived oil, animal fats and vegetable fats and oils. One of such source is shea butter. Shea butter is an ivory colored fat extracted from shea nut of sub-Saharan African shea tree (Vitellaria paradoxa) with high free fatty acid (FFA) content (Glew *et al*., 2014). The FFA contents are majorly of oleic acid and steric acid. Shea butter enjoyed wide utilization in confectionery and cosmetic industry. This leads to rapid growth in shea market, about 350,000 tons of shea export in the past decade (Lovett, 2010). Table 4.1 presents the properties of crude shea butter.

Table 4.1: Properties of crude shea butter (Enweremadu *et al*., 2010).

Properties	Values
Density (kg m^{-3}) at 25 ^{o}C	0.91
Viscosity (mm^2 s^{-1}) at 38 ^{o}C	39.98
Acid value	3.62
Iodine value (I_2 g 100 g^{-1})	59.5
Saponification value (mg KOH g^{-1})	190
Peroxide value (meq O_2 kg^{-1})	12.15
Water content (wt%)	0.037
Fatty acid composition (%)	
Palmitic (C16:0)	5.4
Stearic (C18:0)	35.7
Oleic (C18:1)	49.6
Linoleic (C18:2)	7.8
Arachidic (C20:0)	1.3

There are four strategies for biodiesel production; these include transesterification, thermal cracking, micro-emulsions, and hydrodeoxygenation. The most popular of these strategies is transesterification (Farag *et al*., 2012). Generally, transesterification proceeds with the aid of homogeneous basic catalysts such as KOH, NaOH and other hydroxides (Carrero *et al*., 2011). The preference of homogeneous basic catalysts to their acidic counterparts is basically due to their better activity especially for triglycerides with low free fatty acid (FFA) content (Farag *et al*., 2012). However, transesterification with homogeneous catalysts have various drawbacks. These include catalyst separation to purify the biodiesel, soap formation and separation of glycerol and water quenching which requires a large amount of water. These generates a large amount of wastewater (Intarapong *et al*., 2012; Reinoso *et al*., 2014; Xie *et al*., 2006). Solid acid catalyzed transesterification is a promising route that could overcome these shortcomings because of ease of separation. However, some authors reported the limitations of solid acid catalysts such as leaching and diffusion limitations (Carrero *et al*., 2011; Helwani *et al*., 2009; Reinoso *et al*., 2014; Zabeti *et al*., 2009). Consequently, synthesis of mesoporous stable solid acid catalysts is necessary to avoid leaching of the active sites, which leads to catalyst deactivation.

Zeolites are crystalline microporous aluminosilicate minerals, which exhibit remarkable attributes such as high surface area and selectivity strong acidity. This engenders their wide range of utilization in process industries (Čejka *et al*., 2012; Konno *et al*., 2013). Moreover, ZSM-5 zeolites possess suitable pore structure for biomass conversion and bio-oil valorization into biodiesel because it has internal pore space and controlled pore openings that reduce deactivation (Foster *et al*., 2012; Yu *et al*., 2012). Nevertheless, because ZSM-5 zeolites exhibit steric hindrance, they are less suitable for conversion of bulky reactants. Conversion of bulky molecules can only occur at the zeolite matrix, which constitutes a smaller percentage of ZSM-5 zeolite. Further, the matrix lacks enough active sites for effective conversion of bulky molecules (Yu *et al*., 2012). Hierarchical ZSM-5 zeolite (HMZeol) is a choice catalyst that could enhance conversion of bulky reactants and simultaneously produce a high yield of aromatics (Bakala *et al*., 2006; Ishihara *et al*., 2012). While the auxiliary mesoporosity helps to enhance conversion, the microporosity provides the active site (Yu *et al*., 2012). Therefore, it is imperative to investigate a suitable method for synthesis of mesoporous zeolite. This study explored the use of HMZeol synthesized by desilication of conventional ZSM-5 for biodiesel production from shea butter, a triglyceride with a high value of FFA.

4.2 Experimental

4.2.1 Materials

R&M Chemicals Sdn. Bhd., Malaysia supplied the NaOH pellet, NH_4NO_3 (99.0%), MeOH and ZSM-5 zeolite. Crude shea butter was purchased from Lagos, Nigeria. The study utilized the materials without further purification.

4.2.2 Methods

Initially, 30 g of reference ZSM-5 was mixed with 300 mL aqueous solutions of NaOH for 2 h at 70 °C. The mixture was filtered under vacuum, washed with deionized water and dried overnight at 100 °C. The sample was further transformed to hydronium form with 0.2 M NH_4NO_3 solution at 80 °C for 24 h before drying overnight at 100 °C and calcination at 550 °C for 5 h. The synthesized samples were designated nHMZeol, where n is the molar concentration of aqueous NaOH solution. For instance, the sample treated with 0.3 M NaOH solution is 0.3HMZeol.

4.2.3 Catalyst characterization

The Si/Al ratio of the samples were determined by x-ray fluorescence (XRF). X-ray diffractometer (Seifert X-ray Diffractometer JSO 2002) recorded XRD pattern for all the samples the using nickel-filtered Cu Kα radiation (λ = 1.544 Å) ranging from 5.018 to 69.966° (2) with a step size of 0.026°. The Nitrogen adsorption/desorption analysis was carried out using surface area and porosity analyzer (Micrometrics ASAP 2020) under analysis bath Temperature of 77.350 K. SEM images were obtained with an SEM, FEI Quanta 400 FE-SEM microscope, using an accelerating voltage of 20 kV and 20 mA current. All the samples were coated with 5 nm Pt prior to the analysis to enhance the electrical conductivity. Further, the strength and number of acid sites of the samples were determined by ammonia temperature programmed desorption (NH_3-TPD) analysis using Chemosorp 2720 apparatus.

4.2.4 Valorization of shea butter

Valorization of shea butter proceeded over the synthesized HMZeol by transesterification. The reaction occurred in excess methanol in airtight stainless steel autoclave reactor. The catalyst concentration, temperature, and methanol/oil molar ratio

were varied to optimize the process. The reaction proceeded at 150 ^{o}C and 200 ^{o}C, 600 rpm with methanol/oil molar ratio of 5:1 to 20:1 and the catalyst amount was from 1 to 3 wt %. On completion, the glycerol was removed using separating funnel and vacuum pump. The samples are designated nHMZeol-T-5-m_x where T is the reaction temperature, m is the methanol/oil ratio and x is the catalyst amount (wt %). Further, the samples were analyzed with thermogravimetric analysis (TGA) using TGA Q500 to determine the shea butter conversion. TGA is a cheap and fast method for quantitative analysis of a mixture of materials (Chand *et al*., 2009; Farag *et al*., 2012). Biodiesel conversion with TGA is comparable with GC method (Farag *et al*., 2012). Chand *et al*. (2009) investigated the suitability of TGA compared to proton NMR, HPLC and GC method for determination of biodiesel composition in transesterification reaction mixtures. They reported that the TGA results are comparable to those of proton NMR, HPLC, and GC. The effectiveness of TGA method relative to 1HNMR method is within ±1.5%. The TGA analysis of shea butter and the synthesized biodiesels was done by filling the crucible with a specific sample amount. The operating temperature was set to 50-500 ^{o}C with the heating rate of 20 ^{o}C/min in the presence of nitrogen. Fourier transform infrared spectroscopy (FTIR) analysis of the samples was carried out using a Bruker Tensor 27 FT-IR in the range of 700 cm^{-1} to 4000 cm^{-1} at 4 cm^{-1} resolution. Determination of higher heating value (HHV) was done using an oxygen bomb calorimeter (Parr 6100) according to ASTM M240 (2009). Anton Paar density meter (DMA 4500 M USA) and Brookfield (USA) DV-E viscometer were used in the measurement of sample density and viscosity respectively. Further, determination of elemental composition was done with the aid of Perkin Elmer 2400 Series II CHNS analyzer (Perkin Elmer Sdn Bhd, Selangor, Malaysia).

4.2.5 Influence transport phenomena on the catalysts

Investigation of transport influence in heterogeneous catalysis is of vital importance especially in a system that involve transfer of bulky molecules. This was investigated by using turnover frequency (TOF) value to comparatively check the activity of the catalyst. TOF is defined as the moles reacted per second per surface mole of the active species (Madon *et al*., 1982). It quantifies the activity of the active center for catalytic reaction under a specific reaction condition by a number of molecules converted per unit time (Boudart, 1995).

$$TOF = \frac{M_{actual}}{t \times f_m \times m_{cat}} \quad (4.1)$$

Where M_{actual} is the amount in moles of biodiesel produced; t is the reaction time; f_m is the amount of acid sites on the surface and m_{cat} is the mass of catalyst.

4.3 Results and discussion

4.3.1 Catalysts characterization

Table 4.2 presents the chemical compositions and Si/Al molar ratio of ZSM-5 and that of the synthesized HMZeol from XRF analysis. Figure 4.1 shows the XRD patterns of the synthesized catalysts with standard XRD peak positions. The entire samples spectrum showed a slight decrease in intensity of the characteristic peaks (~8° and 23-25°) of ZSM-5. This is an indication that the MFI framework of ZSM-5 is intact. However, the decrease in intensity shows a decrease in crystallinity. The crystallinity decreases with increase in the concentration of NaOH used for the desilication.

The acidity of the samples were measured by ammonia TPD analysis and the results are presented in Table 4.3. Generally, both acid density and strength decreased after desilication. This is evident in 0.3HMZeol and 0.4HMZeol samples with 2.96 mmol/g

and 2.75 mmol/g respectively. The strong acid strength exhibited by the parent zeolite around 435 °C disappeared after desilication. Both HMzeol samples exhibited shoulder around 300 °C. This shows that synthesized products possessed mild acidity, which is capable of suppressing deactivation.

Table 4.2: Catalyst composition

Sample	Si	Al_2O_3	Si/Al	Na (wt%)
ZSM-5	31.76	1.47	20.76	0.00
0.3HMZeol	27.45	1.90	12.51	0.78
0.4HMZeol	31.12	2.95	10.13	1.55

Table 4.3: Textural parameters of ZSM-5 and the synthesized HMZeol.

Sample	S_{BET} (m^2/g)	S_{micro}[a] (m^2/g)	S_{meso}[a] (m^2/g)	V_{total}[a] (cm^3/g)	V_{mic}[a] (cm^3/g)	D_{meso} (nm)	Tpeak (°C)	Acidity (mmol/)g
ZSM-5	385.20	356.54	28.66	0.1540	0.1383	1.60	219.7, 435.0	3.8085
0.3HMZeol	374.88	240.23	134.65	0.367	0.1114	3.92	210.0	2.9635
0.4HMZeol	340.36	215.01	125.35	0.3938	0.0998	4.63	200.0	2.7539

[a] Calculated from the t-plot curve.

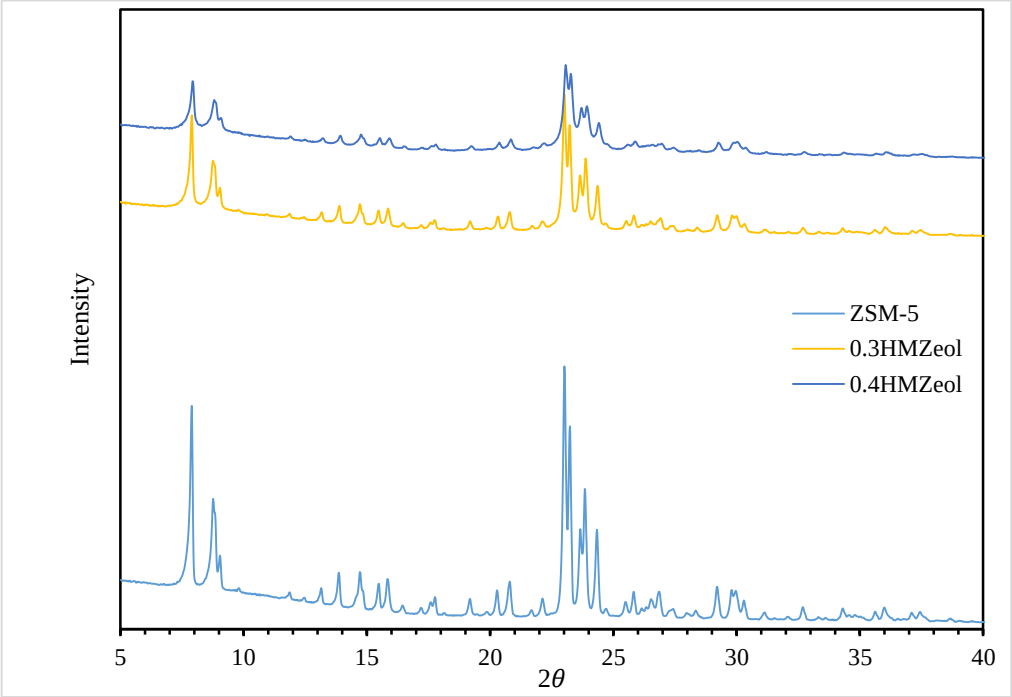

Figure 4.1: XRD pattern of the starting ZSM-5 and the synthesized HMZeol.

Table 4.3 also presents the results of the surface area and porosity analysis from N_2 adsorption/desorption analysis. BET model gives the specific surface area (SSA) and the pore size distribution of the samples (Figure 4.2). The result shows that desilication with 0.3M NaOH slightly decreases the surface area but increases the external surface area (ESA), pore volume and pore size of the zeolite. Further increase in desilication leads to significant decrease in SSA but with a subsequent increase in pore volume and pore size. This is due to collapse in the mesopore walls, which increases mesoporosity. Moreover, the reference ZSM-5 experienced a noticeable increase in ESA upon desilication. In fact, the hierarchical mesoporous ZSM-5 had almost 37% of the total SSA as ESA.

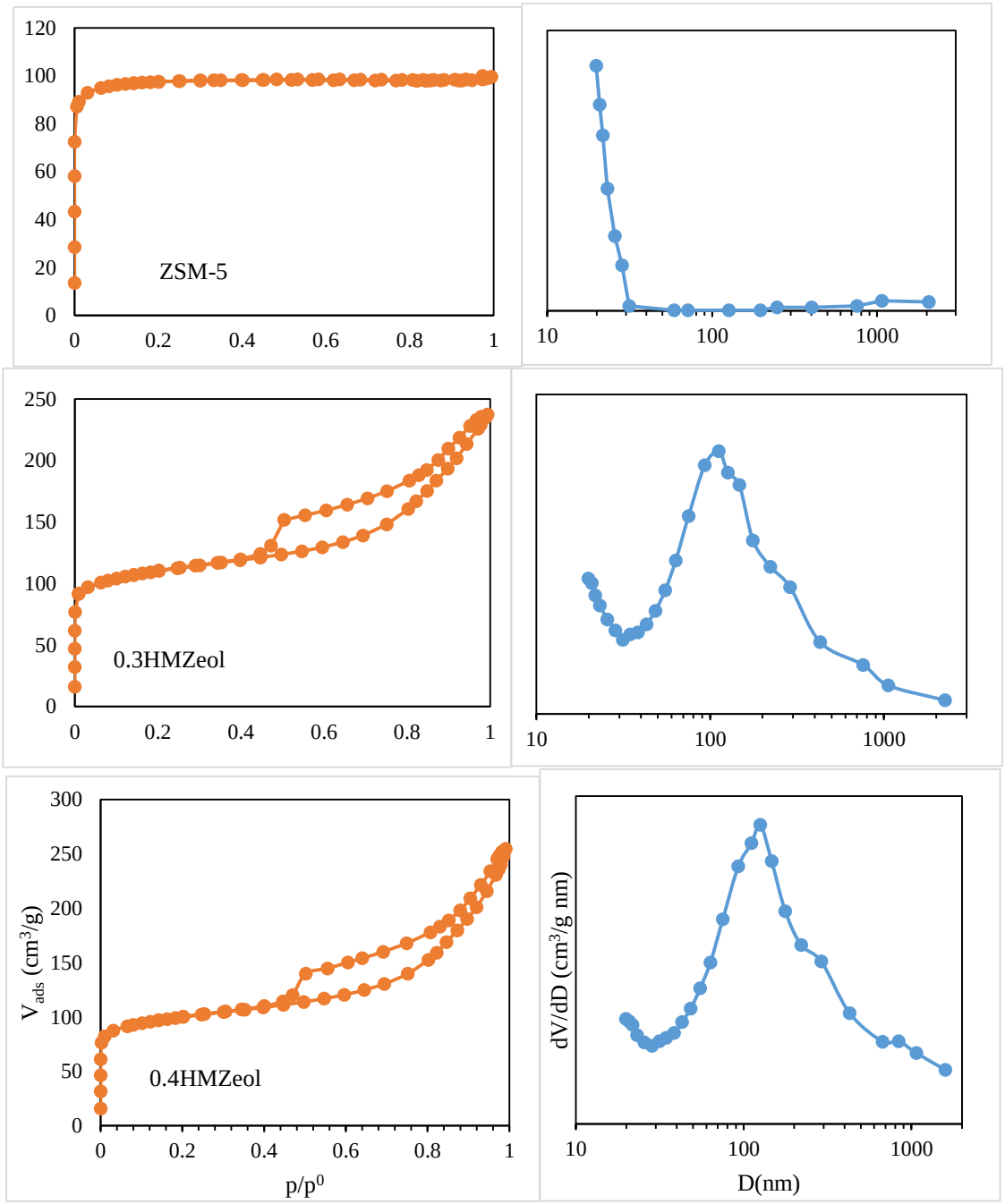

Figure 4.2: Isotherms of nitrogen adsorption and pore size distribution of parent and modified zeolites.

The SEM images in Figure 4.3 shows the morphology of the reference ZSM-5 and the modified zeolite samples. The modified samples maintain the same surface structure as the reference ZSM-5. However, the surface of the modified samples crystals are some way rough and void.

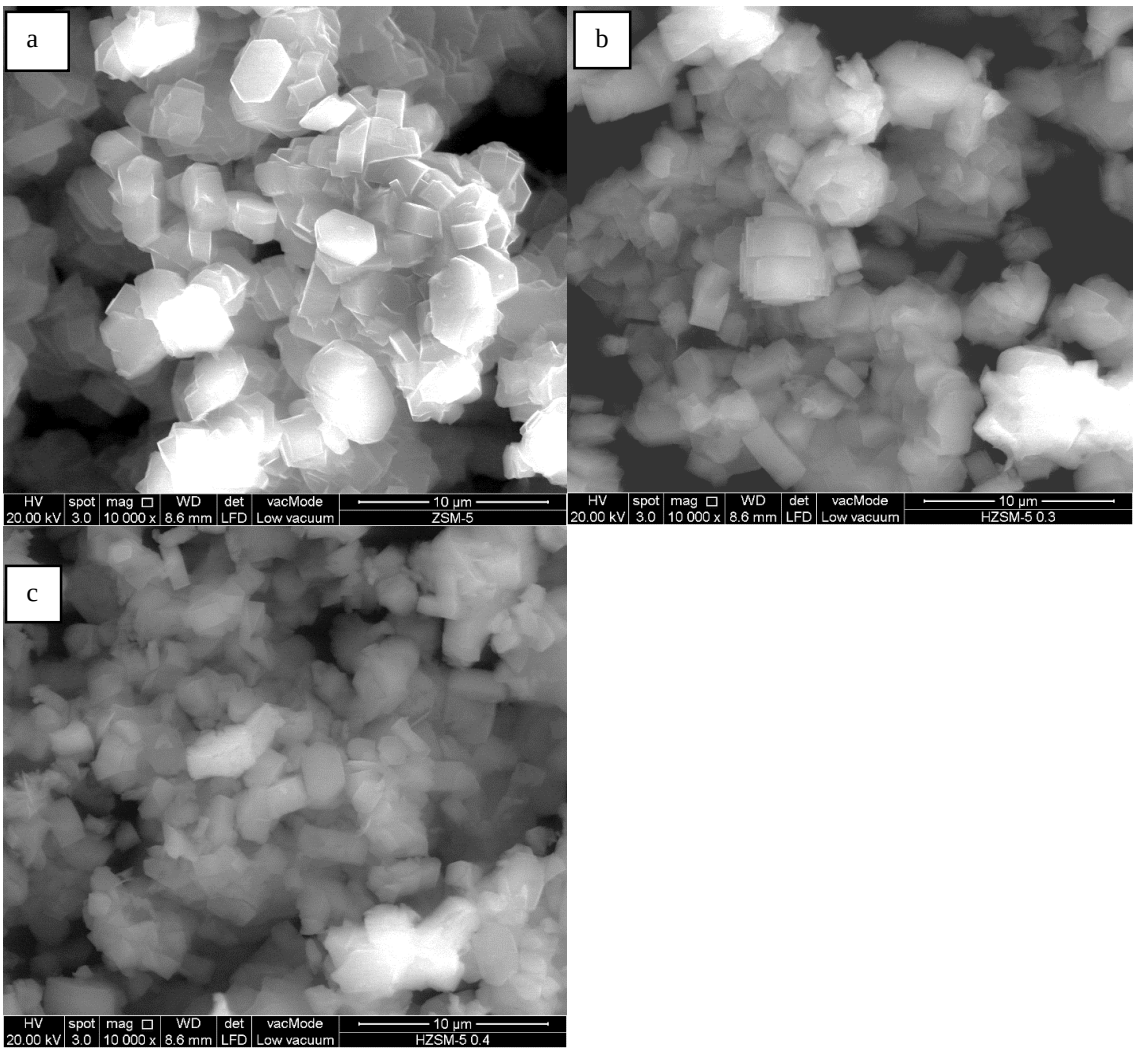

Figure 4.3: SEM images of parent (a) and modified zeolites ((b) 0.3HMZeol and (c) 0.4HMZeol).

4.3.2 Thermogravimetric analysis of shea butter

Figure 4.4 shows the TGA of shea butter. The plot presents weight percent as a function of sample temperature. Shea butter exhibited small weight loss between 170 and 220 ^{o}C, which corresponds to breaking down of unsaturated bond. Further, remaining shea butter starts to decompose from 300 and ends at 470 ^{o}C.

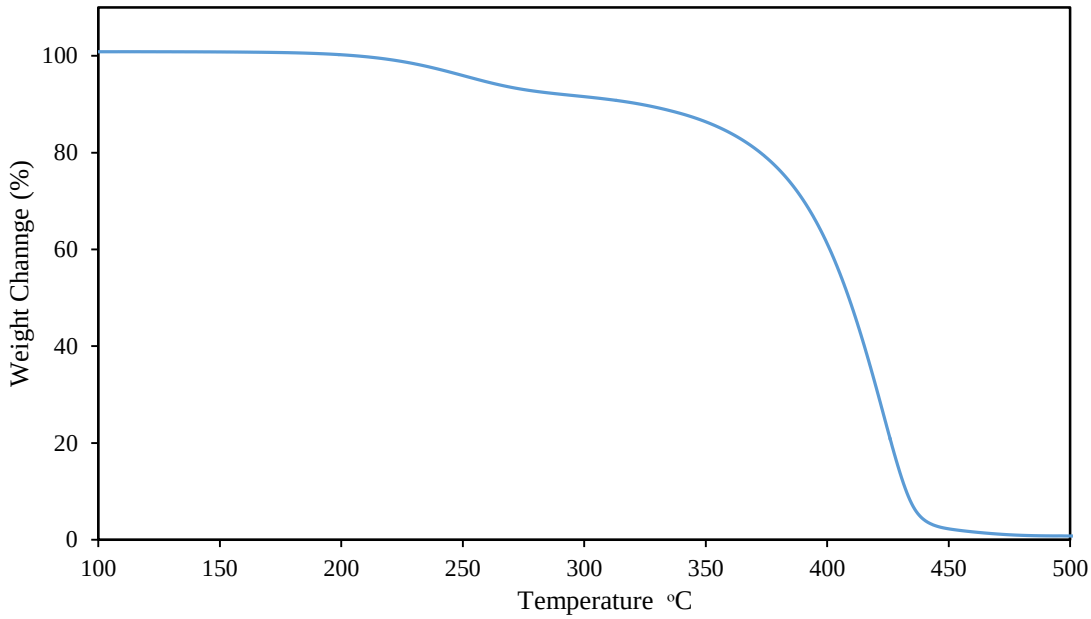

Figure 4.4: TGA curve of the shea samples.

4.3.3 Catalytic activity

To identify the most promising of these heterogeneous catalysts, all the catalytic materials were screened under the same reaction conditions. The optimal catalyst was selected based on biodiesel yield. Table 4.4 presents the experimental results. From the table it is obvious that the parent ZSM-5 showed the lowest catalytic activity with biodiesel yield of 72.13% after 12 h reaction with methanol/oil molar ratio of 5:1 and 1% catalyst loading at 200 °C. However, the synthesized hierarchical mesoporous zeolites (HMZeol) showed superior biodiesel yield due to their mesopore advantage. For instance, at methanol/oil molar ratio of 5:1 and 1% catalyst loading over 0.3HMZeol, a biodiesel yield of 79.21% was obtained, and a yield of 82.12% was attained with 0.4HMZeol catalyst after 12 h. Based on the above results, HMZeol catalysts showed greater potential for biodiesel production and, therefore, were subsequently studied.

Table 4.4: Effect of operating parameters on shea butter conversion to biodiesel.

Catalyst	Catal. w.%	Temp. (°C)	MeOH/oil	Time (h)	Yeild (%)
ZSM-5	1	200	5	3	46.05
ZSM-5	1	200	5	6	57.49
ZSM-5	1	200	5	12	72.13
ZSM-5	1	200	5	18	86.17
ZSM-5	2	200	5	3	32.09
0.4HMZeol	1	200	5	3	74.17
0.4HMZeol	1	200	5	6	78.45
0.4HMZeol	1	200	5	12	82.12
0.3HMZeol	1	200	5	3	41.84
0.3HMZeol	1	200	5	6	56.1
0.3HMZeol	1	200	5	12	79.21
0.3HMZeol	2	200	5	3	54.41
0.3HMZeol	2	200	10	3	35.51
0.3HMZeol	1	160	10	3	14.34
0.3HMZeol	0.5	200	5	3	38.48
0.3HMZeol	1	200	10	3	51.15
0.4HMZeol	0.5	200	5	3	41.29
0.4HMZeol	2	200	5	3	45.55
0.3HMZeol	1	200	5	18	82.82
0.4HMZeol	1	200	5	18	83.36
0.3HMZeol	1	180	10	3	31.68

4.3.4 Effect of reaction parameters on biodiesel yield

The 0.3HMZeol catalyst was tested for biodiesel yield at 10:1 methanol/oil molar ratio, 1 wt % catalyst varying temperature from 160 to 200 ^{o}C. The obtained result showed that the biodiesel yield was less than 20% at 160 ^{o}C. However, the yield increased rapidly to 51.15% upon increase to 200 ^{o}C (Figure 4.5). The increase in yield with an increase in reaction temperature was due to increase in reaction rate as well as an increase in the solubility of methanol in shea butter (Xie *et al*., 2011).

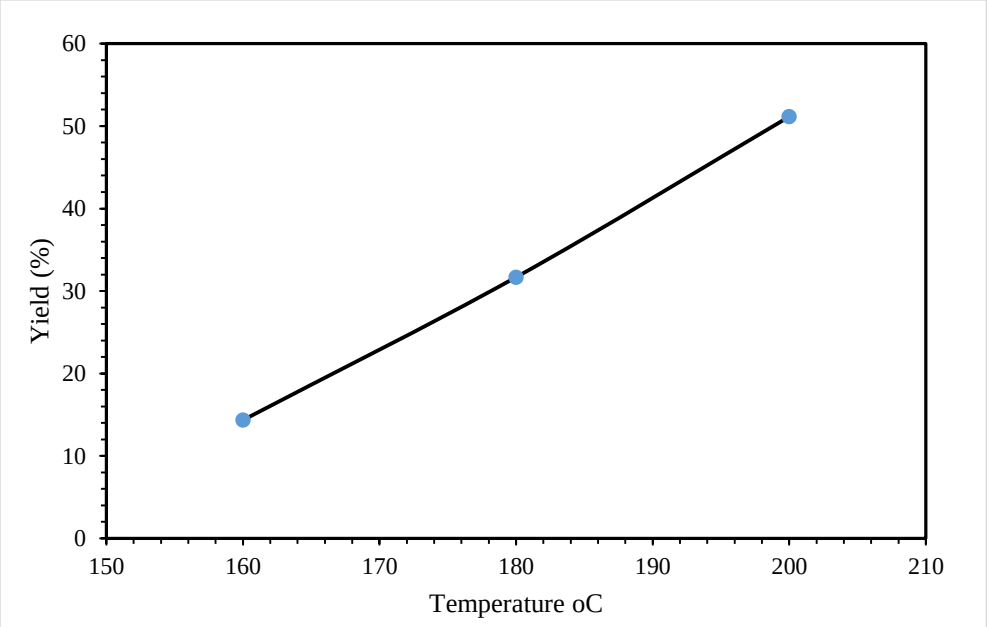

Figure 4.5: Effect of reaction temperature on biodiesel yield over 0.3HMZeol catalyst. Reaction conditions: catalyst loading, 1 wt%; reaction time 3 h; methanol/oil molar ratio, 5:1.

Stoichiometrically, the ratio of methanol to oil required for transesterification is 3:1. However, the use of excess methanol is essential to shift the equilibrium of the reaction to favor the desired product. The influence of methanol/oil molar ratio was studied over the 0.3HMZeol catalyst. Ratio 5:1 gave 41.84% biodiesel yield after 3 h with 1 wt% catalyst, on increasing the ratio to 10:1 the yield increased to 51.15%. The excess methanol were separated from the product by distillation, and glycerol was separated using centrifuge and follow by decantation.

The effect of catalyst loading was studied for both 0.3HMZeol and 0.4HMZeol. Methanol/oil molar ratio of 5:1 and 3 h reaction time at 200 ^{o}C was used varying the catalyst loading from 0.5 to 2 wt%. Figure 6.6 presents the effect of catalyst loading on biodiesel yield. For 0.3HMZeol, biodiesel yield increased from 38.48 to 54.41% as the catalyst loading increases from 0.5 to 2 wt %. This is attributed to increased contact area between the reactants and the catalyst active sites. However, the optimum loading of

0.4HMZeol is 1 wt%. Increasing the loading from 1 to 2 wt% leads to decrease in biodiesel yield from 74 to 45.55%. Presumably, the decrease in the biodiesel yield at 2 wt% catalyst loading results from higher Na loading (1.55 wt%) compared to that of 0.3HMZeol (0.78 wt%). This is because the basicity of the catalyst increases as the Na loading increases, which is detrimental to shea butter conversion due to its high free fatty acids (FFA) content (2.279%). Naik *et al*. (2008) reported that basic catalysts show inferior catalytic activity when the FFA content of the oil is beyond 2%. The excess FFA could react with the alkaline content of the catalyst to form soap and water rather than methyl ester once the process exceeds the neutralization limit (Lotero *et al*., 2005; Ma *et al*., 1999). This also facilitates a formation of gel/emulsion-like product thereby hindering glycerol separation. Therefore, the optimal loading of 0.4HMZeol catalyst was maintained at 1 wt%.

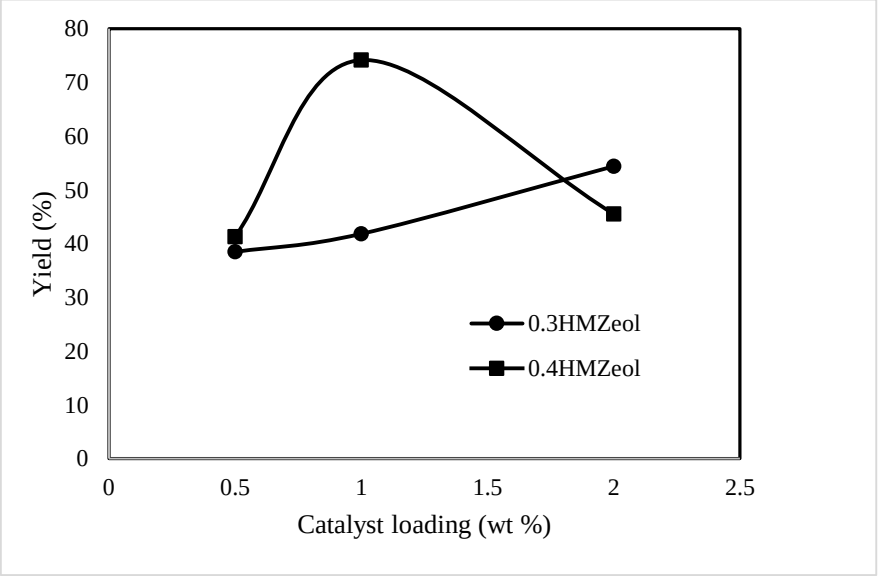

Figure 4.6: Effect of catalyst loading on biodiesel yield over HMZeol catalysts. Reaction conditions: reaction temperature, 200 °C; reaction time 3 h; methanol/oil molar ratio, 5:1.

Figure 4.7 presents the effect of reaction time on biodiesel yield. The parent ZSM-5 and the synthesized HMZeol catalysts were tested varying the reaction time from 3 to 18 h

using 1 wt% catalyst loading, methanol/oil ratio of 5:1 at 200 °C. For the parent ZSM-5, the result showed that biodiesel yield increased rapidly with increase in reaction time to optimal time of 18 h. The reaction rate was constantly high from 6 to 18 h as the biodiesel yield increased from 57.49 to 86.17%. The lower activity at reaction time of 3h was due to diffusion limitation, which slows the reaction rate. However, the parent ZSM-5 took advantage of its strong acid strength at higher reaction time to give high biodiesel yield over the same period. The biodiesel yield also increased rapidly with increase in reaction time for 0.3HMZeol catalyst until 12 h (79.21%). Further increase to 18 h resulted in small increase in the yield to 82.82%. Therefore, the suitable reaction time for shea butter methanolysis over 0.3HMZeol is ca. 14 h. Similarly, 0.4HMZeol catalyst showed the highest yield of 74.17% at 3 h reaction time, which increased to 78.45% when the reaction time was extended to 6 h. The reaction rate reduced as the reaction time increased from 6 to 12 h and there was no significant increase in the biodiesel yield when the reaction time was extended from 12 to 18 h. The outstanding performance of the 0.4HMZeol catalyst is ascribed to its large BET pore size (4.63 nm).

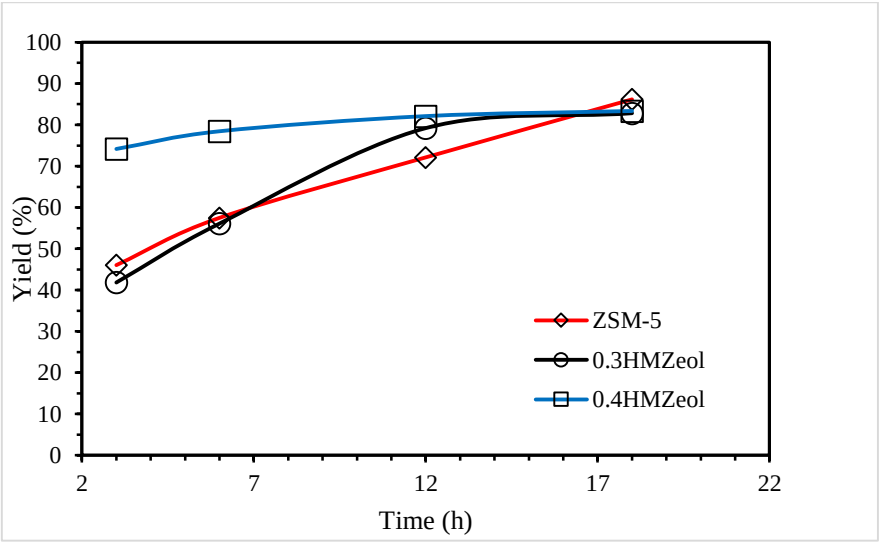

Figure 4.7: Effect of catalyst loading on biodiesel yield over the parent ZSM-5 and HMZeol catalysts. Reaction conditions: reaction temperature, 200 °C; catalyst loading, 1 wt%; methanol/oil molar ratio, 5:1.

Biodiesel yield increases with an increase in methanol/oil molar ratio and catalyst loading for 0.3HMZeol. The maximum yield was obtained with 0.3HMZeol using 10:1 methanol/oil molar ratio, 2 wt % catalyst at 200 ^{o}C while ZSM-5 gave the least at the same condition. However, 0.4HMZeol gave the overall maximum conversion (74.01%) at 5:1 molar ratio, 200 ^{o}C and 1 wt% catalyst loading. Further increase in these parameters for 0.4HMZeol leads to decrease in conversion. The abnormal behavior exhibited by 0.4HMZeol is probably because of the severe desilication of the parent material. This is because desilication leads to decrease in Si/Al molar ratio, which culminate in a severe reduction of the catalyst acidity thereby increasing its basicity. This result is corroborated by the report of Ma *et al*. (1999) that basic catalysts require lower methanol to oil ratio than acid catalyst. Moreover, higher methanol/oil molar ratio could increase the glycerol solubility thereby making it difficult to separate from the methyl ester. This explains the observed trend of methanol/oil molar ratio beyond 5:1 over 0.4HMZeol at 200 ^{o}C for 5 h, which leads to decrease in biodiesel yield.

Lotero *et al*. (2005) reported that there is a significant decrease in conversion when the FFA content is beyond 2% for basic catalysts. The excess FFA could react with the alkaline content of the catalyst to form soap rather than methyl ester once the process exceeds the neutralization limit (Dhanasekaran *et al*., 2014). This facilitates formation of gel/emulsion-like product, which hinders glycerol separation. This becomes clear why increasing the catalyst amount to 3 wt% of 0.4HMZeol leads to decrease in conversion.

4.3.5 Influence of transport phenomena on the catalysts

Table 6.5 shows the activity with respect to TOF for the parent ZSM-5 and the desilicated samples. The optimal activity was observed with sample 0.4HMZeol followed by 0.3HMZeol. This attributed to their mesoporosity. The shows that sample 0.4HMZeol

exhibits little or no mass transfer limitation as compared to other samples. Apart from mesoporosity, the outstanding performance of 0.4HMZeol could also be attributed to Na (wt%) loading due to desilication.

Table 4.5: TOF showing the activity of ZSM-5 and the synthesized HMZeol.

Catalyst	ZSM-5	0.3HMZeol	0.4HMZeol
TOF (s^{-1})	0.0041	0.0048	0.0091

4.3.6 Biodiesel Confirmation

FTIR techniques confirmed biodiesel yield fingerprint. Figure 4.8 presents the spectrum of shea butter and those of biodiesel from the two HMZeol catalysts at varying parameters. The spectrum exhibits strongly stretched alkane groups at 2914.68 cm^{-1} and strong vibration stretching of carboxylic at 1731.63 cm^{-1}. Then C-O joined with a carboxylic group at 1239.32 and 1174.60 cm^{-1}. Further, strongly stretch alkane groups were observed at 2914.68, 2848.80 and 1470.85 cm^{-1}. The HMZeol spectrum exhibited symmetric and asymmetric carboxylic group strong vibration stretching from 3000 to 2500 cm^{-1} as well as alcohol bonded with hydroxyl (broad O-H stretching) between 3500 and 3300 cm^{-1} including phenols and alcohol group. Further, the spectrum also shows ketones, aldehyde along with a carboxylic group and strongly stretch ester group between 1470 and 1744 cm^{-1} band. Then C-O joined with carboxylic group and strongly stretch ester group appeared around 1029-1245 cm^{-1}. Further, strongly stretch alkane groups also appeared around 1363-1463.12 cm^{-1}.

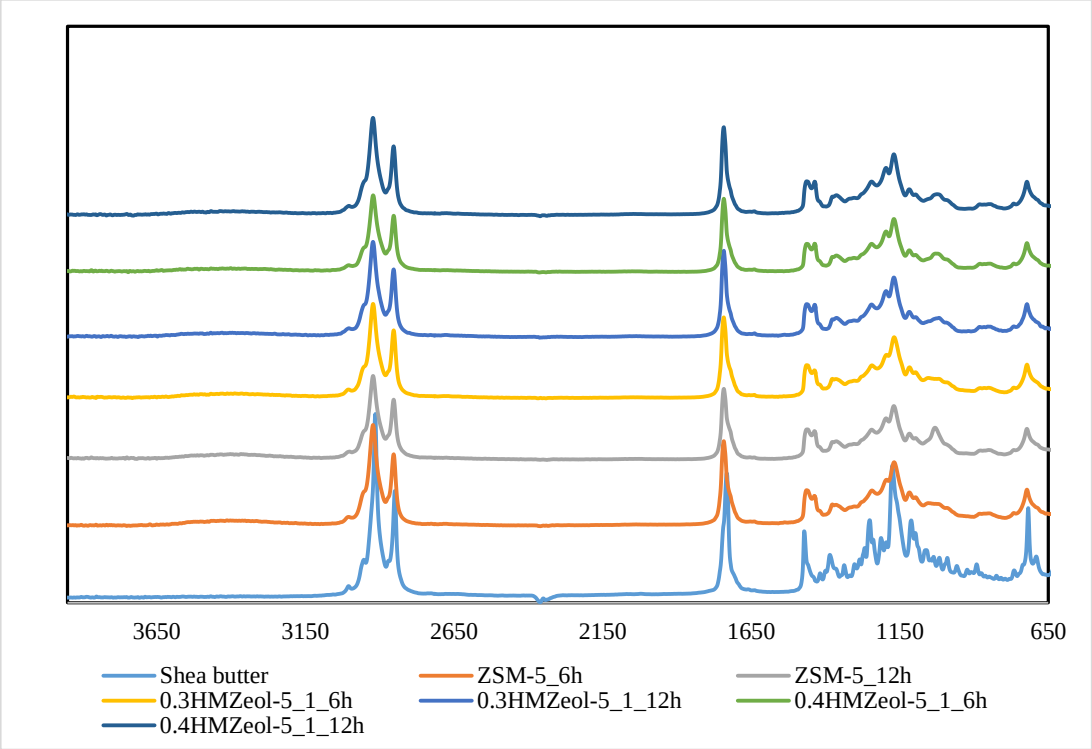

Figure 4.8: FTIR spectrums comparison between shea butter and synthesized biodiesel samples using methanol/ oil ratio of 5:1 and catalyst loading of 1 wt% at 200 ºC for 6 - 12 h.

The broad O-H stretching between 3500 and 3300 cm^{-1} could be ascribed to the strength and density of Bronsted acid sites on the catalysts. The reference ZSM-5 possesses strong Bronsted acid sites, which became weak upon desilication. The figure shows that transesterification over ZSM-5 shows the highest intensity between 3500 and 3300 cm^{-1}. Furthermore, an increase in catalyst amount also increases the intensity. This corroborates with the reports of Farag *et al*. (2012).

The properties of the sample produced over 1 wt% 0.4HMZeol with MeOH/oil ratio of 5 at 200 °C for 12 h in Table 6.6 shows that shea butter is a viable feedstock for high-quality biodiesel. The sample possesses higher HHV and lower oxygen content compared to the report of Hoekman *et al*. (2012) and Fukuda *et al*, (2001). Although, the cost of shear butter is relatively higher than most reported feedstock like palm oil and jatropha oil, the

higher unsaponifiable fraction of shea butter as well as higher product quality gives it an edge. Further, high biodiesel yield was attained with a low molecular weight of alcohol and a small amount of catalyst, thereby reducing the cost of production.

Table 4.6: Properties of biodiesel sample produced with 0.4HMZeol.

Properties	**Values**
Weight of shea butter fed (g)	21.14
Weight of methanol fed (g)	12.02
Weight of biodiesel produced (g)	17.36
Biodiesel Yield (%)	82.12
Density (kg m^{-3}) at 25 ^{o}C	0.86
Viscosity (mm^2 s^{-1}) at 38 ^{o}C	3.38
HHV ($MJkg^{-1}$)	40.01
Carbon	77.33
Hydrogen	12.82
Oxygen	9.76

4.3.7 Catalyst reusability

Reusability of 0.4HMZeol was studied using methanol/ oil ratio of 5:1 and catalyst loading of 1 wt% at 200 ^{o}C for 3 h to ascertain its durability and economic viability. Spent 0.4HMZeol sample was regenerated by rinsing with n-hexane to remove off the remaining product on it. The washed sample was dried overnight to remove physically absorbed water.

The regenerated sample was reused for the next 4 cycles of reaction (Figure 4.9).

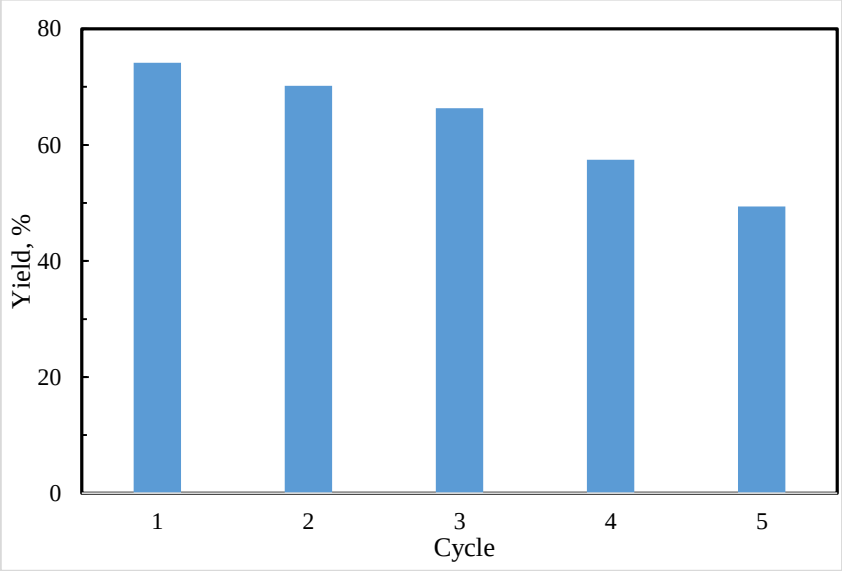

Figure 4.9: Reusability of hierarchical mesoporous ZSM-5 on transesterification of shea butter.

4.4 Summary

Desilicating conventional ZSM-5 with an aqueous solution of NaOH produced mesoporous HMZeol. The technique enhances the matrix area, pore size, and mesopore volume of the zeolite. These ensure the suitability of the synthesized hierarchical material for conversion of large molecules of shea butter into biodiesel. A comparative study showed that HMZeol exhibits higher catalytic activity than the parent ZSM-5. The optimum operating condition within the parameters investigated are 5:1 methanol/oil molar ratio, 1.0 wt% catalyst, 12 h reaction time at 200 ^{o}C over 0.4HZSM-5. This gave biodiesel yield of 82.12%. This is a clear evidence that hierarchical mesoporous HMZeol prepared by desilication of conventional ZSM-5 zeolite is a promising catalyst for biodiesel production from shea butter.

CHAPTER 5: SYNTHESIS AND CHARACTERIZATION OF SULFATED HIERARCHICAL NANOPOROUS HY FOR EFFICIENT TRANSESTERIFICATION OF SHEA BUTTER

5.1 Introduction

The use of animal fats or vegetable oils/fats, with short-chain alcohols for production of biodiesel is emerging as a smart alternative to fossil diesel to proffer solution to petroleum shortage, greenhouse gas emission and increasing energy demand (Ramos *et al*., 2008). Biodiesel is normally produced with the aid of homogeneous basic catalysts such as KOH, NaOH and other hydroxides (Carrero *et al*., 2011). The preference of homogeneous basic catalysts to their acidic counterparts is basically due to their better activity especially for triglycerides with low free fatty acid (FFA) content (Farag *et al*., 2012). Likewise, homogeneous acids like H_2SO_4 and HCl are more suitable for triglycerides with high FFA content. However, the use of homogeneous catalysts are challenged in catalyst separation, long reaction time, corrosion, soap formation and separation of glycerol and water quenching which requires a large amount of water. These generate a large amount of wastewater (Reinoso *et al*., 2014; Xie *et al*., 2006; Intarapong *et al*., 2012; Suarez *et al*., 2007). Heterogeneous catalysts are suitable alternatives because of their ease of separation from the reaction medium, corrosion reduction and reusability (de Almeida *et al*., 2008). Their development could aid process design for a continuous production of biodiesel to minimize purification costs. However, they gives rather lower biodiesel yield due to drawbacks such as leaching and diffusion limitations (Reinoso *et al*., 2014; Carrero *et al*., 2011; Zabeti *et al*., 2009; Helwani *et al*., 2009).

For better performance in transesterification system, an efficient heterogeneous catalyst needs mesopores to minimize steric hindrance, higher acid strength, and density as well

as thermal and hydrothermal stability to minimize poisoning and leaching. Solid superacids are promising catalysts for transesterification process to produce biodiesel. Chemists synthesized them in both solid and liquid forms and their amazing acid strength makes it easier to carry out difficult reactions under satisfactory experimental conditions. For instance, Misono and Okuhara (1993) reported that activation of alkanes proceeds at low temperatures over superacid catalyst. Conventional superacids such as liquid HF and AlCl [sub 3] are hazardous to the environment contrary to solid superacids, which are more attractive for industrial utilization. Solid superacid catalysts are indeed more environmentally benign in many industrial processes (Misono & Okuhara, 1993).

Recently, several authors have tested sulfated metal oxide as solid superacid catalysts in transesterifying triglycerides and esterifying FFA (de Almeida *et al*., 2008; Furuta *et al*., 2004, 2006; Jiputti *et al*., 2006; Lopez *et al*., 2007). Ordered mesoporous silicas and aluminosilicates such as MCM-41, HMS, SBA-15 and USY zeolite are viable support due to their high specific surface area (SSA) and hierarchical mesoporosity (Testa *et al*., 2010, 2014; Venezia *et al*., 2011; Usai *et al*., 2013; Zhou *et al*., 2013). The major problems attributed to such materials are hydrophobicity and lower catalytic activity as compared to microporous zeolites (Ryoo *et al*., 1997). However, functional groups that are more reactive are added to improve their surface hydrophobicity as well as reactivity. Similarly, several authors have investigated the use of sulfated silicas as catalysts for esterification and transesterification (de Almeida *et al*., 2008; Testa *et al*., 2010; Cano-Serrano *et al*., 2003). Testa *et al*. (2013) comparatively studied glycerol acetylation over different solid acid catalysts. They reported that mesoporous sulfated silica showed superior performance with respect to reactivity.

There is presently no literature that describes the use of sulfated hierarchical nanoporous HY zeolites from kaolin as a superacid catalyst for effective transesterification of shea butter. Shea butter is an ivory colored fat extracted from shea nut of sub-Saharan African shea tree (Vitellaria paradoxa) with high free fatty acid (FFA) content (Glew and Lovett, 2014). The FFA contents are majorly of oleic acid and steric acid. Shea butter enjoyed wide utilization in confectionery and cosmetic industry. This leads to rapid growth in shea market, about 350,000 tons of shea export from sub-Saharan Africa in the past decade (Lovett, 2010). The catalytic activity of the sulfated HY zeolite was investigated under varying experimental conditions.

Kaolin is a solid mineral with up to about 10–95% of kaolinite ($Si_2Al_2O_5(OH)_5$) and components such as mica, quartz and metal oxides (K_2O, CaO, TiO_2, Fe_2O_3, Na_2O, MgO, MnO, and P_2O_5) as impurities (Alaba *et al.*, 2015). Kaolin has found popular application as a raw material in synthesis of active catalyst and has been an invention for several industrial processes such as petrol chemistry and processes that need solid acid catalysts, co-catalyst or promoter application catalyst support, for positive environmental impact and economic viability (Alaba *et al.*, 2015). Therefore, this report is aimed to study the synthesis and characterization of sulfated HY zeolite (SHY) synthesized from kaolin and the influence of sulfation. The effect of sulfation was investigated on methanolysis of shea butter. The preference of HY zeolite in this work is because of the low cost of kaolin being the precursor.

5.2 Experimental

5.2.1 Materials

The kaolin and NaOH and H_2SO_4 (95-98% pure) used for this investigation was purchased from R&M Chemicals Sdn. Bhd., Malaysia. The study utilized the reagents

without further purification. The shea butter was obtained Ikotun, Lagos, Nigeria. It was heated in an oven at 110 ^{o}C to get rid of the moisture therein. Table 5.1 presents the properties of crude shea butter.

Table 5.1: Properties of crude shea butter (Enweremadu *et al*., 2010).

Properties	Values
Density (kg m^{-3}) at 25 ^{o}C	0.91
Viscosity (mm^2 s^{-1}) at 38 ^{o}C	39.98
Acid value	3.62
Iodine value (I_2 g 100 g^{-1})	59.5
Saponification value (mg KOH g^{-1})	190
Peroxide value (meq O_2 kg^{-1})	12.15
Water content (wt%)	0.037
Fatty acid composition (%)	
Palmitic (C16:0)	5.4
Stearic (C18:0)	35.7
Oleic (C18:1)	49.6
Linoleic (C18:2)	7.8
Arachidic (C20:0)	1.3

5.2.2 Experimental techniques

5.2.2.1 Synthesis of reference HY zeolite (HY)

The synthesis of HY zeolites precursor was by thermal activation at 850 °C for 2 h and subsequent activation with 6M H_2SO_4 at 90 °C for 2 h to produce amorphous aluminosilicate. The precursor was added to an aqueous NaOH solution (14%) at ratio 1:6. The solution was aged at room temperature for 36 h and subsequently crystallized at 100 °C for 24 h. Further, the gels were washed and filtered with distilled water using vacuum pump until pH of 9-10. The sample was dried at 110 °C overnight and subsequently soaked with a solution saturated with NaCl to their equilibrium water content (Enweremadu *et al*., 2010). Further, they were placed in a fume cupboard to remove excess water and ensure adequate drying. The samples were transformed into hydronium form by treating with 1 M ammonium nitrate solution for 24 h. The resulting solution was filtered and dried at 110 °C overnight and then calcined at 550 °C for 2 h.

5.2.2.2 Sulfated HY zeolite (SHY)

Sulfated HY zeolite was prepared by incipient impregnation of sulfuric acid into the prepared HY zeolite. The impregnation was done by addition of 10 g of the HY to 100 mL of sulfuric acid solution (1M). The mixture was stirred for 1 h at room temperature. Afterward, the sample was kept inside fume cupboard to reduce the moisture content before transferring to the oven for 24 h drying. The dried sample was calcined at 450 °C for 3 h.

5.2.3 Catalyst characterization

The Sulfur content and Si/Al ratio of the samples were determined by x-ray fluorescence (XRF). X-ray diffractometer (Seifert X-ray Diffractometer JSO 2002) recorded X-ray Diffraction (XRD) pattern for all the samples the using nickel-filtered CuKα radiation (λ = 1.544 Å) ranging from 5.018 to 69.966° (2) with a step size of 0.026°. The Nitrogen adsorption/desorption analysis was measured with surface area and porosity analyzer (Micrometrics ASAP 2020) under analysis bath Temperature of 77.350 K. The samples were degassed for 3 h at 180 °C before measurement. Fourier transform infrared spectroscopy (FTIR) analysis of the samples was carried out using a Bruker Tensor 27 FT-IR in the range of 600 cm^{-1} to 4000 cm^{-1} at 4 cm^{-1} resolution.

Further, the acidities of the samples were determined by ammonia temperature programmed desorption (NH_3-TPD) analysis using Chemosorp 2720 apparatus. The desorption experiment was carried out from 100 to 1200 °C with 10 °C/min ramp and monitored with thermal conductivity detector.

The morphology of the synthesized HY and SHY zeolites were visualized by Scanning electron microscopy (SEM, FEI Quanta 400 FE-SEM) using 20 kV as the accelerating

voltage. The samples were coated with gold, prior to examination, to enhance the electrical conductivity.

5.2.4 Methanolysis of shea butter

Methanolysis of shea butter proceeded over SHY in a stainless steel high-pressure reactor. The reaction occurred in excess methanol in air tight stainless steel autoclave reactor. The temperature, catalyst loading and MeOH/oil molar ratio were varied to optimize the process. The reaction proceeded at 150 ^{o}C and 200 ^{o}C, MeOH /oil molar ratio of 5:1 to 30:1 and the catalyst amount was from 1 to 5 wt %. Afterward, the glycerol was removed using separating funnel and vacuum pump. Further, the samples were analyzed with thermogravimetric analysis (TGA) using TGA Q500 to determine the biodiesel yield. TGA is a cheap and fast method for quantitative analysis of a mixture of materials (Farag *et al*., 2007; Foster *et al*., 2012). Biodiesel yield with TGA is comparable with GC method (Farag *et al*., 2007). Chand *et al*., (2009) investigated the suitability of TGA compared to proton NMR, HPLC and GC method for determination of biodiesel yield composition in transesterification reaction mixtures. They reported that the TGA results are comparable to those of proton NMR, HPLC, and GC. The effectiveness of TGA method relative to 1HNMR method is within ±1.5%. The TGA analysis of shea butter and the synthesized biodiesels was done by filling the crucible with a specific sample amount. The operating temperature was set to 50-500 ^{o}C with the heating rate of 20 ^{o}C/min in the presence of nitrogen.

5.2.5 Influence of transport phenomena on the catalysts.

Investigation of transport influence in heterogeneous catalysis is of vital importance especially in a system that involves transfer of bulky molecules. This is investigated by using turnover frequency (TOF) value to comparatively check the activity of the catalyst.

TOF is defined as the moles reacted per second per surface mole of the active species (Madon and Boudart, 1902). It quantifies the activity of the active center for catalytic reaction under a specific reaction condition by a number of molecules converted per unit time (Boudart, 1995).

$$TOF = \frac{M_{actual}}{t \times f_m \times m_{cat}} \quad (5.1)$$

Where M_{actual} is the amount in moles of biodiesel produced; t is the reaction time; f_m is the amount of acid sites on the surface and m_{cat} is the mass of catalyst.

5.3 Results and discussion

5.3.1 Catalysts characterization

The XRD pattern in Figure 5.1 showed the transformation from kaolin to SHY after series of treatment steps. The crystalline peaks of kaolin gave way to the emergence of characteristic peaks of Y zeolite (at 2θ= 18.5, 20.2, 23.5 and 26.8°) after hydrothermal crystallization. Upon sulfation, the crystallinity of the zeolite dropped from 90.37 to 12.38%. This is evident in a sharp decrease in intensity and disappearance of some of the zeolite peaks and decrease in crystallite size from 30.41 to 30.33 nm (Table 5.2). The loss of crystallinity was due to the sulfuric acid attack, which leads to severe dealumination, increasing the Si/Al ratio, thereby reducing the hydrophilicity for enhanced stability.

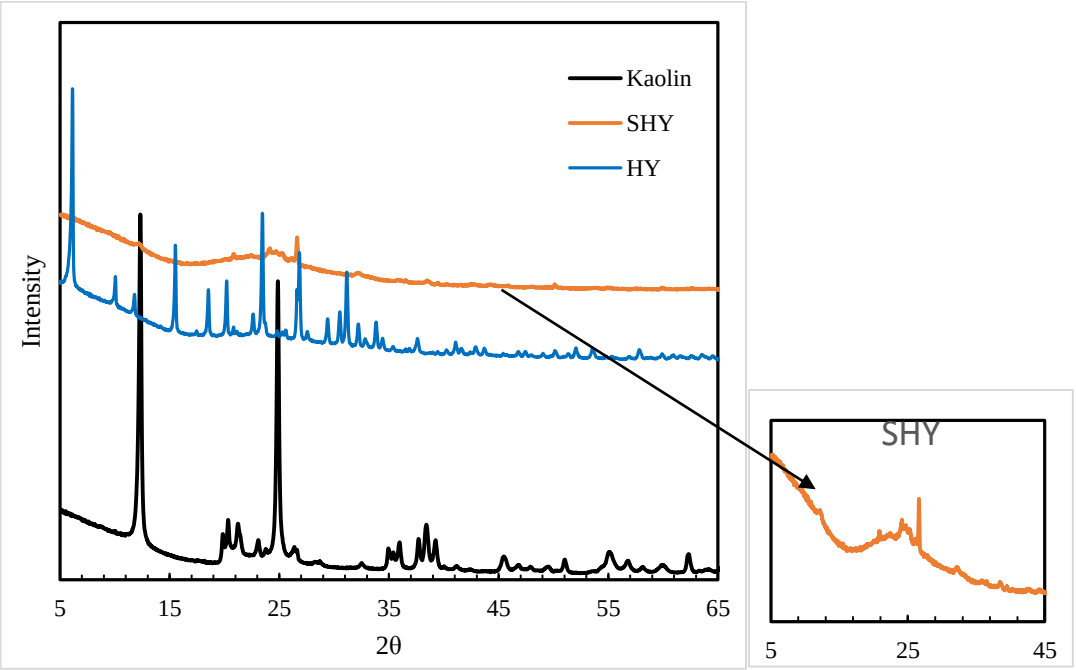

Figure 5.1: X-ray diffraction patterns of the kaolin, HY and SHY.

Table 5.2: Characterization of sulfated HY zeolite and reference zeolite.

Catalyst	Crystallite size (nm)	Sulfur (wt%)	Si/Al	SBET (m^2 g^{-1})	Pore Vol. (cm3 g^{-1})	Pore (nm)	Temp. (°C)	Acidity (mmol g^{-1})	Total acidity (mmol g^{-1})
HY	30.41	-	1.67	443.78	0.23	2.07	248.7	1.41	2.26
							694.1	0.24	
							761.0	0.43	
							992.7	0.19	
SHY	30.33	5.78	2.89	65.81	0.06	3.84	729.2	0.12	2.05
							749.4	1.93	

Table 5.2 shows large decreased in the BET specific surface area (SSA) and the pore volume upon sulfation of the HY zeolite. However, SHY exhibited enhanced pore size because the sulfuric acid leaching culminated in the collapse of the pore walls. Further, the pore walls collapse and severe pore blockage by the sulfate ions may be responsible for the decreased SSA and pore volume. The nitrogen adsorption isotherms in Figure 5.2 revealed the enhancement in pore size. The result shows that sulfation with 1 M H_2SO_4 considerably decreases the surface area but increases the mesoporosity as evident by the change in the hysteresis loop as well as reduction in the adsorbed volume (Vads).

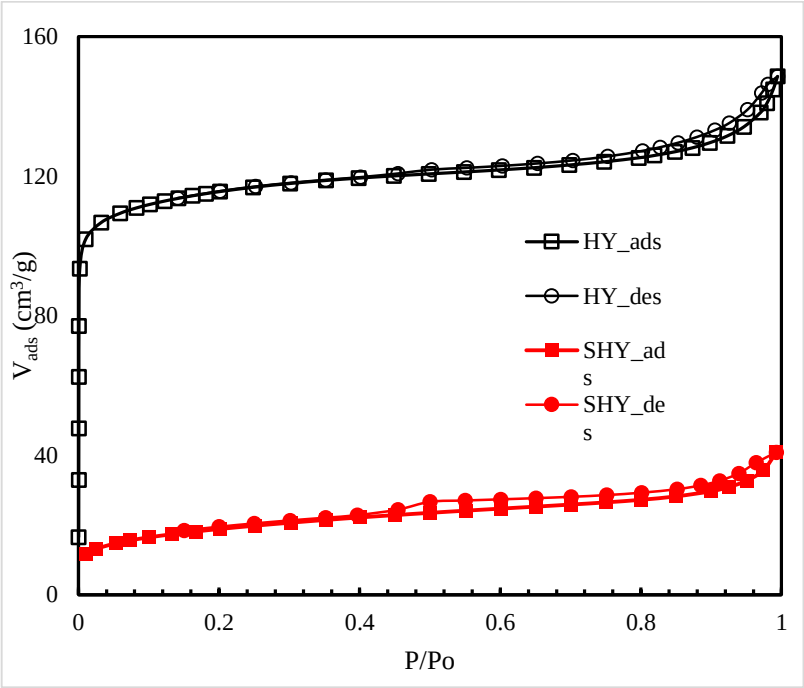

Figure 5.2: Isotherms of nitrogen adsorption/desorptio of HY and SHY

The FTIR spectra in Figure 5.3 revealed the presence of sulfate groups in SHY. The bands that are located at 704.96 cm^{-1} and 796.36 cm^{-1} are due to stretching of S-O bond. The broad band that extends from 1064.73 cm^{-1} to 1170 cm^{-1} are assigned to symmetric and asymmetric stretching vibration of and S=O bonds being sulfate of inorganic chelating bidenate (Zhou *et al*., 2013; Kalbasi *et al*., 2011; Saravanan *et al*., 2012). However, the broad band that covers 1064.73 cm^{-1} to 1170 cm^{-1} overlapped the HY band at 1032.75 cm^{-1} due to Si-O-Si stretching. The incorporated S=O bond increased the Bronsted acid sites of the zeolite due to its partial ionic nature. The results showed that sulfate groups were successfully embedded on the surface of HY to form SHY.

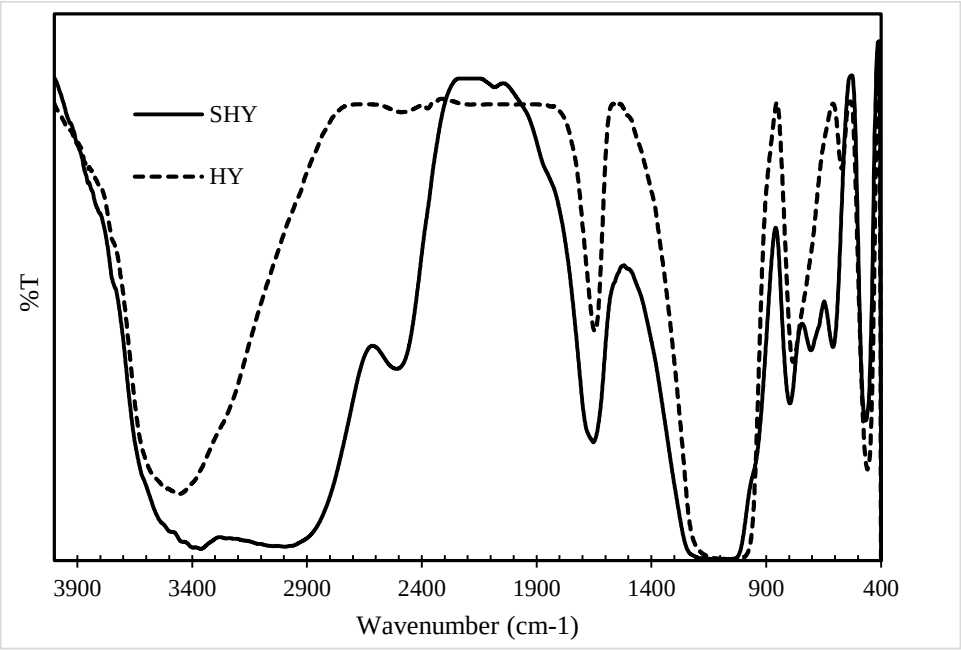

Figure 5.3: FTIR spectra for catalyst HY and SHY.

The NH_3-TPD spectra shown in Figure 5.4 confirms the super acidity of SHY with two intense peaks related to SO_3H groups at 729.2 and 749.4 °C, which shows higher density of acid site as compared with that of HY at approximately the same temperature. This revealed that SHY has higher acid strength compared to HY. However, the amount of acid site in HY is slightly higher than that of SHY due to the effect of dealumination via acid activation. Moreover, the SO_3 content of SHY determined by EDX is 5.78 %, which was greater than that of HY (Table 5.2). These suggest that the SO_3H groups were successfully grafted on HY.

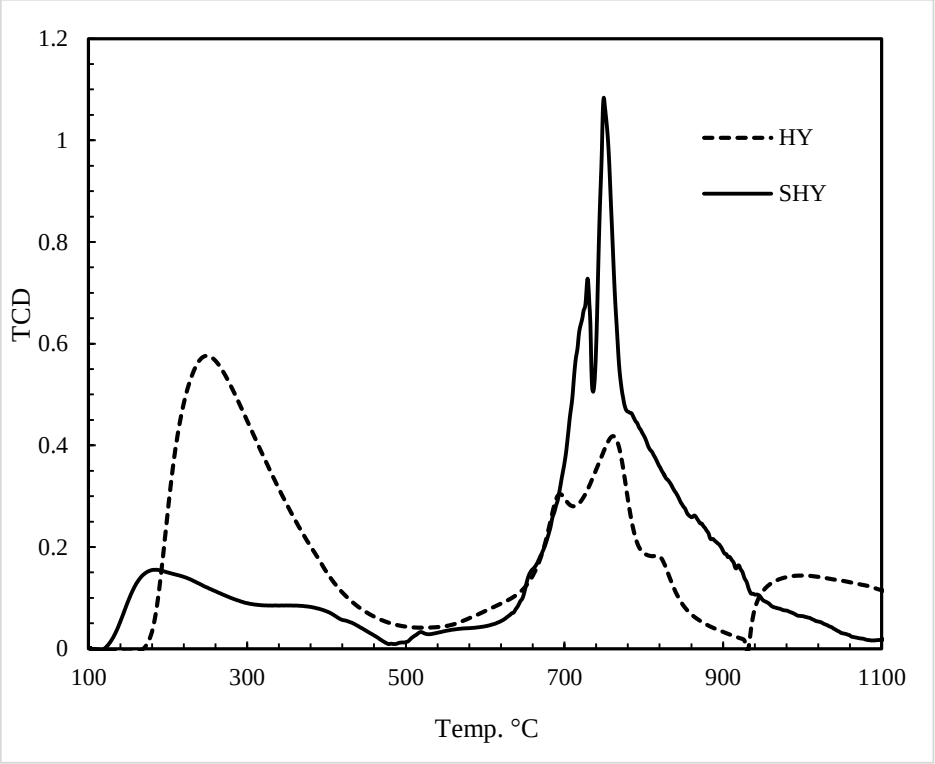

Figure 5.4: NH_3–TPD profiles of the HY and SHY catalysts.

SEM was used to observe the morphology of synthesized HY and SHY zeolites as shown in Figure 5.5. The two samples show both the octahedral morphology ascribed to conventional Y zeolite and globular particles with rugged surfaces, which confirms the mesoporosity of the samples. However, SHY appeared to be more amorphous texturally due to loss of crystallinity of the parent HY ascribed to the acid attack (Qin *et al*., 2013).

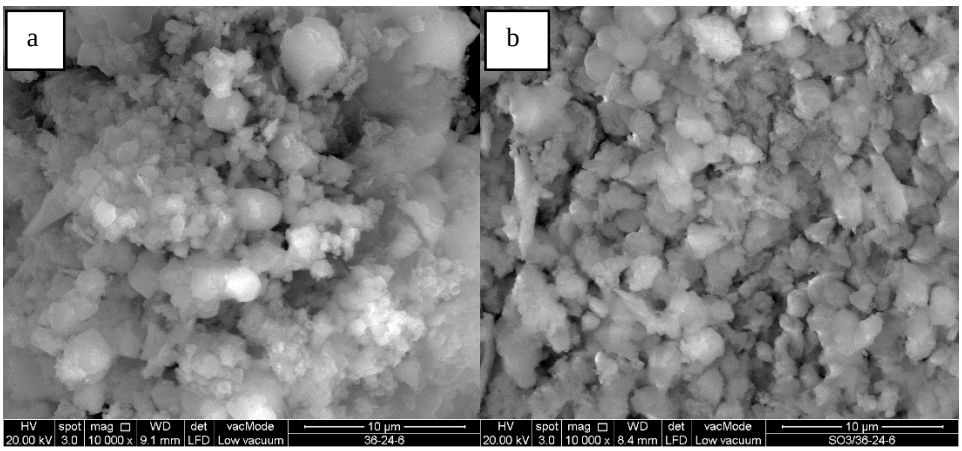

Figure 5.5: SEM image for catalyst HY (a) and SHY (b).

5.3.2 Catalytic activity

The catalytic activity of SHY was studied in methanolysis of shea butter to obtain the best reaction condition such as temperature, MeOH/oil ratio and catalyst loading to attain the best yield of biodiesel. The activity of SHY was also compared with that of HY.Effect of reaction parameters on biodiesel yield

The reaction was initially studied under varying temperature from 100 to 200 °C over catalyst loading of 1 wt% and MeOH/oil ratio of 5:1 for 3 h. The result obtained showed that the biodiesel yield was less than 8.37% at 100 °C. However, the yield increased rapidly to 74.77% upon increase to 200 °C (Figure 5.6a). The yield increased with increase in reaction temperature because the reaction rate as well as the solubility of methanol in shea butter increase with an increase in temperature (Xie *et al*., 2012).

Theoretically, the ratio of methanol to oil required for transesterification is 3:1. However, there is equilibrium shift in the reaction to favor the desired product in excess methanol. The influence of methanol/oil molar ratio was studied over SHY catalyst. Ratio 5:1 gave 74.77% biodiesel yield after 3 h with 1 wt% catalyst at 200 ^{o}C, on increasing the ratio to 30:1 the yield increased to 90.76% (Figure 5.6b). This confirmed that increase in MeOH/oil ratio favors biodiesel yield. The excess methanol were separated from the product by distillation and glycerol was separated using centrifugation follow by decantation.

Figure 5.6c presents the effect of SHY catalyst loading on biodiesel yield. The MeOH/oil molar ratio of 5:1 and 3 h reaction time at 200 °C were used with varying the catalyst loading from 1 to 5 wt%. The results show that biodiesel yield increased from 74.77 to 96.89% as the catalyst loading increases from 1 to 3 wt %. This is because an increase in

catalyst loading enhanced the availability of active sites, which improve the approachability of more reactant molecules to the active site thereby favoring biodiesel yield. This is an indication that the best activity was obtained at 3 wt% catalyst loading because further increase to 5 wt% yield no significant increase.

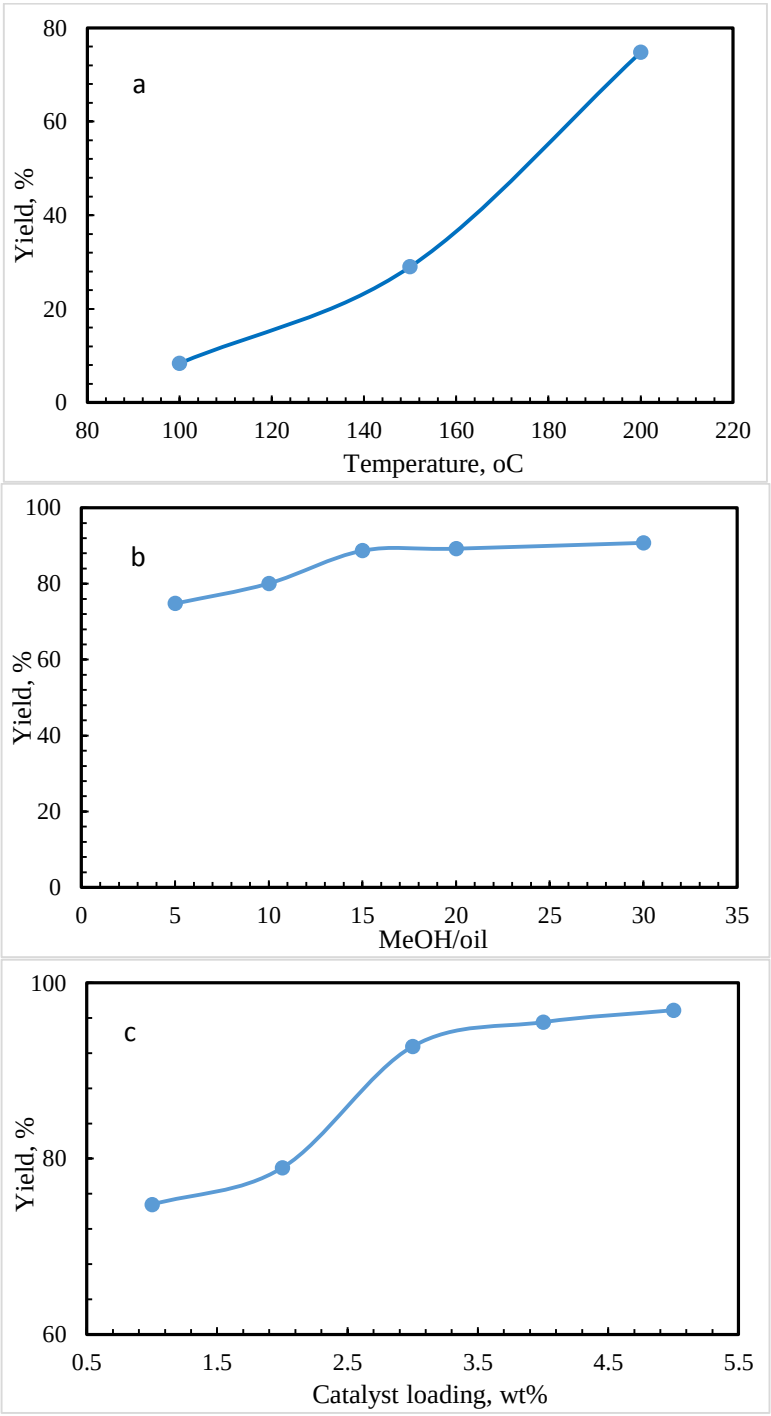

Figure 5.6: Effect of operating parameters on biodiesel yield over SHY catalyst; (a) temperature, (b) MeOH/oil ratio, and (C) catalyst loading.

In comparison to HY, SHY showed outstanding performance in methanolysis of shea butter. Both catalysts were tested at 200 °C, MeOH/oil molar ratio of 5:1 for 6 h. The results showed biodiesel yield of 72.42 and 90.76% for HY and SHY respectively. This was attributed to the fact that SHY possesses stronger acid strength and larger pore size compared to HY. The pore diameter of HY is approximately 2 nm (Table 5.2), which shows that it is a microporous material, and suffers mass transfer limitation. Similarly, Table 5.3 shows the catalytic activity of SHY with respect to TOF for all the experimental runs. The optimal activity was observed at 200 °C, MeOH/oil molar ratio of 5:1, 3 wt% catalyst loading for 3 h. This was ascribed to increase in surface contact between the reactants and the catalyst active sites.

Table 5.3: Catalytic performance with TOF.

Catalyst	Temp. (°C)	Cat wt%	MEOH/oil	Time (h)	Yield (%)	TOF
SHY	100	1	5	3	8.37	0.0014
SHY	150	1	5	3	28.99	0.0048
SHY	200	1	5	3	74.77	0.0124
SHY	200	2	5	3	78.96	0.0131
SHY	200	3	5	3	92.77	0.0153
SHY	200	1	5	6	90.76	0.0075
SHY	200	1	10	3	80.06	0.0147
SHY	200	1	15	3	88.68	0.0132
HY	200	1	5	6	72.42	0.0054

5.3.3 Catalyst Reusability

Reusability of the catalyst is of vital importance in any industrial process. For this reason, the reusability of SHY was tested in repeated cycle at 200 °C, MeOH/oil molar ratio of 5:1, and 3 wt% catalyst loading for 3 h. After the first cycle, the spent SHY sample was regenerated by rinsing with n-hexane to remove the remaining product on it. The washed sample was dried overnight to remove physically absorbed water and the calcined at 300 °C. The regenerated sample was reused for the next cycle of reaction. The results showed

a little decrease in the activity (about 14.55%) of SHY after four cycles (Figure 5.7). The decrease in the catalytic activity is due to leaching of the incorporated sulfate group, which reduced the sulfur content from 5.78 to 4.42 % and a corresponding reduction in a number of acid sites. This result is comparable with the reusability report of khder *et al*. (2008) and is attributed to the higher amount of Bronsted acid sites of the catalyst.

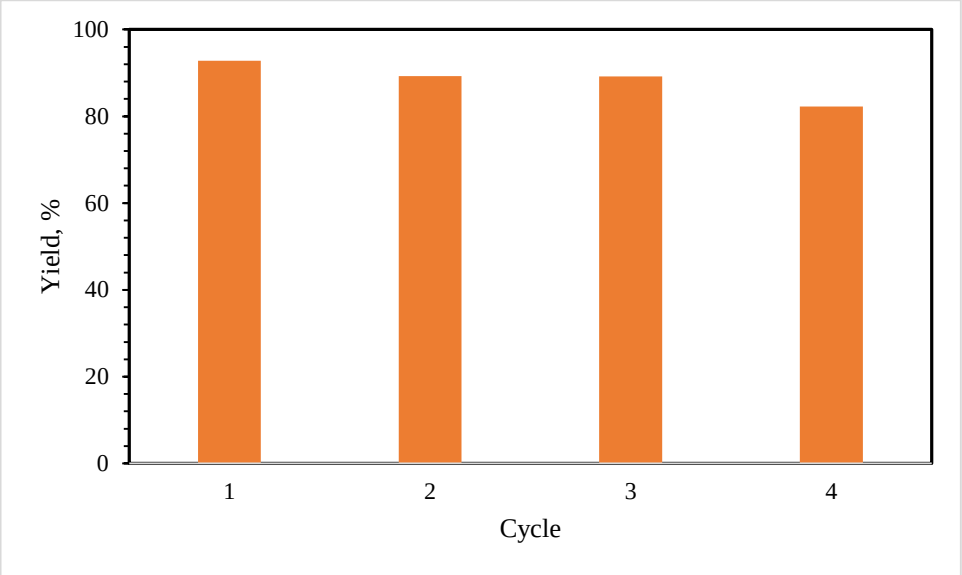

Figure 5.7: Reusability of SHY catalyst on transesterification of shea butter.

5.4 Conclusion

Sulfated hierarchical nanoporous HY zeolite was successfully prepared by incipient impregnation with sulfuric acid. The sulfation remarkably improved the acid strength and the porosity of the sample, which efficiently catalyzed methanolysis of shea butter. The sulfated zeolite showed better catalytic activity in biodiesel production in comparison with the reference zeolite. Despite the sharp decrease in the SSA (443.78 to 65.81 m^2 g^{-1}) and pore volume (0.23 to 0.06 cm^3 g-1), the sulfated zeolite took advantage of the enhanced pore size, which enhance the FAME diffusion, acid strength and hydrothermal stability to give a better performance. The best operating condition within the parameters investigated are 5:1 methanol/oil molar ratio, 3.0 wt% catalyst, and 3 h reaction time at

200 °C. This gave biodiesel yield of 92.77%. This is a clear evidence that the sulfated zeolite is an efficient catalyst for biodiesel production from shea butter.

CHAPTER 6: A COMPARATIVE STUDY ON THERMAL DECOMPOSITION BEHAVIOR OF BIODIESEL SAMPLES PRODUCED FROM SHEA BUTTER OVER MICRO AND MESOPOROUS ZSM-5 ZEOLITES USING DIFFERENT KINETIC MODELS

6.1 Introduction

Demand for sustainable production of biodiesel as an alternative energy source is ever increasing. This is because of their environmental friendliness, acceptable quality of exhaust gasses and similarity to petroleum diesel (Biswas *et al*., 2013). This demand arise from the need to minimize the use of fossil fuel by replacement with a suitable alternative energy source that is renewable and sustainable. This effort is being accelerated by depletion of fossil fuel reserve, ever-increasing fuel price and environmental pollution via greenhouse gas (GHG) emission (Ounas *et al*., 2011). Therefore, there arise a need to find fuel processing techniques that could help to obtain quality fuel products. Biodiesel is an essential renewable and sustainable energy source of this repute.

Pyrolysis kinetics of biodiesel is of vital importance in thermochemical transformation process for energy production (Sait *et al*., 2012). Pyrolysis is a thermochemical treatment that culminate in decomposition of organic materials at elevated temperature in an oxygen or any halogen free environment (Apaydin-Varol *et al*., 2014). As it proceeds, the physical and chemical phase of the materials are transformed irreversibly. Pyrolysis kinetics help to model thermochemical conversion of biomass to biodiesel. Pyrolysis breaks the molecules to volatiles and residue. Pyrolysis kinetic is very complex because biofuel decomposition, yield and composition are influenced by many parameters. This includes moisture content, temperature, heating rate, resident time, size biofuel composition and particles (Fasina *et al*., 2012; Ounas *et al*., 2011; Slopiecka *et al*., 2012).

Thermogravimetric analysis (TGA) is a useful tool for evaluation of thermal decomposition because of its precision and well controlled experimental conditions (Singh *et al*., 2012; Zhou *et al*., 2009). Several researchers investigated the use of TGA for evaluation of biomass kinetic parameters (Mehrabian *et al*., 2012; Skreiberg *et al*., 2011; Syed *et al*., 2011; Tiwari *et al*., 2012). Likewise, various models have been used varying the heating rates to avoid confusion that may arise from single heating rate (Biswas *et al*., 2013). Therefore, it is needful to study pyrolysis of shea butter and the produced biodiesel under non-isothermal thermogravimetric condition to have a better understanding of their kinetic analysis as well as stability. This will give insight into the biodiesel production process.

This study investigates the kinetic analysis of shea butter transesterification over microporous and mesoporous ZSM-5. The technology employed was TGA, being the most popularly used techniques for thermal decomposition kinetics of biomass. Coats-Redfern, Ingraham-Marrier, Arrhenius and Differential model were engaged in evaluating the non-isothermal TGA data. This helps to provide insight into the transesterification process. The kinetics analysis was performed to investigate the effect of different catalysts on activation energy and frequency factor.

6.2 Experimental

6.2.1 Materials and Methods

Crude Shea butter was procured from Lagos, Nigeria. The biodiesel samples were synthesized over conventional ZSM-5 and desilicated ZSM-5. Two samples of desilicated ZSM-5 were used. One is desilicated with 0.3 M NaOH (0.3HZSM-5) and the other with 0.4 M (0.4HZSM-5). The biodiesel produced from ZSM-5, 0.3HZSM-5 and

0.4HZSM-5 are designated ZBio, 0.3mesoZBio and 0.4mesoZBio respectively. The detail of the catalysts and biodiesel synthesis are explained elsewhere.

The shea butter and biodiesel samples were pyrolyzed using TA Q60. The analysis proceed in the presence of nitrogen at constant heating rate of 20 °C until 550 °C. The nitrogen flow helped to maintain inert atmosphere to avoid unwanted oxidation.

6.2.2 Determination of Kinetic parameters

Due to numerous reactions in both series and parallel, kinetic study of pyrolysis process is a complex process (Aboulkas *et al*., 2009). Generally, the decomposition rate is given by

$$\frac{dx}{dt} = K(T)f(x)^n \tag{6.1}$$

Where x is the degree of conversion, T is temperature and t is time. The conversion rate $\frac{dx}{dt}$ for pyrolysis at constant heating rate,

$\beta = \frac{dT}{dt}$, could be written as;

$$\frac{dx}{dt} = \beta\frac{dx}{dT} = K(T)f(x) \tag{6.2}$$

Also, the degree of advance, x is;

$$x = \frac{w_0 - w}{w_0 - w_f} \tag{6.3}$$

Where w_0, wf and w refers to weight of samples at the beginning, end and time t respectively. Since weight loss is temperature dependent, K(T) is often modelled by Arrhenius equation (Aboulkas *et al*., 2009).

$$K(T) = Aexp(-\frac{E_A}{RT}) \quad (6.4)$$

where R is the gas constant (8.314 J/mole K), A is the frequency factor (min-1), E_A is the activation energy (kJ/mol) and T is the absolute temperature (K). Combination of equation (8.1) and (8.2) gives;

$$\beta \frac{dx}{dT} = Aexp(-\frac{E_A}{RT})f(\mathrm{x}) \quad (6.5)$$

To analyze the TGA data, kinetic models are employed. Coats-Redfern, Ingraham-Marrier, Arrhenius and Differential model are used.

Arrhenius model suggests that the total rate of decomposition depends on temperature, sample weight remaining and rate constant. Therefore, Eq. (8.5) becomes:

$$\log[\frac{\frac{dW}{dt}}{w}] = logA - (E_A/2.303RT) \quad (6.6)$$

Plotting log[dW /dt / w] vs. 1/T gives a linear plot whose slope corresponds to $-E_A/2.303R$ and the intercept gives log A. This gives the value of activation energy and frequency factor.

The integral model developed by Coats and Redfern (Apaydin-Varol *et al*., 2014) suggests that the correct order leads to the best straight-line plot. Therefore, Eq. (6.5) becomes:

$$\ln(\frac{\mathrm{g(x)}}{T^2}) = \ln(\frac{AR}{\beta E_A}) - E_A/(RT) \qquad (6.7)$$

Plotting ln(g(x)/T2) vs. 1/T results in a linear plot whose slope corresponds to - E_A/R and the intercept gives ln(AR/ β E_A). This gives the value of activation energy and Arrhenius constant/frequency factor. Table 6.1 gives the values of the function g(x).

Ingraham and Marrier (Kök *et al*., 2000) expressed rate constant K as d*w*/d*t* for linear kinetics of heterogeneous reaction. Where d*w* is the weight loss per unit area at dt period. Therefore, Eq. (6.5) becomes:

$$\log\left(\frac{dw}{\mathrm{dT}}\right) = -\log \mathrm{T} - \log\beta + \log A - E_A/(2.303RT) \qquad (6.8)$$

The graph of log(dw/dT) + log T + log β vs. 1/T offers a linear plot whose slope corresponds E_A/ 2.303R and the intercept gives log A. This gives the value of activation energy and Arrhenius constant/frequency factor.

Differential model combine Eq. (6.1) and (6.4) to give (Aboulkas *et al*., 2007; Dollimore, 1992):

$$\ln((\frac{\mathrm{dx}}{\mathrm{dt}})/f(x)) = \ln A - E_A/(RT) \qquad (8.9)$$

The graph of ln((dx/dt)/ f(x)) vs. 1/T offers a linear plot whose slope corresponds to -E_A/R and the intercept gives ln A. This gives the value of activation energy and Arrhenius constant/frequency factor. Table 6.1 gives the values of the function f(x).

Table 6.1: Algebraic expressions of functions of the most common reaction mechanism (Aboulkas *et al*., 2007).

Mechanism	f(x)	g(x)
Power law	$2\,x^{1/2}$	$x^{1/2}$
Power law	$3\,x^{2/3}$	$x^{1/3}$
Power law	$4\,x^{3/4}$	$x^{1/4}$
One dimensional diffusion model	½ x	x^2
Two dimensional diffusion model	$[-\ln(1-x)]^{-1}$	[(1-x)ln(1-x)]+x
Three dimensional diffusion model	$3(1-x)^{2/3}/[2(1-(1-x)^{1/3})]$	$1-(2x/3)-(1-x)^{2/3}$
First-order reaction model	(1-x)	-ln(1-x)
Second-order reaction model	$(1-x)^2$	$(1-x)^{-1}-1$
Third-order reaction model	$(1-x)^3$	$[(1-x)^{-2}-1]/2$

6.3 Result and discussion

6.3.1 TGA pyrolysis of shea butter and biodiesel samples

Figure 6.1 and Figure 6.2 presents the TGA and DTG curve for shea butter and biodiesel samples. Decomposition of shea butter in two steps evident in DTG curve with a small peak and a long one. The former corresponds to breakage of unsaturated/bulky triglyceride molecules while the latter corresponds to total decomposition of shea butter. Moreover, biodiesel decomposition proceed in two step as evident in the DTG curve with two peaks. The first peak shows total devolatilization of methyl ester while the other is for decomposition of unconverted shea butter. Table 6.2 give the DTG decomposition characteristics of shea butter and that of biodiesel samples. The sample DTG peak temperature shows is a measure of its stability. The sample stability is in the in the order of Shea butter>ZBio>0.4mesoZBio>0.3mesoZbio.

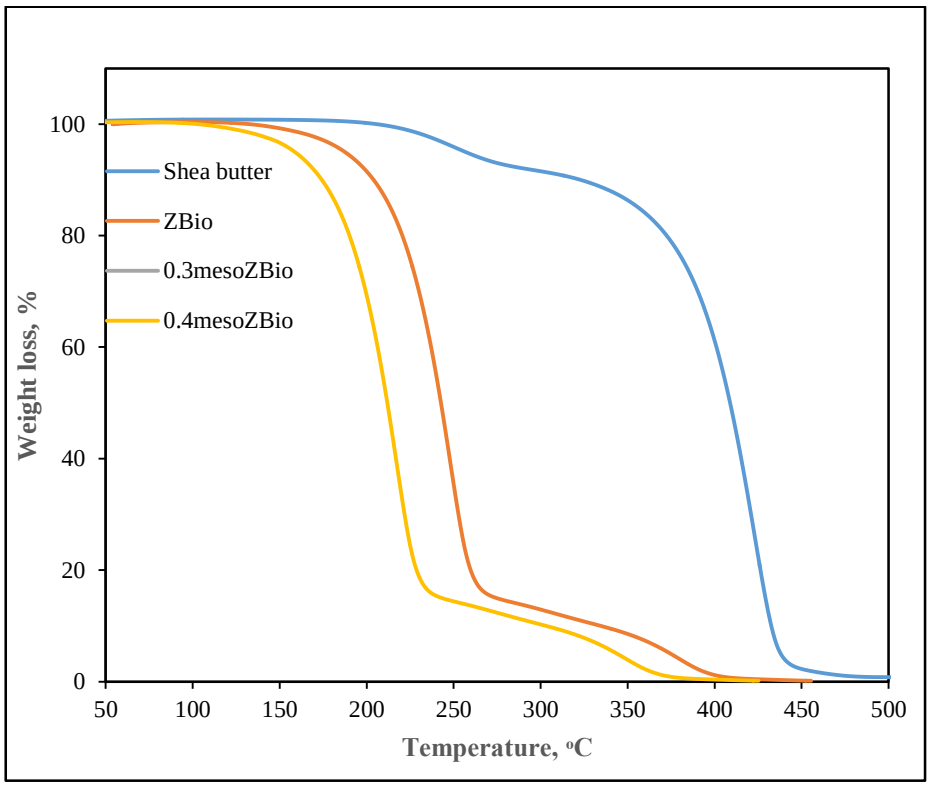

Figure 6.1: TG curves of shea butter and biodiesel samples.

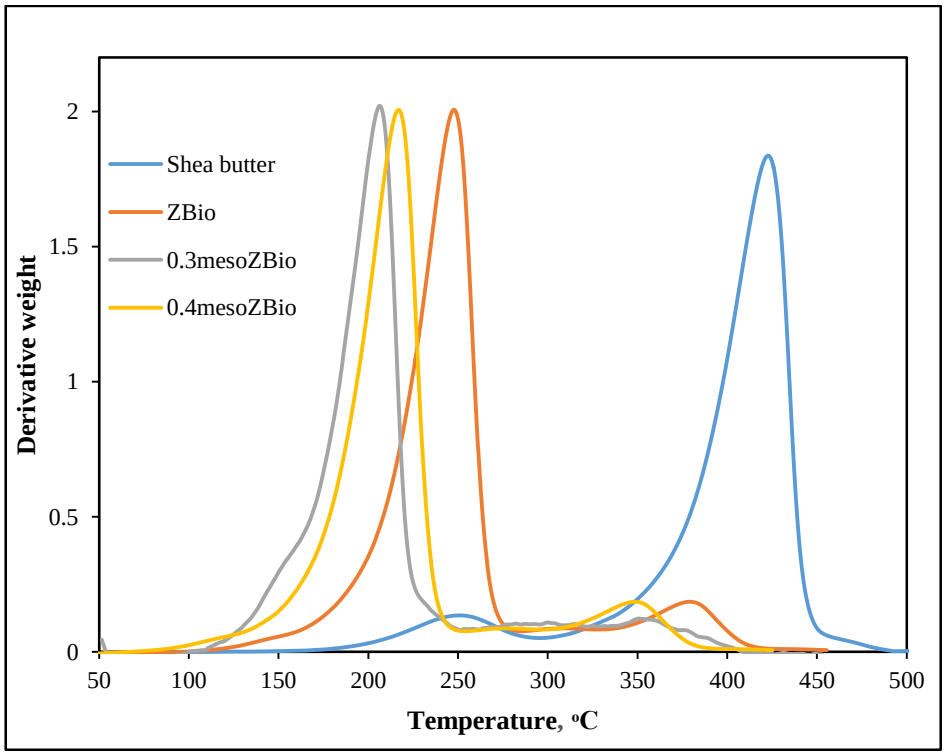

Figure 6.2: DTG curves of shea butter and biodiesel samples.

Table 6.2: DTG decomposition characteristics of shea butter and biodiesel samples.

Sample	β,˚C/min	Reaction Region	Peak Temp	Weight loss, %
ZBio	10	110 - 212	189.08	87.67
	15	115-236.96	227.75	85.85
	20	125-285	247.98	86.17
0.3mesoZBio	10	108-250	205.27	84.7
	15	112-270	224.15	84.08
	20	125-255	207	82.82
0.4mesoZBio	10	115-260	217.4	87.3
	15	125-177	229.54	85.46
	20	115-265	217	83.36
Shea butter				
Region 1	20	165- 290	250	
Region 2	20	300 - 470	423	

6.3.2 Kinetics Analysis

The reaction models for shea butter and biodiesel samples were developed from TGA data with the aid of Microsoft Excel spreadsheet. The reaction region used are the most linear region of the TGA curve. The slopes and intercept of the linear curves were used for computation of corresponding E_A and A values as presented in Table 6.3 and Table 6.4 respectively. Variation in the E_A and A values with respect to different kinetic models is mainly because the models are developed with different parameter and different assumption. The first reaction region of shea butter follows third order process with lower E_A (91.17 KJ/mol) value while the second region follows first order with high E_A (115.82 KJ/mol). From the assessment of the average E_A values of the samples (Table 6.5), the E_A value of shea butter>ZBio >0.3mesoZBio > 0.4mesoZBio. This shows that shea butter is more stable than biodiesel samples. It also authenticates the effect of transesterification mechanism on the samples. Moreover, among the biodiesel samples ZBio is the most stable while 0.4mesoZBio is the least stable since stability decrease with a decrease in E_A (Souza *et al*., 2007). Therefore, more heat is required for ZBio sample to be oxidized than

0.3mesoZBio and 0.4meso ZBio. Further, the low E_A value of ZBio is due to the higher acidity of ZSM-5 used compared to the desilicated ZSM-5 used for 0.3mesoZBio and 0.4mesoZBio. This shows that E_A a direct function of catalyst acidity.

Table 6.3: TGA/DTG Activation energies (E_A, kJ/mol) of shea butter and biodiesel samples.

Sample	β,˚C/min	Arrhenius	Coast-R.. n=1	Ingraham-M.	Diff. n=1
ZBio	10	57.64	95.46	61.36	102.38
	15	69.11	101.50	61.05	123.38
	20	68.48	102.80	72.70	122.54
0.3mesoZBio	10	54.14	122.83	56.14	137.61
	15	49.28	89.33	80.02	107.83
	20	56.08	101.30	56.68	92.08
0.4mesoZBio	10	67.67	105.39	69.15	119.72
	15	76.63	93.79	80.65	87.71
	20	67.21	92.14	70.52	107.49
Shea butter					
Region 1	20	75.83	102.10, n =3	79.84	76.92, n =3
Region 2	20	115.39	77.24	120.79	149.88

C-R.= Coats-Redfern, P(1)= Power law 1, I-M.= Ingraham-Marrier, Diff.= Differential

Table 6.4: TGA/DTG Arrhenius (A, min^{-1}) of shea butter and biodiesel samples.

Sample	β,˚C/min	Arrhenius	Coast-R. n=1	Ingraham-M.	Diff. n=1
ZBio	10	5.05E+06	6.39E+07	2.05E+10	1.02E+02
	15	6.22E+06	3.52E+07	1.50E+09	1.03E+11
	20	1.68E+06	1.03E+08	2.19E+10	1.09E+12
0.3mesoZBio	10	4.99E+05	1.22E+08	2.97E+09	2.22E+15
	15	1.42E+05	1.84E+06	3.96E+11	2.34E+11
	20	1.68E+06	8.39E+10	1.53E+09	3.14E+10
0.4mesoZBio	10	5.94E+06	1.54E+08	4.07E+10	1.22E+13
	15	3.40E+07	3.87E+06	3.30E+11	6.39E+08
	20	1.29E+07	4.74E+06	3.33E+10	5.16E+11
Shea butter					
Region 1	20	1.34E+06	9.25E+08, n =3	9.13E+09	1.80E+06, n =3
Region 2	20	1.78E+05	2.16E+05	1.63E+12	1.57E+11

C-R.= Coats-Redfern, P(1)= Power law 1, I-M.= Ingraham-Marrier, Diff.= Differential

Table 6.5: Average activation energies.

Sample	β,°C/min	E_A (kJ/mol)	Average E_A (kJ/mol)
ZBio	10	79.21	
	15	88.76	
	20	91.63	86.53
0.3mesoZBio	10	92.68	
	15	81.62	
	20	76.53	83.61
0.4mesoZBio	10	80.74	
	15	84.70	
	20	84.34	83.26
Shea butter			
Region 1	20	91.17	91.17
Region 2	20	115.82	115.82

6.4 Conclusion

Pyrolysis of shea butter follows two region and the first region proceeds in third order while the second in first order process. Activation energy is lower in the first region than the second. The pyrolysis kinetics of all the biodiesel samples were computed based on first order. Further, activation energy is in the order of shea butter>ZBio >0.3mesoZBio > 0.4mesoZBio because ZBio exhibits higher acidity. Therefore, more heat is required to oxidize ZBio than the other samples. However, the high conversion was also achieved over both 0.3mesoZBio and 0.4mesoZBio due to the combination of mesopore advantage. This shows that pyrolysis kinetics and reaction mechanism of the produced biodiesel depend on acidity and porosity of the catalyst. Moreover, the activation energy of all the biodiesel samples are less than that of the source shea butter. This implies that the monoglyceride molecules of biodiesel samples became less stable due effect of the transesterification reaction.

CHAPTER 7: CONCLUSION AND RECOMMENDATIONS

7.1 Conclusion

Viable solidacid catalysts had been synthesized using various methodologies, some of which were tested in biodiesel production via transesterification.

A novel highly ordered crystalline solid acid catalyst was synthesized from kaolin. This was achieved by thermal activation followed by acid treatment and subsequently, NaOH impregnation. The synthesized catalyst exhibits kaolinite with higher XRD peak intensity than the starting kaolin. This shows that its crystallinity is higher than that of kaolin. The value of the crystallinity indices (HI, AGFI and WIRI also attests to this claim. Among all the crystallinity index, WIRI proves the most appropriate because HPLK8-6M4h is expected to have lower crystallinity than NaPLk8-6M4h. The crystallinity of the product is also attested to by the FTIR analysis because all the disappeared bands after thermal and acid activation reappeared. However, more work needs to be done to increase the surface area because the synthesized catalyst exhibits extremely low surface area.

Pure phase crystalline hierarchical nanoporous Y zeolites of Si/Al ratio ranging from 1.39 to 1.61 was synthesized from kaolin. This was achieved by aging the mesoporous aluminosilicate obtained from kaolin with NaOH. Further, the gel was hydrothermally crystallized and subsequently, NaCl was incorporated. The aging was varied from 24 – 72 h and the optimum aging period is 48 h. Comparative crystallization was done for 16 and 24 h for sample aged for 48 h and higher relative crystallinity, surface area and HF were achieved at 24 h. Incorporation of salt after hydrothermal crystallization also enhanced relative crystallinity and preserve the mesopore structure. Highly crystalline and pure hierarchical nanoporous Y zeolite could is achievable by prolonging the crystallization time beyond 24 h after aging for 48 h.

Further, the hierarchical nanoporous Y zeolite was optimized using central composite design of RSM. The Optimum formulation for this hierarchical nanoporous HY zeolite was obtained as 43.60 h, 64.23 h and 6.97 ml/g for aging, crystallization and NaOH solution to kaolin ratio, respectively. The developed models show that for aging, crystallization and NaOH solution to kaolin ratio is the most statistically significant variable.

HMZeol were synthesized by desilication of conventional ZSM-5 with aqueous solution of NaOH. The desilication enhanced the zeolite matrix area, pore size and mesopore volume. This makes them suitable for bio-oil upgrade. High conversion of shea butter to biodiesel was achieved by varying the catalyst amount and methanol to shea butter molar ratio. The shea butter was upgraded by transesterification in excess methanol over the synthesized HMZeol and ZSM-5. HMZeol exhibits better catalytic activities than compared to ZSM-5. The methanol/shea butter ratio and catalyst wt.% were optimized. HMZeol showed superior activity on biodiesel yield when compared with the parent ZSM-5 zeolite. The catalytic material treated with 0.4 M NaOH (0.4HMZeol) gave 74% biodiesel yield at 5:1 methanol/oil molar ratio, 1 wt % catalyst, and 200 ^{o}C for 3 h reaction time while ZSM-5 gave 46.05% yield under the same reaction conditions. Further increase in the reaction time to 12 h for 0.4HMZeol, 0.3HMZeol and ZSM-5 gave 82.12%, 79.21%, and 72.13% biodiesel yield respectively. These results showed that hierarchical mesoporous HZSM-5 is a promising solid acid catalyst for biodiesel production via methanolysis.

Sulfated HY zeolite was prepared by functionalizing with sulfuric acid as sulfate precursor. The effect of sulfation was observed on the textural and acidity properties as well as its catalytic activity. There was a remarkable improvement in the acid strength of

hierarchical HY zeolite upon sulfation though with a small reduction in density due to dealumination, which enhanced the stability. Sulfated hierarchical HY was efficient for the transesterification of shea butter. It gave biodiesel yield of 90.76% at 200 °C for 6 h while hierarchical HY gave the yield of 72.42% at the same condition. This indicates that both pore structure and acid strength decide the activity of solid acids catalysts in biodiesel production.

The pyrolysis of each biodiesel synthesized over mesoporous ZSM-5 zeolites (0.3mesoZBio and 0.4mesoZBio) and conventional ZSM-5 zeolites (ZBio) were carried out using thermographymetric equipment. Reaction order, activation energy (EA) and frequency factor (A) were computed using four different models. The models are Arrhenius, Coats-Redfern, Ingraham-Marrier and Differential model. According to the computed average activation energy based on first order, the activation energies of the produced biodiesel are very close. ZBio exhibits higher EA (86.53 KJ/mol) compared to 0.3mesoZBio and 0.4mesoZBio (84.92 and 83.26 KJ/mol respectively). Therefore, it is tenable to adduce ZBio as the most stable because higher activation energy engenders higher stability.

In comparison, sulfated HY zeolite gives the best catalytic performance compared to HY zeolite and the microporous and hierarchical mesoporous ZSM-5. This is mainly due to its superior acid strength, which was engendered by the incorporation sulfate group.

7.2 Recommendations

Based on the findings of this dissertation, we recommend the use of kaolin as the starting aluminosilicate material for cheaper synthesis of HY zeolite and its derivatives as solid acid catalysts. In addition, we recommend the use of sulfated Y zeolite for efficient

production of biodiesel from feedstock with high percentage of FFA. Sulfated Y zeolite enables high yield of biodiesel using minimal MeOH/oil ratio, catalyst loading, and reaction time.

REFERENCES

Aboulkas A, El Harfi K, El Bouadili A, Benchanaa M, Mokhlisse A, Outzourit A. Kinetics of co-pyrolysis of Tarfaya (Morocco) oil shale with high-density polyethylene. Oil Shale 2007; 24: 15-33.

Aboulkas A, Nadifiyine M, Benchanaa M, Mokhlisse A. Pyrolysis kinetics of olive residue/plastic mixtures by non-isothermal thermogravimetry. Fuel Processing Technology 2009; 90: 722-728.

Aboyade AO, Hugo TJ, Carrier M, Meyer EL, Stahl R, Non-isothermal kinetic analysis of the devolatilization of corn cobs and sugar cane bagasse in an inert atmosphere. Thermochim Acta 2011; 517:81-89.

Absil RP, Herbst JA. (1993). Cracking catalysts comprising phosphorus and method of preparing and using the same: Google Patents.

Absil RP, Kowalski JA. (1994). Catalytic cracking, phosphorus modified zeolite, large pore molecular sieve: Google Patents.

Ahmadi M, Vahabzadeh F, Bonakdarpour B, Mofarrah E, Mehranian M. Application of the central composite design and response surface methodology to the advanced treatment of olive oil processing wastewater using Fenton's peroxidation. Journal of Hazardous Materials 2005; 123: 187-195.

Alaba PA, Sani YM, Daud WMAW. Kaolinite properties and advances for solid acid and basic catalyst synthesis, RSC Advances. 2015; 5:101127-101147

Angamuthu M, Ramalingam A. Balanced key tree management for multi-privileged groups using (N, T) policy. Security and Communication Networks 2011.

Anthony S. Adsorption of aromatic compounds in large MFI zeolite crystals. Journal of the Chemical Society, Faraday Transactions 1996; 92: 3445.

Aparicio P, Ferrell R, Galán E. (1999). *A new kaolinity crystallinity index from mathematical modelling of XRD data.* Paper presented at the CONFERENCE OF THE EUROPEAN CLAY GROUP ASSOCIATION, Kraków.

Aparicio P, Galan E. Mineralogical interference on kaolinite crystallinity index measurements. Clays and Clay Minerals 1999; 47: 12-27.

Apaydin-Varol E, Polat S, Putun AE. Pyrolysis kinetics and thermal decomposition behavior of polycarbonate-a TGA-FTIR study. Thermal Science 2014; 18: 833-842.

Atta A, Ajayi O, Adefila S. Synthesis of faujasite zeolites from Kankara kaolin clay. J Appl Sci Res 2007; 3: 1017-1021.

Aud S, Hussar W, Kena G, Bianco K, Frohlich L, Kemp J, Tahan K. The Condition of Education 2011. NCES 2011-033. National Center for Education Statistics 2011.

Avhad M, Marchetti J. A review on recent advancement in catalytic materials for biodiesel production. Renewable and Sustainable Energy Reviews 2015; 50: 696-718.

Ayodele OB. Effect of phosphoric acid treatment on kaolinite supported ferrioxalate catalyst for the degradation of amoxicillin in batch photo-Fenton process. Applied Clay Science 2013.

Bakala PC, Briot E, Salles L, Brégeault J-M. Comparison of liquid-phase olefin epoxidation over MoO x inserted within mesoporous silica (MCM-41, SBA-15) and grafted onto silica. Applied Catalysis A: General 2006; 300: 91-99.

Balat M. New biofuel production technologies. Energy Education Science and Technology Part A 2009; 22: 147–161.

Baoyu Liu CL, Yanqun Ren, Yanzhi Tan, Hongxia Xi, Yu Qian. Direct synthesis of mesoporous ZSM-5 zeolite by a dual-functional surfactant approach. Chemical Engineering Journal 210 2012: 96–102.

Barker TB. (2005). *Quality by experimental design* (Vol. 183): CRC Press.

Barrett E, Joyner L, Halenda P. An example of a method of analysis based on the assumption of cylindrical pores is found in J. Am Chem Soc 1951; 73: 373.

Bell NS, Tallant DR, Raymond R, Boyle TJ. Synthesis and self-assembly of zinc oxide nanoparticles with septahedral morphology. Journal of Materials Research 2008; 23: 529-535.

Belver C, Bañares Muñoz MA, Vicente MA. Chemical activation of a kaolinite under acid and alkaline conditions. Chemistry of materials 2002; 14: 2033-2043.

Belviso C, Cavalcante F, Lettino A, Fiore S. A and X-type zeolites synthesised from kaolinite at low temperature. Applied Clay Science 2013; 80: 162-168.

Benoit K, Laver M, Mikhaylov S. Treating words as data with error: Uncertainty in text statements of policy positions. American Journal of Political Science 2009; 53: 495-513.

Bhattacharyya KG, Gupta SS. Removal of Cu (II) by natural and acid-activated clays: An insight of adsorption isotherm, kinetic and thermodynamics. Desalination 2011; 272: 66-75.

Biswas S, Sharma D. Studies on cracking of Jatropha oil. Journal of Analytical and Applied Pyrolysis 2013; 99: 122-129.

Bizaia N, de Faria EH, Ricci GP, Calefi PS, Nassar EJ, Castro KA, Nakagaki S, Ciuffi KJ, Trujillano R, Vicente MA. Porphyrin− Kaolinite as Efficient Catalyst for Oxidation Reactions. ACS Applied Materials & Interfaces 2009; 1: 2667-2678.

Blasco T, Corma A, Díaz-Cabañas MJ, Rey F, Vidal-Moya JA, Zicovich-Wilson CM. Preferential location of Ge in the double four-membered ring units of ITQ-7 zeolite. The Journal of Physical Chemistry B 2002; 106: 2634.

Botas J, Serrano D, García A, de Vicente J, Ramos R. Catalytic conversion of rapeseed oil into raw chemicals and fuels over Ni- and Mo-modified nanocrystalline ZSM-5 zeolite. Catalysis Today 2012; 195: 59–70.

Boudart M. Turnover rates in heterogeneous catalysis. Chemical reviews 1995; 95: 661-666.

Box GE, Hunter WG, Hunter JS. Statistics for experimenters. 1978.

Boz N, Degirmenbasi N, Kalyon DM. Conversion of biomass to fuel: Transesterification of vegetable oil to biodiesel using KF loaded nano-γ-Al< sub> 2</sub> O< sub> 3</sub> as catalyst. Applied Catalysis B: Environmental 2009; 89: 590-596.

Bozell JJ, Petersen GR. Technology development for the production of biobased products from biorefinery carbohydrates – the US Department of Energy's "top 10" revisited. Green Chem 2010; 12: 539–554.

Brady PV, Cygan RT, Nagy KL. Molecular controls on kaolinite surface charge. Journal of Colloid and Interface Science 1996; 183: 356-364.

Brown SM, Woltermann GM. (1979). In situ zeolitic catalyst: Google Patents.

Brown SM, Woltermann GM. (1980). Zeolitized composite bodies and manufacture thereof: Google Patents.

Busto M, Grau J, Vera C. Screening of optimal pretreatment and reaction conditions for the isomerization-cracking of long paraffins over Pt/WO< sub> 3</sub>–ZrO< sub> 2</sub> catalysts. Applied Catalysis A: General 2010; 387: 35-44.

Campelo JM, Lee AF, Luque R, Luna D, Marinas JM, Romero AA. Preparation of Highly Active and Dispersed Platinum Nanoparticles on Mesoporous Al-MCM-48 and Their Activity in the Hydroisomerisation of n-Octane. Chemistry-A European Journal 2008; 14: 5988-5995.

Campos A, Dimitrov L, Da Silva C, Wallau M, Urquieta-González E. Recrystallisation of mesoporous SBA-15 into microporous ZSM-5. Microporous and mesoporous materials 2006; 95: 92-103.

Cardona-Martínez N, Dumesic J. Acid strength of silica-alumina and silica studied by microcalorimetric measurements of pyridine adsorption. Journal of Catalysis 1990; 125: 427-444.

Carrero A, Vicente G, Rodríguez R, Linares M, Del Peso G. Hierarchical zeolites as catalysts for biodiesel production from Nannochloropsis microalga oil. Catalysis Today 2011; 167: 148-153.

Castellano M, Turturro A, Riani P, Montanari T, Finocchio E, Ramis G. Bulk and surface properties of commercial kaolins. Applied Clay Science 2010; 48: 446-454.

Čejka J, Centi G, Perez-Pariente J, Roth WJ. Zeolite-based materials for novel catalytic applications: Opportunities, perspectives and open problems. Catalysis Today 2012; 179: 2-15.

Chand P, Reddy CV, Verkade JG, Wang T, Grewell D. Thermogravimetric quantification of biodiesel produced via alkali catalyzed transesterification of soybean oil. Energy & Fuels 2009; 23: 989-992.

Chandrasekhar S, Pramada P. Kaolin-based zeolite Y, a precursor for cordierite ceramics. Applied Clay Science 2004; 27: 187-198.

Chang Y-F, Martens LR, Vaughn SN. (2006). Forming slurry of molecular sieve and binder; catalytic conversion of feedstock to olefin such as ethylene, propylene: Google Patents.

Chen F, Ma L, Cheng D-g, Zhan X. Synthesis of hierarchical porous zeolite and its performance in n-heptane cracking. Catalysis Communications 2012; 18: 110-114.

Chen N, Degnan Jr TF, Smith CM. (1994). *Molecular transport and reaction in zeolites: design and application of shape selective catalysis*: Wiley. com.

Chen Z-x, Jin X-y, Chen Z, Megharaj M, Naidu R. Removal of methyl orange from aqueous solution using bentonite-supported nanoscale zero-valent iron. Journal of colloid and interface science 2011; 363: 601-607.

Cheng H, Liu Q, Yang J, Ma S, Frost RL. The thermal behavior of kaolinite intercalation complexes-A review. Thermochimica Acta 2012; 545: 1-13.

Cheng H, Yang J, Liu Q, Zhang J, Frost RL. A spectroscopic comparison of selected Chinese kaolinite, coal bearing kaolinite and halloysite—A mid-infrared and near-infrared study. Spectrochimica Acta Part A: Molecular and Biomolecular Spectroscopy 2010; 77: 856-861.

Chmielová M, Weiss Z. Determination of structural disorder degree using an XRD profile fitting procedure. Application to Czech kaolins. Applied clay science 2002; 22: 65-74.

Cho K, Cho HS, De Menorval L-C, Ryoo R. Generation of mesoporosity in LTA zeolites by organosilane surfactant for rapid molecular transport in catalytic application. Chemistry of materials 2009; 21: 5664-5673.

Choi M, Cho HS, Srivastava R, Venkatesan C, Choi D-H, Ryoo R. Amphiphilic organosilane-directed synthesis of crystalline zeolite with tunable mesoporosity. Nature materials 2006; 5: 718-723.

Choi M, Na K, Kim J, Sakamoto Y, Terasaki O, Ryoo R. Stable single-unit-cell nanosheets of zeolite MFI as active and long-lived catalysts. Nature 2009; 461: 246-249.

Colina FG, Esplugas S, Costa J. High-temperature reaction of kaolin with sulfuric acid. Industrial & engineering chemistry research 2002; 41: 4168-4173.

Copperthwaite R, Hutchings G, Johnston P, Orchard S. Ozone reactivation of a synthetic zeolite catalyst for methanol conversion. Journal of the Chemical Society, Chemical Communications 1985: 644.

Coriolano AC, Silva CG, Costa MJ, Pergher SB, Caldeira VP, Araujo AS. Development of HZSM-5/AlMCM-41 hybrid micro-mesoporous material and application for pyrolysis of vacuum gasoil. Microporous and Mesoporous Materials 2013: 208-211.

Corma A, Fornes V, Martınez-Triguero J, Pergher S. Delaminated zeolites: Combining the benefits of zeolites and mesoporous materials for catalytic uses. Journal of Catalysis 1999; 186: 57-63.

Corma A, Grande M, Gonzalez-Alfaro V, Orchilles A. Cracking activity and hydrothermal stability of MCM-41 and its comparison with amorphous silica-alumina and a USY zeolite. Journal of catalysis 1996; 159: 375-382.

Corma A, Navarro MT, Rey F, Valencia S. Synthesis of pure polymorph C of Beta zeolite in a fluoride-free system. Chemical Communications 2001: 1486.

Cui Y, Zhang Q, He J, Wang Y, Wei F. Pore-structure-mediated hierarchical SAPO-34: Facile synthesis, tunable nanostructure, and catalysis applications for the conversion of dimethyl ether into olefins. Particuology 2013; 11: 468-474.

Cundy CS, Cox PA. The hydrothermal synthesis of zeolites: Precursors, intermediates and reaction mechanism. Microporous and Mesoporous Materials 2005; 82: 1-5.

da Silva Lacerda Junior O, Cavalcanti RM, de Matos TM, Angélica RS, da Rocha Filho GN, Barros IdCL. Esterification of oleic acid using 12-tungstophosphoric supported in< i> flint</i> kaolin of the Amazonia. Fuel 2013.

DA SILVA RR, GUERRA DL. APPLICATIONS OF BRAZILIAN ILLITE-KAOLINITE IN NATURAL AND INTERCALATED FORMS AS ADSORBENTS TO REMOVAL OF ZINC FROM AQUEOUS SOLUTIONS: KINETIC AND THERMODYNAMIC STUDIES. Journal of the Chilean Chemical Society 2013; 58: 1678-1683.

Dang TH, Chen B-H, Lee D-J. Application of kaolin-based catalysts in biodiesel production via transesterification of vegetable oils in excess methanol. Bioresource technology 2013; 145: 175-181.

Davis ME. Ordered porous materials for emerging applications. Nature 2002; 417: 813.

Davis ME, Hathaway PE, Montes C. VPI-5, AlPO< sub> 4</sub>-8, and MCM-9: similarities and differences. Zeolites 1989; 9: 436-439.

Davis TM, Drews TO, Ramanan H, He C, Dong J, Schnablegger H, Katsoulakis MA, Kokkoli E, McCormick AV, Penn RL. Mechanistic principles of nanoparticle evolution to zeolite crystals. Nature materials 2006; 5: 400-406.

de Almeida RM, Noda LK, Gonçalves NS, Meneghetti SM, Meneghetti MR. Transesterification reaction of vegetable oils, using superacid sulfated TiO 2–base catalysts. Applied Catalysis A: General 2008; 347: 100-105.

de Oliveira AdN, da Silva Costa LR, de Oliveira Pires LH, do Nascimento LAS, Angélica RS, da Costa CE, Zamian JR, da Rocha Filho GN. Microwave-assisted preparation of a new esterification catalyst from wasted< i> flint</i> kaolin. Fuel 2012.

de Oliveira AdN, da Silva Costa LR, de Oliveira Pires LH, do Nascimento LAS, Angélica RS, da Costa CE, Zamian JR, da Rocha Filho GN. Microwave-assisted preparation of a new esterification catalyst from wasted flint kaolin. Fuel 2013; 103: 626-631.

Dellisanti F, Valdrè G. The role of microstrain on the thermostructural behaviour of industrial kaolin deformed by ball milling at low mechanical load. International Journal of Mineral Processing 2012; 102: 69-77.

Demirbas A. Combustion of biomass. Energy Sources Part A 2007; 29: 549–561.

Demirbas A. Biofuels securing the planet's future energy needs. Energy Convers Manag 2009; 50: 2239–2249.

Deng Y, White GN, Dixon JB. Effect of structural stress on the intercalation rate of kaolinite. Journal of colloid and interface science 2002; 250: 379-393.

Dhanasekaran K, Dharmendirakumar M. Optimization study of biodiesel used frying oil. Int J Curr Microbiol App Sci 2014; 3: 727-735.

Di Blasi C., Modeling chemical and physical processes of wood and biomass pyrolysis. Prog Energy Comb Sci 2008; 34 47-90.

do Nascimento LAS, Angélica RS, Da Costa CE, Zamian JR, da Rocha Filho GN. Comparative study between catalysts for esterification prepared from kaolins. Applied Clay Science 2011; 51: 267-273.

do Nascimento LAS, Tito LM, Angélica RS, Da Costa CE, Zamian JR, da Rocha Filho GN. Esterification of oleic acid over solid acid catalysts prepared from Amazon< i> flint</i> kaolin. Applied Catalysis B: Environmental 2011; 101: 495-503.

Dollimore D. The application of thermal analysis in studying the thermal decomposition of solids. Thermochimica acta 1992; 203: 7-23.

Doremieux-Morin C, Ramsaran A, Le Van Mao R, Batamack P, Heeribout L, Semmer V, Denes G, Fraissard J. 1H broad-line and MAS NMR: application to the study of acid sites of desilicated zeolite ZSM-5. Catalysis letters 1995; 34: 139-149.

Du E, Yu S, Zuo L, Zhang J, Huang X, Wang Y. Pb (II) sorption on molecular sieve analogues of MCM-41 synthesized from kaolinite and montmorillonite. Applied Clay Science 2011; 51: 94-101.

Dudkin BN, Loukhina IV, Avvakumov E, Isupov VP. Application of mechnochemical treatment of disintegration of kaolinite with sulphuric acid. Chemical and Sustainable Development 2004; 12: 327-330.

EL-Mekkawi DM, Selim MM. Removal of Pb< sup> 2+</sup> from water by using Na-Y zeolites prepared from Egyptian kaolins collected from different sources. Journal of Environmental Chemical Engineering 2013.

Elbokl TA, Detellier C. Intercalation of cyclic imides in kaolinite. Journal of colloid and interface science 2008; 323: 338-348.

Eng-Poh Ng XZ, and Svetlana Mintova. Environmental Synthesis Concerns of Zeolites. School of Chemical Sciences, Universiti Sains Malaysia, 11800 USM, Penang, Malaysia 2013: 303-306.

Enweremadu C, Alamu O. Development and characterization of biodiesel from shea nut butter. Int Agrophysics 2010; 24: 29-34.

Farag H, El-Maghraby A, Taha NA. Transesterification of esterified mixed oil for biodiesel production. International Journal of Chemical and Biochemical Sciences 2012; 2: 105-114.

Fasina O, Littlefield B. TG-FTIR analysis of pecan shells thermal decomposition. Fuel Processing Technology 2012; 102: 61-66.

Fatourehchi N, Sohrabi M, Royaee SJ, Mirarefin SM. Preparation of SAPO-34 catalyst and presentation of a kinetic model for methanol to olefin process (MTO). Chemical Engineering Research and Design 2011; 89: 811-816.

Foster AJ, Jae J, Cheng Y-T, Huber GW, Lobo RF. Optimizing the aromatic yield and distribution from catalytic fast pyrolysis of biomass over ZSM-5. Applied Catalysis A: General 2012; 423: 154-161.

Frenkel M. Surface acidity of montmorillonites. Clays Clay Miner 1974; 22: 435-441.

Freyhardt C, Tsapatsis M, Lobo R. KJB Jr and ME Davis. Nature 1996; 381: 295-296.

Frunz L, Prins R, Pirngruber GD. ZSM-5 precursors assembled to a mesoporous structure and its subsequent transformation into a zeolitic phase—from low to high catalytic activity. Microporous and mesoporous materials 2006; 88: 152-162.

Fukuda H, Kondo A, Noda H. Biodiesel fuel production by transesterification of oils. Journal of bioscience and bioengineering 2001; 92: 405-416.

Furuta S, Matsuhashi H, Arata K. Catalytic action of sulfated tin oxide for etherification and esterification in comparison with sulfated zirconia. Applied Catalysis A: General 2004; 269: 187-191.

Gallis K, Landry CC. Rapid calcination of nanostructured silicate composites by microwave irradiation. Advanced Materials 2001; 13: 23.

Garrett D, Pruitt J. Problems encountered with the Average Potential Method of analyzing substation grounding systems. Power Apparatus and Systems, IEEE Transactions on 1985: 3585-3596.

Gasparini E, Tarantino SC, Ghigna P, Riccardi MP, Cedillo-González EI, Siligardi C, Zema M. Thermal dehydroxylation of kaolinite under isothermal conditions. Applied Clay Science 2013; 80: 417-425.

Ghorbel A, Fourati M, Bouaziz J. Microstructural evolution and phase transformation of different sintered Kaolins powder compacts. Materials Chemistry and Physics 2008; 112: 876-885.

Glew D, Lovett PN. Life cycle analysis of shea butter use in cosmetics: from parklands to product, low carbon opportunities. Journal of Cleaner Production 2014; 68: 73-80.

Gorgulho HF, Mesquita JP, Gonçalves F, Pereira MFR, Figueiredo JL. Characterization of the surface chemistry of carbon materials by potentiometric titrations and temperature-programmed desorption. Carbon 2008; 46: 1544-1555.

Graça I, Fernandes A, Lopes J, Ribeiro M, Laforge S, Magnoux P, Ramôa Ribeiro F. Effect of phenol adsorption on HY zeolite for n-heptane cracking: comparison with methylcyclohexane. Applied Catalysis A: General 2010; 385: 178–189

Groen J, Peffer LA, Moulijn J, Pérez-Ramırez J. On the introduction of intracrystalline mesoporosity in zeolites upon desilication in alkaline medium. Microporous and mesoporous materials 2004; 69: 29-34.

Groen JC, Bach T, Ziese U, Paulaime-van Donk AM, de Jong KP, Moulijn JA, Pérez-Ramírez J. Creation of hollow zeolite architectures by controlled desilication of Al-zoned ZSM-5 crystals. Journal of the American Chemical Society 2005; 127: 10792.

Groen JC, Jansen JC, Moulijn JA, Pérez-Ramírez J. Optimal aluminum-assisted mesoporosity development in MFI zeolites by desilication. The Journal of Physical Chemistry B 2004; 108: 13062.

Groen JC, Moulijn JA, Pérez-Ramírez J. Decoupling mesoporosity formation and acidity modification in ZSM-5 zeolites by sequential desilication–dealumination. Microporous and mesoporous materials 2005; 87: 153-161.

Groen JC, Moulijn JA, Pérez-Ramírez J. Desilication: on the controlled generation of mesoporosity in MFI zeolites. Journal of Materials Chemistry 2006; 16: 2121-2131.

Groen JC, Peffer LA, Moulijn JA, Pérez-Ramírez J. Mechanism of hierarchical porosity development in MFI zeolites by desilication: The role of aluminium as a pore-directing agent. Chemistry-A European Journal 2005; 11: 4983-4994.

Groen JC, Zhu W, Brouwer S, Huynink SJ, Kapteijn F, Moulijn JA, Pérez-Ramírez J. Direct demonstration of enhanced diffusion in mesoporous ZSM-5 zeolite obtained via controlled desilication. Journal of the American Chemical Society 2007; 129: 355-360.

Grudzien RM, Grabicka BE, Jaroniec M. Effective method for removal of polymeric template from SBA-16 silica combining extraction and temperature-controlled calcination. Journal of Materials Chemistry 2006; 16: 819.

Guo H-F, Yan P, Hao X-Y, Wang Z-Z. Influences of introducing Al on the solid super acid SO 4 2−/SnO 2. Materials Chemistry and Physics 2008; 112: 1065-1068.

Guo W, Huang L, Deng P, Xue Z, Li Q. Characterization of Beta/MCM-41 composite molecular sieve compared with the mechanical mixture. Microporous and mesoporous materials 2001; 44: 427-434.

Haden Jr WL, Dzierzanowski FJ. (1970). Microspherical zeolitic molecular sieve composite catalyst and preparation thereof: Google Patents.

Haden Jr WL, Dzierzanowski FJ. (1972). Microspherical zeolitic molecular sieve composite catalyst and preparation thereof: Google Patents.

Hamilton BK, Gardner CR, Colton CK. Effect of diffusional limitations on lineweaver-burk plots for immobilized enzymes. AIChE Journal 1974; 20: 503-510.

Han Y, Wu S, Sun Y, Li D, Xiao F-S, Liu J, Zhang X. Hydrothermally stable ordered hexagonal mesoporous aluminosilicates assembled from a triblock copolymer and preformed aluminosilicate precursors in strongly acidic media. Chemistry of materials 2002; 14: 1144-1148.

Hassan A, Lopez-Linares F, Nassar NN, Carbognani-Arambarri L, Pereira-Almao P. Development of a support for a NiO catalyst for selective adsorption and post-

adsorption catalytic steam gasification of thermally converted asphaltenes. Catalysis Today 2013; 207: 112-118.

Hawthorn R. (1974). *Afterburner catalysts-effects of heat and mass transfer between gas and catalyst surface.* Paper presented at the AIChE Symp Ser.

Helwani Z, Othman M, Aziz N, Kim J, Fernando W. Solid heterogeneous catalysts for transesterification of triglycerides with methanol: a review. Applied Catalysis A: General 2009; 363: 1-10.

Heng S, Lau PPS, Yeung KL, Djafer M, Schrotter J-C. Low-temperature ozone treatment for organic template removal from zeolite membrane. Journal of membrane science 2004a; 243: 69.

Heng S, Lau PPS, Yeung KL, Djafer M, Schrotter J-C. Low-temperature ozone treatment for organic template removal from zeolite membrane. Journal of membrane science 2004b; 243: 69-78.

Hino M, Arata K. Reaction of butane to isobutane catalyzed by iron oxide treated with sulfate ion. Solid superacid catalyst. Chemistry Letters 1979; 8: 1259-1260.

Hoekman SK, Broch A, Robbins C, Ceniceros E, Natarajan M. Review of biodiesel composition, properties, and specifications. Renewable and Sustainable Energy Reviews 2012; 16: 143-169.

Hölderich W, Heitmann G. Synthesis of intermediate and fine chemicals on heterogeneous catalysts with respect to environmental protection. Catalysis today 1997; 38: 227-233.

Holmberg BA, Wang H, Norbeck JM, Yan Y. Controlling size and yield of zeolite Y nanocrystals using tetramethylammonium bromide. Microporous and mesoporous materials 2003; 59: 13-28.

Horváth E, Frost RL, Makó É, Kristóf J, Cseh T. Thermal treatment of mechanochemically activated kaolinite. Thermochimica Acta 2003; 404: 227-234.

Horváth E, Kristóf J, Frost RL, Jakab E, Makó É, Vágvölgyi V. Identification of superactive centers in thermally treated formamide-intercalated kaolinite. Journal of colloid and interface science 2005; 289: 132-138.

Hosseinpour N, Mortazavi Y, Bazyari A, Khodadadi A. Synergetic effects of Y-zeolite and amorphous silica-alumina as main FCC catalyst components on triisopropylbenzene cracking and coke formation. Fuel Processing Technology 2009; 90: 171-179.

Hu P, Yang H. Insight into the physicochemical aspects of kaolins with different morphologies. Applied Clay Science 2012.

Huang J, Liu Y, Wang X. Influence of differently modified palygorskites in the immobilization of a lipase. Journal of Molecular Catalysis B: Enzymatic 2008; 55: 49-54.

Huang L, Guo W, Deng P, Xue Z, Li Q. Investigation of synthesizing MCM-41/ZSM-5 composites. The Journal of Physical Chemistry B 2000; 104: 2817-2823.

Hussin F, Aroua MK, Daud WMAW. Textural characteristics, surface chemistry and activation of bleaching earth: A review. Chemical Engineering Journal 2011; 170: 90-106.

Hutchings GJ, Comninos H, Copperthwaite RG, van Rensburg LJ, Hunter R, Themistocleous T. Reactivation of zeolite and oxide catalysts using nitrous oxide. J Chem Soc, Faraday Trans 1 1989; 85: 633.

Intarapong P, Luengnaruemitchai A, Jai-In S. Transesterification of palm oil over KOH/NaY zeolite in a packed-bed reactor. International Journal of Renewable Energy Research (IJRER) 2012; 1: 271-280.

Ishihara A, Kimura K, Owaki A, Inui K, Hashimoto T, Nasu H. Catalytic cracking of VGO by hierarchical ZSM-5 zeolite containing mesoporous silica–aluminas using a Curie point pyrolyzer. Catalysis Communications 2012; 28: 163-167.

Ivanova I, Kuznetsov A, Knyazeva E, Fajula F, Thibault-Starzyk F, Fernandez C, Gilson J-P. Design of hierarchically structured catalysts by mordenites recrystallization: Application in naphthalene alkylation. Catalysis Today 2011; 168: 133-139.

Jacobsen CJ, Madsen C, Houzvicka J, Schmidt I, Carlsson A. Mesoporous zeolite single crystals. Journal of the American Chemical Society 2000a; 122: 7116.

Jacobsen CJ, Madsen C, Houzvicka J, Schmidt I, Carlsson A. Mesoporous zeolite single crystals. Journal of the American Chemical Society 2000b; 122: 7116-7117.

Janicke M, Landry C, Christiansen S, Kumar D, Stucky G, Chmelka B. Aluminum incorporation and interfacial structures in MCM-41 mesoporous molecular sieves. Journal of the American Chemical Society 1998; 120: 6940-6951.

Jiang J, Yu J, Corma A. Extra-Large-Pore Zeolites: Bridging the Gap between Micro and Mesoporous Structures. Angewandte Chemie International Edition 2010; 49: 3120.

Jin L, Auerbach SM, Monson PA. Simulating the Formation of Surfactant-Templated Mesoporous Silica Materials: A Model with Both Surfactant Self-Assembly and Silica Polymerization. Langmuir 2012; 29: 766-780.

Jin T, Yamaguchi T, Tanabe K. Mechanism of acidity generation on sulfur-promoted metal oxides. The Journal of Physical Chemistry 1986; 90: 4794-4796.

Johnston C, Stone D. Influence of hydrazine on the vibrational modes of kaolinite. Clays and Clay Minerals 1990; 38: 121-128.

Jones CW, Tsuji K, Davis ME. Organic-functionalized molecular sieves as shape-selective catalysts. Nature 1998; 393: 53.

Jones CW, Tsuji K, Takewaki T, Beck LW, Davis ME. Tailoring molecular sieve properties during SDA removal via solvent extraction. Microporous and mesoporous materials 2001; 48: 57-64.

M. C. D Jose, Kaolin containing fluid cracking catalyst, US Pat., 5,082,815, 1992.

Jung J, Jo C, Cho K, Ryoo R. Zeolite nanosheet of a single-pore thickness generated by a zeolite-structure-directing surfactant. Journal of Materials Chemistry 2012; 22: 4637-4640.

Kaeding W, Chu C, Young L, Weinstein B, Butter S. Selective alkylation of toluene with methanol to produce para-xylene. Journal of Catalysis 1981; 67: 159-174.

Karami D, Rohani S. Synthesis of pure zeolite Y using soluble silicate, a two-level factorial experimental design. Chemical Engineering and Processing: Process Intensification 2009; 48: 1288-1292.

Khder A, El-Sharkawy E, El-Hakam S, Ahmed A. Surface characterization and catalytic activity of sulfated tin oxide catalyst. Catalysis Communications 2008; 9: 769-777.

Kim S-S, Shah J, Pinnavaia TJ. Colloid-imprinted carbons as templates for the nanocasting synthesis of mesoporous ZSM-5 zeolite. Chemistry of materials 2003; 15: 1664-1668.

Koekkoek AJ, Tempelman CH, Degirmenci V, Guo M, Feng Z, Li C, Hensen EJ. Hierarchical zeolites prepared by organosilane templating: A study of the synthesis mechanism and catalytic activity. Catalysis Today 2011; 168: 96-111.

Kök MV, Pamir MR. Comparative pyrolysis and combustion kinetics of oil shales. Journal of Analytical and Applied Pyrolysis 2000; 55: 185-194.

Komvokis V, Karakoulia S, Iliopoulou E, Papapetrou M, Vasalos I, Lappas A, Triantafyllidis K. Upgrading of Fischer–Tropsch synthesis bio-waxes via catalytic cracking: Effect of acidity, porosity and metal modification of zeolitic and mesoporous aluminosilicate catalysts. Catalysis Today 2012.

Konan K, Peyratout C, Smith A, Bonnet J-P, Rossignol S, Oyetola S. Comparison of surface properties between kaolin and metakaolin in concentrated lime solutions. Journal of colloid and interface science 2009; 339: 103-109.

Konno H, Okamura T, Kawahara T, Nakasaka Y, Tago T, Masuda T. Kinetics of n-hexane cracking over ZSM-5 zeolites–effect of crystal size on effectiveness factor and catalyst lifetime. Chemical Engineering Journal 2012; 207: 490-496.

Konno H, Tago T, Nakasaka Y, Ohnaka R, Nishimura J-i, Masuda T. Effectiveness of nano-scale ZSM-5 zeolite and its deactivation mechanism on catalytic cracking of representative hydrocarbons of naphtha. Microporous and Mesoporous Materials 2013; 175: 25-33.

Köroğlu HJ, Sarıoğlan A, Tatlıer M, Erdem-Şenatalar A, Savaşçı ÖT. Effects of low-temperature gel aging on the synthesis of zeolite Y at different alkalinities. Journal of crystal growth 2002; 241: 481-488.

Kosanović C, Havancsák K, Subotić B, Svetličić V, Radić TM, Cziráki Á, Huhn G, Buljan I, Smrečki V. Study of the mechanism of formation of nano-crystalline zeolite X in heterogeneous system. Microporous and Mesoporous Materials 2011; 142: 139-146.

Kotrel S, Knözinger H, Gates B. The Haag–Dessau mechanism of protolytic cracking of alkanes. Microporous and Mesoporous Materials 2000; 35: 11-20.

Koyuncu H, Kul AR, Yıldız N, Çalımlı A, Ceylan H. Equilibrium and kinetic studies for the sorption of 3-methoxybenzaldehyde on activated kaolinites. Journal of hazardous materials 2007; 141: 128-139.

Kresge C, Leonowicz M, Roth W, Vartuli J, Beck J. Ordered mesoporous molecular sieves synthesized by a liquid-crystal template mechanism. nature 1992; 359: 710-712.

Krishna R, Paschek D. Molecular simulations of adsorption and siting of light alkanes in silicalite-1. Phys Chem Chem Phys 2001; 3: 453-458.

Kruk M, Jaroniec M. Gas adsorption characterization of ordered organic-inorganic nanocomposite materials. Chemistry of Materials 2001; 13: 3169-3183.

Kulkarni MG, Gopinath R, Meher LC, Dalai AK. Solid acid catalyzed biodiesel production by simultaneous esterification and transesterification. Green Chemistry 2006; 8: 1056-1062.

Kumar S, Davis TM, Ramanan H, Penn RL, Tsapatsis M. Aggregative growth of silicalite-1. The Journal of Physical Chemistry B 2007; 111: 3398-3400.

Kumar S, Panda AK, Singh R. Preparation and characterization of acid and alkaline treated kaolin clay. Bulletin of Chemical Reaction Engineering & Catalysis 2013a; 7.

Kumar S, Panda AK, Singh R. Preparation and Characterization of Acids and Alkali Treated Kaolin Clay. Bulletin of Chemical Reaction Engineering & Catalysis 2013b; 8.

Lai Y-H, Yen Y-F, Chen L-A. Validation of tolerance interval. Journal of Statistical Planning and Inference 2012; 142: 902-907.

Lami EB, Fajula F, Anglerot D, Des Courieres T. Single step dealumination of zeolite beta precursors for the preparation of hydrophobic adsorbents. Microporous Materials 1993; 1: 237-245.

Lee AF, Bennett JA, Manayil JC, Wilson K. Heterogeneous catalysis for sustainable biodiesel production via esterification and transesterification. Chemical Society Reviews 2014; 43: 7887-7916.

Lee H, Zones SI, Davis ME. Zeolite synthesis using degradable structure-directing agents and pore-filling agents. The Journal of Physical Chemistry B 2005; 109: 2187-2191.

Lee S, Carr CS, Shantz DF. Anionic microemulsion-mediated low temperature synthesis of anisotropic silicalite-1 nanocrystals. Langmuir 2005; 21: 12031-12036.

Lenarda M, Storaro L, Talon A, Moretti E, Riello P. Solid acid catalysts from clays: preparation of mesoporous catalysts by chemical activation of metakaolin under acid conditions. Journal of colloid and interface science 2007; 311: 537-543.

Letaief S, Detellier C. Functionalized nanohybrid materials obtained from the interlayer grafting of aminoalcohols on kaolinite. Chemical Communications 2007: 2613-2615.

Letaief S, Tonle IK, Diaco T, Detellier C. Nanohybrid materials from interlayer functionalization of kaolinite. Application to the electrochemical preconcentration of cyanide. Applied Clay Science 2008; 42: 95-101.

Li J, Li X, Zhou G, Wang W, Wang C, Komarneni S, Wang Y. Catalytic fast pyrolysis of biomass with mesoporous ZSM-5 zeolites prepared by desilication with NaOH solutions. Applied Catalysis A: General 2014; 470: 115-122.

Li Q, Amweg ML, Yee CK, Navrotsky A, Parikh AN. Photochemical template removal and spatial patterning of zeolite MFI thin films using UV/ozone treatment. Microporous and mesoporous materials 2005; 87: 45-51.

Li W, Ma F, Su F, Ma L, Zhang S, Guo Y. One-Step Preparation of Efficient and Reusable SO42−/ZrO2-Based Hybrid Solid Catalysts Functionalized by Alkyl-Bridged Organosilica Moieties for Biodiesel Production. ChemSusChem 2011; 4: 744-756.

Liu B, Li C, Ren Y, Tan Y, Xi H, Qian Y. Direct synthesis of mesoporous ZSM-5 zeolite by a dual-functional surfactant approach. Chemical Engineering Journal 2012.

Liu X, Chen Z, Chen Z, Megharaj M, Naidu R. Remediation of Direct Black G in wastewater using kaolin-supported bimetallic Fe/Ni nanoparticles. Chemical Engineering Journal 2013.

Liu X, Lu X, Sprik M, Cheng J, Meijer EJ, Wang R. Acidity of edge surface sites of montmorillonite and kaolinite. Geochimica et Cosmochimica Acta 2013.

Liu X, Yan Z, Wang H, Luo Y. In situ synthesis of NaY zeolite with coal-based kaolin. Journal of Natural Gas Chemistry 2003; 12: 63-70.

Liu Y, Zhang W, Pinnavaia TJ. Steam-stable aluminosilicate mesostructures assembled from zeolite type Y seeds. Journal of the American Chemical Society 2000; 122: 8791-8792.

Liu Y, Zhang W, Pinnavaia TJ. Steam-stable MSU-S aluminosilicate mesostructures assembled from zeolite ZSM-5 and zeolite beta seeds. Angewandte Chemie International Edition 2001; 40: 1255-1258.

Liu Z, WANG Y, XIE Z. Thoughts on the future development of zeolitic catalysts from an industrial point of view. Chinese Journal of Catalysis 2012; 33: 22-38.

Loiola A, Andrade J, Sasaki J, Da Silva L. Structural analysis of zeolite NaA synthesized by a cost-effective hydrothermal method using kaolin and its use as water softener. Journal of colloid and interface science 2012; 367: 34-39.

Lopez DE, Goodwin JG, Bruce DA, Lotero E. Transesterification of triacetin with methanol on solid acid and base catalysts. Applied Catalysis A: General 2005; 295: 97-105.

Lotero E, Liu Y, Lopez DE, Suwannakarn K, Bruce DA, Goodwin JG. Synthesis of biodiesel via acid catalysis. Industrial & engineering chemistry research 2005; 44: 5353-5363.

Louis FO B, Yun HS, Tessonnier JP, Maciel Pereira M. Hierarchical pore ZSM-5 zeolite structures: From micro- to macro-engineering of structured catalysts. Chemical Engineering Journal 2010; 161: 401.

Lovett P. Sourcing shea butter in 2010: a sustainability check. Global ingredients & formulations guide 2010: 62-68.

Ma F, Hanna MA. Biodiesel production: a review. Bioresource technology 1999; 70: 1-15.

Ma Y, Yan C, Alshameri A, Qiu X, Zhou C. Synthesis and characterization of 13X zeolite from low-grade natural kaolin. Advanced Powder Technology 2013.

Mackinnon ID, Millar GJ, Stolz W. Hydrothermal syntheses of zeolite N from kaolin. Applied Clay Science 2012; 58: 1-7.

Madon RJ, Boudart M. Experimental criterion for the absence of artifacts in the measurement of rates of heterogeneous catalytic reactions. Industrial & Engineering Chemistry Fundamentals 1982; 21: 438-447.

Mahmoud S, Saleh S, Effect of acid activation on the de-tert-butylation activity of some Jordanian clays, Clays and Clay Minerals 1999; 47:481–486.

Makó É, Kristóf J, Horváth E, Vágvölgyi V. Mechanochemical intercalation of low reactivity kaolinite. Applied Clay Science 2013; 83: 24-31.

Makó É, Senkár Z, Kristóf J, Vágvölgyi V. Surface modification of mechanochemically activated kaolinites by selective leaching. Journal of colloid and interface science 2006; 294: 362-370.

Maniar RN, Johorey AC, Pujary CT, Yadava AN. Margin of error in alignment: a study undertaken when converting from conventional to computer-assisted total knee arthroplasty. The Journal of arthroplasty 2011; 26: 82-87.

Massiot D, Dion P, Alcover JF, Bergaya F. 27Al and 29Si MAS NMR study of kaolinite thermal decomposition by controlled rate thermal analysis. Journal of the American Ceramic Society 1995; 78: 2940-2944.

Matsuhashi H, Miyazaki H, Kawamura Y, Nakamura H, Arata K. Preparation of a solid superacid of sulfated tin oxide with acidity higher than that of sulfated zirconia and its applications to aldol condensation and benzoylation1. Chemistry of materials 2001; 13: 3038-3042.

Matsuzaki I, Nitta M, Tanabe K. Application of Hammett indicators to estimating coverages of acid sites of silica-alumina by nitrogen, ethylene, water, ethyl alcohol, pyridine and n-butylamine. JOURNAL OF THE RESEARCH INSTITUTE FOR CATALYSIS HOKKAIDO UNIVERSITY 1969; 17: 46-53.

Matusik J, Kłapyta Z. Characterization of kaolinite intercalation compounds with benzylalkylammonium chlorides using XRD, TGA/DTA and CHNS elemental analysis. Applied Clay Science 2013; 83: 433-440.

Mehrabian R, Scharler R, Obernberger I. Effects of pyrolysis conditions on the heating rate in biomass particles and applicability of TGA kinetic parameters in particle thermal conversion modelling. Fuel 2012; 93: 567-575.

Melero JA, Bautista LF, Morales G, Iglesias J, Sánchez-Vázquez R. Biodiesel production from crude palm oil using sulfonic acid-modified mesostructured catalysts. Chemical Engineering Journal 2010; 161: 323-331.

Melero JA, Stucky GD, van Grieken R, Morales G. Direct syntheses of ordered SBA-15 mesoporous materials containing arenesulfonic acid groups. Journal of Materials Chemistry 2002; 12: 1664-1670.

Meyer TM, Jenny M. Measuring error for adjacent policy position estimates: Dealing with uncertainty using CMP data. Electoral Studies 2013; 32: 174-185.

Mohammed A, Karim S, Rahman AM. Characterization and Cracking Activity of Zeolite Prepared from Local Kaolin. Iraqi Journal of Chemical and Petroleum Engineering 2010; 11: 35-42.

Mortensen PM, Grunwaldt J-D, Jensen PA, Knudsen K, Jensen AD. A review of catalytic upgrading of bio-oil to engine fuels. Appl Catal A Gen 2011; 407: 1–19.

Müller M, Harvey G, Prins R. Comparison of the dealumination of zeolites beta, mordenite, ZSM-5 and ferrierite by thermal treatment, leaching with oxalic acid and treatment with SiCl< sub> 4</sub> by< sup> 1</sup> H,< sup> 29</sup> Si and< sup> 27</sup> Al MAS NMR. Microporous and mesoporous materials 2000; 34: 135-147.

Na K, Choi M, Park W, Sakamoto Y, Terasaki O, Ryoo R. Pillared MFI zeolite nanosheets of a single-unit-cell thickness. Journal of the American Chemical Society 2010; 132: 4169-4177.

Na K, Jo C, Kim J, Cho K, Jung J, Seo Y, Messinger RJ, Chmelka BF, Ryoo R. Directing zeolite structures into hierarchically nanoporous architectures. Science 2011a; 333: 328-330.

Na K, Jo C, Kim J, Cho K, Jung J, Seo Y, Messinger RJ, Chmelka BF, Ryoo R. Directing zeolite structures into hierarchically nanoporous architectures. Science 2011b; 333: 328-332.

Na K, Park W, Seo Y, Ryoo R. Disordered assembly of MFI zeolite nanosheets with a large volume of intersheet mesopores. Chemistry of Materials 2011; 23: 1273-1279.

Naik M, Meher L, Naik S, Das L. Production of biodiesel from high free fatty acid Karanja (Pongamia pinnata) oil. Biomass and Bioenergy 2008; 32: 354-357.

Narkhede N, Singh S, Patel A. Recent progress on supported polyoxometalates for biodiesel synthesis via esterification and transesterification. Green Chemistry 2015; 17: 89-107.

Niederberger M, Cölfen H. Oriented attachment and mesocrystals: Non-classical crystallization mechanisms based on nanoparticle assembly. Physical Chemistry Chemical Physics 2006; 8: 3271-3277.

Nourmohammadi M, Jozani MJ, Johnson BC. Distribution-free tolerance intervals with nomination samples: Applications to mercury contamination in fish. Statistical Methodology 2015; 26: 16-33.

Ogura M, Shinomiya S-y, Tateno J, Nara Y, Nomura M, Kikuchi E, Matsukata M. Alkali-treatment technique—new method for modification of structural and acid-catalytic properties of ZSM-5 zeolites. Applied Catalysis A: General 2001; 219: 33-43.

Ooi Y-S, Zakaria R, Mohamed AR, Bhatia S. Synthesis of composite material MCM-41/Beta and its catalytic performance in waste used palm oil cracking. Applied Catalysis A: General 2004; 274: 15-23.

Ounas A, Aboulkas A, Bacaoui A, Yaacoubi A. Pyrolysis of olive residue and sugar cane bagasse: Non-isothermal thermogravimetric kinetic analysis. Bioresource technology 2011; 102: 11234-11238.

Ovramenko N, Kalenchuk V, Zakharchenko O, Ovcharenko F. Effect of intercalation of (HBO 2) n and mechanochemical treatment on acid-base properties of kaolinite. 1994.

Pan F, Lu X, Wang Y, Chen S, Wang T, Yan Y. Organic template-free synthesis of ZSM-5 zeolite from coal-series kaolinite. Materials Letters 2014a; 115: 5-8.

Pan F, Lu X, Wang Y, Chen S, Wang T, Yan Y. Synthesis and crystallization kinetics of ZSM-5 without organic template from coal-series kaolinite. Microporous and Mesoporous Materials 2014b; 184: 134-140.

Panda AK, Mishra B, Mishra D, Singh R. Effect of sulphuric acid treatment on the physico-chemical characteristics of kaolin clay. Colloids and Surfaces A: Physicochemical and Engineering Aspects 2010; 363: 98-104.

Panda AK, Singh R. Catalytic performances of kaoline and silica alumina in the thermal degradation of polypropylene. Journal of Fuel Chemistry and Technology 2011; 39: 198-202.

Parikh AN, Navrotsky A, Li Q, Yee CK, Amweg ML, Corma A. Non-thermal calcination by ultraviolet irradiation in the synthesis of microporous materials. Microporous and mesoporous materials 2004; 76: 17.

Pastore HO, Martins GA, Strauss M, Pedroni LG, Superti GB, de Oliveira EC, Gatti G, Marchese L. The CAL family of molecular sieves: Silicoaluminophosphates prepared from a layered aluminophosphate. Microporous and Mesoporous Materials 2008; 107: 81-89.

Patel A, Brahmkhatri V. Kinetic study of oleic acid esterification over 12-tungstophosphoric acid catalyst anchored to different mesoporous silica supports. Fuel Processing Technology 2013; 113: 141-149.

Pérez-Ramıīrez J, Verboekend D, Bonilla A, Abelló S. Zeolite catalysts with tunable hierarchy factor by pore-growth moderators. Adv Funct Mater 2009; 19: 3972-3979.

Pérez-Ramírez J, Verboekend D, Bonilla A, Abelló S. Zeolite Catalysts with Tunable Hierarchy Factor by Pore-Growth Moderators. Advanced Functional Materials 2009; 19: 3972-3979.

Perissinotto M, Lenarda M, Storaro L, Ganzerla R. Solid acid catalysts from clays: Acid leached metakaolin as isopropanol dehydration and 1-butene isomerization catalyst. Journal of Molecular Catalysis A: Chemical 1997; 121: 103-109.

Peters TA, Benes NE, Holmen A, Keurentjes JT. Comparison of commercial solid acid catalysts for the esterification of acetic acid with butanol. Applied Catalysis A: General 2006; 297: 182-188.

Phung TK, Casazza AA, Aliakbarian B, Finocchio E, Perego P. Catalytic conversion of ethyl acetate and acetic acid on alumina as models of vegetable oils conversion to biofuels. Chemical Engineering Journal 2013; 215–216: 838–848.

Plançon A, Zacharie C. Expert system for structural characterization of kaolinites. Clay Minerals 1990; 25: 249-260.

Platz T, Pinkowski C, van Wijck F, Kim I-H, Di Bella P, Johnson G. Reliability and validity of arm function assessment with standardized guidelines for the Fugl-Meyer Test, Action Research Arm Test and Box and Block Test: a multicentre study. Clinical Rehabilitation 2005; 19: 404-411.

Prokešová P, Mintova S, Čejka J, Bein T. Preparation of nanosized micro/mesoporous composites. Materials Science and Engineering: C 2003a; 23: 1001-1005.

Prokešová P, Mintova S, Čejka J, Bein T. Preparation of nanosized micro/mesoporous composites via simultaneous synthesis of Beta/MCM-48 phases. Microporous and mesoporous materials 2003b; 64: 165-174.

Ptáček P, Kubátová D, Havlica J, Brandštetr J, Šoukal F, Opravil T. The non-isothermal kinetic analysis of the thermal decomposition of kaolinite by thermogravimetric analysis. Powder Technology 2010; 204: 222-227.

Ptáček P, Opravil T, Šoukal F, Wasserbauer J, Másilko J, Baráček J. The influence of structure order on the kinetics of dehydroxylation of kaolinite. Journal of the European Ceramic Society 2013.

Qin Z, Shen B, Yu Z, Deng F, Zhao L, Zhou S, Yuan D, Gao X, Wang B, Zhao H. A defect-based strategy for the preparation of mesoporous zeolite Y for high-performance catalytic cracking. Journal of Catalysis 2013; 298: 102-111.

Ramos MJ, Casas A, Rodríguez L, Romero R, Pérez Á. Transesterification of sunflower oil over zeolites using different metal loading: a case of leaching and agglomeration studies. Applied Catalysis A: General 2008; 346: 79-85.

Reinoso D, Damiani D, Tonetto G. Synthesis of biodiesel from soybean oil using zinc layered hydroxide salts as heterogeneous catalysts. Catalysis Science & Technology 2014; 4: 1803-1812.

Rinaldi R, Schüth F. Design of solid catalysts for the conversion of biomass. Energy & Environmental Science 2009; 2: 610-626.

Rong T-J, Xiao J-k. The catalytic cracking activity of the kaolin-group minerals. Materials Letters 2002; 57: 297-301.

Ropero-Vega J, Aldana-Pérez A, Gómez R, Niño-Gómez M. Sulfated titania [TiO 2/SO 4 2−]: a very active solid acid catalyst for the esterification of free fatty acids with ethanol. Applied Catalysis A: General 2010; 379: 24-29.

Rosa PA, Azevedo AM, Aires-Barros MR. Application of central composite design to the optimisation of aqueous two-phase extraction of human antibodies. Journal of Chromatography A 2007; 1141: 50-60.

Sabu K, Sukumar R, Rekha R, Lalithambika M. A comparative study on H2SO4, HNO3 and HClO4 treated metakaolinite of a natural kaolinite as Friedel-Crafts alkylation catalyst. Catalysis today 1999a; 49: 321-326.

Sabu K, Sukumar R, Rekha R, Lalithambika M. A comparative study on H 2 SO 4, HNO 3 and HClO 4 treated metakaolinite of a natural kaolinite as Friedel–Crafts alkylation catalyst. Catalysis today 1999b; 49: 321-326.

Sait HH, Hussain A, Salema AA, Ani FN. Pyrolysis and combustion kinetics of date palm biomass using thermogravimetric analysis. Bioresource technology 2012; 118: 382-389.

Saito A, Foley HC. High-resolution nitrogen and argon adsorption on ZSM-5 zeolites: effects of cation exchange and SiAl ratio. Microporous Materials 1995; 3: 543-556.

Sánchez RT, Basaldella E, Marco J. The effect of thermal and mechanical treatments on kaolinite: characterization by XPS and IEP measurements. Journal of colloid and interface science 1999; 215: 339-344.

Sani YM, Daud WMAW, Abdul Aziz A. Activity of solid acid catalysts for biodiesel production: A critical review. Applied Catalysis A: General 2014; 470: 140-161.

Saravanan K, Tyagi B, Bajaj H. Sulfated zirconia: an efficient solid acid catalyst for esterification of myristic acid with short chain alcohols. Catalysis Science & Technology 2012; 2: 2512-2520.

Sastre G, Pulido A, Castañeda R, Corma A. Effect of the Germanium Incorporation in the Synthesis of EU-1, ITQ-13, ITQ-22, and ITQ-24 Zeolites. The Journal of Physical Chemistry B 2004; 108: 8830.

Sato K, Nishimura Y, Matsubayashi N, Imamura M, Shimada H. Structural changes of Y zeolites during ion exchange treatment: effects of Si/Al ratio of the starting NaY. Microporous and mesoporous materials 2003; 59: 133-146.

Scherzer J. Octane-enhancing, zeolitic FCC catalysts: scientific and technical aspects. Catalysis Reviews—Science and Engineering 1989; 31: 215-354.

Schüth F. Endo-and exotemplating to create high-surface-area inorganic materials. Angewandte Chemie International Edition 2003; 42: 3604.

Serrano D, Pizarro P. Synthesis strategies in the search for hierarchical zeolites. Chemical Society Reviews 2013; 42: 4004-4035.

Shen S, Chen Q, Chow P, Tan G, Zeng X, Wang Z, Tan RB. Steam-assisted solid wet-gel synthesis of high-quality nanorods of boehmite and alumina. The Journal of Physical Chemistry C 2007; 111: 700-707.

Shen B, Wang P, Yi Z, Zhang W, Tong X, Liu Y, Guo Q, Gao J, Xu C, Synthesis of zeolite β from kaolin and its catalytic performance for FCC naphtha aromatization, Energy Fuels 2008; 23:60–64.

Shi L, Zhang X, Chen Z, Removal of chromium (VI) from wastewater using bentonite-supported nanoscale zero-valent iron, Water Resources, 2011; 45: 886–892.

Shi G, Lin X-Y, Fan Y, Bao X-J. Desilication modification of ZSM-5 zeolite and its catalytic properties in hydro-upgrading. Journal of Fuel Chemistry and Technology 2013; 41: 589-594.

Shi JC, Albers EW, Wilson GR. (1998). Process for improving the physical and catalytic properties of a fluid cracking catalyst: Google Patents.

Singh S, Wu C, Williams PT. Pyrolysis of waste materials using TGA-MS and TGA-FTIR as complementary characterisation techniques. Journal of Analytical and Applied Pyrolysis 2012; 94: 99-107.

Skreiberg A, Skreiberg Ø, Sandquist J, Sørum L. TGA and macro-TGA characterisation of biomass fuels and fuel mixtures. Fuel 2011; 90: 2182-2197.

Slaty F, Khoury H, Wastiels J, Rahier H. Characterization of alkali activated kaolinitic clay. Applied Clay Science 2013.

Slopiecka K, Bartocci P, Fantozzi F. Thermogravimetric analysis and kinetic study of poplar wood pyrolysis. Applied Energy 2012; 97: 491-497.

Song K-h, Wang X, Qian P, Zhang C, Zhang Q. Theoretical study of interaction of formamide with kaolinite. Computational and Theoretical Chemistry 2013; 1020: 72-80.

Soriano NU, Venditti R, Argyropoulos DS. Biodiesel synthesis via homogeneous Lewis acid-catalyzed transesterification. Fuel 2009; 88: 560-565.

Soualah A, Lemberton J-L, Pinard L, Chater M, Magnoux P, Moljord K. Hydroisomerization of long-chain< i> n</i>-alkanes on bifunctional Pt/zeolite catalysts: Effect of the zeolite structure on the product selectivity and on the reaction mechanism. Applied Catalysis A: General 2008; 336: 23-28.

Souza A, Danta H, Silva MC, Santos IM, Fernandes V, Sinfrônio FS, Teixeira LS, Novák C. Thermal and kinetic evaluation of cotton oil biodiesel. Journal of thermal analysis and calorimetry 2007; 90: 945-949.

Speronello BK. (1986). Calcining kaolin, catalyst supports: Google Patents.

Srilatha K, Kumar CR, Devi BP, Prasad R, Prasad PS, Lingaiah N. Efficient solid acid catalysts for esterification of free fatty acids with methanol for the production of biodiesel. Catalysis Science & Technology 2011; 1: 662-668.

Stoch L. Mineraly Ilaste ('Clay Minerals'). Wydaw geologiczne, Warszawa 1974; 503.

Strohmaier KG, Vaughan DE. Structure of the first silicate molecular sieve with 18-ring pore openings, ECR-34. Journal of the American Chemical Society 2003; 125: 16035.

Suitch P, Young R. Atom positions in highly ordered kaolinite. CLAYS CLAY MINER Clays Clay Miner 1983; 31: 357.

Sun D, Li B, Li Y, Yu C, Zhang B, Fei H. Characterization of exfoliated/delamination kaolinite. Materials Research Bulletin 2011; 46: 101-104.

Sun J, Bonneau C, Cantín Á, Corma A, Díaz-Cabañas MJ, Moliner M, Zhang D, Li M, Zou X. The ITQ-37 mesoporous chiral zeolite. Nature 2009; 458: 1154.

Syed S, Qudaih R, Talab I, Janajreh I. Kinetics of pyrolysis and combustion of oil shale sample from thermogravimetric data. Fuel 2011; 90: 1631-1637.

Takewaki T, Beck LW, Davis ME. Zincosilicate CIT-6: A precursor to a family of* BEA-type molecular sieves. The Journal of Physical Chemistry B 1999a; 103: 2674.

Takewaki T, Beck LW, Davis ME. Zincosilicate CIT-6: A precursor to a family of* BEA-type molecular sieves. The Journal of Physical Chemistry B 1999b; 103: 2674-2679.

Tan Q, Bao X, Song T, Fan Y, Shi G, Shen B, Liu C, Gao X. Synthesis, characterization, and catalytic properties of hydrothermally stable macro–meso–micro-porous composite materials synthesized via in situ assembly of preformed zeolite Y nanoclusters on kaolin. Journal of Catalysis 2007; 251: 69-79.

Tanabe K, Misono M, Hattori H, Ono Y. (1990). *New solid acids and bases: their catalytic properties*: Elsevier.

Tao Y, Kanoh H, Kaneko K. Uniform mesopore-donated zeolite Y using carbon aerogel templating. The Journal of Physical Chemistry B 2003; 107: 10974-10976.

Tatsumi T, Matsuhashi H, Arata K. A Study of the Preparation Procedures of Sulfated Zirconia Prepared from Zirconia Gel. The Effect of the pH of the Mother Solution

on the Isomerization Activity of n-Pentane. Bulletin of the Chemical Society of Japan 1996; 69: 1191-1194.

Testa ML, La Parola V, Venezia AM. Esterification of acetic acid with butanol over sulfonic acid-functionalized hybrid silicas. Catalysis Today 2010; 158: 109-113.

Testa ML, La Parola V, Venezia AM. Transesterification of short chain esters using sulfonic acid-functionalized hybrid silicas: Effect of silica morphology. Catalysis Today 2014; 223: 115-121.

Tironi A, Trezza M, Irassar E, Scian A. Thermal treatment of kaolin: effect on the pozzolanic activity. Procedia Materials Science 2012; 1: 343-350.

Tiwari P, Deo M. Compositional and kinetic analysis of oil shale pyrolysis using TGA–MS. Fuel 2012; 94: 333-341.

Tombácz E, Szekeres M. Surface charge heterogeneity of kaolinite in aqueous suspension in comparison with montmorillonite. Applied Clay Science 2006; 34: 105-124.

Tosheva L, Valtchev VP. Nanozeolites: Synthesis, crystallization mechanism, and applications. Chemistry of Materials 2005; 17: 2494.

Touillaux R, Salvador P, Vandermeersche C, Fripiat J. Study of Water Layers Adsorbed on Na-and Ca-Montmorillonite by the Pulsed Nuclear Magnetic Resonance Technique. Israel Journal of Chemistry 1968; 6: 337-348.

Trong On D, Kaliaguine S. Large-Pore Mesoporous Materials with Semi-Crystalline Zeolitic Frameworks. Angewandte Chemie 2001; 113: 3348-3351.

Trong On D, Kaliaguine S. Zeolite-coated mesostructured cellular silica foams. Journal of the American Chemical Society 2003; 125: 618-619.

Usai EM, Sini MF, Meloni D, Solinas V, Salis A. Sulfonic acid-functionalized mesoporous silicas: Microcalorimetric characterization and catalytic performance toward biodiesel synthesis. Microporous and Mesoporous Materials 2013; 179: 54-62.

Üzüm Ç, Shahwan T, Eroğlu A, Hallam K, Scott T, Lieberwirth I. Synthesis and characterization of kaolinite-supported zero-valent iron nanoparticles and their application for the removal of aqueous Cu< sup> 2+</sup> and Co< sup> 2+</sup> ions. Applied Clay Science 2009; 43: 172-181.

Vaccari A. Preparation and catalytic properties of cationic and anionic clays. Catalysis Today 1998; 41: 53-71.

Valášková M, Barabaszová K, Hundáková M, Ritz M, Plevová E. Effects of brief milling and acid treatment on two ordered and disordered kaolinite structures. Applied Clay Science 2011; 54: 70-76.

Valášková M, Rieder M, Matějka V, Čapková P, Slíva A. Exfoliation/delamination of kaolinite by low-temperature washing of kaolinite–urea intercalates. Applied clay science 2007; 35: 108-118.

Van Donk S, Janssen AH, Bitter JH, de Jong KP. Generation, characterization, and impact of mesopores in zeolite catalysts. Catalysis Reviews 2003; 45: 297-319.

Varga G. The structure of kaolinite and metakaolinite. Epitoanyag 2007; 59: 6-9.

Vega AJ. Heteronuclear chemical-shift correlations of silanol groups studied by two-dimensional cross-polarization magic angle spinning NMR. Journal of the American Chemical Society 1988; 110: 1049-1054.

Verhoef MJ, Kooyman PJ, van der Waal JC, Rigutto MS, Peters JA, van Bekkum H. Partial transformation of MCM-41 material into zeolites: formation of nanosized MFI type crystallites. Chemistry of materials 2001; 13: 683-687.

Vining GG, Kowalski S. (2010). *Statistical methods for engineers*: Cengage Learning.

Vizcayno C, De Gutierrez R, Castello R, Rodriguez E, Guerrero C. Pozzolan obtained by mechanochemical and thermal treatments of kaolin. Applied Clay Science 2010; 49: 405-413.

Volkens A. Quantifying the election programmes: Coding procedures and controls. I Budge et al(sous la direction) Mapping Policy Preferences, Oxford: Oxford University Press Age 2001.

Wang D, Li X, Liu Z, Zhang Y, Xie Z, Tang Y. Hierarchical structured ZSM-5 zeolite of oriented nanorods and its performance in the alkylation of phenol with isopropanol. Journal of colloid and interface science 2010; 350: 290-294.

Wang D, Liu Z, Wang H, Xie Z, Tang Y. Shape-controlled synthesis of monolithic ZSM-5 zeolite with hierarchical structure and mechanical stability. Microporous and Mesoporous Materials 2010; 132: 428-434.

Wang H, Liu Y, Pinnavaia TJ. Highly acidic mesostructured aluminosilicates assembled from surfactant-mediated zeolite hydrolysis products. The Journal of Physical Chemistry B 2006; 110: 4524-4526.

Wang H, Liu Z, Shen J, Liu H. High-throughput characterization of heterogeneous catalysts by temperature-programmed analysis method. Catalysis Communications 2004; 5: 55-58.

Wang L, Lin K, Di Y, Zhang D, Li C, Yang Q, Yin C, Sun Z, Jiang D, Xiao F-S. High-temperature synthesis of stable ordered mesoporous silica materials using mesoporous carbon as a hard template. Microporous and mesoporous materials 2005; 86: 81-88.

Wang L, Yin C, Shan Z, Liu S, Du Y, Xiao F-S. Bread-template synthesis of hierarchical mesoporous ZSM-5 zeolite with hydrothermally stable mesoporosity. Colloids and Surfaces A: Physicochemical and Engineering Aspects 2009; 340: 126-130.

Wang P, Lv A, Hu J, Xu Ja, Lu G. In situ synthesis of SAPO-34 grown onto fully calcined kaolin microspheres and its catalytic properties for the MTO reaction. Industrial & Engineering Chemistry Research 2011; 50: 9989-9997.

Wang P, Shen B, Shen D, Peng T, Gao J. Synthesis of ZSM-5 zeolite from expanded perlite/kaolin and its catalytic performance for FCC naphtha aromatization. Catalysis Communications 2007; 8: 1452-1456.

Wang T, Lu X, Yan Y. Synthesis, characterization and crystallization mechanism of SAPOs from natural kaolinite. Microporous and Mesoporous Materials 2010; 136: 138-147.

Wang X, Jimmy CY, Liu P, Wang X, Su W, Fu X. Probing of photocatalytic surface sites on SO 4 2−/TiO 2 solid acids by in situ FT-IR spectroscopy and pyridine adsorption. Journal of Photochemistry and Photobiology A: Chemistry 2006; 179: 339-347.

Wilson K, Lee AF. Rational design of heterogeneous catalysts for biodiesel synthesis. Catalysis Science & Technology 2012; 2: 884-897.

Xie W, Peng H, Chen L. Transesterification of soybean oil catalyzed by potassium loaded on alumina as a solid-base catalyst. Applied Catalysis A: General 2006; 300: 67-74.

Xie W, Wang H, Li H. Silica-supported tin oxides as heterogeneous acid catalysts for transesterification of soybean oil with methanol. Industrial & Engineering Chemistry Research 2011; 51: 225-231.

Xu H, Guan J, Wu S, Kan Q. Synthesis of Beta/MCM-41 composite molecular sieve with high hydrothermal stability in static and stirred condition. Journal of colloid and interface science 2009; 329: 346-350.

Xu M, Cheng M, Bao X. Growth of ultrafine zeolite Y crystals on metakaolin microspheres. Chemical Communications 2000: 1873-1874.

Yamaguchi T, Jin T, Tanabe K. Structure of acid sites on sulfur-promoted iron oxide. The Journal of Physical Chemistry 1986; 90: 3148-3152.

Yang C, Xuaf Q. States of aluminum in zeolite β and influence of acidic or basic medium. Zeolites 1997; 19: 404-410.

Yang G, Wei Y, Xu S, Chen J, Li J, Liu Z, Yu J, Xu R. Nanosize-enhanced lifetime of SAPO-34 catalysts in methanol-to-olefin reactions. The Journal of Physical Chemistry C 2013; 117: 8214-8222.

Yang H, Lu R, Wang L. Study of preparation and properties on solid superacid sulfated titania–silica nanomaterials. Materials Letters 2003; 57: 1190-1196.

Yang S-T, Kim J-Y, Chae H-J, Kim M, Jeong S-Y, Ahn W-S. Microwave synthesis of mesoporous SAPO-34 with a hierarchical pore structure. Materials Research Bulletin 2012; 47: 3888-3892.

Yang W, Zaoui A. Uranyl adsorption on (001) surfaces of kaolinite: A molecular dynamics study. Applied Clay Science 2013; 80: 98-106.

Yoo WC, Zhang X, Tsapatsis M, Stein A. Synthesis of mesoporous ZSM-5 zeolites through desilication and re-assembly processes. Microporous and Mesoporous Materials 2012; 149: 147-148.

Yu H, Wang X-q, Long Y-c. Synthesis of< i> b</i>-axis oriented high silica MFI type zeolite crystals introduced with co-template role. Microporous and mesoporous materials 2006; 95: 234-240.

Yu J, Shi J-L, Chen H-R, Yan J-N, Yan D-S. Effect of inorganic salt addition during synthesis on pore structure and hydrothermal stability of mesoporous silica. Microporous and mesoporous materials 2001; 46: 153-162.

Yu Y, Li X, Su L, Zhang Y, Wang Y, Zhang H. The role of shape selectivity in catalytic fast pyrolysis of lignin with zeolite catalysts. Applied Catalysis A: General 2012; 447: 115-123.

Yurdakoc M, Akcay M, Tonbul Y, Yurdakoc K. Acidity of silica-alumina catalysts by amine titration using Hammett indicators and FT-IR study of pyridine adsorption. Turkish Journal of Chemistry 1999; 23: 319-328.

Yuwono VM, Burrows ND, Soltis JA, Penn RL. Oriented aggregation: formation and transformation of mesocrystal intermediates revealed. Journal of the American Chemical Society 2010; 132: 2163-2165.

Zabeti M, Daud WMAW, Aroua MK. Activity of solid catalysts for biodiesel production: a review. Fuel Processing Technology 2009; 90: 770-777.

Zhang W, Han X, Liu X, Bao X. The stability of nanosized HZSM-5 zeolite: a high-resolution solid-state NMR study. Microporous and mesoporous materials 2001; 50: 13-23.

Zhang X, Guo Q, Qin B, Zhang Z, Ling F, Sun W, Li R. Structural features of binary microporous zeolite composite Y-Beta and its hydrocracking performance. Catalysis Today 2010; 149: 212-217.

Zhang Z, Han Y, Xiao F-S, Qiu S, Zhu L, Wang R, Yu Y, Zhang Z, Zou B, Wang Y. Mesoporous aluminosilicates with ordered hexagonal structure, strong acidity, and extraordinary hydrothermal stability at high temperatures. Journal of the American Chemical Society 2001; 123: 5014-5021.

Zhang Z, Sun H, Shao X, Li D, Yu H, Han M. Three-Dimensionally Oriented Aggregation of a Few Hundred Nanoparticles into Monocrystalline Architectures. Advanced Materials 2005; 17: 42-43.

Zhao D, Feng J, Huo Q, Melosh N, Fredrickson GH, Chmelka BF, Stucky GD. Triblock copolymer syntheses of mesoporous silica with periodic 50 to 300 angstrom pores. Science 1998; 279: 548-552.

Zhao G, Teng J, Xie Z, Jin W, Yang W, Chen Q, Tang Y. Effect of phosphorus on HZSM-5 catalyst for C< sub> 4</sub>-olefin cracking reactions to produce propylene. Journal of Catalysis 2007; 248: 29-37.

Zheng J, Yi Y, Wang W, Guo K, Ma J, Li R. Synthesis of bi-phases composite zeolites MFZ and its hierarchical effects in isopropylbenzene catalytic cracking. Microporous and Mesoporous Materials 2013; 171: 44-52.

Zheng J, Zeng Q, Yi Y, Wang Y, Ma J, Qin B, Zhang X, Sun W, Li R. The hierarchical effects of zeolite composites in catalysis. Catalysis Today 2011; 168: 124-132.

Zheng J, Zeng Q, Zhang Y, Wang Y, Ma J, Zhang X, Sun W, Li R. Hierarchical Porous Zeolite Composite with a Core− Shell Structure Fabricated Using β-Zeolite Crystals as Nutrients as Well as Cores. Chemistry of Materials 2010; 22: 6065-6074.

Zhou L, Luo T, Huang Q. Co-pyrolysis characteristics and kinetics of coal and plastic blends. Energy Conversion and Management 2009; 50: 705-710.

Zhu J, Cui Y, Wang Y, Wei F. Direct synthesis of hierarchical zeolite from a natural layered material. Chemical Communications 2009: 3282-3284.

Zorn ME, Gibbons RD, Sonzogni WC. Evaluation of approximate methods for calculating the limit of detection and limit of quantification. Environmental science & technology 1999; 33: 2291-2295.

LIST OF PUBLICATIONS AND PAPERS PRESENTED

PUBLICATIONS

- Peter Adeniyi Alaba, Yahaya Muhammad Sani, Isah Y Mohammed, Wan Mohd Ashri Wan Daud, Insight into Catalyst Deactivation Mechanism and Suppression Techniques in Thermocatalytic Deoxygenation of Bio-oil over Zeolites. Reviews in Chemical Engineering (2015).
- Peter Adeniyi Alaba, Yahaya Muhammad Sani, Wan Mohd Ashri Wan Daud, Synthesis of hierarchical nanoporous HY zeolites from activated kaolin, a central composite design optimization study. Chinese Journal of Catalysis (2015) 36: 1846–1851. DOI: 10.1016/S1872-2067(15)60962-7. http://www.sciencedirect.com/science/journal/18722067.
- Peter Adeniyi Alaba, Yahaya Muhammad Sani, Isah Y Mohammed, Yousif Abakr, Wan Mohd Ashri Wan Daud, Synthesis and Application of Hierarchical Mesoporous HZSM-5 for Biodiesel Production from Shea Butter. Journal of the Taiwan Institute of Chemical Engineers (2015) 000:1-8. http://dx.doi.org/10.1016/j.jtice.2015.09.006.
- Peter Adeniyi Alaba, Yahaya Muhammad Sani, Wan Mohd Ashri Wan Daud, Kaolinite properties and advances for solid acid and basic catalyst synthesis. RSC advances (2015) 2015, DOI: 10.1039/C5RA18884A.
- Yahaya Muhammad Sani, Peter Adeniyi Alaba, Aisha Olatope Raji-Yahya, A. R. Abdul Aziza, Wan Mohd Ashri Wan Daud, Acidity and catalytic performance of Yb-doped SO_4^{2-}/Zr in comparison with SO_4^{2-}/Zr catalysts synthesized via different preparatory conditions for biodiesel production. Journal of the Taiwan Institute of Chemical Engineers (2015) 000:1–10. http://dx.doi.org/10.1016/j.jtice.2015.07.016
- Yahaya M. Sani, Peter A. Alaba, Aisha O. Raji-Yahya, A. R. Abdul Aziza, Wan Mohd A. Wan Daud, Palm Frond and Spikelet as Environmentally Benign Alternative Solid Acid Catalysts for Biodiesel Production. BioResources 10(2) 2015, 3393-3408.
- Yahaya Muhammad Sani, Peter Adeniyi Alaba, Aisha Olatope Raji-Yahya, A. R. Abdul Aziza, Wan Mohd Ashri Wan Daud, Facile synthesis of sulfated mesoporous Zr/ZSM-5 with improved Brønsted acidity and superior activity over SZr/Ag, SZr/Ti, and SZr/W in transforming UFO into biodiesel. Journal of the Taiwan Institute of Chemical Engineers (2015) 000:1–11. http://dx.doi:10.1016/j.jtice.2015.10.010

CONFERENCE ATTENDED AND SEMINAR PRESENTATION

- 2014 Regional conference on chemical Engineering, Yogyakarta, Indonesia, December 23, 2014, "Synthesis and characterization of highly ordered solid acid catalyst from kaolin" (ISBN: 978-602-71398-0-0).

- 2014 Regional conference on chemical Engineering, Yogyakarta, Indonesia, December 23, 2014, "Effect of Preparation Method in Activating Active Sites and Catalytic Activity of SO42-/Zro2 in Biodiesel Production" (ISBN: 978-602-71398-0-0).

- Seminar presentation at Chemical Engineering Department, Faculty of Engineering, The University of Malaya, 25th Nov. 2014, "Synthesis and application of hierarchical mesoporous HZSM-5 for biodiesel production from shea butter".

- 2015 World Conference on Engineering & Applied Sciences, Kuala Lumpur, Malaysia, 30-31 May, 2015 "Synthesis and Characterization of Hierarchical Nanoporous HY Zeolite from Acid Activated Kaolin".

- Thirteenth TheIIER International Conference, Dubai, UAE, 1st March 2015, "Palm Frond and Spikelet as Environmentally Benign Alternative Solid Acid Catalysts For Biodiesel Production" (ISBN: 978-93-84209-96-4).